UNIVERSITY OF CALGARY

Towards a Real-World Quantum Repeater

by

Marcel.li Grimau Puigibert

A THESIS

SUBMITTED TO THE FACULTY OF GRADUATE STUDIES

IN PARTIAL FULFILLMENT OF THE REQUIREMENTS FOR THE

DEGREE OF DOCTOR OF PHILOSOPHY

GRADUATE PROGRAM IN PHYSICS AND ASTRONOMY

CALGARY, ALBERTA

December, 2017

Abstract

"Quantum communication is the art of transferring a quantum state from one place to another" [1]. The capability of distributing quantum states allows, for instance, provably secure communication and, in the near future, will enable the interconnection of quantum computers to establish a quantum internet [2]. A convenient way to send quantum states from one place to another is to encode them into photons and distribute them using optical fibres. The distance over which this can be achieved is still limited to a few hundred of kilometers. However, it can be extended in principle to arbitrary long distances by means of quantum repeaters. The realization of such quantum repeaters will require the engineering and interfacing of heterogeneous elements such as entangled photon-pair sources, quantum memories and entanglement swapping operations.

The main goal of this thesis is to develop and study the compatibility of the main elements required to build a frequency multiplexed quantum repeater. This architecture requires a frequency multimode entangled photon pair source which, for example, could be implemented exploiting the process that involves the interaction of a strong light pulse with a non-linear crystal. Such a process is versatile and allows easy tailoring of the photon-pair spectral properties in order to match the requirements of the frequency multiplexed quantum repeater architecture. First, as a precursor of such a photon pair source, we developed a novel heralded single photon source that involves spectrally resolved single photon detection and on-demand frequency shifting. These capabilities are also essential tools in a frequency multiplexed quantum repeater. Next, we demonstrated the compatibility of such a sources with frequency multimode photonic quantum memories by performing spectrally multiplexed storage of single photons. We also tested the capability of high-fidelity storage of photons encoding quantum information in their polarization degree of freedom. Finally, we showed that entanglement swapping operations,

i.e. Bell-state measurements, can be performed using photon pair sources compatible with quantum memories, quantum repeater architectures, and real-world scenarios.

While a lot of effort remains to be done, in the work presented in this thesis we demonstrated that all the key elements required to build a frequency multiplexed quantum repeater can be built and eventually be interfaced. The main obstacles towards that goal and possible ways to overcome them are also discussed.

Preface

Below is a list of papers that are included in this thesis. Papers are listed according to the order in which they are introduced:

- **Paper 1:** *Heralded Single Photons Based on Spectral Multiplexing and Feed-Forward Control*, M. Grimau Puigibert, G. H. Aguilar, Q. Zhou, F. Marsili, M. D. Shaw, V. B. Verma, S. W. Nam, D. Oblak, and W. Tittel, Phys. Rev. Lett. 119, 083601, Published 25 August 2017.

- **Paper 2:** *A multiplexed light-matter interface for fibre-based quantum networks*, E. Saglamyurek, M. Grimau Puigibert, Q. Zhou, L. Giner, F. Marsili, V. B. Verma, S. W. Nam, L. Oesterling, D. Nippa, D. Oblak, and W. Tittel, Nature Communications 7, 11202, Published 05 April 2016.

- **Paper 3:** *Telecom-Wavelength Atomic Quantum Memory in Optical Fiber for Heralded Polarization Qubits*, J. Jin, E. Saglamyurek, M. Grimau Puigibert, V. B. Verma, F. Marsili, S. W. Nam, D. , and Wolfgang Tittel, Phys. Rev. Lett. 115, 140501, Published 28 September 2015.

- **Paper 4:** *Entanglement swapping with quantum-memory-compatible photons*, J. Jin, M. Grimau Puigibert, L. Giner, J. A. Slater, M. R. E. Lamont, V. B. Verma, M. D. Shaw, F. Marsili, S. W. Nam, D. Oblak, and W. Tittel, Phys. Rev. A 92, 012329, Published 27 July 2015.

- **Paper 5:** *Quantum teleportation across a metropolitan fibre network*, R. Valivarthi, M. Grimau Puigibert, Q. Zhou, G. H. Aguilar, V. B. Verma, F. Marsili, M. D. Shaw, S. W. Nam, D. Oblak, and W. Tittel, Nature Photonics 10, 676680, Published 19 September 2016.

Acknowledgements

I want to acknowledge all those who have accompanied me during this trip and made this possible. I would especially wish to recognize my family and friends for impressing on me the values that are guiding me through life.

Gràcies Irene per donar-me tot el teu suport, per formar part i omplir amb una nova vida "Gael" la meva vida.

Figure 0.1: Collection of moments with QC2Lab members

Figure 0.2: QC2Lab members in summer of 2015

Table of Contents

List of Tables

List of Figures and Illustrations

Chapter 1

Introduction

At a first glance, basic scientific discoveries often seem irrelevant for future technological applications. And yet, pure scientific research has led in innumerable cases to tangible technological applications. The foundations of quantum physics were established during the 20^{th} century out of scientific curiosity with the innocent aim of understanding reality. This provided a new set of rules and possibilities that would eventually lead to the interdisciplinary revolution of quantum technologies. Quantum technologies exploit the framework set by quantum physics to perform tasks more efficiently than what is possible based on the "classical" laws of physics [3].

As an example, quantum communication [1] exploits the capability to encode information onto quantum states in order to outperform communication tasks utilizing classical resources. For instance, quantum communication allows one to establish secure communication, guaranteed by the laws of quantum physics, between different parties [4] or distribute quantum states over long distances using quantum teleportation, required for a future quantum internet [2].

Specifically, in this thesis we will describe the possibility of using quantum technologies to distribute quantum states over long distances through optical fibres. This would be required in order to realize a globally interconnected quantum network, allowing the distribution of quantum resources on a planetary scale. Different experiments towards this goal will be presented and discussed.

The structure of the thesis is as follows: First, the basic elements of quantum communication are introduced. Second, we will describe how to achieve quantum communication over long distances by means of quantum repeaters (QR). Next, in chapters 4, 5, 6 the

different elements to built a quantum repeater and their requirements will be introduced. These chapters also detail different experiments performed during my Ph.D., mostly in form of published papers. Finally, in chapter 7 conclusions will be presented and future direction discussed.

The work in this thesis it has been only possible thanks to different collaborations and a team effort amongst the members of our QC2lab group. My specific contributions to each paper are outlined before each manuscript.

Chapter 2

Quantum communication

In the following section the basic elements and resources required in quantum communication will be introduced and described.

2.1 Quantum bit: Qubit

The bit is the basic unit of classical information; it is represented by one of two possible perfectly distinguishable states, e.g "0" or "1", true or false, etc. Analogously, a qubit, [5] is the elementary unit of quantum information; it is represented by an arbitrary superposition of two orthogonal quantum states $|0\rangle$ and $|1\rangle$ of bits

$$|\psi\rangle = \alpha|0\rangle + \beta|1\rangle. \tag{2.1}$$

Here α and β are complex numbers and must fulfill the normalization condition $|\alpha|^2 + |\beta|^2 = 1$. A convenient way to represent an arbitrary qubit is using the Bloch-sphere shown in figure 2.1. Any possible qubit can be represented on the sphere surface using two angular coordinates θ and ϕ. The angles θ and ϕ are defined with respect to the $X+$ and $Z+$ axis (see figure 2.1), this allows to express any qubit state as follows

$$|\psi\rangle = \cos\left(\frac{\theta}{2}\right)|0\rangle + e^{i\phi}\sin\left(\frac{\theta}{2}\right)|1\rangle. \tag{2.2}$$

Notice that any pair of states diametrally opposed are orthogonal and thus form a complete basis that allows to express any qubit state.

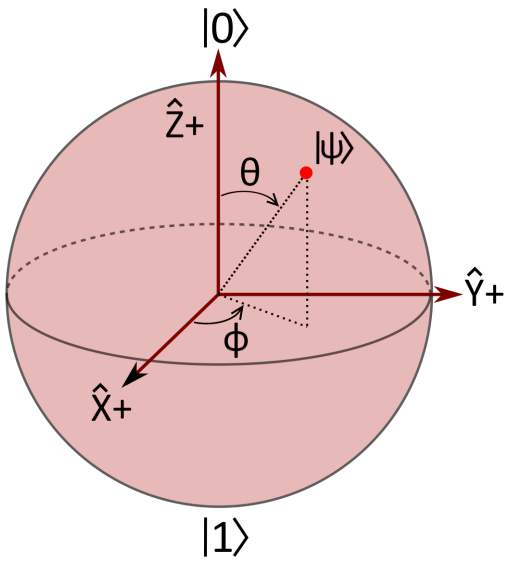

Figure 2.1: A qubit $|\psi\rangle$ represented as a point on the surface of the Bloch-sphere parametrized by the angular coordinates θ and ϕ.

Quantum information can be encoded and distributed using different physical systems. In our case we chose to encode qubits into degrees of freedom (DOF) of photons (elemental particles of light) since they can be easily distributed and measured. For example, photonic qubits could be encoded using the polarization DOF [6], in which case horizontal $|H\rangle$ and $|V\rangle$ polarizations form a complete basis. Alternatively, two distinct (orthogonal) pre-defined emission times of a photon, early $|e\rangle$ or late $|l\rangle$ can be used, creating a so called time-bin qubit [7]. The type of encoding used is commonly determined by the characteristics and requirements of each specific application.

2.2 No-cloning theorem

The no-cloning theorem states that it is impossible to perfectly copy an unknown quantum state [8]. Thanks to this result, it is possible to establish secure communi-

cation between two parties using Quantum Key Distribution (QKD)[4] (see section 2). Intuitively, the non cloning theorem implies that an eavesdropper cannot intercept the message here established between the two parties without disturbing it and thus being noticed.

The concept can be understood by following the reasoning found in [4]. Let us imagine that we want to copy a quantum state $|0\rangle$ using a perfect cloning machine. This process can be represented by the following transformation

$$\widehat{U}|0\rangle \otimes |b\rangle \rightarrow |0\rangle \oplus |0\rangle, \tag{2.3}$$

where $\widehat{U}$ is a unitary transformation performed by the cloning machine and $|b\rangle$ is a blank quantum state that "receives" the copied quantum state from the cloning machine. Similarly, the cloning operation acting on the orthogonal quantum state $|1\rangle$ will result in

$$\widehat{U}|1\rangle \otimes |b\rangle \rightarrow |1\rangle \otimes |1\rangle. \tag{2.4}$$

Now, if we try to copy an arbitrary state $\alpha|0\rangle + \beta|1\rangle$ we obtain, using the linearity of quantum mechanics,

$$\widehat{U}\left(\alpha|0\rangle + \beta|1\rangle\right) \otimes |b\rangle \rightarrow \alpha|0\rangle \otimes |0\rangle + \beta|1\rangle \otimes |1\rangle. \tag{2.5}$$

Hence our ideal cloning machine fails when trying to copy an arbitrary quantum state, since

$$\alpha|0\rangle \otimes |0\rangle + \beta|1\rangle \otimes |1\rangle \neq \left(\alpha|0\rangle + \beta|1\rangle\right) \oplus \left(\alpha|0\rangle + \beta|1\rangle\right). \tag{2.6}$$

This proves that an ideal quantum cloning machine capable of copying arbitrary quantum states perfectly does not exist.

2.3 Entanglement

Two states are entangled if the properties of the compound state $|\psi\rangle_{12}$ can not be inferred by simply analyzing the properties of the individual states $|\psi\rangle_1$ and $|\psi\rangle_2$. Mathematically this can be expressed as follows

$$|\psi\rangle_{12} \neq |\psi\rangle_1 \otimes |\psi\rangle_2 = |\psi\rangle_1 |\psi\rangle_2. \tag{2.7}$$

Entangled states are strongly correlated, these correlations can be used as a resource in quantum communication in order to, for example, establish secure communication between parties or perform quantum teleportation[9]. The most commonly used entangled states in quantum communication are the so called Bell-states [10]

$$|\psi^{\pm}\rangle_{12} = \frac{1}{\sqrt{2}} \left[|0\rangle_1 |1\rangle_2 \pm |1\rangle_1 |0\rangle_2 \right] \tag{2.8}$$

$$|\phi^{\pm}\rangle_{12} = \frac{1}{\sqrt{2}} \left[|0\rangle_1 |0\rangle_2 \pm |1\rangle_1 |1\rangle_2 \right], \tag{2.9}$$

The four Bell-states are maximally entangled two-qubit states and they form a complete basis of the two-qubit Hilbert space. Notice that, when individual subsystems of a maximally entangled state are considered independently they are maximally mixed states and when measured do not reveal any information about the second system. On the other hand, if the measurement outcomes of the two subsystems are pairwise compared, they can exhibit perfect correlations or anti-correlations.

Entanglement between photon pairs can be obtained in different DOF, e.g. polarization [11], frequency [12], energy-time [13, 14] or time-bin [15, 16]. And also, entangled photon pairs can be generated via different approaches, for example by making use of the radiative decay of two electronhole pairs (bi-excitons) trapped in a semiconductor

quantum dot [17, 16] or by nonlinear optical interactions such as spontaneous parametric down-conversion (SPDC) [11, 15, 14] (see chapter 4) or spontaneous four wave mixing (SFWM) [18].

2.4 Quantum Cryptography: Quantum Key Distribution

The security of current worldwide communications is based on unproven assumptions that public key crypto-systems are hard to break with known algorithms and available computational powers. Therefore, sensitive data and communications could become unsafe with a sudden increase of accessible computational power, the discovering of new decryption algorithms or with the emergence of the quantum computers [19]. An important example is the extensively used cryptographic protocol RSA [20], which relies on the assumption that factorization of large integers is computationally hard using known algorithms and classical computational methods [21].

In contrast to classical cryptography, that establishes its security relying on unproven assumptions, the security of quantum cryptography is based on the unbreakable laws of nature. The security of quantum criptography is based on the impossibility for an eavesdropper to intercept and copy and arbitrary quantum state without perturbing the quantum state and thus being noticed (no cloning-theorem). An example of quantum cryptography is the so called quatum key distribution (QKD) that is used to establish secret key between parties. The secure established key can then be used in combination with the informationally-secure method one-time pad [22] encryption method. To use the one-time pad, a message, written as a string of bits, is added (modulo two) to the key and sent publicly to the receiver where the encoded message is added again with the the shared key, thus decoding the message.

The first protocol for QKD was proposed in 1984 [23] and since then many differ-

ent protocols have been developed. In order to illustrate the principle we will describe the basics of a protocol based on the distribution and measurement of entangled photon pairs, exemplifying how quantum entanglement can be used as a resource [24, 4]. Imagine that two parties, commonly referred to as Alice an Bob, want to share a secret key using a public channel. First, entangled photon pairs need to be generated, for example in the state $|\phi^+\rangle = \frac{1}{\sqrt{2}}\left[|0\rangle_1|0\rangle_2 + |1\rangle_1|1\rangle_2\right]$, and distributed to Alice and Bob, respectively. Alice and Bob will randomly measure their photons in different mutually unbiased bases, e.g. $\widehat{Z} \equiv \{|0\rangle, |1\rangle\}$ and $\widehat{X} \equiv \{|+\rangle = \frac{1}{\sqrt{2}}\left[|0\rangle + |1\rangle\right], |-\rangle = \frac{1}{\sqrt{2}}\left[|0\rangle - |1\rangle\right]\}$, and share publicly which basis they measured in each trial. Unmatched measurements basis attempts are discarded since the measurements results will show no correlations, whereas results obtained from matched measurement bases should be perfectly correlated and therefore secret key could be extracted from them. A key, commonly referred as sifted key, is then generated by assigning different bits to different measurement results e.g. $|0\rangle(|1\rangle) \rightarrow 0(1)$ and $|+\rangle(|-\rangle) \rightarrow 0(1)$.

In order to detect the presence of an eavesdropper, Alice and Bob share a random subset of key to compute the so called quantumbit error rate (QBER), i.e. the ratio between erroneous bits and the total number of shared bits. Errors are introduced by an eavesdropper who tries to intercept the message between Alice and Bob (no cloning-theorem), but system imperfections can also lead to an increase of the QBER. Importantly, secure key can be obtained if the QBER is below a certain threshold using classical error correction and privacy amplification protocols [4], which allows us to erase any possible information gained by an eavesdropper.

2.5 Quantum teleportation

Quantum teleportation was proposed in 1993 [9]. It allows the disembodied transfer

of a quantum state from one system to another. Conceptually, the protocol was crucial for the development of quantum information theory but it also serves as a key ingredient for quantum technologies, e.g. quantum communication or quantum computing, and it has been demonstrated using several physical systems since 1997 [25].

The ingredients required to perform quantum teleportation using photons and linear optics are: a photon encoding the qubit to teleport, a pair of entangled photons, the possibility to perform a joint projective measurement between two photons called Bell-state measurement (BSM) (see chapter 6 for more details) and classical communication. The original three photon state $|\Psi\rangle_{ABC}$ can be represented mathematically by

$$|\Psi\rangle_{ABC} = (\alpha|0\rangle_A + \beta|1\rangle_A) \otimes \frac{1}{\sqrt{2}} \left(|0\rangle_B|0\rangle_C + |1\rangle_B|1\rangle_C\right), \tag{2.10}$$

where the first term describes photon (A) encoding the state to teleport, and the second term describes a maximally entangled photon pair (BC) state ($|\phi^+\rangle$ in this example). In order to transfer the qubit encoded in A onto C it is necessary to jointly measure photons AB, projecting them onto a maximally entangled state (BSM). This can be seen in the following expression

$$\begin{aligned} |\Psi\rangle_{ABC} = & \\ & = |\Phi^+\rangle_{AB} \otimes (\alpha|0\rangle_C + \beta|1\rangle_C) \\ & = |\Phi^-\rangle_{AB} \otimes (\alpha|0\rangle_C - \beta|1\rangle_C) \\ & = |\Psi^+\rangle_{AB} \otimes (\beta|0\rangle_C + \alpha|1\rangle_C) \\ & = |\Phi^-\rangle_{AB} \otimes (\beta|0\rangle_C - \alpha|1\rangle_C)\,. \end{aligned} \tag{2.11}$$

We can see from equation 2.11 that the initial state from particle A is now transferred to particle C except for a unitary transformation corresponding depending onto which Bell-state we project photons AB. Note that, if photon A would be a member of an en-

tangled photon pair, entanglement would be swapped onto particles that never interacted before. This is known as entanglement swapping or teleportation of entanglement (see chapter 6).

Chapter 3

Long distance quantum communication

As discussed in the previous chapter, a convenient way to send a quantum state from one place to another is to encode it into a DOF of a photon and then distribute it either through free space or using optical fibres. The maximum distance at which light at the single photon level has been distributed is 1200km [26] using a (ground to satellite) free space link and 404 km [27] using an optical fibre link.

The maximum distance and rate at which photons, and thus quantum information, can be distributed is ultimately limited by the optical attenuation introduced by the distribution link. For free space links (outside earth‘s atmosphere) the loss is mainly due to diffraction: the spatial mode of the photons expand with the square of the traveled distance and thus the probability to detect photons using a limited-size telescope gets reduced accordingly. On the other hand, in optical fibre links the photons experience attenuation that grows exponentially with the distance (0.2-0.3 dB/km using standard telecommunication fibres and photons at telecommunication wavelength of $\sim$ 1550nm due to the scattering and absorption. In classical communication systems the attenuation is overcome by placing repeater stations along the total communication link, which copy and regenerate the intensity of the signals before they become too weak. However, in quantum communication the same approach can not be used since, as discussed in chapter 2, quantum information can not be copied without being disturbed. Therefore, other approaches need to be implemented.

Obviously, the possibility to use existing telecommunication fibre infrastructure for future quantum communication is very appealing [28]. However, in order to achieve intercontinental distances (>1000 km) the attenuation problem needs to be addressed. In

the following we will introduce a plausible solution for that problem known as a quantum repeater (QR) [29]. Experimental results exploring the new physics and technical difficulties towards achieving that goal will also be presented.

3.1 Quantum repeaters

The quantum repeater was proposed by H. J. Briegel, W. Dür, J. I. Cirac, and P. Zoller in 1998 [29]. The main idea consists in dividing the total communication length L into shorter segments L_0, named elementary links, creating entanglement across all elementary links, and swapping entanglement between elementary links until entanglement is distributed between the end nodes of the communication link (see figure 3.1).

In more detail, first, entanglement needs to be distributed in a heralded fashion between the end nodes of an elementary link where entanglement is stored in what we will refer to as a quantum memory (QM). Second, when neighboring elementary links have successfully distributed and stored entanglement, entanglement is swapped between them. The swapping is realised by means of a joint projective measurement (BSM), creating a longer entangled link. Finally, the process is repeated and concatenated until the end nodes of the communication link end up sharing entanglement (see figure 3.1). Note that the capability to swap entanglement between nodes that previously have heralded the presence of entanglement is what allows to overcome the exponential attenuation as a function of a distance.

Generally, a QR can be defined as a device capable of distributing quantum information over long distances by correcting for two types of errors: loss and decoherence. An interesting classification of quantum repeaters is made in [30] according to how these errors are corrected. The original proposal [29] already contemplated the use of purifi-

cation [31] in order to correct for the decoherence introduced during the entanglement distribution. But, current experimental efforts ,including in our group, often ignore the added errors due to decoherence, since the small amount of errors introduced when links of relevant length are considered (<1000 km) can be corrected by simple classical error correction protocols, at least when QKD is the application considered.

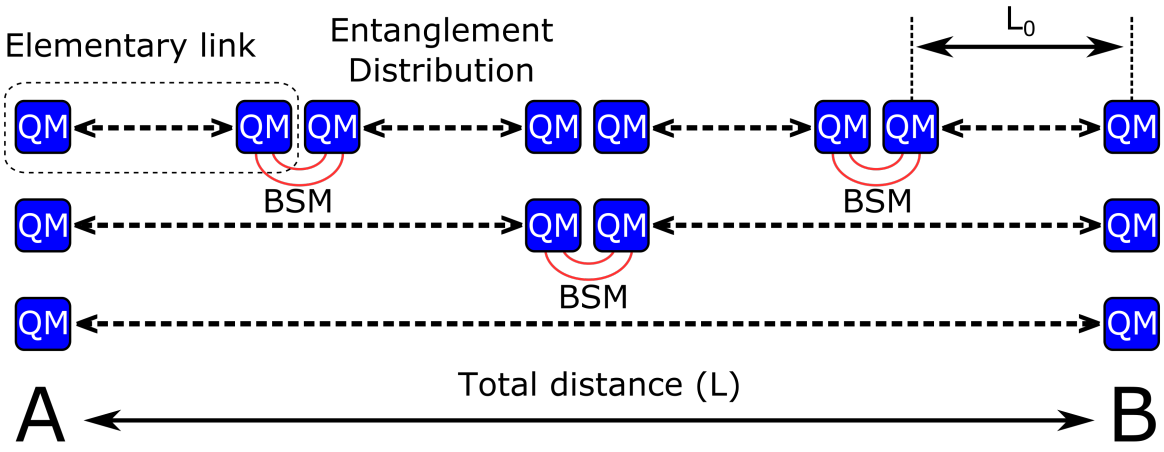

Figure 3.1: Schematic quantum repeater diagram with its main components: elementary links, quantum memories (QM) and Bell-state measurements (BSM). Heralded entanglement distribution is represented by a bidirectional arrow.

There are different proposals for protocols and physical implementations for a quantum repeater, e.g. quantum repeaters based on linear optics and atomic ensambles [32], based on single atoms in cavities [2], or based on color defects in diamonds [33]. In this thesis we focus on a QR architecture based on photon pair sources and absorptive quantum memories [34, 35]. In this architecture, each elementary link is composed of two entangled photon pair sources, two QMs and, in order to swap entanglement, a BSM performed by merging two photons in a beam splitter. For more details see figure 3.2.

Note that if the quantum memories are just capable to store a single photon, then entanglement distribution over elementary links can be repeated only once the BSM

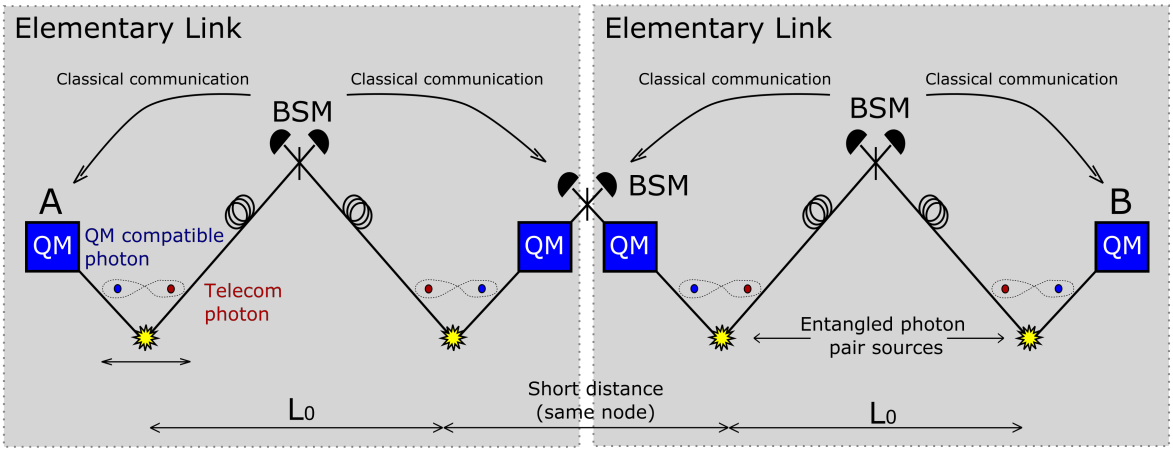

Figure 3.2: Quantum repeater architecture based on entangled photon pair sources and absorptive quantum memories. Each photon pair source generates an entangled photon pair. One photon of each pair is stored in a quantum memory while the other two photons (at telecommunication wavelength) travel through a long fibre link and meet in a beam splitter (if both survived the link loss) where a BSM will be attempted. If the BSM is succesful (using linear optics and no extra resources a BSM is limited to 50 % efficiency), this heralds the presence of entanglement between the two QMs. Then, when neighboring elementary links successfully heralded the presence of entanglement, the photons are retrieved and a BSM is attempted to swap entanglement between elementary links. The process is repeated until entanglement is distributed across the total communication length.

result has been announced and communicated via classical communication to the elementary link nodes. This leads to a maximum attempt rate of $\sim c/L_0$ if elementary links are symmetric, i.e. the BSM station is exactly in-between the QMs. L_0 correspond to the elementary link length and c to the speed of light. On the other hand, if the memories are capable of storing n photons simultaneously (multimode capability) entanglement distribution can be attempted at a rate (R) n times faster, $R = nc/L_0$, increasing the probability of entanglement distribution per time over an elementary link and thus reducing the time required to distribute entanglement over the entire length. Many quantum repeater architectures therefore rely on the capability to simultaneously

store multiple copies of entangled qubits. In the next section we will present a quantum repeater architecture based on frequency multiplexing that was developed in our group [36].

3.2 Frequency multiplexed quantum repeater: ingredients and protocol

In this section we will briefly introduce the QR architecture based on frequency multiplexing proposed by our group [36]. As discussed in the previous section, the use of multiple photons simultaneously generally allows increasing the entanglement distribution rate compared with the single photon case (see figure 3.3).

The main idea consists in simultaneously generating multiple entangled photons pairs with different frequencies and attempting a BSM independently with all the frequency modes at once. The scope is to distribute entanglement over an elementary link ideally deterministically, which can be accomplished if enough frequency modes are synchronously employed. Moreoever, since entanglement over each elementary link would be distributed in every attempt, the quantum memories do not need to allow recall on demand, which relaxes the requirements for the quantum memories (see chapter 5). In order to swap entanglement between elementary links, the successfully stored modes need to be recalled from the QMs and shifted to a common reference frequency since the photons involved in a BSM need to be indistinguishable in all DOF (see chapter 6).

In our group we are working on developing and interfacing the different elements required to build a frequency multiplexed QR. Essentially, a frequency multiplexed QR is composed of three functional elements.

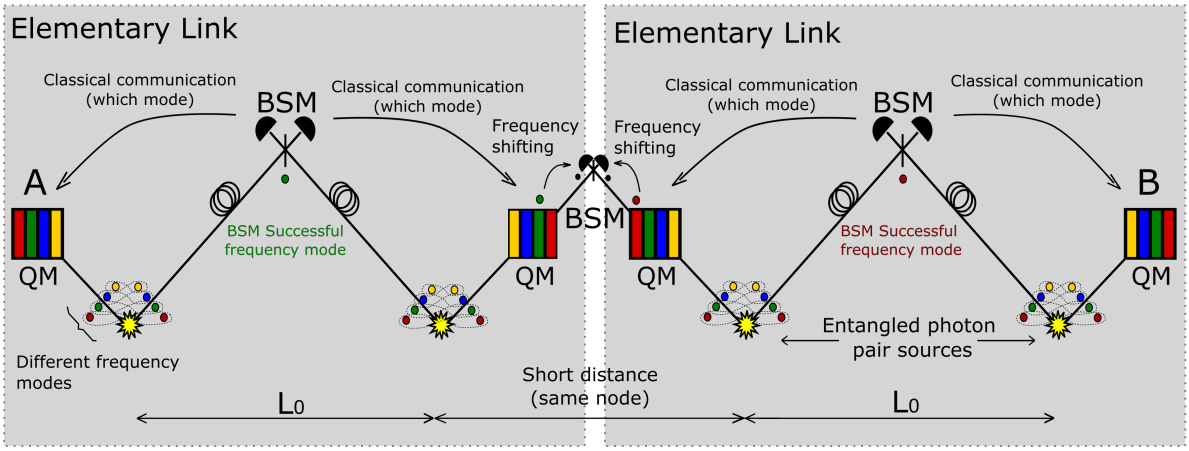

Figure 3.3: **Frequency multiplexed quantum repeater scheme**. In each elementary link two frequency multiplexed sources generate many pairs of entangled photon pairs in different spectral regions. One photon from each entangled pair is sent to the center of the elementary link where a spectrally resolved Bell-state measurement (BSM) is performed in order to swap entanglement. A probability close to unity to succeed in at least one BSM is ensured by having a sufficiently large number of frequency modes. Simultaneously, the other photon from each pair is sent to quantum memories (QMs) where all frequency modes are stored. The information about which frequency modes succeeded in the BSM is sent classically to the QMs. Next, all frequency modes are recalled from the QMs. After appropriate frequency shifting, only the mode corresponding to the successful BSM is allowed to pass through a filter with previously agreed-upon reference resonance frequency, all the other photons are rejected. The last step ensures indistinguishability between the two photons coming from different elementary links, which is required in order to perform a BSM at the interface of two elementary links. This BSM leads to entanglement swapping across neighboring elementary links.

- **Frequency multiplexed entangled photon pair sources**. Sources capable of generating simultaneously multiple entangled photon pairs in different frequency modes. In our group we focus on developing a frequency multiplexed time-bin entangled photon pair source based on SPDC (see chapter 4).

- **Spectrally multimode quantum memories**. Memories capable of storing simultaneously multiple frequency modes for a predefined storage time. In our group we focus on developing a frequency multimode quantum memory based on rare-earth ion (REI) doped solids and the so called atomic frequency comb (AFC) protocol (see chapter 5).

- **Entanglement swapping operations**. In our group we utilize a photonic BSM based on linear optics (see chapter 6).

In the following chapters, the required elements to build a frequency multiplexed QR will be explained in more detail, and different experiments performed during my Ph.D. will be described.

Chapter 4

Photon sources for quantum repeaters

An entangled photon pair source is one of the key ingredients to build a QR based on the protocol introduced in section 3. Ideally an entangled photon source for QR applications should emit perfect entangled photon states (Bell-states) at a high rate and with one of its photons at telecommunication wavelengths in order to be sent through long optical fibre links experiencing low loss. Moreover, the entangled photon pair source needs to be perfectly matched with the other two required QR constituents: QMs and entanglement swapping operations.

For instance, one of the photons emitted by the entangled photon pair source needs to be stored in a QM, which requires its wavelength to match the chosen atomic transition. Likewise, the photon spectral bandwidth needs to match the available QM bandwidth, which will depend generally on the material and protocol chosen to implement the QM (see chapter 5). Generally, the spectral bandwidth of the photons needs to be constrained in order to match the limited available bandwidth of a QM. The use of photons with large spectral bandwidths is desirable since it allows the use of shorter temporal wavepackets, and thus increases the communication repetition rate. In addition, in order to be able to perform entanglement swapping operations (BSM) the emitted photons need to be indistinguishable (see chapter 6), this basically requires that photons emitted in different trials and by different photon pair sources to have the same properties, i.e. temporally and spectrally.

Moreover, to implement the frequency multiplexed repeater scheme presented in section 3, in addition to the requirements listed above, the simultaneous generation of many entangled photon pairs in different frequency channels is also required. This in principle

can be achieved, by the use of a multimode entangled photon source capable of emitting many frequency modes simultaneously, or by integrating several single mode entangled photon sources. Additionally, the capacity of frequency shifting and selecting different frequency modes on demand is also necessary.

In this chapter we are going to describe one of the most common physical implementations of entangled photon sources, which is based on the interaction between strong light and a non-linear crystal. These sources are versatile and can be easily tailored to fulfill the requirements to be implemented in our QR architecture. Moreover, its multimode nature allows the generation of multiple frequency modes simultaneously, which is required for a frequency multiplexed QR architecture. As a precursor of such sources, an experiment involving frequency multimode generation of single photons and frequency shifting on demand will be presented and discussed in paper 1. In the same paper the advantages and disadvantages of using different approaches for the generation of single photons are also discussed.

4.1 Spontaneous parametric down-conversion

One of the most common realizations of entangled photon pairs are based on nonlinear optical interaction between strong light with a nonlinear crystal. The experimental simplicity and versatility of such sources have earned them a role in numerous quantum information applications [37].

The polarization $P(t)$, i.e. the dipole moment per unit volume, of a material system depends on the strength $E(t)$ of an applied optical field. The induced polarization by an external field can be written by expressing the polarization as a power series in the field strength [38]

$$P(t) = \epsilon_0 \left[\chi^{(1)}E(t) + \chi^{(2)}E(t)^2 + \chi^{(3)}E(t)^3 + ...\right], \tag{4.1}$$

where ϵ_0 is the vacuum eletrical permeability and $\chi^{(n)}$ correspond to the different orders of the polarizability. The most commonly used processes to generate photon pairs exploit the relatively large second ($\chi^{(2)}$) and third order ($\chi^{(3)}$) electrical susceptibilities present in some materials, and they are referred to as Spontaneous Parametric Down-Conversion (SPDC) and Spontaneous Four Wave Mixing (SFWM), respectively. Specifically, in this thesis we are going to focus on the SPDC process on which the photon sources presented in the following sections are going to be based on.

In SPDC a pump photon can probabilistically be split into two photons thanks to the interaction with a nonlinear crystal with a non-zero $\chi^{(2)}$ and the electromagnetic field vacuum fluctuations. This process needs to fulfill the conservation of energy (equation

4.2) and momentum (equation 4.3):

$$E_p = E_i + E_s, \tag{4.2}$$

$$\vec{k_p} = \vec{k_i} + \vec{k_s} \tag{4.3}$$

here the subscript p denotes the pump photon and the subscript i and s identifies the down-converted photons commonly referred to as idler and signal photons, respectively. The energy conservation determines the possible wavelength pairs of the down-converted photons. On the other hand, the momentum conservation condition, or also know as a phase-matching condition, determines the directionality of the down-converted photons as well as the possibility to use a specific material since the magnitude of the photon's momenta depend on the index of refraction experienced for each photon. Later different techniques to achieve phase-matching will be briefly discussed.

The SPDC process can be described in the interaction picture representation by the following Hamiltonian [39]

$$\mathcal{H}_i = i\hbar\zeta \left[\widehat{a_i}^\dagger \widehat{a_s}^\dagger - \widehat{a_i}\widehat{a_s}\right], \tag{4.4}$$

Where $\hbar$ is the reduced Planck constant, $\widehat{a_i}$ ($\widehat{a_s}$) the anhilation operator of an a photon in the idler (signal) modes and ζ is a constant proportional to $\chi^{(2)}$ and the pump intensity. In order to find the state after the interaction with the crystal $|\psi\rangle_{is}$ we apply the time evolution operator on the vacuum state using the previous Hamiltonian 4.4

$$|\psi_{is}\rangle = e^{i\mathcal{H}_i/\hbar}|0\rangle = \cosh(\zeta t)^{-1} \sum_{n=1}^{\infty} \tanh(\zeta t)^n |n_i n_s\rangle, \tag{4.5}$$

where t correspond to the interaction time and $|n\rangle$ describe photon number states. The outcome is a a thermal bi-photon state with average photon pair number $\langle\mu\rangle =$

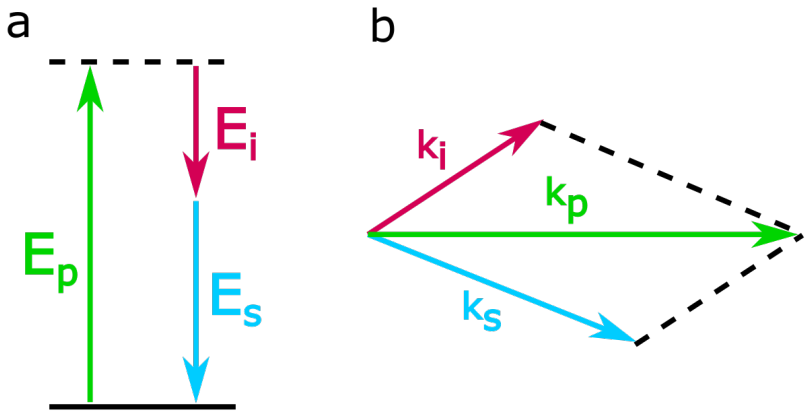

Figure 4.1: **SPDC energy and momentum conservation**. **a.** Energy conservation condition, arrow lengths represent the energy of the photons involved in the SPDC process. The sum of the arrow lengths representing idler (E_i) and signal (E_s) photons must be equal to the length of the arrow representing the pump photon energy (E_p). **b.** Momentum conservation condition, arrow lengths represent the momentum of the photons involved in the SPDC process. The vectorial sum of the arrows representing the idler ($\vec{k_i}$) and signal ($\vec{k_s}$) photons must be equal to ($\vec{k_p}$).

$\sinh(\zeta t)^2$. Since the photons are created in pairs $|n_i n_s\rangle$ there is perfect correlation between the photon number in each mode, resulting in the fact that each mode, if analyzed independently, features a thermal photon number distribution. For many applications multi-photon events ($n > 1$) are undesired since they introduce white noise in our operations and could render unsafe quantum cryptography protocols (PNS attack [40]). The presence of the thermal photon number distribution of an SPDC based photon pair source might be the main disadvantage of this kind of photon sources.

The typical efficiency η_{SPDC} of the SPDC process, defined as a ratio between down-converted photon pairs (N_{SPDC}) to the pump photons (N_p) is around $\eta_{SPDC} = N_{SPDC}/N_p = 10^{-6} - 10^{-11}$ for commonly used non-linear waveguides or bulk crystals [41], and it mostly depends on the $\chi^{(2)}$ magnitude and the strength of the pump field.

Phase-matching

The momentum conservation condition (equation 4.3), or phase-matching condition, is not automatically fulfilled for energy-correlated photons due to different index of refraction n experienced by each photon involved in the SPDC process. As a consequence, equation 4.6 assuming collinear beams can be written as

$$k_p(n_p) = k_i(n_i) + k_s(n_s) \rightarrow 2\pi\frac{n_p}{\lambda_p} = 2\pi\frac{n_i}{\lambda_i} + 2\pi\frac{n_s}{\lambda_s}, \tag{4.6}$$

where λ denotes to the wavelength and n represent the index of refraction experienced for each photon. The perfect phase-matching condition ($\Delta k = k_p - k_i - k_s = 0$) is often difficult to achieve because the refractive index of materials that are lossless, for the wavelengths involved, show normal dispersion, i.e. the refractive index is a decreasing function with respect to wavelength. Fortunately, there are different techniques that ease the phase-matching in some cases. For example, in certain cases the phase-matching can be achieved by carefully orienting the crystal with respect the optical optical axes (angular tunning) by exploiting its birefringence. Alternatively, for some crystals the amount of birefringence is strongly temperature-dependent, and as a result, it may be possible to achieve phase-matching by adjusting the temperature of the crystal (temperature tuning) [38].

A particulary flexible and efficient way to a achieve phase-matching is using the so called quasi phase-matching (QPM) technique. This technique allows to compensate for large phase mismatches and thus access large non-linear coefficients of the $\chi^{(2)}$ tensor that otherwise would not be accessible with angular or temperature tuning. It can be shown that by periodically reversing (periodically poling) the polarity of the non-linearity over the entire length of the nonlinear crystal, a fixed phase mismatch can be compensated

$$\Delta k = k_p(n_p) - k_i(n_i) - k_s(n_s) - \frac{2\pi}{\Lambda}, \tag{4.7}$$

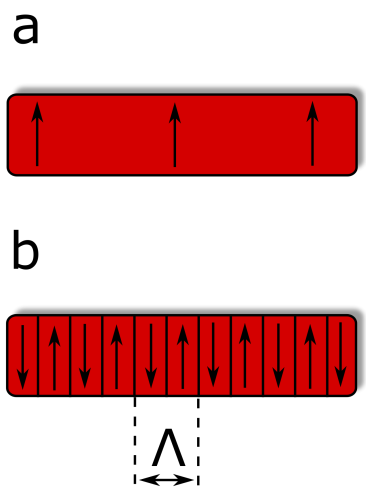

Figure 4.2: **Ferroelectric domain orientation of a non-linear crystal.** **a** Representation of the ferroelectric domains orientation of a non-linear crystal not being periodically poled. **b** Representation of the ferroelectric domains orientation of a periodically poled non-linear crystal, Λ correspond to the periodic separation between domains orientations.

where the last term correspond to the phase mismatch introduced by periodically poling the crystal and Λ correspond to the distance between differently polarized non-linear coefficients (see figure 4.2). A common way to achieve such a periodical poling is the use of static electric fields to locally invert the orientation of the ferroelectric domains of an existing crystal. Notice that, in order to achieve larger phase-mismatch compensations the period of alternated domains needs to be smaller, which is more challenging to fabricate. The periodical poling technique is commonly used in lithium-niobate ($LiNbO_3$) crystals and allows to access one of the largest nonlinear coefficients existent amongst all known materials. In the work presented in this thesis we use periodically poled lithium-niobate (PPLN) crystals to genereate photon pairs.

4.2 Time bin entangled photon source based on spontaneous parametric down-conversion

Time-bin encoding is a very robust against decoherence under fibre transmission. The qubit is encoded in a coherent superposition of a photon being in two distinct temporal modes, i.e. early ($|e\rangle$) and late ($|l\rangle$) (see figure 4.3). In that way, each temporal mode experiences the same transformation in the fibre link, and the qubit becoems insensitive to polarization mode dispersion (birefringence) and chromatic dispersion [4].

The generation of time-bin entangled photons based on SPDC is achieved by pumping a non-linear crystal with a coherent superposition of pump photons being in an early or late temporal mode, where the coherent length of the pump photons must be shorter than the temporal separation of the time-bins. This method was first proposed and implemented in [7]. A simple way of obtaining a coherent superposition of pump photons is by sending a pulse of light through an unbalanced Mach-Zender interferometer (MZI) where the phase between the temporal modes can be controlled by finely adjusting the path-length difference between the two arms. The resulting time-bin entangled photons, created after the interaction of the pump pulses with a non-linear crystal, can be projected onto superpositions of $|e\rangle$ and $|l\rangle$ (depicted on the on the equator of the Bloch-sphere, see figure 2.1) by using interferometers with path lengths differences identical to that of the pump interferometer. Trivially, to measure the qubits in the canonical basis, i.e. $\{|e\rangle, |l\rangle\}$ the arrival time needs to be recorded, see figure.4.3 for more details.

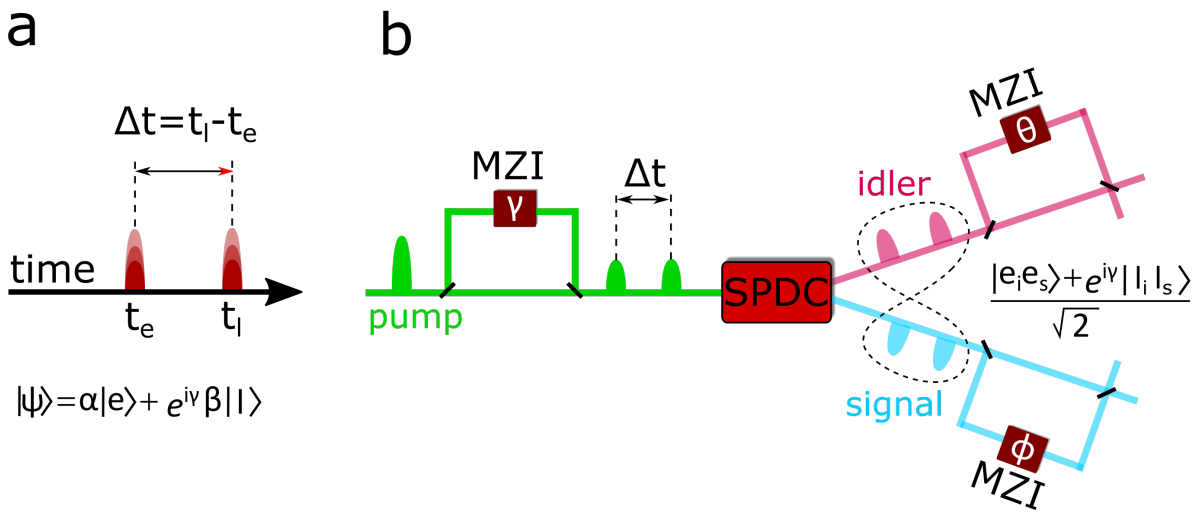

Figure 4.3: **Schematic representation of a time-bin qubit and a time-bin entangled photon source based on SPDC**. **a** Schematic representation of a time-bin qubit showing a coherent superposition of two photon wavepackets temporally separated by Δt, with relative probability amplitudes α and β and with a relative phase γ. **b** Schematics of an time-bin entangled photon pair source based on SPDC. Pump photons pass through an unbalanced Mach-Zender interferometer (MZI). Then, the emerging photons are used to pump an SPDC crystal, which with small probability, down-convert a pump photon and produces the entangled state $\left[|e_i e_s\rangle + e^{i\gamma}|l_i l_s\rangle/\sqrt{2}\right]$, where the subscripts i(s) represent the idler (signal) photon mode. MZIs with identical path lengths differences and controlled relative phases θ and ϕ can be used to project individual qubits of the entangled state onto states depicted on the equator of the Bloch-sphere. Alternatively, to measure qubits on the canonical bases $\{|e\rangle, |l\rangle\}$ the arrival time needs to be recorded.

4.3 Paper 1: Heralded single photons based on spectral multiplexing and feed-forward control

Summary - We implement a frequency multiplexed heralded photon source based on SPDC. We explore the possibility of defining different spectral modes within the broadband emission of one of the down-converted photons and feed-forward the information of which mode is detected to frequency shift, accordingly, the other down-converted photon to a common frequency reference.

Here, in our proof of principle experiment, we demonstrate how by implementing spectral multiplexing and feed-forward control can lead to a deterministic single-photon source as proposed in [42, 43]. The tools developed in this paper for an efficient frequency shift and recall on demand of different spectral modes could be directly implemented in our frequency multiplexed QR architecture.

Contributions - This experiment was conducted in collaboration with Gabriel H. Aguilar and Qiang Zhou. The single photon detectors were designed, built and tested by Francesco Marsili, Matthew D. Shaw, Varun B. Verma and Sae Woo Nam. The experiment was co-supervised by Daniel Oblak and Wolfgang Tittel. I specifically contributed to the conception of the experiment, to the design, development and setup of the experiment as well as to data taking and analysis of the measurement results. I furthermore wrote the first draft of the manuscript together with Gabriel H. Aguilar, and in conjunction with the other co-authors who contributed to all the editing steps until publication.

Heralded single photons based on spectral multiplexing and feed-forward control

Physical Review Letters 119, 083601 (2017)

25 August 2017

M. Grimau Puigibert[1], G.H. Aguilar[1,†], Q.Zhou[1,‡], F. Marsili[2], M. D. Shaw[2], V. B. Verma[2], S.W. Nam[3], D. Oblak[1] and W. Tittel[1]

[1]*Institute for Quantum Science and Technology, and Department of Physics and Astronomy, University of Calgary, 2500 University Drive NW, Calgary, Alberta T2N 1N4, Canada*

[2]*Jet Propulsion Laboratory, California Institute of Technology, 4800 Oak Grove Drive, Pasadena, California 91109, USA*

[3]*National Institute of Standards and Technology, Boulder, Colorado 80305, USA*

[†]*Current Address: Instituto de Fsica, Universidade Federal do Rio de Janeiro, CP 68528, 21941-972, Rio de Janeiro, Brazil*

[‡]*Current Address: Institute of Fundamental and Frontier Science, University of Electronic Science and Technology of China, Chengdu 610054, China*

Abstract

We propose and experimentally demonstrate a novel approach to a heralded single photon source based on spectral multiplexing (SMUX) and feed-forward-based spectral manipulation of photons created by means of spontaneous parametric down-conversion in a periodically-poled $LiNbO_3$ crystal. As a proof-of-principle, we show that our 3-mode SMUX increases the heralded single-photon rate compared to that of the individual modes without compromising the quality of the emitted single-photons. We project that by adding further modes, our approach can lead to a deterministic SPS.

4.3.1 Introduction

Photonic quantum information processing promises delivering optimal security for sensitive communication [1], solving certain computational problems much faster than classical computers [2, 3], and estimating physical parameters with significantly improved resolution [4]. Many of these applications rely on sources of deterministic (on-demand) and near-perfect single photons [5].

The most common realization of a single-photon source (SPS) is based on the generation of correlated pairs of photons (usually coined idler and signal photons) followed by the detection of one member of the pair (henceforth assumed to be the idler), which heralds the presence of the other. In this scheme, a crucial step is the pair generation process, which is achieved through spontaneous parametric down-conversion (SPDC) or spontaneous four-wave-mixing in a nonlinear optical medium. The experimental simplicity and versatility of such heralded sources have earned them a key role in numerous quantum information applications [6]. In terms of quality, these sources can produce highly indistinguishable photons, but their main limitation lies in the spontaneous nature of the pair generation. Pairs of single photons are generated only with a certain

probability $p_{n=1} < 1$ and, moreover, there is a chance of generating multiple photon pairs, which results in multi-photon emission from the SPS (for $p_{n=1} \ll 1$ the probability for generating multiple pairs is $p_{n\geq 2} \approx p_{n=1}^2$) and hence non-pure single photon states. If the collection and detection efficiency of the idler photon is large photon-number resolving detectors [7, 8] will increase the purity, but the maximum single-photon emission probability will still be limited to $p_{n=1} = 0.25$ [9].

An alternative approach to implement SPSs uses single emitters [10] such as diamond colour centers [11], single molecules [12] and quantum dots [13, 14]. Such conceptually simple sources are in principle capable of deterministically emitting a pure single photon within the emitter's excitation lifetime. For diamond colour centers a number of recent experiments has shown nearly pure and indistinguishable photons emitted from separate sources [15, 16]. If these properties can be combined with the large collection efficiencies demonstrated in other experiments, and emission into phonon side-bands can be suppressed, colour centers have potential to realize ideal SPSs. Furthermore, the rapid progress in fabrication methods and active control of the properties of quantum dots has also yielded photon emitters with high purity, close-to deterministic emission and good indistinguishability, however, only for photons emitted by the same source at different times [17, 43]. Indistinguishability between photons emitted from two independent quantum dots has also been demonstrated, but with low collection efficiency [18]. Yet another shared impediment of all single-emitter sources is the complexity of their fabrication and emission wavelength tuning, and the need for a cryogenic environment.

A promising avenue to overcome the limitations of the above types of sources is based on revisiting the heralded SPSs. The scheme proposed in [19, 20] realizes in principle a deterministic SPS by actively multiplexing many non-deterministic heralded photon sources that emit photons in different modes. In that way one retains the advantageous properties of the HSPS — such as indistinguishability and ability to widely tune the

output spectral width and wavelength — while overcoming the limitations to the single photon purity. In the multiplexing scheme, the detection of an idler photon in any mode out of the chosen set heralds the presence of a signal photon in a corresponding optical mode. Then, using a feed-forward signal from the idler photon detector, the signal mode is mapped onto a (predetermined) single mode. In doing so, the probability to generate a single pair in at least one of the modes increases linearly with the number of modes m (for small $p_{n=1}$), and the photon emission probability after feed-forward-based mode mapping of the signal mode can hence be made to approach unity. At the same time, the probability for multi-pair emissions into the feed-forward-mapped output mode also increases proportionally to m, which means that the ratio $p_{n=1}/p_{n=2}$ after mode-mapping, and hence the single-photon purity, remains constant. Though, initially, this seems unsatisfactory, it turns out to be far superior to the scaling for an individual heralded SPS. In this case, if the same increase of $p_{n=1}$ by a factor of $k = m$ were to be achieved by increasing the SPDC pump-power, it would result in an increase of $p_{n\geq 2}$ by a factor of k^2. Hence the ratio $p_{n=1}/p_{n=2} \propto 1/k$. In other words the non-multiplexed HSPS would produced more and more multi-photons as the emission rate is increased.

Multiplexed heralded sources have thus far been realized using spatial [21, 22, 23], temporal [24] and spatio-temporal modes [25]. In some cases, they have shown to outperform non multiplexed sources in terms of throughput and quality. However, scaling up the number of modes in the employed degrees of freedom requires more resources, and generally impacts the overall performance. In the case of spatial multiplexing, each additional mode requires an independent source and an added switching connection that induces some amount of extra loss [26]. Temporal multiplexing does not necessarily consume more physical resources but does inevitably encroach on the repetition rate of the source and hence limits the single photon throughput.

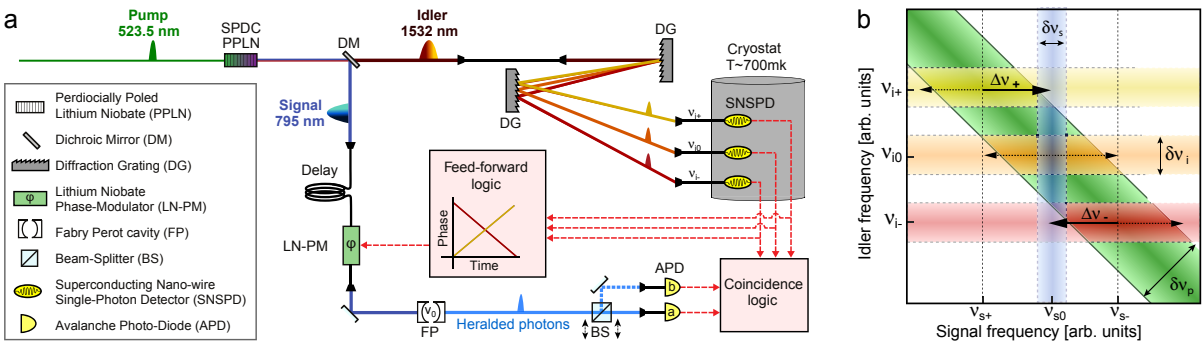

Figure 4.4: **a. Schematic of experimental setup. b. Illustration of concept using the Joint spectral amplitude** Details in the main-text

4.3.2 Experiment, measurements and results

Here, we propose and demonstrate an SPS based on a novel spectral multiplexing (SMUX) scheme in which the source requirements and the system loss are independent of the number of modes being multiplexed. The scheme is based on defining spectral modes within the broadband spectrum of an SPDC pair source and applying a feed-forward frequency-shift operation on the heralded photon. We experimentally show that the single-photon character is preserved by measuring a heralded auto-correlation function $g^{(2)}_{\mathrm{H},0} \ll 1$ for the heralded photons with and without multiplexing and feed-forward control. Moreover, directly comparing the multiplexed and non-multiplexed output we deduce that, as expected, the heralded single-photon emissions increase linearly with the number of modes. This allows compensating for the additional loss caused by the non-ideal elements used for the feed-forward operation for as few as three modes.

The experimental implementation of the scheme is shown in Fig. 6.8a. A pulsed laser (80 MHz repetition rate) creating 18 ps-long pulses centred at 523.5 nm wavelength, with average power of 7 mw, pumps a 2 cm long periodically-poled lithium-niobate (PPLN) crystal to produce 350 GHz-wide, frequency non-degenerate photon pairs, each composed of a signal photon centred at 795 nm and an idler at 1532 nm. The spectral

distribution of the pairs is conveniently illustrated by their joint spectral amplitude (JSA) shown in Fig. 6.8b. The JSA represents the probability amplitude to detect a pair of photons centered at the frequencies ν_s and ν_i. Since each pair of photons has to satisfy energy conservation, the JSA is confined to the diagonal band (green region), whose cross-sectional width is given by the spectral width of the pump laser $\delta\nu_p$. (Under our experimental conditions the phase-matching condition is less restrictive than the energy conservation and thus phase-matching is not considered in the pictorial representation)

Both signal and idler modes are coupled into single mode fibers (the number of detected photon pairs before any spectral filtering is 640 kHz). Subsequently, the signal photons are transmitted to an optical delay line while the idler photons exit the optical fiber and are sent to a pair of orthogonally oriented 50×50 mm square diffraction gratings (DGs, 600 lines/mm) that map photons with spectra centred at $\nu_{i0} = 195.612$ THz (1532.59 nm), $\nu_{i+} = \nu_{i0} + 19$ GHz (1532.44 nm) and $\nu_{i-} = \nu_{i0} - 22$ GHz (1532.76 nm), each featuring a spectral width of 12 GHz [27], onto distinct spatial modes. In the JSA of Fig. 6.8b these idler spectral modes are highlighted as orange (middle), yellow (upper) and red (lower) horizontal bands. The idler photons in each mode are detected using WSi superconducting nanowire single-photon detectors (SNSPDs) cooled to 700 mK in a closed-cycle cryostat. When an idler photon is detected in mode ν_{i+}, ν_{i0} or ν_{i-}, it heralds the presence of a signal photon with a central frequency of $\nu_{s0} = 377.059$ THz (795.08 nm), $\nu_{s+} = \nu_{s0} - 19$ GHz (795.12 nm) or $\nu_{s-} = \nu_{s0} + 22$ GHz (795.03 nm), respectively.

The heralding signals from the output of the SNSPDs are processed by a logic circuit that triggers the creation of a feed-forward signal in the form of a 700 ps long pulse with suitable, linearly changing voltage. This ramp signal is applied to the electrical input of a lithium-niobate ($LiNbO_3$) phase-modulator (LN-PM) that is optically connected to the output of the 512 ns-duration delay line for the signal-photon. As is shown in [27]

the resulting linear phase-ramp applied during the passage of the signal photon actively shifts the spectrum of the heralded signal photon to a spectral band — shown as vertical blue area in the JSA — determined by the transmission of a Fabry Perot cavity (FP) with bandwidth $\delta\nu_s = 6$ GHz. Note that the frequency shifts are applied to the entire spectrum of the signal photons, as indicated by the dotted arrows in Fig. 6.8b. As a consequence, signal photons not corresponding to the heralded spectral band are shifted out of the cavity resonance and thus rejected. Finally, the signal photons are detected by a silicon avalanche photodiode (APD) and another logic circuit records coincidences with the heralding signals from all SNSPDs.

We first characterize the spectral difference between signal photons depending on which idler photon serves as a herald. Towards this end we measure the heralded single photon rates for each idler frequency mode (ν_{i+}, ν_{i0} and ν_{i-}) while tuning the resonance frequency of the FP cavity that acts on the signal photon. To centre the spectral transmission of the FP at ν_{s0}, we maximize the coincidence counts when heralding exclusively with idler photons detected in mode ν_{i0}. Note that although the LN-PM is part of the measurement set-up, it is not active. The results are shown in Fig. 4.5a. For all modes, we measure bandwidths of the heralded photon spectra of around 37 GHz, which matches the convolution of the pump laser bandwidth $\delta\nu_p = 24$ GHz with the filter bandwidths $\delta\nu_s = 6$ GHz and $\delta\nu_i = 12$ GHz. Furthermore, we find that the maximum coincidence rate for each pair of photons is at the relative frequency differences of $\Delta\nu_- = -19$ GHz and $\Delta\nu_+ = +22$ GHz.

Next, we assess the performance of the linear ramp frequency shifting (LRFS) by again recording the heralded-photon spectra for each idler frequency-mode, but now with the corresponding feed-forward signal applied to the LN-PM. For these measurements, the resonance frequency of the FP cavity remains fixed at ν_{s0}. As expected, the spectra shown in Fig. 4.5b now completely overlap. Moreover, by comparing with the results in

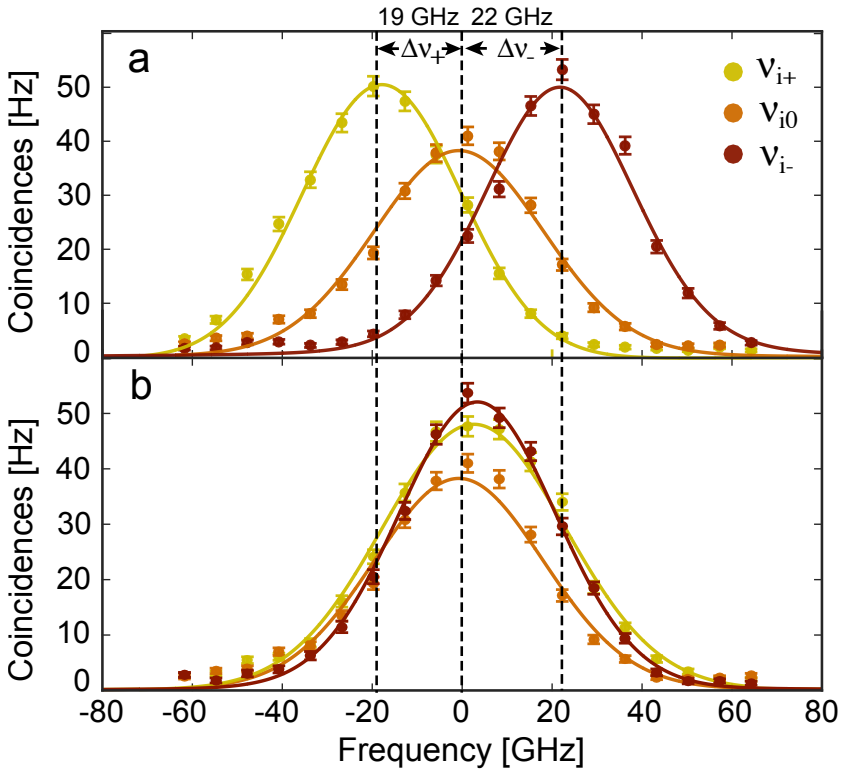

Figure 4.5: Coincidences count rates without (**a**) and with (**b**) frequency shifting. The horizontal axis correspond to the relative frequency difference of the cavity resonance with respect to ν_{s0}. Coincidence rates between the signal and (heralding) idler photons at frequencies ν_{+i}, ν_{0i} and ν_{-i} are presented in yellow, orange and red, respectively. The solid lines are fits using $\mathcal{F} = \mathcal{G}_{\nu_s} \star \mathcal{H}_{\nu_i} \star \mathcal{I}_{\nu_p}$, where $\mathcal{G}_{\nu_s}$ is a Lorentzian function describing the frequency response of the FP cavity; $\mathcal{H}_{\nu_i}$ and $\mathcal{I}_{\nu_p}$ are Gaussians characterizing the filtering by the DGs and the spectrum of the pump laser, respectively; and $\star$ denotes convolution.

Fig. 4.5a, we observe that the detection rates with and without LRFS are essentially equal. This shows that our setup is capable of applying the on-demand frequency shift at the single-photon level with nearly 100% efficiency.

Now we activate the full setup and evaluate the performance of our frequency multiplexed heralded source in view of the requirements of an ideal single photon source. First, we measure the heralded single photon (HSP) rate as a function of the pump power with and without multiplexing. The red, yellow and orange circles in Fig. 4.6 show the rates of signal photons (after spectral filtering by the FP cavity) heralded by the individual

frequency modes at ν_{i+}, ν_{i0} and ν_{i-}. The multiplexed HSP rate for the SMUX source (green circles) is about 2.7 times larger than that of the average of the individual sources, i.e. a significant improvement over that for the individual modes. Yet, to make a fair comparison of the effect of the SMUX, we compare the multiplexed HSP rate to the rate when heralding with only the ν_{i0} mode and with the LN-PM removed, which, for the specific modulator used in our experiment, adds 5 dB loss and is not needed in the case of using only a standard HSPS without multiplexing. However, we keep the spectral filtering elements on both idler and signal fields as these are necessary to achieve pure states [37]. The rate obtained with the thus modified source (purple circles) is similar to the SMUX rate, which can be explained by the increased transmission due to having removed the LN-PM compensating for the lack of multiplexing. Hence, in our experiment, which employs 3 modes, spectral multiplexing does not yet create an advantage in view of the HSP rate and in creating a deterministic source. However, we emphasize that increasing the number of modes would neither increase the system loss nor require additional elements in the signal mode. Hence, we can assume that the HSP rate will continue to increase as more spectral modes are added, rapidly surpassing that of the non-multiplexed source.

Next, we verify that multiplexing maintains the single photon character of our light source. One of the most common methods for this is to determine its purity [43], which, for a heralded source, is generally quantified in terms of its heralded auto-correlation function. To measure this, we direct the heralded signal photons after the FP cavity through a 50/50 beam splitter (BS), and record the individual counts $C_{\mathrm{H}}^{(\mathrm{i})}(i \in \{a, b\})$ in, as well as coincidences $C_{\mathrm{H}}^{(\mathrm{ab})}$ between, the APDs — labelled a and b — placed at its two outputs (see Fig. 6.8a). Denoting the total number of heralding signals, H, we define the heralded auto-correlation as $g_H^{(2)}(0) = C_{\mathrm{H}}^{(\mathrm{ab})} H/(C_{\mathrm{H}}^{(\mathrm{a})} C_{\mathrm{H}}^{(\mathrm{b})})$ [27]. Since detection in both detectors can only occur if two or more photons are present, we expect $C_{\mathrm{H}}^{(\mathrm{ab})}/H \approx p_{n=2}^{\mathrm{H}}/2$,

where $p^{\mathrm{H}}_{n=2}$ is the heralded two-photon probability. On the other hand, the individual detector counts are dominated by single photon events such that e.g $C^{(\mathrm{a})}_{\mathrm{H}}/H \approx p^{\mathrm{H}}_{n=1}/2$ (assuming $p_{n=1} \gg p_{n=2}$). Clearly these considerations hold for the multiplexed and non-multiplexed sources alike [27]. Hence, the autocorrelation function is approximated by $g^{(2)}_H(0) \approx 2p^{\mathrm{H}}_{n=2}/(p^{\mathrm{H}}_{n=1})^2$, which provides a direct relation to the photon-statistics. In particular, $g^{(2)}_H(0) \sim 0$ would indicate $p^{\mathrm{H}}_{n=2} \sim 0$ and $p^{\mathrm{H}}_{n=1} > 0$.

Operating the source at maximum power with the LN-PM (and hence the multiplexing) removed, we obtain a value of $g^{(2)}_H(0) = 0.05 \pm 0.01$. With the SMUX activated and using the same pump power, we measure $g^{(2)}_H(0) = 0.06 \pm 0.01$, which equals the value without multiplexing within experimental uncertainty. If the LN-PM loss were lower we would thus achieve a larger HSP rate without increasing the $g^{(2)}_H(0)$ [27]. Both experimentally measured $g^{(2)}_H(0) \ll 1$, which indicates a highly pure single photon character of the output mode. Hence, we establish that the SMUX maintains the single photon nature of the source. This conclusion is supported by additional measurements of the so-called coincidence to accidental ratio (CAR) measured with and without the SMUX [29].

We did not directly measure the degree of distinguishability of single photons from our source, but based on the experimental setup, we conjecture they must be nearly indistinguishable. The reason for this is that the photons emitted by our SMUX source pass through a FP-cavity and are coupled into single mode fibre, which removes any distinguishability in the frequency and spatial degrees of freedom. Finally, the fact that all signal photons travel along the same path, from the point where they are created to the point where they are detected, means that their arrival times and polarization are the same (irrespective of which spectral mode they belong to), provided that chromatic dispersion and polarization mode dispersion can be ignored.

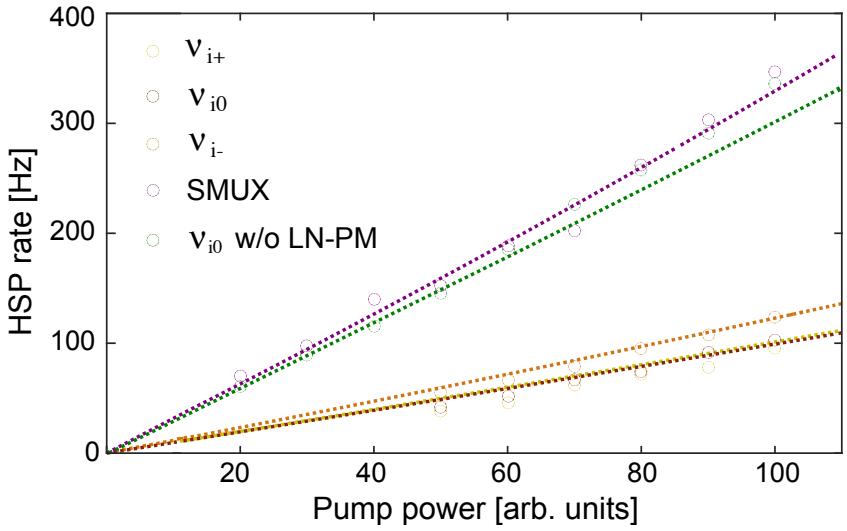

Figure 4.6: **a** HSP rate versus pump power for the individual frequency modes (red, yellow and orange circles), for SMUX of three modes (green circles) and for the ν_0 mode without the LN-PM in the signal photon mode (purple circles). Lines are linear fits to the data.

4.3.3 Discussion and conclusions

In conclusion, we have introduced the idea of a spectrally multiplexed SPS and experimentally demonstrated that multiplexing three spectral modes leads to the expected increase in the heralded single photon rate while keeping the purity constant. To achieve these results we have implemented on-demand frequency shifting of single photons over approximately ±20 GHz with nearly 100% efficiency by driving a commercially available $LiNbO_3$ phase modulator with a linear voltage ramp. This technical advance also finds application in the proposed spectrally multiplexed quantum repeater protocols [41].

There is a number of avenues to increase the heralded single-photon rate of our source. An evident path is to reduce the loss incurred by imperfect components, spectral mismatch between the filters and the SPDC pump, and imperfect coupling of the SPDC output modes. For instance, employing phase-modulator with a realistic lower loss of 1.5 dB would yield a 2.5 times improvement of the HSP rate.

Also, cavity-enhanced SPDC would allow one to define the spectral modes for the multiplexing, and thus remove loss due to spectral narrowing [30]. In addition, the increased efficiency of the SPDC process in the cavity would demand less pump power [27]. Finally, the spatial mode matching of the SPDC output to optical fibers would also be assisted by cavity enhanced SPDC, in particular if integrated with a waveguide-patterned non-linear crystal [31, 32].

At a more fundamental level, more spectral modes must be multiplexed. This can be achieved both by increasing the spectral mode density (e.g. using commercially available ultra-dense wavelength division multiplexers with 6 GHz bandwidth), as well as by improving the total bandwidth – the latter necessitating improvement of the maximum frequency shifts by using higher-bandwidth electronics [39, 33, 40, 34]. Assuming 6 GHz wide spectral channels and an 8-fold increase of the shifting range to 350 GHz (the spectral width of the photon-pairs created by our source), it is feasible to reach 60 spectral channels. This will suffice for creating at least one heralding event per pump pulse and for making the source as close to deterministic as allowed by the loss in the signal path [9], which is independent of the number of multiplexed modes. Changing the length of the non-linear crystal and phase-matching conditions an even broader SPDC spectrum and thus more modes may be feasible.

Acknowledgments

The authors thank Vladimir Kiselyov for technical support and Raju Valivarthi for discussions. This work was funded through Alberta Innovates Technology Futures (AITF), and the National Science and Engineering Research Council of Canada (NSERC). VBV and SWN acknowledge partial funding for detector development from the Defense Advanced Research Projects Agency (DARPA) Information in a Photon (InPho) program. Part of the detector research was carried out at the Jet Propulsion Laboratory,

California Institute of Technology, under a contract with the National Aeronautics and Space Administration. WT furthermore acknowledges funding as a Senior Fellow of the Canadian Institute for Advanced Research (CIFAR).

4.3.4 Supplementary information

Spectral mode selection

In order to select the different spectral modes for the heralding photons, i.e. the idler modes at ~ 1532 nm, we use a home-made spectrometer that is composed of two diffraction gratings (DGs) (Thorlabs GR50-0616) orthogonally oriented with respect to each other. The idler mode is expanded to a spot-size of ~ 23 mm in order to illuminate a large number of grooves on both diffraction gratings (recall that the spectral resolution scales linearly with the number of groves that the optical mode covers [35]). After the two DGs, the different spectral modes are coupled into separate single-mode fibres. The spectral bandwidth of each mode is determined by the angular spread caused by the gratings together with the size of the spatial mode supported by the optical fibre.

The bandwidth and transmission of each spectral mode (ν_{i-}, ν_{i0} and ν_{i+}) is measured by scanning the wavelength of a tuneable continuous wave laser and recording the transmitted light intensity coupled into each of the three fibres. The results are plotted in Fig. 4.7. The bandwidth $\delta\nu_i$ is around 12 GHz for each of the three modes, and the transmissions are 25%, 22% and 30% for the modes centered at ν_{i-}, ν_{i0} and ν_{i+}, respectively. Note that the mode overlap is negligible. The frequency separation between the modes is matched to the frequency shifts of our feed-forward system, which we describe in the next section.

A more effectively spectral mode selection could be achieved, for example, by using

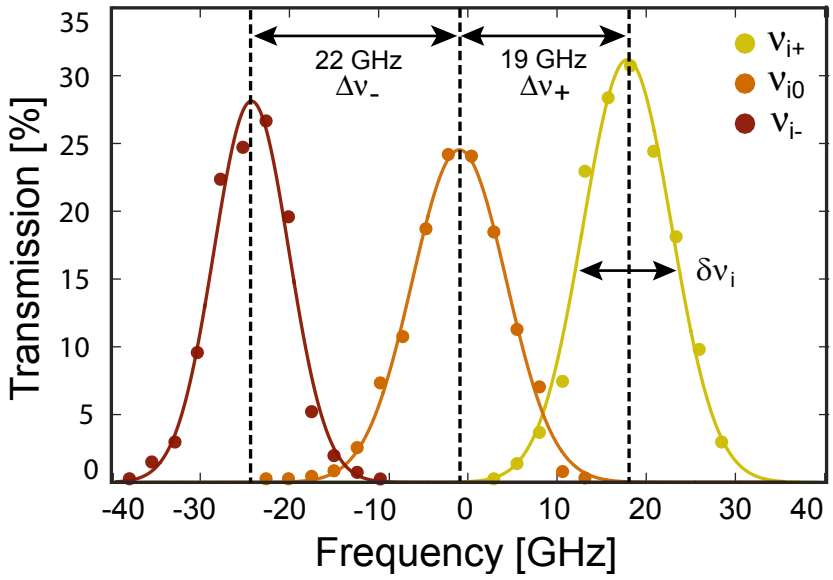

Figure 4.7: Spectra of the different spectral modes defined in the idler photon by the DGs. The total transmission through the spectrometer (in percentage) shown for each relative frequency mode, measured with respect the central mode ν_{i0} (1532.59 nm). The modes ν_{i-} and ν_{i+} are separated by $\Delta\nu_+ \approx 19$ GHz and $\Delta\nu_- \approx 22$ GHz, respectively. The bandwidth is $\delta\nu_i \approx 12$ GHz for the three modes. Experimental points are fitted with Gaussian functions.

a cavity enhanced SPDC crystal with appropriate choice of cavity parameters i.e. free-spectral range and finesse [36]. The resonant longitudinal cavity modes would constitute the spectral modes to be multiplexed. Hence the cavity, would reduce and potentially remove the requirement for external spectral filtering, which in turn would decrease the optical loss due to filtering. In addition, a cavity enhanced SPDC source can generate high purity photon pairs states [37] without any additional spectral filtering. Such high purity single photon are necessary for quantum information processing tasks and, moreover, can be coupled more efficiently into optical fibres. As a result, higher coincidence count-rates can be achieved. Notice, however, that cavity enhanced SPDC merely increases the brightness of each spectral mode, thus reducing the requisite pump power, but it does not change the ratio between single and multiphoton events the way that a multiplexed source does.

Frequency-shifting of single photons and ramp-signal generation

Frequency-multiplexing of heralded single photons requires photonic devices that actively change the frequency of the photons. To show how this is realized by means of the LN-PM, we consider a pulse of light described in the slowly-varying-envelope approximation by $\mathcal{E}_{\text{in}}(x,t) = |\mathcal{E}(x,t)| \exp(i2\pi\nu_{s0}t - ikx)$. The electro-optic effect in the LN-PM translates a linearly changing voltage signal $V(t) = \mathcal{A}t$ — applied during the passage of the optical pulse — into a linear phase-ramp $\varphi(t) = \pi V(t)/V_\pi = \mathcal{A}t\pi/V_\pi$ of the optical pulse. Here, $\mathcal{A}$ is the slope of the voltage-signal and V_π is the π-voltage of the LN-PM i.e. the voltage required to obtain a π phase-shift. Hence, upon exiting the LN-PM, the pulse is described by $\mathcal{E}_{\text{out}}(x,t) = |\mathcal{E}(x,t)| \exp(i[2\pi\nu_{s0}t + \varphi(t)] - ikx) = |\mathcal{E}(x,t)| \exp(i2\pi[\nu_{s0} + \mathcal{A}/(2V_\pi)]t - ikx)$[38]. This highlights that the output pulse is frequency shifted by $\Delta\nu = \mathcal{A}/(2V_\pi)$ — which is the ratio of the voltage slope to the 2π-voltage — while the temporal shape is unchanged. In sum, the magnitude $\Delta\nu$ of the frequency-shift in hertz can be expressed as

$$\Delta\nu = \frac{d\phi(t)}{2\pi dt} = \frac{\pi}{V_\pi}\frac{dV(t)}{2\pi dt} = \frac{\mathcal{A}}{2V_\pi}, \tag{4.8}$$

We assume that V_π is independent of the rate of change of the applied voltage modulation or, in other words, that the bandwidth of the phase-modulator is greater than the relevant spectral components of the input voltage signal. Furthermore, we assume that V_π is constant over the total spectral width of the signal photons.

In our set-up the voltage signal is generated from a home-built ramp-signal generator. Figure 4.8a depicts the schematic of our electronic circuit. The key component in the circuit is a high-voltage and large-bandwidth radio frequency (RF) transistor that acts as an inverting electrical amplifier. The ramp-signal generator takes an input signal, such as an appropriately shaped single-photon detector output, and outputs a π-phase shifted

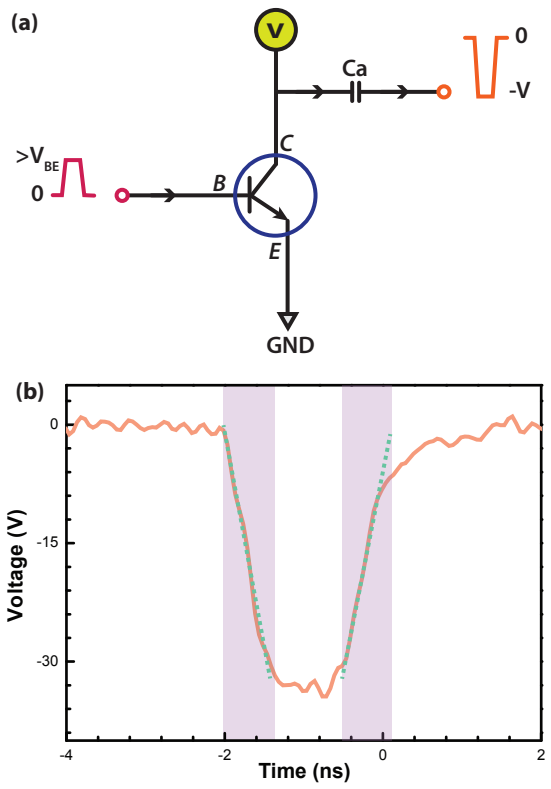

Figure 4.8: (a) Schematic circuit for ramp-signal generation; (b) Typical output of the generator.

(negative) high-voltage pulse with linearly increasing falling and rising edges as shown in Fig. 4.8b. The pulse amplitude is -35 V, and the falling and rising edges (shaded regions) are around 700 ps long. When the temporal wave-packet of the photon overlaps with the falling or rising edge of the pulse, Eq. (4.8) predicts that the spectrum of the photon is shifted in the negative or positive direction, respectively. Since the slope of the rising and falling edges are slightly different the negative and positive frequency shifts are not exactly identical. More precisely, the negative ramp is $\mathcal{A}_- \approx -70$ V/ns, which provides a frequency shift of $\Delta\nu_- = -22$ GHz while the postive ramp is $\mathcal{A}_+ \approx 53$ V/ns, which provides frequency shift of $\Delta\nu_+ = +19$ GHz. The magnitudes of these shifts agree with the spectral mode filtering shown in Fig. 4.7.

The feed-forward control circuitry, which selects the correct value for the frequency

shift depending on which idler mode provides the heralding detection, also adjusts the timing of the input pulse of the ramp generator. More specifically, the heralding signals from the ν_{i-} and ν_{i+} modes are delayed with respect to each other such that for the former, the falling (front) and for the latter the rising (back) edge of the output pulse coincides with the passage of the signal photon through the LN-PM. If a herald originates from the ν_{i0} mode no frequency shifting is required and the heralding signal is just not input into the ramp-generator.

Frequency shifting at the single-photon level has been employed in previous experimental demonstrations [39, 28]. To put our ramp-signal-based frequency-shifting method into context with these single-photon frequency shifters, we define a 'time-bandwidth-like' product that can serve as a figure-of-merit to gauge the performance of different approaches. The 'time' factor in our figure-of-merit is the maximum temporal duration $\Delta\tau$ of the optical pulse that will experience a constant frequency-shift. For a Fourier-transform-limited optical wave-packet, a larger $\Delta\tau$ indicates that a spectral mode with smaller spectral width can be defined, thus more distinct spectral modes can be obtained given the total spectral range of the frequency shifter. The 'bandwidth' factor is the maximum absolute frequency-shift $\Delta\nu_{max}$ of the optical spectrum. A larger $\Delta\nu_{max}$ means a broader spectral range that a frequency shifter can cover. Putting both of them together, a frequency shifter with larger 'time-bandwidth-like' product indicates that it can manipulated more spectral modes, which is desired for spectrally multiplexed heralded single photon sources and for light-matter interfaces based, spectrally multiplexed quantum repeaters [41, 42].

We are able to achieve a time-bandwidth product of $0.7\ \text{ns} \times 22\ \text{GHz} = 15.4$. Although larger frequency shifts have been demonstrated, the above-defined figure-of-merit in those experiments was one order of magnitude smaller. For example the time-bandwidth product was $6.25\ \text{ps} \times 200\ \text{GHz} = 1.25$ in [39] and $4\ \text{ps} \times 150\ \text{GHz} = 0.6$ in [28]. The key factor

that allows us to achieve the large 'time-bandwidth-like' product is that the frequency of our single photons is shifted with a single ramp-signal pulse of < 2 ns duration. As a consequence, even though we use a high-voltage signal at the LN-PM input, the root-mean-square (RMS) power applied to the LN-PM is very small. This is in contrast to the electronic signals with large RMS power that were used in [39, 28].

Heralded auto-correlation function

In this section we provide some basic insight into how the auto-correlation function can be used to gauge the performance of a heralded single photon source and how it is affected by multiplexing. The heralded auto-correlation function, $g_H^{(2)}(0)$, is commonly used to determine the single photon purity [43, 44] of the signal mode after heralding by the detection of photon in the idler mode. Values of $g_H^{(2)}(0)$ below 1 indicate a non-classical light field with a value of 0 corresponding to an ideal single photon.

To measure the auto-correlation function, the signal mode is split equally on a beam-splitter ,and from detectors placed at the two outputs we record the individual counts $C_{\mathrm{H}}^{(\mathrm{i})}$ ($i \in \{a, b\}$), the coincidental counts $C_{\mathrm{H}}^{(\mathrm{ab})}$ as well as the number of heralding signals H (see Fig. 1a in the main text). This allows us to define the heralded detection probabilities, e.g. $p_{\mathrm{H}}^{(\mathrm{ab})} = C_{\mathrm{H}}^{(\mathrm{ab})}/H$, and thus the heralded auto-correlation function as

$$\begin{aligned} g_H^{(2)}(0) &\equiv \frac{p_{\mathrm{H}}^{(\mathrm{ab})}}{(p_{\mathrm{H}}^{(\mathrm{a})} p_{\mathrm{H}}^{(\mathrm{b})})} = \frac{C_{\mathrm{H}}^{(\mathrm{ab})} H}{(C_{\mathrm{H}}^{(\mathrm{a})} C_{\mathrm{H}}^{(\mathrm{b})})} \\ &\approx \frac{2 p_{n=2}^{\mathrm{H}}}{(p_{n=1}^{\mathrm{H}})^2} \ . \end{aligned} \tag{4.9}$$

Here $P_{n=1}^{\mathrm{H}}$ and $p_{n=2}^{\mathrm{H}}$ correspond to the heralded probabilities of having a single photon or two photons, respectively, in the signal field, i.e. in the output of the photon source. The definition in Eq. (4.9) does not distinguish between single mode and multiplexed operation and is thus valid for both cases. The approximation, which holds for $p_{n=1} \ll 1$, provides an intuitive link between $g_H^{(2)}(0)$ and the photon number distribution, more

specifically the ratio of the undesired multi-photon probabilities (which is usually dominated by the two-photon contribution) to the desired single-photon probability in the heralded output.

Experimentally, $p^{\mathrm{H}}_{n=1}$ ($p^{\mathrm{H}}_{n=2}$) can be estimated by counting the number of single (two) photon events and dividing it by the number of heralding signals H. For a multiplexed source with a degree of multiplexing m and assuming each mode operating under the same conditions, the total number of single (two) photon events and the total number of heralding signals both increase proportional to m. This means that $p^{\mathrm{H}}_{n=1}$ ($p^{\mathrm{H}}_{n=2}$) remain the same as in the single mode case, and, consequently, the value of $g^{(2)}_H(0)$ is independent of the number of multiplexed modes m.

The advantage of using a multiplexed source versus a single mode source is that for a given value of $g^{(2)}_H(0)$ — which is related to the quality of the individual modes of the source — the rate of heralded photons in the multiplexed case ($C_{\mathrm{H}} \propto m p_{n=1}$) is m-times larger than for the non-multiplexed case ($C_{\mathrm{H}} \propto p_{n=1}$). If the multiplexed operation adds extra loss, η, to the signal channel, the multiplexed rate will be lowered to $C_{\mathrm{H}} \propto m(1-\eta)p_{n=1}$. In conclusion, for a given $g^{(2)}_H(0)$ a multiplexed heralded photon source will outperform a non multiplexed source in terms of photon output rates only if $(1-\eta) < (1/m)$. Due to extra loss introduced by the LN-PM in our current implementation, $(1-\eta) = 0.32$. In comparison, using three modes, we find $(1/m) = 0.33$.

Efficiencies and transmissions

Table 1 list the transmissions and efficiencies of the elements used in the experiment and identified in figure 1a of the main text. Furthermore, detector efficiencies are 60 % for the Si-APD, and $\approx$ 70 % for the SNSPDs (slight variations between different detectors are due to different external losses).

Element	label	Transmission [%]
Optical Fiber loop	Delay	81
Fabry-Perot Cavity	FP	45
$LiNbO_3$ Phase-Modulator	LN-PM	32

Table 4.1: Optical transmission for the different elements use in our demonstration.

Bibliography

[1] N. Gisin and R. Thew, Nat. Phot. **1**, 165-171 (2007).

[2] P. W. Shor, SIAM J. Comput. **26**, 1484 (1997).

[3] T. D. Ladd, F. Jelezko, R. Laflamme, Y. Nakamura, and C. Monroe, Nature **464**, 4553 (2010).

[4] V. Giovannetti, S. Lloyd, and L. Maccone, Phys. Rev. Lett. **96**, 010401 (2006).

[5] E. Knill, R. Laflamme, and G. Milburn, Nature 409, 46-52 (2001).

[6] J. W. Pan, Z. B. Chen, C. Y. Lu, H. Weinfurter, A. Zeilinger, and M. Zukowski, Rev. Mod. Phys. **84**, 777-838 (2012).

[7] A. E. Lita, A. J. Miller, and S. W. Nam, Optics Express **16**, 5, 3032-3040 (2008).

[8] M. S. Allman, V. B. Verma, M. Stevens, T. Gerrits, R. D. Horansky, A. E. Lita, F. Marsili, A. Beyer, M. D. Shaw, D. Kumor, R. Mirin and S. W. Nam, Appl. Phys. Lett. 106, 192601 (2015).

[9] A. Christ and C. Silberhorn, Phys. Rev. A **85**, 023829 (2012).

[10] I. Aharonovich, D. Englund, and M. Toth, Nat. Phot. **10**, 631-641 (2016).

[11] T. M. Babinec, B. J. M. Hausmann, M. Khan, Y. Zhang, J. R. Maze, P. R. Hemmer, and M. Loncar, Nat. Nano. **5**, 195-199 (2010).

[12] B. Lounis and W. E. Moerner, Nature **407**, 491-493 (2000).

[13] P. Michler, A. Kiraz, C. Becher, W. V. Schoenfeld, P. M. Petroff, Lidong Zhang, E. Hu, and A. Imamoglu, Science **290**, 2282-2285 (2000).

[14] A. J. Shields, Nat. Phot. **1**, 215-223 (2007).

[15] W. Pfaff, B. J. Hensen, H. Bernien, S. B. van Dam, M. S. Blok, T. H. Taminiau, M. J. Tiggelman, R. N. Schouten, M. Markham, D. J. Twitchen, R. Hanson, Science **345**:6196, 532-535 (2014)

[16] A. Sipahigil, K.D. Jahnke, L.J. Rogers, T. Teraji, J. Isoya, A.S. Zibrov, F. Jelezko, and M.D. Lukin, Phys. Rev. Lett. **113**, 113602 (2014).

[17] X. Ding, Y. He and Z.-C. Duan and N. Gregersen and M.-C. Chen, S. Unsleber, S. Maier, C. Schneider, M. Kamp, S. Höfling and C.-Y. Lu and J.-W. Pan, Phys. Rev. Lett., **116**, 020401 (2016).

[18] W.B. Gao, P. Fallahi, E. Togan, A. Delteil, Y.S. Chin, J. Miguel-Sanchez and A. Imamoğlu, Nat. Comm. **4** 2744 (2013).

[19] A. L. Migdall, D. Branning, and S. Castelletto, Phys. Rev. A **66**, 053805 (2002).

[20] J. H. Shapiro and F. N. Wong, Opt. Lett. **32**, 2698-2700 (2007).

[21] X.-S. Ma, S. Zotter, J. Kofler, T. Jennewein, and A. Zeilinger, Phys. Rev. A **83**, 043814 (2011).

[22] M. J. Collins, C. Xiong, I. H. Rey, T. D. Vo, J. He, S. Shahnia, C. Reardon, M. J. Steel, T. F. Krauss, A. S. Clark, and B. J. Eggleton, Nat. Comm. **4**, 2582 (2013).

[23] R. J. A. Francis-Jones, R. A. Hoggarth, and P. J. Mosley, Optica **3**, Issue 11, 1270-1273 (2016).

[24] C. Xiong, X. Zhang, Z. Liu, M. J. Collins, A. Mahendra, L. G. Helt, M. J. Steel, D.-Y. Choi, C. J. Chae, P. H. W. Leong, and B. J. Eggleton, Nat. Comm. **7**, 10853 (2016).

[25] G. J. Mendoza, R. Santagati, J. Munns, E. Hemsley, M. Piekarek, E. Martín-López, G. D. Marshall, D. Bonneau, M. G. Thompson, and J. L. O'Brien, Optica **3**, 127-132 (2016).

[26] D. Bonneau, G. J. Mendoza, J. L. OBrien, and M. G. Thompson, New J. Phys. **17**, 043057 (2015).

[27] See Supplemental Material, which includes Refs. [34-43].

[28] L. Fan *et al.*, Nature Photonics, Nature Photonics **10**, 766770 (2016.)

[29] Manuscript in preparation

[30] J. Jin, M. Grimau Puigibert, L. Giner, J. A. Slater, M. R. E. Lamont, V. B. Verma, M. D. Shaw, F. Marsili, S. W. Nam, D. Oblak, and W. Tittel Phys. Rev. A **92**, 012329 (2015)

[31] Z. Vernon, M. Menotti, C. C. Tison, J. A. Steidle, M. L. Fanto, P. M. Thomas, S. F. Preble, A. M. Smith, P. M. Alsing, M. Liscidini, and J. E. Sipe, arXiv:1703.10626 (2017)

[32] M. Bock and A. Lenhard and C. Chunnilall and C. Becher, Opt. Express, **24**, 23992–24001, (2016)

[33] Q. Li, M. Davano, and K. Srinivasan, Nat. Phot. **10**, 406-414 (2016)

[34] B. Albrecht, P. Farrera, X. Fernandez-Gonzalvo, M. Cristiani, and H. de Riedmatten, Nat. Comm. **5**, 3376 (2014).

[35] www.horiba.com/scientific/products/optics-tutorial/diffraction-gratings/, visited november 2016.

[36] J. Moreno, S. Rodriguez-Benavides and, A. B. URen, Laser Phys. **20**, 1221 (2010).

[37] P. J. Mosley, J. S. Lundeen, B. J. Smith and, I. A. Walmsley, New Journal of Physics, **10** (2008).

[38] B. Brecht, D. V. Reddy, C. Silberhorn, and M. Raymer, Phys. Rev. X **5**, 041017 (2015).

[39] L. J. Wright, M. Karpiǹski, C. Söller and B. J. Smith, arXiv:1605.00640v1, (2016).

[40] L. Fan, C. Zou, M. Poot, R. Cheng, X. Guo, X. Han, and Hong X. Tang, Nat. Phot. **10**, 766-770 (2016).

[41] N. Sinclair, E. Saglamyurek, H. Mallahzadeh, J. A. Slater, M. George, R. Ricken, M. P. Hedges, D. Oblak, C. Simon, W. Sohle, and W. Tittel, Phys. Rev. Lett. **113**, 053603 (2014)

[42] E. Saglamyurek, M. Grimau Puigibert, Q. Zhou, L. Giner, F. Marsili, V. B. Verma, S. W. Nam, L. Oesterling, D. Nippa, D. Oblak and, W. Tittel, Nature Communications **7**, 11202 (2016).

[43] N. Somaschi, V. Giesz, L. De Santis, J. C. Loredo, M. P. Almeida, G. Hornecker, S. L. Portalupi, T. Grange, C. Antn, J. Demory, C. Gmez, I. Sagnes, N. D. Lanzillotti-Kimura, A. Lematre, A. Auffeves, A. G. White, L. Lanco, and P. Senellart, Nat. Phot., **10** 340-345, (2016).

[44] P. Sekatski, N. Sangouard, F. Bussires, C. Clausen, N. Gisin and H. Zbinden Journal of Physics B, **45** (2012).

Chapter 5

Quantum light storage for quantum repeaters

An optical Quantum Memory (QM) is a device capable of reversibly storing and retrieving a photon carrying quantum information. Usually the photon is mapped and stored onto long lived atomic excitations in the storage medium. QMs have been implemented in different physical systems, for example cold atomic ensambles, single atoms inside optical cavities, warm atomic vapours, and impurities doped into crystals operated at cryogenic temperatures etc [44].

Generally, in QRs, QMs are used to store photons for a certain amount of time, allowing to synchronize and swap entanglement between elementary links. Specifically, in the frequency multiplexed QR scheme presented in section 3, a QM needs to preserve the photon state during the time required for the photon to reach the BSM station plus the time required for the result of the BSM projection to reach again the QM (see figure 3.1). If the elementary links are symmetric, i.e. the BSM station is located at the center between the two QMs, the QMs need to preserve the photon state by $L_o n_f/c$, where L_o correspond to the total length of an elementary link, n_f correspond to the index of refraction of an optical fibre and c to the speed of light.

In the following section we will introduce the basic principles of the QM protocols and materials developed in our group. We will also discuss the specific requirements for a QM to be used in QR applications. Two experiments involving quantum light storage will also be presented and discussed.

5.1 Optical quantum memory materials and protocols

For efficient reversible mapping of photons onto long lived atomic excitations, strong light-matter interaction is required. This can be easily overcome by the use of an atomic ensemble where the interaction strength is enhanced thanks to the presence of a large number of atoms [45]. Another approach is to use individual atoms and to increase the ligh-matter interaction by means of a high finesse optical cavity ; however, that approach is technically more demanding. Here we will focus on a particular photon echo based QM protocol [46] based on atomic frequency comb (AFC) [47] implemented with rare-earth ions (REI) doped into solids. In the following section we will describe the basics physical properties of REI doped solids and how their properties are well matched for the implementation of the AFC protocol.

5.1.1 Rare earth-ion doped solids

REIs display optical, visible and infrared, transitions between 4f-4f electronic orbitals with narrow homogeneous linewidths, moreover, they often exhibit long-lived spin states. Usually, when atomic impurities are doped into solids, their optical and spin properties are strongly affected by the interaction with the host material, but this is not the case for REIs. The transitions of interest, are effectively screened by fully or partially filled outer orbitals thus being protected from the host environment (see figure 5.1) and thereby exhibiting atom like properties, even when doped into solids.

In order to reduce vibrations in the host, which may affect the optical and spin properties, REI doped solids are usually cooled to cryogenic temperatures (<4K). At these temperatures inhomogeneous broadening is the dominating broadening process; it determines the overall optical absorption profile. The inhomogeneous broadening is due to different local environments experienced by different ions (e.g. due to strain and crystal

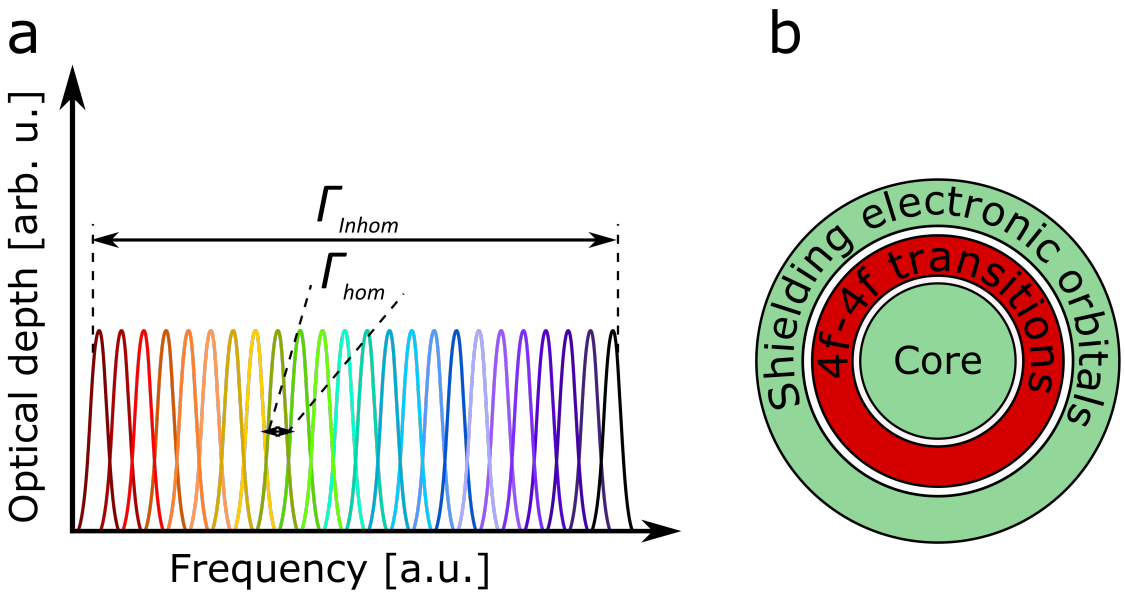

Figure 5.1: **Rare-earth ion doped solid absorption profile and rare-earth ion electronic structure**. **a** Schematic Rare-Earth Ion (REI) electronic structure showing the 4f-4f transitions being screened by outer electronic orbitals **b** Schematic representation of an inhomogeneously broadened asboroption profile with width Γ_{inhom} composed of narrow (Γ_{hom}) homogeneous spectral lines.

imperfections); their optical transition frequencies are shifted by different amounts while their narrow homogeneous linewidth is weakly affected (see figure 5.1).

Homogenous linewidths of optical transitions at $\sim$ 4K of REI doped solids can range from <1 kHz to 1 MHz [45], where the main limitations are often due to magnetic interactions with other rare-earth ion dopants or magnetic constituents of the lattice. Moreover, the optical inhomogeneous linewidth varies strongly between crystal hosts, it usually ranges from a few hundred of MHz to tens of GHz [45].

5.1.2 The Atomic Frequency Comb (AFC) quantum memory protocol

Photon-echo based QMs rely on the possibility to map a photon onto an inhomogeneously broadened absorption profile and, by controlling the rephasing of the collective

excitation, retrieve the photon some time later. Different photon-echo quantum memory protocols use different procedures to rephase the atomic dipoles. Here we will focus on the so called AFC protocol. This protocol is particularly well suited for our frequency multiplexed QR since its multimode capacity is independent of the overall optical depth of the QM medium [48].

In order to implement the AFC protocol the inhomogeneously broadened absorption profile needs to be tailored into a comb-like structure, usually referred to as atomic frequency comb, by means of selective optical pumping (see figure 5.2). For the implementation of this protocol the atomic system require an extra atomic level in which the population, removed to create the comb-like structure, can be shelved for much longer than the coherence time of the optical transition. Before a single photon is absorbed, the photon-atomic ensemble system can be represented mathematically as

$$|\Psi\rangle_{pa} = |1\rangle_p \otimes |g_0, ..., g_i, ...g_N\rangle_a, \tag{5.1}$$

where the first term represents a single photon state and the second term corresponds to the atomic state with all N, atoms forming the atomic ensemble, being in the ground state $|g\rangle$. If now a single photon is absorbed by the spectrally tailored absorption structure with peaks of width γ that are separated by Δ, a collective excitation shared amongst all the atoms is created. The resulting state can be described by

$$|\Psi\rangle_{pa} = |0\rangle_p \otimes \sum_{i=1}^{N} c_i e^{i2\pi\delta_i t} e^{-ik_i z_i} |g_0...e_i...g_N\rangle_a, \tag{5.2}$$

Where $|e_i\rangle$ represents the ith atom being in the excited state, δ_i is the detuning of atom's transition frequency with respect to the central frequency of the absorbed photon, z_i its position measured along the propagation direction of the light, k the wavevector corresponding to the photon wavelength, c_i the absorption probability amplitude that depends on the atom's resonance frequency and position, and t the elapsed time after

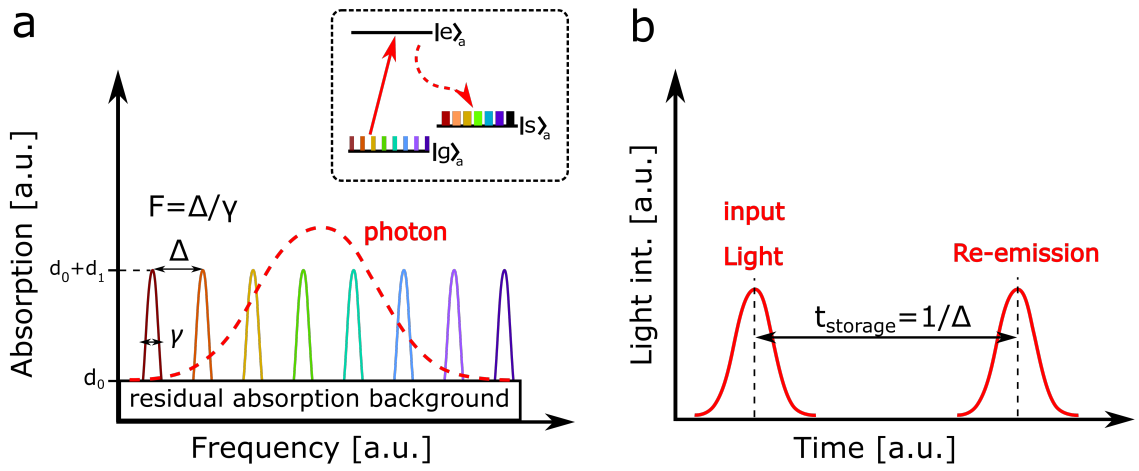

Figure 5.2: **Schematic Atomic Frequency Comb (AFC) profile and photon echo retrieval**. **a** An idealized AFC structure composed of a series of equally spaced absorption peaks with height d_1 width γ and separation Δ on a residual absorption background d_0. The dashed line represents the spectrum of a photon mapped onto the AFC. Inset: representation of frequency-selective optical pumping into a shelving state $|s\rangle_a$. **b** Representation of a photon echo being re-emitted after a time corresponding to $t_{storage} = 1/\Delta$.

the photon is absorbed.

Next, the collective excitation described by equation 5.2 rapidly dephases since each atom has a different transition frequency or detuning δ_i. In this case, due to the particularly shaped absorption structure, the detunning factor δ_i only take discrete values of the teeth separation separation $\delta_i = \Delta m_i$ ($m_i \in \mathcal{Z}$). Thus, due to this periodicity, after a time $t_{storage} = 1/\Delta$ the atomic coherence is recovered and the photon automatically re-emitted.

The photon recall efficiency is determined by the details of the comb-like structure. If the teeth are gaussian shaped, the recall efficiency in the forward direction (η_{AFC}) can be analytically expressed as [47]

$$\eta_{AFC} = \left(\frac{d_1}{F}\right)^2 e^{-d_1/F} e^{-7/F^2} e^{-d_0} \tag{5.3}$$

where d_1 is the optical depth of the comb teeth, d_o is the background optical depth and

F corresponds to the comb finesse defined as $F = \Delta/\gamma$ (see figure 5.2). The maximum achievable efficiency when the recall is in the forward direction is limited to 54% [47] since the re-emitted photon can be re-absorbed. A 100 % recall efficiency can be reached if the photon is recalled in the backward direction [47] or the crystal is embedded in an impedance-matched optical cavity [49]. In terms of storage time, the limit is determined by the closest separation between comb teeth, which ultimately is given by Γ_{hom}. Notice that the storage time is pre-programmed in the above-described protocol, in order to achieve temporal recall on demand the collective excitation can be transferred to a long-lived spin state (3 level AFC) and recalled after applying optical control pulses (π pulses) [47].

Our group has developed AFC-based QMs in different REI doped solids with different properties. For example, a titanium indifused Tm^{3+}:$LiNbO_3$ waveguide has been used to demonstrate a broadband QM for entangled photons [50]. It exhibits coherence times (T_2) on the optical transition of 117 μs ($T_2 = 1/\pi\Gamma_{hom}$) at <1K [51], with a large inhomogenous broadening of $\sim$ 400 GHz. The group has also developed a QM based on a commercial Erbium doped fibre, which was used in the experiments presented in the following [52, 53, 54].

5.2 Figures of merit and requirements for quantum repeater applications

In this section we will describe the figures of merit and requirements for a QM to be used in QR applications. We will focus on QM based on REI solids, and comment on the state of the art and feasible improvements.

Storage time

QMs are used to store photon states for a certain amount of time, thereby allowing to synchronize and swap entanglement between elementary links. The required storage time depends on the specific QR architecture choosen. For example, in order to implement our frequency multiplexed QR [36] (section 3) we would need a storage time of around $500\mu s$ if using an elementary link length of 100km (the storage time is given by the elementary link length (L_o) divided by the speed of light in fibre). On the other hand, for some other protocols the storage time needs to be on the order of the total communication length (L) divided by the speed of light in fibre. For instance, for L=1000km, the storage time required would be $\approx$ 5 ms.

For the AFC QM protocol previously discussed the ultimate limit to the storage time is set by the inverse of the homogeneous linewidth Γ_{hom}, provided the photon state is mapped onto optical coherence. Coherence times corresponding to an homogeneous linewidths of <1KHz have been observed in REI doped materials but practically, the narrowest AFC teeth realized so far are on order of tens to hundreds of kHz. The storage time could be drastically increased if the excitation is mapped onto a longer lived spin level [55, 56].

Efficiency

The QM recall efficiency is defined as the combined probability for a single photon to be stored and retrieved by the QM. The ultimate purpose of a QR is to overcome the fibre transmission loss in a storage spool that introduces the same delay, e.g. for an storage time of $500\mu s$ the memory should be greater than 1%, which would correspond of a fibre loop of 100km [57]. Modern optical fibres have an attenuation of around 0.2dB/km and is mainly due to material absorption, light scattering and imperfect splicing and connection

losses.

As stated previously, the maximal attainable efficiency with the AFC protocol is 54% when re-emission is triggered in the forward direction. However, 100 % efficiency can be reached if the photon is recalled in the backward direction or if an impedance matched cavity is used. The highest reported QM recall efficiency using an impedance matched REI doped material based toghether with the AFC protocol is 56 % with an storage time of 1.1 μs [58]. To date, the state-of-the-art for the recall efficiency of a QM using a REI doped material is 69% using the so called Gradient Echo Memory (GEM) protocol [59].

Fidelity

The fidelity ($\mathcal{F}$) of a quantum state (ρ_{in}) is defined as the overlap with respect a reference state ρ_{out}; and is defined as

$$\mathcal{F} = \left(Tr \left\{ \sqrt{\sqrt{\rho_{out}} \rho_{in} \sqrt{\rho_{out}}} \right\} \right)^2 . \tag{5.4}$$

Ideally, a QM should be able to store and input quantum states without altering them, thus the fidelity should be equal to 1. Any process is said to be in the quantum regime if the measured fidelity of such a process surpasses the maximum value that can achieved by means of classical strategies $\mathcal{F}_{classical}$. Depending on the number of particles (N) used to encode the quantum state this is given by [60]

$$\mathcal{F}_{classical}(N) \leq \frac{N+1}{N+2}. \tag{5.5}$$

In the case of using a single photon to encode qubits $\mathcal{F}_{classcical}(1) \leq 2/3$. In [36] is shown how decoy-state method, can be used to asses the quantumness of a QM even though qubits are encoded into attenuated laser pulses.

In the context of QR and QMs it is common to refer to the post-selected fidelity, in

that case, the fidelity is computed conditioned on the fact that a photon is retrieved. The QM protocols are designed in order to not affect the stored states, and most of the observed corruptions reside in technical imperfections.

Bandwidth

In order to efficiently store a photon, the photon's spectral bandwidth needs to be smaller than the AFC bandwidth (see figure 5.2). Large available bandwidths allow the use of short photonic wavepackets and thus to increase repetition rates. Moreover, large bandwidth allow multiplexed storage of many small-bandwidth photons.

REI solid-state materials are in general good candidates to implement broad bandwidth QMs since they exhibit good coherence properties over a large extent of their inhomogeneous broadening e.g. $\sim$ 400GHz Tm^{3+}:$LiNbO_3$ [50]. Record QM bandwidths have been achieved by the QMs developed in our group, $\sim$ 6 GHz using a Tm^{3+}:$LiNbO_3$ waveguide [50] and $\sim$ 18 GHz using an Er doped fibre (see paper 2).

Multiplexing capabilities

The capability to store multiple photons occupying different modes (frequency, temporal, polarization, etc.) is necessary to achieve higher rates in QRs. In a QR architecture, a multimode QM allows to attempt to distribute entanglement simultaneously across elementary links. Specifically, in the frequency multiplexed QR architecture described previously, (section 3) the multimode capability of the QM is a crucial factor since the architectures is based on the possibility to use a large number of modes (10^2-10^6 modes).

The capacity to simultaneosuly store many modes is a natural capability for certain QMs based on atomic ensembles. The AFC protocol, in contrast to other protocols [48], is particularly well suited in terms of multiplexing capabilities, since the number

of modes does not depend on the available optical depth [48]. It can be seen easily that, it is roughly equal to the number of teeth created in the comb-like absorption profile. Therefore it is clear that having a large available bandwidth is advantageous and plays a crucial role on the multimode. For instance, in paper 2, by exploiting the huge inhomogeneous broadening of our Er doped optical fibre, we demonstrate the feasibility of storing and manipulating around 800 modes simultaneously.

5.3 Paper 2: A multiplexed light-matter interface for fibre-based quantum networks

Summary - We explore the multimode capability of our AFC based QM by storing, retrieving and manipulating different frequency modes, defined by different spectral intervals, of photons emitted by an integrated SPDC photon source. As a QM storage device we utilize a standard Er doped fibre operated at cryogenic temperatures [52, 53, 54] with the atomic transition of interest in the telecommunication band. Due to its huge inhomogeneous broadening a large number of frequency modes can be stored simultaneously, which is a feature required for implementing a frequency multiplexed QR and for the scalability of future quantum networks. As a photon source we employ a fully integrated periodically poled $LiNbO_3$ waveguide emitting degenerate photon pairs in the telecommunication band, interfaceable with our AFC QM. Specifically, we demonstrate the possibility of simultaneously storing and manipulating different frequency modes while preserving quantum correlations, verified by measuring the cross-correlation function between the down-converted photons. Our proof-of-principle demonstration is important in view of building future quantum networks.

Contributions - This experiment was conducted in collaboration with Jeongwan Jin, Erhan Saglamyurek, Lambert Giner, Qiang Zhou and Daniel Oblak. The single photon detectors were designed, built and tested by Francesco Marsili, Matthew D. Shaw, Varun B. Verma and Sae Woo Nam. The periodically poled $LiNbO_3$ SPDC waveguide was designed and manufactured by Lee Oesterling and David Nippa. The experiment was conceived and supervised by Wolfgang Tittel. I specifically contributed to the design and development of the setup of the SPDC photon pair source as well as its interface with the AFC based QM. I also contributed in data taking and the analysis of the measurement

results. Regarding the manuscript, I contributed writing the technical details of the experiment and, in conjuction with the other co-authors, to all the editing steps until publication.

A multiplexed light-matter interface for fibre-based quantum networks

Nature Communications 7, 11202

5 April 2016

E. Saglyamurek[1], M. Grimau Puigibert[1], Q.Zhou[1], L. Giner[1,†], F. Marsili[2], M. D. Shaw[3], V. B. Verma[4], S.W. Nam[4], L. Oesterling[5], D. Nippa[5], D. Oblak[1] and W. Tittel[1]

[1]*Institute for Quantum Science and Technology, and Department of Physics and Astronomy, University of Calgary, 2500 University Drive NW, Calgary, Alberta T2N 1N4, Canada*

[2]*Jet Propulsion Laboratory, California Institute of Technology, 4800 Oak Grove Drive, Pasadena, California 91109, USA*

[3]*National Institute of Standards and Technology, Boulder, Colorado 80305, USA*

[4]*Battelle, 505 King Avenue, Columbues, Ohio 43201, USA*

†*Present Address: Department of Physics, University of Ottawa, 150 Louis Pasteur, Ottawa, Ontario, Canada K1N 6N5*

Abstract

Processing and distributing quantum information using photons through fibre-optic or free-space links is essential for building future quantum networks. The scalability needed for such networks can be achieved by employing photonic quantum states that are multiplexed into time and/or frequency, and light-matter interfaces that are able to store and process such states with large time-bandwidth product and multimode capacities. Despite important progress in developing such devices, the demonstration of these capabilities using non-classical light remains challenging. Employing the atomic frequency comb quantum memory protocol in a cryogenically cooled erbium-doped optical fibre, we report the quantum storage of heralded single photons at a telecom-wavelength (1.53 μm) with a time-bandwidth product approaching 800. Furthermore we demonstrate frequency-multimode storage as well as memory-based spectral-temporal photon manipulation. Notably, our demonstrations rely on fully integrated quantum technologies operating at telecommunication wavelengths, i.e. a fibre-pigtailed nonlinear waveguide for the generation of heralded single photons, an erbium-doped fibre for photon storage and manipulation, and fibre interfaced superconducting nanowire devices for efficient single photon detection. With improved storage efficiency, our light-matter interface may become a useful tool in future quantum networks.

5.3.1 Introduction

Multiplexing, particularly in the form of wavelength division multiplexing, is key for achieving high data rates in modern fibre-optic communication networks. The realization of scalable quantum information processing demands adapting this concept, if possible using components that are compatible with the existing telecom infrastructure. One of the challenges to achieve this goal is to develop integrated light-matter interfaces that

allow storing and processing multiplexed photonic quantum information. In addition to efficient operation, ease of integration and feed-forward controlled recall, the suitability of such interfaces depends on the storage time for a given acceptance bandwidth, i.e. the interface's time-bandwidth product, as well as its multimode storage and processing capacities. It is important to note that while the multimode capacity of a light-matter interface determines the maximum number of simultaneously storable and processable photonic modes, the time-bandwidth product only sets an upper bound to the multimode capacity for temporally and/or spectrally multiplexed photons.

Over the past decade there has been significant progress towards the creation of such light-matter interfaces. One promising approach is based on a far off-resonant Raman transfer in warm atomic vapour, for which a time-bandwidth product of 5000 has been reported [1]. However, due to noise arising from (undesired) four-wave mixing, the storage and recall of quantum states of light has proven elusive [2]. This problem can be alleviated by implementing the Raman protocol in other media, e.g., diamonds (with storage in optical phonon modes) and laser-cooled atomic ensembles, for which time-bandwidth products around 22 have been obtained with non-classical light [3, 4]. However, the multimode operation of any Raman-type memory and hence the utilization of the potentially achievable large time-bandwidth products will remain challenging due to unfavourable scaling of this scheme's multimode capacity with respect to optical depth [5].

Another promising avenue for a multiplexed light-matter interface is the atomic frequency comb (AFC)-based quantum memory scheme in cryogenically cooled rare-earth ion doped materials [6, 7]. An attractive feature of this approach is that, unlike in many other protocols, the multimode storage capacity is independent of optical depth; it is solely given by the time-bandwidth product of the storage medium, which can easily go up to several thousands due to the generally large inhomogeneous broadening

(enabling large storage bandwidth) and narrow homogeneous linewidth (allowing long storage times) of optical transitions in rare-earth ion doped materials. This aspect has already allowed several important demonstrations, including the simultaneous storage of 64 and 1060 temporal modes by AFCs featuring pre-programmed delays [8, 9], 5 temporal modes by an AFC with recall on-demand [10], and 26 spectral modes supplemented with frequency-selective recall [11], respectively. Despite the importance of these demonstrations, they were restricted to the use of strong or attenuated laser pulses rather than non-classical light, as required in future quantum networks. The only exception is the very recent demonstration of the storage of photons, emitted by a quantum dot, in up to 100 temporal modes [12].

In this paper we present a spectrally multiplexed light-matter quantum interface for non-classical light. More precisely, we demonstrate large time-bandwidth-product and multimode storage of heralded single-photons at telecom wavelength by implementing the AFC protocol in an ensemble of erbium ions. As an important feature for future quantum networks, our demonstrations rely on fully integrated quantum technologies, i.e. a fibre-pigtailed $LiNbO_3$ waveguide for the generation of heralded single photons by means of parametric down-conversion, a commercially available, cryogenically-cooled erbium-doped single-mode fibre for photon storage and manipulation, and superconducting nanowire devices for high efficiency single photon detection.

5.3.2 Measurement and results

Our experimental setup, illustrated in Figure 5.12, is composed of an integrated, heralded single photon source, an AFC-based erbium-doped fibre memory, and a measurement unit including two superconducting nanowire single-photon detectors (SNSPDs).

We generate pairs of energy-time quantum correlated telecom-wavelength photons – commonly referred-to as *signal* (s) and *idler* (i) – by sending pump light from a

continuous wave (CW) laser operating at 766 nm wavelength to a periodically poled lithium niobate (PPLN) waveguide, as shown in Fig 5.12a. Spontaneous parametric down conversion (SPDC) based on type-0 phase matching results in the creation of frequency-degenerate photon pairs centred at 1532 nm wavelength and having a bandwidth of about 40 nm. We note that the PPLN waveguide is fibre pigtailed at both input and output faces (i.e. for the pump light as well as the down-converted photons), which makes the source alignment free. After filtering away the remaining pump light, the spectra of the generated photons are filtered down to 50 GHz resulting in a photon-pair generation rate of 0.35 MHz. The ensuing photons are probabilistically separated into two standard telecommunication fibres using a 50/50 fibre-optic beam splitter (BS2). One member of each split pair is sent into an SNSPD featuring a system detection efficiency of around 70% (see the Methods for details of the SNSPDs). Its electronic output heralds the other member, which travels through standard telecommunication fibre to our light-matter interface (for more details about the heralded single photon source see the Supplementary Note 1).

To store or manipulate the heralded single photons, we prepare an AFC-based memory in a twenty-meter long erbium-doped silica fibre maintained at a temperature of 0.6-0.8 K and exposed to a magnetic field of 600 G (see Fig. 5.12b and the Methods for details). The memory relies on spectral tailoring of the inhomogenously broadened, ${}^4I_{15/2} \leftrightarrow {}^4I_{13/2}$ transition in erbium into a comb-shaped absorption feature characterized by the teeth spacing, Δ, as shown in Fig. 5.4a. The spectral tailoring is performed by frequency-selective optical pumping of ions into long-lived auxiliary (spin) levels. When an input photon is absorbed by the ions constituting the comb, a collective atomic excitation is created. It is described by:

$$|\Psi\rangle = \frac{1}{\sqrt{N}} \sum_{j=1}^{N} c_j e^{i2\pi m_j \Delta t} e^{-ikz_j} |g_1, \cdots e_j, \cdots g_N\rangle \ , \tag{5.6}$$

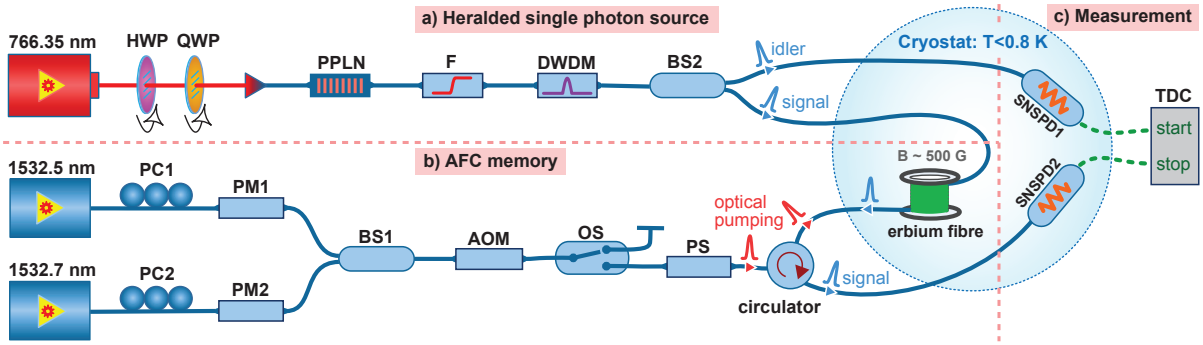

Figure 5.3: **Experimental setup. a) Heralded single photon source.** Narrow linewidth continuous-wave (CW) light at 766.35 nm wavelength and with 100 μW power is sent to a fibre-pigtailed, periodically-poled lithium niobate (PPLN) waveguide that is heated to 52.8°C. A quarter-wave-plate (QWP) and a half-wave-plate (HWP) match the polarization of the light to the crystal's C axis to maximize the non-linear interaction. Spontaneous parametric down conversion (SPDC) in the PPLN crystal results in frequency degenerate photon pairs with 40 nm bandwidth, centred at 1532 nm wavelength. The residual pump light at 766.35 nm is suppressed by 50 dB by a filter (F) and the bandwidth of the created photons is filtered down to 50 GHz using a dense-wavelength-division-multiplexer (DWDM). The filtered photon pairs are probabilistically split using a beam-splitter (BS2). The detection of one member (the *idler* photon) heralds the presence of the other (the *signal* photon), which is directed to the input of the AFC memory. **b) Quantum memory.** The quantum memory is based on an erbium-doped fibre that is exposed to a magnetic field of 600 G and cooled to a temperature below 1 K. Light from two independent CW lasers with wavelengths of 1532.5 and 1532.7 nm, respectively, is used to spectrally tailor the inhomogeneously broadened 1532 nm absorption line of erbium through frequency-selective optical pumping into one or several atomic frequency combs. Towards this end, phase-modulators (PM1 and PM2) followed by an acousto-optic modulator (AOM) are used to generate chirped pulses with the required frequency spectrum. The optical pumping light from the two lasers is merged on a beam-splitter (BS1) and enters the erbium fibre from the back via an optical circulator. Polarization controllers (PM1 and PM2) match the polarization to the phase-modulators active axes, and the polarization scrambler (PS) ensures uniform optical pumping of all erbium ions in the fibre [13]. **c) Measurement unit.** The detection of the heralding photon (*idler*) and subsequently the *signal* photon is performed by two superconducting nano-wire single photon detectors (SNSPD1 and SNSPD2) maintained at the same temperature as the memory. The coincidence analysis of the detection events is performed by a time-to-digital converter (TDC).

where N is the total number of addressed atoms, k is the optical wave number and $|g_j\rangle$ and $|e_j\rangle$ are the j'th atom's ground and excited states, respectively. The detuning of the atom's transition frequency from the photon carrier frequency is given by $m_j\Delta$, while z_j is the position of the atom measured along the propagation direction of the light, and the factor c_j depends on both the resonance frequency and position of the atom. Due to the periodic nature of the AFC, the atomic excitation is converted back to photonic form and the input photon is re-emitted in the originally encoded state after a storage time given by the inverse of the peak spacing, $t_{\text{storage}} = 1/\Delta$, as shown in Fig. 5.4b. The use of erbium doped fibre is particularly attractive for AFC-based quantum memory because of its polarization insensitive operation at wavelengths within the telecom C-band [13], its ability to store photonic entanglement in combination of ease of integration with standard fibre infrastructure [43], and its large usable inhomogeneously broadened absorption line [44], which allows for multimode storage and manipulation of photons with large bandwidth, as detailed below.

Finally, we detect the heralded photons after storage/manipulation using a second SNSPD, featuring similar performance as that used to detect the heralding photon. All detection signals are sent to a time-to-digital converter (TDC) to perform time-resolved coincidence measurements. This allows us to calculate the cross-correlation function

$$g_{si}^{(2)} = \frac{R_{si}}{R_i R_s}, \tag{5.7}$$

where R_{si} is the rate of coincidence detections, and R_s and R_i are the single detection count-rate for *signal* and *idler* photons, respectively. A classical field satisfies the Cauchy-Schwarz inequality $\left[g_{si}^{(2)}\right]^2 \leq g_s^{(2)} g_i^{(2)}$ where $g_s^{(2)}$ and $g_i^{(2)}$ are second-order auto-correlation functions for *signal* and *idler* modes. For photons derived from an SPDC process, the second-order auto-correlation is bounded by $1 \leq g_{s,i}^{(2)} \leq 2$ [16]. Consequently, measuring a cross-correlation $g_{si}^{(2)}$ greater than 2 violates the inequality and thus verifies the presence

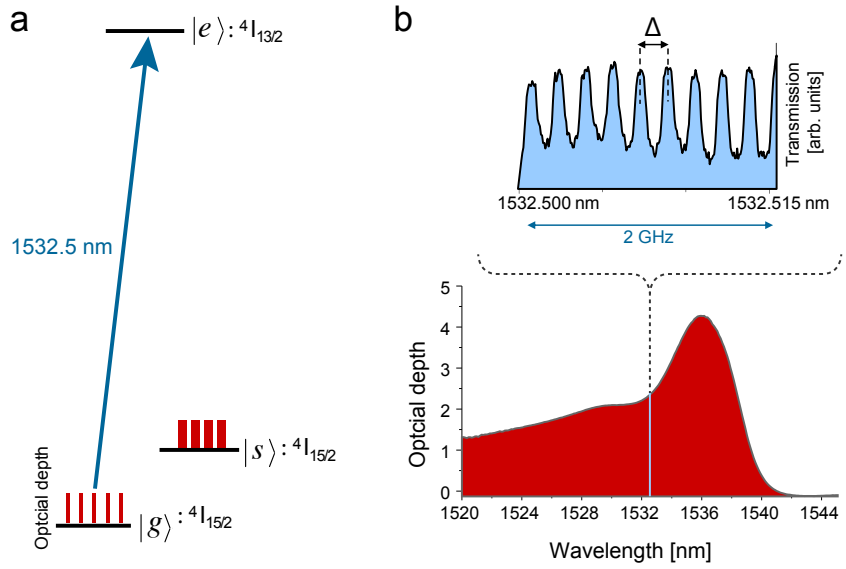

Figure 5.4: **Quantum memory. a) Simplified level scheme of Er^{3+} in silica glass.** Frequency-selective optical pumping from the ${}^4I_{15/2}$ electronic ground state ($|g\rangle$) via the ${}^4I_{13/2}$ excited state ($|e\rangle$) into an auxiliary (spin) state ($|s\rangle$) allows spectral tailoring. **b) Inhomogeneous broadening and AFC structure.** The inhomogeneously broadened optical absorption line of erbium ions in silica fibre at 1 K extends from roughly from 1500 nm to 1540 nm wavelength. A 2 GHz-wide section of a 16 GHz-wide comb at 1532.5 nm with teeth spacing Δ=200 MHz is shown.

of quantum correlations between the members of the photon pairs. We characterize our source for different SPDC pump powers (shown in Supplementary Fig. S1), finding that the cross-correlation function exceeds 1000 for all powers. Since $g_{si}^{(2)} \gg 2$ implies that the heralded autocorrelation function of the stored signal photons is $\ll 1$ [17], we denote these as single photons. The details of how $g_{si}^{(2)}$ is obtained from the coincidence counts are given in the Methods.

First, we investigate the storage of broadband heralded single-photons in an AFC memory – prepared using a single optical pumping laser at 1532.5 nm – with a total bandwidth of 8 GHz and 200 MHz tooth spacing (corresponding to 5 ns storage time), as shown in Fig. 5.4b. The recalled photons are shown as a light-blue trace in the histogram of coincidence detections in Fig. 5.5. Analyzing the correlations between signal and

recalled idler photons, we find $g_{si}^{(2)} = 8.33 \pm 0.47$, which shows that the heralded photons after – and hence also before – storage, are indeed non-classical, and thus confirms the quantum nature of our light-matter interface. To improve the storage efficiency and thus the signal-to-noise ratio in the coincidence counts we increase the storage bandwidth of the memory to 16 GHz – recall that the bandwidth of the input photons is 50 GHz. Due to restrictions imposed by the level structure of erbium (see Supplementary Fig. S2), the bandwidth increase is achieved by generating an additional 8 GHz-wide section separated from the first by around 20 GHz from edge to edge. This entails using two independent lasers operating at 1532.5 nm and 1532.7 nm wavelength for preparation of the two spectrally separated AFCs. As expected, this leads to an improvement of the overall memory efficiency and thus coincidence count rate from 0.59 ± 0.06 Hz to 1.29 ± 0.13 Hz (see Fig. 5.5), and an increase of $g_{si}^{(2)}$ to 18.2 ± 0.9. The number of AFCs, and thus the total storage bandwidth, can be further increased by employing additional pump lasers.

Second, to demonstrate quantum storage with large time-bandwidth product we extend the memory storage time from 5 ns up to 50 ns. To this end we program a 16 GHz wide spectral region with two AFCs having tooth spacing ranging from 200 MHz to 20 MHz. For each case we map heralded photons onto the double AFC and collect coincidence statistics for the recalled photons as shown in Fig. 5.6. As further detailed in the Supplementary Information of [43], decoherence effects and imperfect preparation of the AFCs decreases the memory efficiency as the storage time increases. Nevertheless, as shown in the inset of Fig. 5.6, $g_{si}^{(2)}$ still remains above 2 up to the maximal storage time of 50 ns, and thus we demonstrate the storage of non-classical light with a time-bandwidth product up to 800 (i.e. 16 GHz $\times$ 50 ns). This is an improvement by close to a factor of 40 over that obtained in Raman-based memories [4] and a factor of 3 over the recent AFC-based memory demonstration [12], respectively. We emphasise that this comparison of time-bandwidth products does not reflect the difference in multimode storage

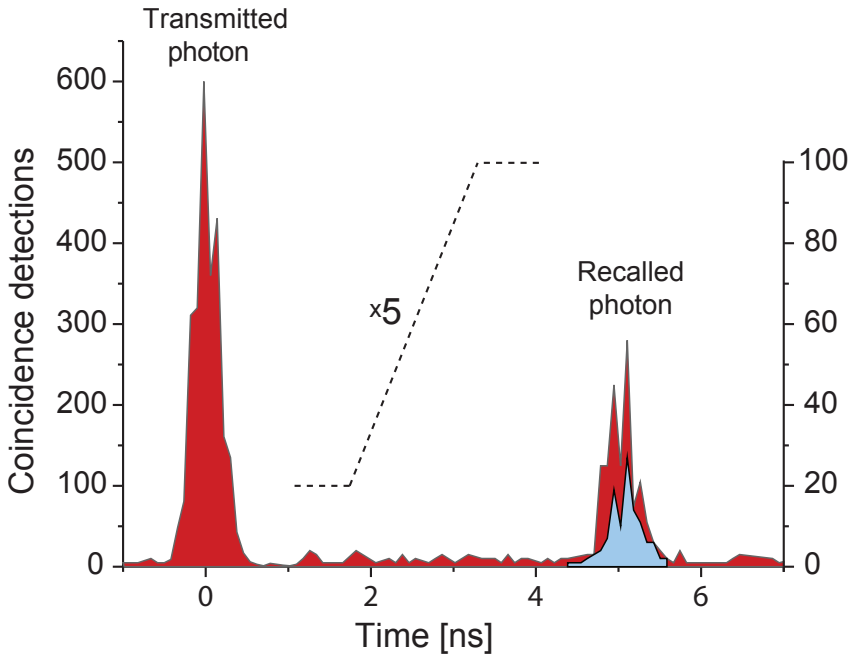

Figure 5.5: **Reversible mapping of broadband, heralded single photons.** Heralded telecom-wavelength photons, centred at 1532.7 nm wavelength and having a bandwidth of 50 GHz, are mapped onto the AFC memory and recalled after time $t_{\text{storage}} = \frac{1}{\Delta} = 5$ ns. The histogram shows time-resolved coincidence detections collected over 3 minutes. Due to non-unit absorption probability by the AFC as well as bandwidth mismatch between the spectra of the photons and the AFC, a significant portion of the input photons is directly transmitted and detected at zero delay. The light blue highlighted section bounded by a dotted line in the trace of the recalled photon (counts scaled by a factor of five) corresponds to the measurement in which the total AFC bandwidth was 8 GHz; the red section corresponds to a measurement using a 16 GHz wide AFC.

capacities of the Raman and AFC based implementations. Whereas the AFC protocol facilitates simultaneous storage of temporal/spectrally multiplexed photons the Raman approach is intrinsically limited in this regard.

Third, to establish the multimode operation of our quantum light-matter interface, we divide the total currently accessible bandwidth – 18 GHz for this experiment – into different numbers of AFC sections, and program each section with a different storage time ranging from 3-13 ns. This allows identifying photons stored in different frequency modes (i.e. different AFC sections) through their recall time. In succession we per-

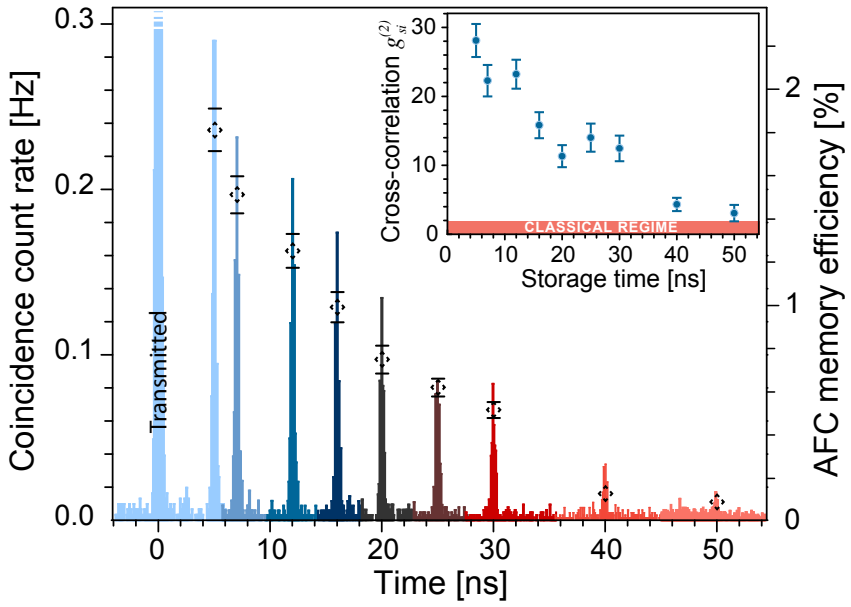

Figure 5.6: **Quantum storage with large time-bandwidth product.** 16 GHz wide AFC regions with teeth spacing ranging from 200 MHz to 20 MHz are subsequently programmed to store heralded single photons for 5 ns to 50 ns. The histograms show measured coincidence rates for recalled photons for each storage time, and the dashed diamonds depict the corresponding memory efficiencies (see Supplementary Note 3). Note that in this figure and henceforth the transmitted pulse at $t = 0$ exceeds the vertical scale and thus is capped at the top. Experimentally obtained $g^{(2)}_{si}$ for each storage time are shown in the inset. The measurement time varied between 5 and 15 minutes.

form measurements with: i) two AFCs of 9 GHz bandwidth; ii) four AFCs of 4.5 GHz bandwidth (this case is shown in Fig. 5.7a); iii) six AFCs of 3 GHz bandwidth. The corresponding histograms of coincidence detections, depicted in Fig. 5.7b, confirm that two, four and six modes, respectively, have been stored simultaneously. For each recalled spectro-temporal mode, we find that $g^{(2)}_{si}$, listed in Table 5.1, exceed the classical limit of 2, thereby confirming multimode storage of non-classical states of light in matter.

The frequency-to-time mapping described above was used to unambiguously distinguish between different frequency modes. This is convenient in our proof-of-principle demonstration, but may not be required in all applications. However, the ability to flexibly reconfigure our light-matter interface in terms of the number, bandwidth, storage

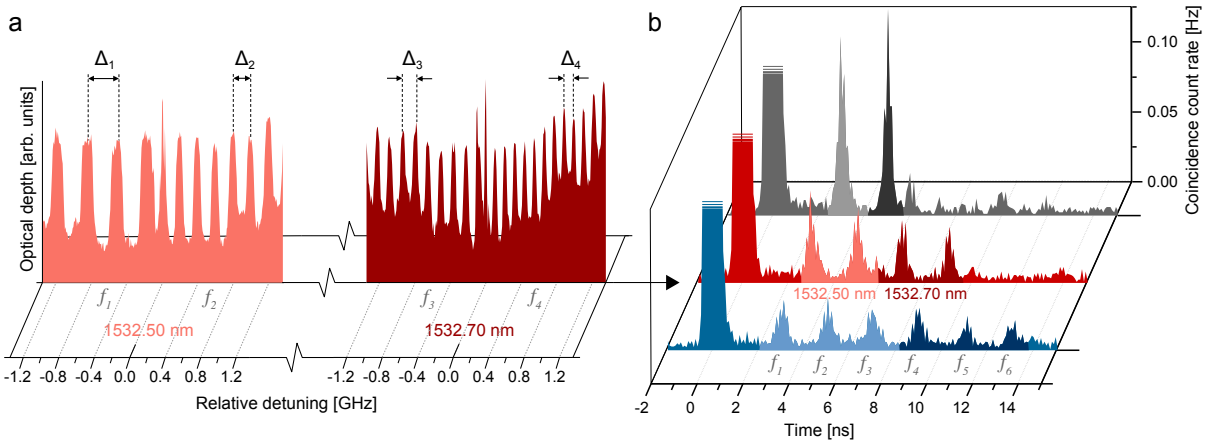

Figure 5.7: **Multimode quantum storage. a) Creation of AFCs.** The total, currently addressable bandwidth of 18 GHz is divided into different spectral sections, each featuring an AFC with distinct peak spacing. Depicted is the case of four, 4.5 GHz-wide AFCs, created using two lasers operating at 1532.50 and 1532.70 nm. The AFCs feature peak spacings of 333 MHz, 200 MHz, 143 MHz and 111 MHz, corresponding to storage times of 3, 5, 7 and 9 ns, respectively. For each AFC, only a 1.3 GHz-wide section is shown. **b) Storage and recall.** When broadband heralded photons with 50 GHz bandwidth are mapped onto a two-section AFC, where each section extends over 9 GHz bandwidth and has a peak spacing of 333 MHz and 200 MHz, respectively, they are stored in two spectral modes and retrieved in two spectro-temporal modes, as shown in the back trace. Decreasing the bandwidth per AFC allows increasing the number of AFCs (spectral modes), as demonstrated with the storage of 4 and 6 spectral modes in the middle and the front trace, respectively. The modes are labeled f_i. For each mode, $g^{(2)}_{si}$ is measured to be larger than 2 (see Table 5.1).

time and frequency separation of the AFCs lends itself to versatile manipulation at the quantum level. In particular, it allows modifying the temporal shape of single photons by recalling different spectral modes at the same time and with adjustable phases. As an illustration Fig. 5.8 shows two different mappings of 6 spectral modes onto 3 distinct temporal modes. We note that additional processing, e.g. pulse sequencing and temporal compressing, relying on the frequency-to-time mapping is possible by combining AFCs

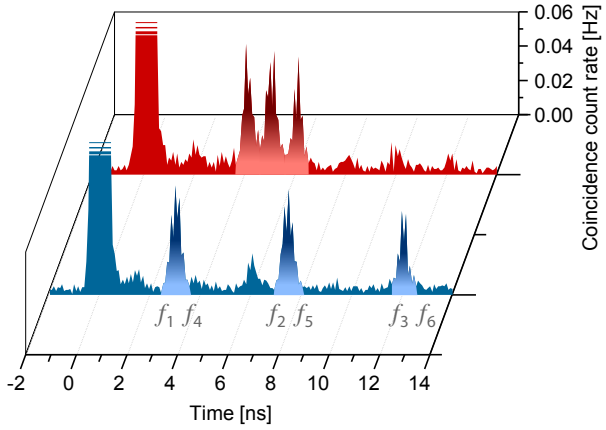

Figure 5.8: **Pulse manipulation:** The AFC memory with total bandwidth of 2×8 GHz $= 16$ GHz is tailored such that simultaneously absorbed photons in 6 spectral modes (from f_1 to f_6), each of 2.65 GHz bandwidth, are recalled in 3 temporal modes either spaced by 4.5 ns (front trace), or by 1 ns (back trace).

with frequency shifters, as demonstrated in [18].

5.3.3 Discussion and conclusions

A central feature of our demonstration is the large multiplexed storage and manipulation capacity of our atomic interface for non-classical light. Yet, as noted above, there are clear avenues to increase this even further. Our additional investigations depicted in Supplementary Fig. S3 show that at least a 14 nm span of the erbium absorption line is suitable for quantum state storage. If we generate 8 GHz broad AFCs separated by 20 GHz, this yields a total of 64 AFCs covering a combined bandwidth of 64×8 GHz $= 512$ GHz. Assuming 50 ns storage time one could thus reach a time-bandwidth product of more than 512 GHz $\times$ 50 ns ≈ 25000, which is equal to the number of temporal–spectral modes that could be stored simultaneously.

On the other hand, a number of improvements are required for our multiplexed light-matter interface to be truly suitable for use in future quantum networks. First, imperfect

mode #	storage time	$g_{si}^{(2)}$ for spectro-temporal modes: 9 GHz	4.5 GHz	3 GHz
f_1	3 ns	16.8 ± 0.8	8.0 ± 0.6	5.7 ± 0.6
f_2	5 ns	16.4 ± 0.8	7.2 ± 0.6	5.3 ± 0.6
f_3	7 ns	–	6.3 ± 0.5	5.4 ± 0.6
f_4	9 ns	–	5.2 ± 0.5	5.0 ± 0.6
f_5	11 ns	–	–	3.4 ± 0.5
f_6	13 ns	–	–	3.4 ± 0.5

Table 5.1: Measured values of the cross correlation function of each recalled spectral mode f_i for different AFC bandwidths and total numbers of modes. The storage times are given in column 2.

optical pumping during the preparation of the AFCs currently results in a storage efficiency at 0.6 K of 1-2 % (see the Supplementary Information of [43]). However, as we describe in [44], we expect that it is possible to substantially improve the optical pumping, e.g. with lower temperatures and smaller erbium concentrations, and hence to yield a significantly higher efficiency under certain conditions, as discussed in Supplementary Note 2.

Second, the ∼10 ms radiative lifetime of the ${}^4I_{15/2} \leftrightarrow {}^4 I_{13/2}$ transition in erbium fundamentally limits the coherence time to 20 ms. However, coupling to so-called two-level systems [19], which are intrinsic to disordered materials such as glass fibres, reduces the coherence time, and the attainable storage time is hence currently restricted to a few tens of nanoseconds. While we anticipate that this value increases with smaller doping concentration, lower temperature [20, 21] (see Supplementary Information of [43] for further discussions), it is an open question whether or not it is possible to extend storage times to hundreds of μs, which would, e.g., allow building a quantum repeater based on spectral multiplexing [11]. Yet, we note that not all applications of quantum memory require long storage times, and that the figure of merit for multiplexing schemes is the time-bandwidth product. Hence, our light-matter interface can be useful even without long storage times.

Finally we point out that our storage device provides pre-programmed delays, which is sufficient for increasing the efficiency of multi-photon applications if one incorporates external elements that allow feed-forward-based mode-mapping, e.g. frequency shifters [11]. However, for some applications, it may be desirable to perform the mode mapping during storage – a familiar example being storage combined with read-out on demand, i.e. the possibility to select the recall time after the photon has been stored. One option to enable this feature is to utilize the Stark effect, which allows 'smearing' out the AFC peaks – whose spacing determines the recall time – after photon absorption [22]. This would inhibit the rephasing of the collective excitation and hence reemission of light after $t_{\text{storage}} = 1/\Delta$, and lead to the possibility to recover the original photon a time $t_{\text{storage}} = n/\Delta$ after absorption, where n is an integer. Another possibility is to map the optical coherence – created by the photon absorption – onto a long-lived spin level (spin-wave storage) [23, 24], e.g. a hyperfine level (caused by the non-zero nuclear spin of $^{167}Er^{3+}$) [25, 26] or a superhyperfine level (caused by the interaction of Er with co-dopants in the host) [27]. However, this possibility remains challenging due to the complex and not fully characterized structure of these levels as well as the typically large inhomogeneous broadening of spin transitions in erbium-doped fibres. Moreover, this approach would limit the memory bandwidth appreciably because of the intrinsically small splitting of nuclear spin levels. But provided these levels afford longer coherence times, and thus storage duration, the large time-bandwidth product need not be affected markedly.

Provided that the performance of our light-matter interface is improved as discussed, it can advance several quantum photonic applications. For instance, by programming AFCs with different storage times into different spectral regions, it can serve as a time-of-flight spectrometer, which would, for example, allow fine-grained, spectrally resolved photon measurements, including two-photon Bell-state measurements in a quantum re-

peater architecture based on frequency multiplexing [11]. As a second example, our interface can be used to spectrally and temporally tailor single photon wave packets, as exemplified in our demonstrations, and thereby adapt their properties for subsequent interfacing with other quantum devices. More generally, by combining the interface with feed-forward-controlled frequency shifters, e.g. broadband electro-optic phase modulators, it can be turned into a programmable atomic processor for arbitrary manipulation of photonic quantum states encoded into time and/or frequency [18]. This would find application in optical quantum computing in a single-spatial mode [28] or in atomic-interface based photonic quantum state processing [29, 30, 31, 32]. In addition, we note that the large multiplexing capacity of our light-matter can be increased further by adapting multiplexing in spatial degree [33], and/or angular orbital momentum degree [34] with use of multimode erbium-doped fibers, as envisioned for future fiber-based classical and quantum networks [35].

In conclusion, we have presented a quantum light-matter interface that is suitable for multiplexed quantum-information-processing applications. More precisely, we have demonstrated a large time-bandwidth-product memory capable of multimode storage of non-classical light created via spontaneous parametric down-conversion, and showed that our light-matter interface can be employed for quantum manipulation of broadband heralded single photons. The fully pigtailed photon source and the fibre-based memory, along with telecommunication-wavelength operation and commercial availability, makes our demonstration important in view of building future fibre-based quantum networks.

Acknowledgments

ES, MG, QZ, LG, DO and WT thank Jeongwan Jin, Neil Sinclair, Charles Thiel and Vladimir Kiselyov for discussions and technical support, and acknowledge funding through Alberta Innovates Technology Futures (AITF) and the National Science and

Engineering Research Council of Canada (NSERC). Furthermore, W.T. acknowledges support as a Senior Fellow of the Canadian Institute for Advanced Research (CIFAR), and VBV and SWN partial funding for detector development from the DARPA Information in a Photon (InPho) program. Part of the research was carried out at the Jet Propulsion Laboratory, California Institute of Technology, under a contract with the National Aeronautics and Space Administration. LO and DN acknowledge Srico Inc. for their assistance with the fabrication of periodically poled lithium niobate wafers.

5.3.4 Methods

Erbium doped silica fibre

We use a 20 m long, commercially available single-mode, 190 ppm-wt erbium-doped silica fibre specified to have 0.6 dB/m absorption at 1532 nm wavelength at room temperature. At 1 K we measure 0.1 dB/m absorption at 1532 nm wavelength (see Fig. 5.6). In addition to Er, the fibre is co-doped with P, Al and Ge. The fibre is spooled in layers around a copper cylinder with ∼4 cm diameter that is thermally contacted with the base plate of an adiabatic demagnetization refrigerator (ADR) maintained at about 0.6-0.8 K and exposed to a field of ∼600 G inside a superconducting solenoid magnet. This setup induces about 70% bending loss from input to output, mainly because of the insufficiently large diameter of the erbium-fibre spool. The fibre is fusion-spliced to standard single mode fibres (SMF-28) at each end with less than 5% loss per splice.

Preparation of AFC

The memory is prepared using the setup described in Fig. 5.12. Frequency chirped laser pulses, applied 500 times per pumping cycle of 500 ms duration, allow frequency-

selective optical pumping of erbium ions into a long-lived Zeeman level, and hence the formation of peaks and troughs of the AFC. A polarization scrambler (PS) randomly changes the polarization of the pump light every 500 μs to ensure that heralded photons, which propagate counter to the optical pumping light, are absorbed regardless their polarization state [13]. Upon completion of the optical pumping, a significant portion of the erbium ions accumulate in the auxiliary ground state Zeeman-level $|s\rangle$ (see Fig. 5.4), whose decay at 0.7 K and under a magnetic field of 600 Gauss is characterized by two lifetimes of 1.3 s and 26 s [44]. However, a considerable amount of atoms remains in excited level $|e\rangle$, and subsequent spontaneous emission from these would mask all recalled photons. Thus, to eliminate this spontaneous emission noise we set a wait time of 300 ms, which is significantly larger than the 11 ms exited level lifetime. Following the wait time, we store and retrieve many heralded single photons during a 700 ms measurement time. The retrieval efficiency of our AFC is about 1-2%, which is primarily limited by residual absorption background as a result of incomplete population transfer during the optical pumping, (see Supplementary Information of [43] for further details)

Superconducting nanowire single photon detectors

The detection of the telecom-wavelength photons is carried out by a set of superconducting nano-wire single-photon detectors (SNSPDs) [36] attached to the base plate of the ADR and maintained at the same temperature as the memory. In our setup, the tungsten silicide (WSi) SNSPDs have efficiencies of about 70% which includes the loss due to fibre-splices and bends. Their detection efficiencies exhibit a small polarization dependence of about 5%. The time jitter of the detectors is around 250 ps, which allows us to resolve detection events separated by 1 ns (see Fig. 5.8). We measure the dark count rate of the detectors to be about 10 Hz, which results in a negligibly small contribution to accidental coincidences and hence high signal-to-noise ratios for the coincidence

detections of the recalled photons.

Coincidence and $g^{(2)}$ measurements

All detection signals are directed to a time-to-digital converter (TDC), which allows recording detection times with a resolution of 80 ps. The detection of the heralding (*idler*) photon on SNSPD1 is used to trigger (start) the TDC. The other member of the pair (the *signal* photon) is detected by SNSPD2 – either as recalled (delayed) photon after storage, or as a directly transmitted photon through the erbium fibre that features no extra delay – and sent to the TDC, which records the time interval from the trigger signal. This allows us to generate histograms of the time-resolved coincidence detections between *signal* and *idler* photons (see, e.g., Fig. 5.5).

To calculate $g_{si}^{(2)}$ using Eq. 5.18, we extract the values for the rates of the coincidence detection $R_{si}(t = 0)$ and the individual detections R_s and R_i from coincidence histograms. Here we have explicitly stated the time difference between the coincidence detections to be 0. We note that, since the photon-pair generation process is spontaneous, there is no statistical correlation between subsequent pair generation events. Hence we can re-write the product $R_s R_i$ as $R_{si}(t \neq 0)$, i.e. as the coincidence detection rates for *signal* and *idler* photons that are not members of the same photon pair, which is often referred to as accidental coincidence count-rate [37]. We extract $R_{si}(t = 0)$ from a coincidence histogram by counting all detections within the "coincidence peak" that is centred at time t_0 and has width t_p, and normalizing this number by measurement time and coincidence window width t_p. Similarly, $R_{si}(t \neq 0)$ is evaluated by appropriate normalization of coincidence counts taken in a window of width t_{bg} that is adjacent to the "coincidence peak". Hence, to evaluate $g_{si}^{(2)}$ from experimental histograms of coincidence counts $R_{si}(t)$

we use

$$g_{si}^{(2)} = \frac{t_{bg} \int_{t_0-t_p/2}^{t_0+t_p/2} R_{si}(t)dt}{t_p \int_{t_0+t_p/2}^{t_0+t_p/2+t_{bg}} R_{si}(t)dt}. \tag{5.8}$$

For all the cross-correlation values in this paper we used coincidence windows $t_p = t_{bg} =$ 0.8 ns.

5.3.5 Supplementary information

Supplementary note 1: Integrated photon pair source

In the following, we detail the structural properties and fabrication of our non-classical light source. Our heralded single photon source (HSPS) operates by creating photon pairs through spontaneous parametric down-conversion (SPDC) in a fibre-pigtailed PPLN crystal waveguide with type-0 phase matching. Although the time at which photon pairs are generated by illumination with a CW pump laser is random and cannot be known precisely, the temporal correlations between a pair of photons created by SPDC are well-defined, and the detection of one photon can be exploited to successfully herald the arrival of its twin. In our HSPS, an optical fibre couples the pump photons that are generated from a CW laser into an optical waveguide, which is located inside the lithium niobate crystal. The optical waveguide extends across the entire length of the 50 mm long, 0.5-mm thick Z-cut lithium niobate chip. In the central region of the lithium niobate chip, the ferroelectric polarization of the lithium niobate is periodically inverted over a total length of approximately 40 mm. The input pump photons are converted to photon pairs in this periodically poled region through the interaction of the pump field with this second order ($\chi^{(2)}$) nonlinear medium. In order to generate photon pairs with high efficiency through SPDC, the periodically poled region and optical waveguides were

designed to satisfy the following quasi-phase matching [38, 39] condition:

$$\frac{n_p}{\lambda_p} - \frac{n_s}{\lambda_s} - \frac{n_i}{\lambda_i} = \frac{1}{\Lambda} \tag{5.9}$$

where Λ is the period of the poled domains and n_p (λ_p), n_s (λ_s), and n_i (λ_i) are the effective refractive indices of the waveguide at the pump, signal, and idler wavelengths λ_p, λ_s, and λ_i, respectively. The effective indices of refraction of the optical waveguides at the pump, signal, and idler wavelengths were determined by performing numerical analysis. For generation of frequency degenerate photon pairs with $\lambda_{s(i)} \approx 1532$ nm from a pump photon with $\lambda_p \approx 766$ nm, the optimal period of the poled domains was observed to be approximately 17 μm.

The PPLN waveguides were fabricated using a Ti-indiffusion process, where a titanium layer was applied to the Z surface of a lithium niobate crystal and Ti-indiffusion was achieved by heating the crystal in a furnace at $T \sim 1000$°C. The PPLN waveguide width was 7 μm, and single mode operation was observed at $\lambda \sim 1532$ nm for PPLN waveguide widths < 8 μm. The photon pairs generated inside the PPLN waveguide are collected in an optical fibre, and SMF-28 fibre was used to ensure single mode propagation. In order to achieve stable and reliable optical coupling, SMF-28 optical fibre connectors were attached to the PPLN crystal using UV-cured epoxy. In order to reduce the optical coupling loss between the PPLN waveguide and the optical fibre and, therefore, increase the heralding efficiency of our single photon source, tapered and periodically segmented waveguide (PSW) geometries[40] were integrated into the optical waveguide design. A detailed description of the optical modeling that supported the development of the PPLN waveguide and the PSW taper designs used in our HSPS has been presented in a prior publication, along with supporting optical test and characterization data[41].

For this work, the CW pump power level was limited to less than ~ 100 μW. This power level constraint was a consequence of the photorefractive effect. For pump power

levels < 100 μW, the rate at which photon pairs are generated scales linearly with pump power. At pump power levels > 100 μW the rate of photon pair generation no longer scales linearly with pump power, and the pair generation rate will start to saturate and eventually degrade as the power level is increased. To enable operation at higher power levels, our team is currently designing Ti-indiffused PPLN waveguides to operate at $T > 120$°C, because photorefractive effects are significantly reduced at elevated temperatures. We are also designing, fabricating, and characterizing proton-exchanged and Zn-indiffused PPLN waveguides, which are less sensitive to photorefractive effects than Ti-indiffused waveguides.

Supplementary note 2: Efficiency, storage time and bandwidth of the AFC memory

The efficiency of our current AFC memory implementation, which is based on the re-emission of the stored photon in forward direction, is theoretically limited to 54%. One method to overcome this limit is to incorporate the AFC into an impedance-matched cavity and retrieve the photon "backwards", in which case the memory efficiency may reach 100%[42]. From a practical viewpoint the efficiency is furthermore limited by the imperfect preparation of the AFC, which leads to irreversible photon absorption, as described in the Methods. There are three main factors contributing to this absorption.

The first arises from the insufficient lifetime of the Zeeman sublevels (~ 1.3 s) compared to that of the excited level (11 ms). More precisely, by the end of the 300 ms wait time which is set to avoid spontaneously emitted photons, i.e. noise, due to decaying atoms a significant portion of the Zeeman level population has decayed, filling the AFC troughs and hence absorb photons in a non-reversible manner. As we detail in the

Supplementary Information of [43], for typical settings in our experiments, the contribution to the overall background coming from insufficient Zeeman level lifetime is about 65%. However, as we reported in [44], it is possible to obtain longer lifetimes for the Zeeman sublevels, and thus almost completely eliminate this contribution background, by lowering the temperature and lowering the erbium concentration.

A second factor is the small branching ratio, i.e. the probability of an atom during spectral hole burning to decay into the spin state (Zeeman sublevel) that differs from that before excitation. This results in incomplete population transfer among the sublevels, and hence residual absorption in the AFC background. With an increased Zeeman level lifetime at lower temperatures, there would be more time available for optical pumping and this contribution to the background could also be reduced.

The third factor contributing to the residual absorption is the restriction imposed by the GHz-bandwidths of the AFCs compared to the small splitting of the Zeeman sublevels (for typical magnetic fields of 600 G) in combination with the very large variation of the splitting (i.e. broadening of the Zeeman splitting) due to disorder in the glassy host. This effect leads to cross pumping during the AFC preparation i.e. a considerable overlap of the AFC troughs (spectral sections with decreased absorption) with the very wide antiholes (sections with increased absorption). Consequently, a significant number of the atoms cannot be removed from the spectral interval of the AFC. As we present in Supplementary Figure 5.10 for a fixed magnetic field, the impact of this factor on the AFC efficiency decreases as the bandwidth is reduced from 6 GHz to 1 GHz. This observation highlights that a larger ratio of magnetic field to bandwidth would allow a significant improvement of the efficiency. For instance, as we showed in [44], the reduction of the bandwidth while keeping the magnetic field at 600 G does indeed lead to much less cross pumping. However, this approach obviously also reduces the time-bandwidth product unless we simultaneously increase the storage time, which is limited by the

optical coherence time. (The latter can be improved by lowering the temperature.) Conversely, focussing instead on increasing the level splitting by means of increasing the strength of the applied magnetic field, our studies in [44] show that for an AFC with a constant bandwidth of about 1 GHz, the cross-pumping can also be decreased. Moreover, as we report in a forthcoming manuscript[45], the effective coherence time does not exhibit strong magnetic field dependence. The field increase does, however, result in a reduction of the persistent hole lifetime [43]. This is caused by the stronger coupling of low-frequency two-level system (TLS) modes to erbium spins with the larger Zeeman splitting, which, once more, points to the temperature as a critical factor. Lowering the temperature would diminish these interactions and make it possible to achieve long persistent hole life-times at large magnetic fields as well.

Supplementary Note 3: Quantum correlations and storage in AFC memory

Below we discuss how the parameters that govern the storage of photons generated by the SPDC source determine the measured cross correlations both before and after storage. We start by restating Eq. (5.18) in the main text for $g_{\mathrm{si}}^{(2)}$ in terms of experimentally measurable quantities

$$g_{\mathrm{si}}^{(2)} = \frac{R_{\mathrm{si}}}{R_{acc}} \ , \tag{5.10}$$

where R_{si} is the photon pair coincidence count rate and R_{acc} is the accidental count rate, which is identical to the quantity $R_{\mathrm{si}}(t \neq 0)$ defined in the Methods section of the main text. R_{acc} has in principle contributions from multi pair emissions of the source as well as detector dark counts. However, at the rate of 10 Hz, the latter is negligible. For the case in which the fibre memory is bypassed, R_{si} can be decomposed as

$$R_{\mathrm{si}} = 0.5\eta_c^2\eta_d^2 R + R_{acc} \ , \tag{5.11}$$

where η_c, η_d and R are the collection efficiency of signal and idler photon, the detection

efficiency of the SNSPDs, and the photon pair generation rate, respectively. We extract η_c from measurements of the coincidence and signal count rates, R_{si} and R_s, respectively, and the detection efficiency of the SNSPD on the *idler* side to be about 8.6%. As shown in Fig. 5.9 we measure $g^{(2)}_{\mathrm{si}}$ values in excess of 1000, which points to R_{acc} being only a very small fraction of R_{si}.

With the addition of the AFC memory for the storage of one member of the photon pair, this expression can be written as

$$R'_{\mathrm{si}} = 0.5\eta_c^2\eta_d^2\eta_s R + R'_{acc} \ , \tag{5.12}$$

where η_s is the system efficiency for the recalled photon in a specific spectral and temporal mode, and R'_{acc} is the accidental coincidence rate measured when the AFC memory is operated. By inspecting Eqs. 5.10 - 5.12, we find that $g^{(2)}_{\mathrm{si}}$ will be reduced if $R'_{acc} > \eta_s R_{acc}$. Hence, $g^{(2)}_{\mathrm{si}}$ will decrease either due to a low η_s or due to additional noise induced by the memory. In the following we elaborate on both effects.

First, the system efficiency η_s can be considered a product of three factors: the retrieval efficiency of the AFC memory η_m, the transmission factor η_t that takes into account the optical loss in the erbium-doped fibre due to splices and bending as well as in the optical circulator, and a filtering factor f ($0 \leq f \leq 1$), which is given by ratio of the bandwidth of the AFC section of interest and the bandwidth of the input photons (50 GHz). While η_t, which we measured to be 14%, is a constant in all experiments, both η_m and f depend on the preparation of the AFC. It is obvious that f is directly proportional to the AFC bandwidth, and we also find that the recall efficiency η_m decreases with increasing bandwidth of a single AFC, as described in Supplementary Fig. 5.10. Of course, a reduction of η_s does not necessarily decrease $g^{(2)}_{\mathrm{si}}$ unless a noise source that is independent of η_s is present, e.g., ultimately, detector dark counts.

Provided the transmission loss and the filtering factor are known, the AFC retrieval

efficiency can directly be determined for any spectro-temporal mode by time-resolved measurements of R_{si} and R'_{si} (corresponding to the cases with and without memory, respectively), since η_m is given by

$$\eta_m = \frac{1}{\eta_t f} \frac{R'_{\mathrm{si}} - R'_{acc}}{R_{\mathrm{si}} - R_{acc}}. \tag{5.13}$$

This formula, combined with independently determined values for the filtering factor and η_t, is used to compute the memory efficiency η_m plotted in Fig. 4 in the main text and Supplementary Fig. 5.10.

Next, we investigate the noise sources contributing to R'_{acc}. We start be writing the accidental coincidence rate as

$$R'_{acc} = \eta_s R_{acc} + R_{noise} \ , \tag{5.14}$$

where R_{acc} is the same as that defined in Eq. (5.11) — note that it appears as a product with the system efficiency η_s. Hence, the cross-correlation function cannot be reduced due to any source of accidental coincidences that is already present without the memory. However, the term R_{noise}, which includes two sources that are unique to the operation of the memory, leads to a reduction of $g^{(2)}_{\mathrm{si}}$. i) The first source of noise is the light spontaneously emitted from the small fraction of atoms that are excited during optical pumping and remain in the excited state after 300 ms of waiting time. In principle, this noise and the resulting accidental coincidences can be further suppressed by extending the waiting time and better optimization of the intensity of the optical pumping light. ii) The second source of noise is due to SPDC photons that are absorbed by atoms that do not contribute to the reversible mapping via the AFC i.e. atoms that either remain in a trough (and hence contribute to the AFC background), or that are outside of the AFC section. These photons are spontaneously re-emitted within the lifetime of the excited level (10 ms) and can be accidentally detected in coincidence with the heralded photons.

To highlight the effect of spontaneous-emission noise, we rewrite Eq. (5.10) taking into account Eqs. (5.12) and (5.14)

$$g_{\mathrm{si}}^{(2)} = \frac{R'_{\mathrm{si}}}{R'_{acc}} = \frac{0.5\eta_c^2\eta_d^2 R + R_{acc} + R_{noise}/\eta_s}{R_{acc} + R_{noise}/\eta_s}. \tag{5.15}$$

This shows that even though the number of spontaneously emitted photons may be much smaller than the number of input SPDC photons within the AFC bandwidth, they can nevertheless cause an significant reduction in $g_{\mathrm{si}}^{(2)}$. This is mainly a consequence of our small current system efficiency η_s, on the order of 0.1%.

There is a number of ways to reduce the effect of spontaneous emission noise, one obviously being to increase the AFC efficiency. Another path is to reduce the bandwidth mismatch between the input photons and the tailored AFC sections. In spectral multiplexing applications this could be accomplished by using multimode sources that produce photons only in spectral modes that are matched to the AFC sections. Another solution is to implement additional filtering to remove the spectrally unmatched portions of the input photons prior to the memory.

Supplementary figures

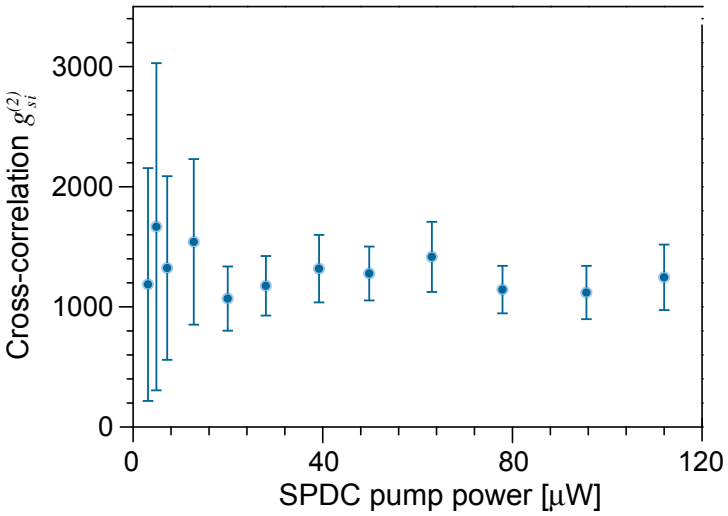

Figure 5.9: **Characterisation of $g^{(2)}_{\mathrm{si}}$ before storage vs. SPDC pump power.** We measure the second-order cross-correlation function given in Eq. (5.18) as a function of SPDC pump power before storage in the AFC memory. Error bars represent the standard deviation computed from the counting statistics of the coincidence and single counts, which are assumed to obey a Poissonian distribution. All measured values of $g^{(2)}_{\mathrm{si}}$ exceed 1000, which is substantially above the classical limit of 2 for thermal light fields – having a photon number distribution following Bose-Einstein statistics). The large uncertainties of $g^{(2)}_{\mathrm{si}}$ for low pump powers are due to small photon pair generation rates in conjunction with the relatively short data accumulating times.

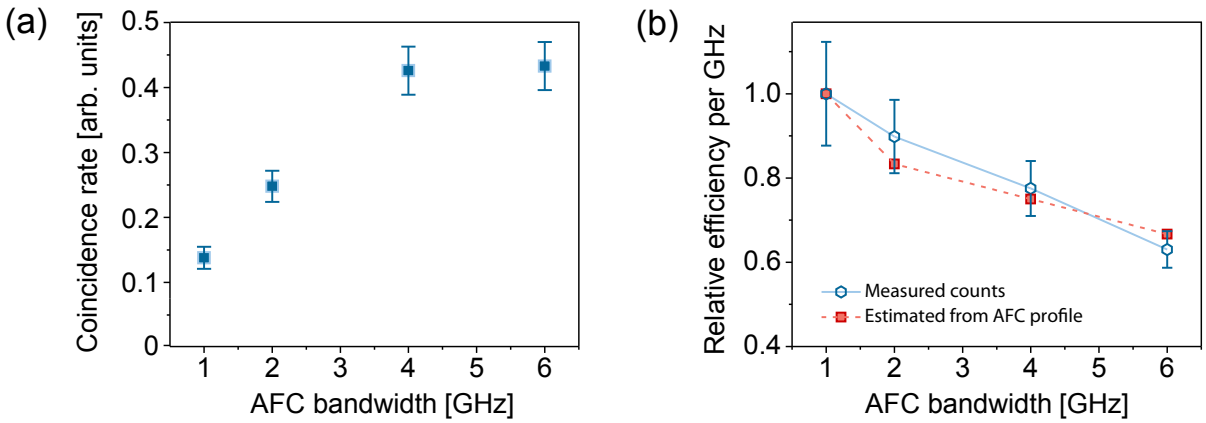

Figure 5.10: **Storage efficiency vs. AFC bandwidth.** Due to the limited splitting and significant broadening of the Zeeman-levels – employed as shelving levels for the population that is optically pumped to tailor an AFC – the bandwidth of each individual AFC is limited. More precisely, as the AFC bandwidth increases, population removed from one edge of the AFC starts filling the troughs at its opposite edge, leading to a reduction of the recall efficiency. This behaviour can be seen from a), where the rate of detected heralded photons at the memory output is plotted as a function of the bandwidth of a single AFC at 1532 nm. As the bandwidth is increased the memory efficiency initially grows, but then reaches a plateaus. In b) we plot measured and estimated efficiencies per AFC bandwidth, normalized to 1 for a 1 GHz broad AFC. As expected, we find a monotonous decrease as the total bandwidth increases. All error bars represent the standard deviation computed from the counting statistics of the coincidence counts, which are assumed to obey a Poissonian distribution.

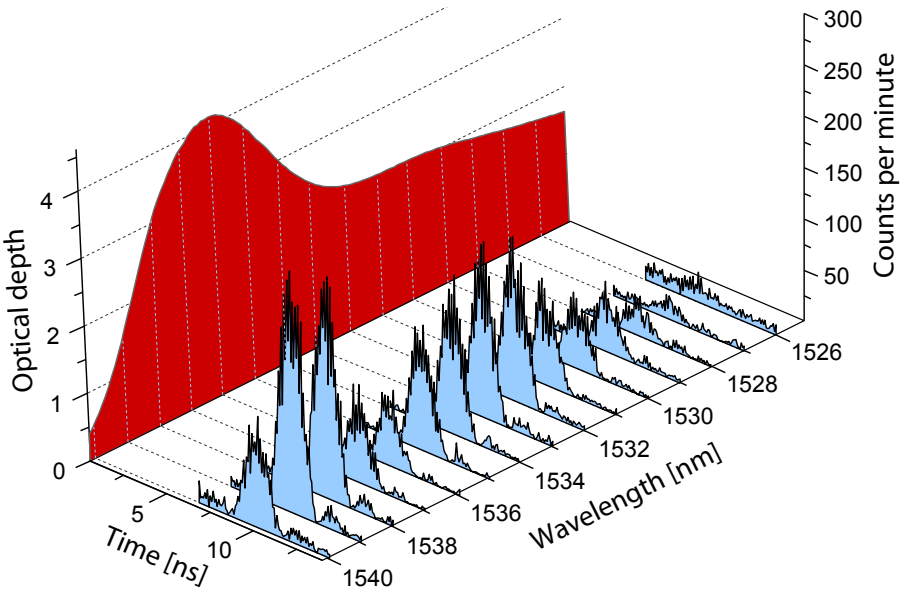

Figure 5.11: **Total accessible AFC bandwidth.** To assess the total width of the inhomogeneously broadened absorption line of the erbium-doped fibre that is accessible for quantum storage, we tune the wavelength of the optical pumping laser to generate 1 GHz wide AFCs with 10 ns storage time over a spectral interval ranging from 1526 nm to 1540 nm wavelength. We then store 2 ns long attenuated laser pulses with mean photon number of 0.5 ± 0.1, generated at an effective mean rate of 100 kHz, in the AFC. We observe recalled photons in all cases, showing that the entire bandwidth of 14 nm is suitable for optical quantum memory (i.e. spin level lifetimes as well as optical coherence times are sufficiently large). The observed variation in the echo intensity is predominantly due to the different initial optical depths of the transition. The temperature of the fiber was 0.8 K and the magnetic field was 600 G.

Bibliography

[1] England, D. G. *et al.* High-fidelity polarization storage in a gigahertz bandwidth quantum memory. *J. Phys. B At. Mol. Opt. Phys.* **45** (2012).

[2] Michelberger, P. S. *et al.* Interfacing ghz-bandwidth heralded single photons with a warm vapour raman memory. *New J. Phys.* **17** (2015).

[3] England, D. G. *et al.* Storage and retrieval of thz-bandwidth single photons using a room-temperature diamond quantum memory. *Phys. Rev. Lett.* **114** (2015).

[4] Ding, D.-S. *et al.* Raman quantum memory of photonic polarized entanglement. *Nat. Photon.* **9**, 332–338 (2015).

[5] Nunn, J. *et al.* Multimode memories in atomic ensembles. *Phys. Rev. Lett.* **101** (2008).

[6] de Riedmatten, H., Afzelius, M., Staudt, M. U., Simon, C. & Gisin, N. A solid-state light -matter interface at the single-photon level. *Nature* **456**, 773–777 (2008).

[7] Afzelius, M., Simon, C., de Riedmatten, H. & Gisin, N. Multimode quantum memory based on atomic frequency combs. *Phys. Rev. A* **79** (2009).

[8] Usmani, I., Afzelius, M., de Riedmatten, H. & Gisin, N. Mapping multiple photonic qubits into and out of one solid-state atomic ensemble. *Nat. Commun.* **1** (2010).

[9] Bonarota, M., Gouët, J. L. L. & Chanelière, T. Highly multimode storage in a crystal. *New. J. Phys.* **13** (2011).

[10] Gündoğan, M., Mazzera, M., Ledingham, P. M., Cristiani, M. & de Riedmatten, H. Coherent storage of temporally multimode light using a spin-wave atomic frequency comb memory. *New J. Phys.* **15** (2013).

[11] Sinclair, N. *et al.* Spectral multiplexing for scalable quantum photonics using an atomic frequency comb quantum memory and feed-forward control. *Phys. Rev. Lett.* **113** (2014).

[12] Tang, J.-S. *et al.* Storage of multiple single-photon pulses emitted from a quantum dot in a solid-state quantum memory. *Nat. Commun.* **6** 8652 (2015).

[13] Jin, J. *et al.* Telecom-wavelength atomic quantum memory in optical fiber for heralded polarization qubits. *Phys. Rev. Lett.* (2015).

[14] Saglamyurek, E. *et al.* Quantum storage of entangled telecom-wavelength photons in an erbium-doped optical fibre. *Nat. Photon.* **9**, 83–87 (2015).

[15] Saglamyurek, E. *et al.* Efficient and long-lived zeeman-sublevel atomic population storage in an erbium-doped glass fiber. *Preprint at arXiv:1507.03012v1* (2015).

[16] Tapster, P. R. & Rarity, J. G. Photon statistics of pulsed parametric light. *J. Mod. Opt.* **45** (1998).

[17] Bashkansky, M., Vurgaftman, I., Pipino, A. C. R. & Reintjes, J. Significance of heralding in spontaneous parametric down-conversion. *Phys. Rev. A* **90** (2014).

[18] Saglamyurek, E. *et al.* An integrated processor for photonic quantum states using a broadband light-matter interface. *New J. Phys.* **16** (2014).

[19] Macfarlane, R. M., Sun, Y., Sellin, P. B. & Cone, R. L. Optical decoherence in Er^{3+} doped silica fiber: Evidence for coupled spin-elastic tunneling systems. *Phys. Rev. Lett.* **96** (2006).

[20] Staudt, M. U. *et al.* Investigations of optical coherence properties in an erbium-doped silicate fiber for quantum state storage. *Opt. Commun.* **266**, 720–726 (2006).

[21] Sun, Y., Cone, R. L., Bigot, L. & Jacquier, B. Exceptionally narrow homogeneous linewidth in erbium-doped glasses. *Opt. Lett.* **31**, 3453–3455 (2006).

[22] Lauritzen, B., Minar, J., de Riedmatten, H., Afzelius, M. & Gisin, N. Approaches for a quantum memory at telecommunication wavelengths. *Phys. Rev. A* **83** (2011).

[23] Gündoğan, M., Ledingham, P. M., Kutluer, K., Mazzera, M. & de Riedmatten, H. Solid state spin-wave quantum memory for time-bin qubits. *Phys. Rev. Lett.* **114** (2015).

[24] Jobez, P. *et al.* Coherent spin ccontrol at the quantum level in an ensemble-based optical memory. *Phys. Rev. Lett.* **114** (2015).

[25] Hashimoto, D. & Shimizu, K. Population relaxation induced by the boson peak mode observed in optical hyperfine spectroscopy of ions doped in a silica glass fibre. *J. Opt. Soc. Am. B* **28** (2011).

[26] Baldit, E. *et al.* Identification of Λ-like systems in Er^{3+}:Y_2SiO_5 and observation of electromagnetically induced transparency. *Phys. Rev. B* **81** (2010).

[27] Thiel, C. W. *et al.* Optical decoherence and persistent spectral hole burning in Er^{3+}:$LiNbO_3$. *J. Lumin* **130** (2010).

[28] Humphrey, P. C. *et al.* Linear optical quantum computing in a single spatial mode. *Phys. Rev.Lett.* **111** (2013).

[29] Hosseini, M., Sparkes, B. M., Longdell, G. H. J. J., Lam, P. K. & Buchler, B. C. Coherent optical pulse sequencer for quantum application. *Nature* **461** (2009).

[30] Buchler, B. C., Hosseini, M., Hetet, G., Sparkes, B. M. & Lam, P. K. Precision spectral manipulation of optical pulses using a coherent photon echo memory. *Opt. Lett.* **35**, 1091–1093 (2010).

[31] Nunn, J. *et al.* Enhancing multiphoton rates with quantum memories. *Phys. Rev. Lett.* **110** (2013).

[32] Campbell, G. T. *et al.* Configurable unitary transformations and linear logic gates using quantum memories. *Phys. Rev. Lett.* **113** (2014).

[33] Lan, S.-Y. *et al.* A multiplexed quantum memory. *Opt. Exp.* **17**, 13639 (2009).

[34] Zhou, Z.-Q. *et al.* Quantum storage of three-dimensional orbital-angular-momentum entanglement in a crystal. *Phys. Rev. Lett.* **115** (2015).

[35] Bozinovic, N. *et al.* Terabit-scale orbital angular momentum mode division multiplexing in fibers. *Science* **340**, 1545–1548 (2013).

[36] Marsili, F. *et al.* Detecting single infrared photons with 93% system efficiency. *Nature Photon.* **7**, 210–214 (2013).

[37] Kuzmich, A. *et al.* Generation of nonclassical photon pairs for scalable quantum communication with atomic ensembles. *Nature* **423**, 731–734 (2003).

[38] Lim, E., Fejer, M., & Byer, R. Efficient quasi-phase-matched blue second-harmonic generation in $LiNbO_3$ channel waveguides by a second-order grating. *Electron. Lett.* **25** 174 (1989).

[39] Webjorn, J., Laurell, F., & Arvidsson, G. Domain inversion in MgO-diffused $LiNbO_3$. *J. Lightwave Technol.* **7** 1597 (1989).

[40] Castaldini, D., Bassi, P., Tascu, S., Aschieri, P., De Micheli, M.P., & Baldi, P. Soft-Proton-Exchange Tapers for Low Insertion-Loss $LiNbO_3$ Devices. *J. Lightwave Technol.* **25** 15881593 (2007).

[41] Oesterling, L., Monteiro, F., Krupa, S., Nippa, D., Wolterman, R., Hayford, D., Stinaff, E., Sanguinetti, B., Zbinden, H., & Thew, R. Development of a Photon Pair Source using Periodically Poled Lithium Niobate and Fiber Optic Components. *Journal of Modern Optics* **62** 1-10 (2015)

[42] Sabooni, M., Li, Q., Kröll, S. & Rippe, L. Efficient Quantum Memory Using a Weakly Absorbing Sample. *Phys. Rev. Lett.* **110** 133604 (2013).

[43] Saglamyurek, E. *et al.* Quantum storage of entangled telecom-wavelength photons in an erbium-doped optical fibre. *Nat. Photon.* **9**, 83–87 (2015).

[44] Saglamyurek, E. *et al.* Efficient and long-lived zeeman-sublevel atomic population storage in an erbium-doped glass fiber. *Phys. Rev. B* **92**, 241111 (2015).

[45] Viessier, L., Falamarzi, M., Lutz, T., Saglamyurek, E., Thiel, C. W., Cone, R. L., Oblak, D., & Tittel, W. Optical decoherence and spectral diffusion in an erbium-doped silica glass fiber featuring long-lived spin sublevels. *in preparation* (2016).

5.4 Paper 3: Telecom-Wavelength Atomic Quantum Memory in Optical Fiber for Heralded Polarization Qubits

Summary - In this work we show the possibility to store polarization qubits at telecom wavelength in our Er doped fibre using the AFC protocol, and retrieve them with near-unity fidelity. This is attainable thanks to the polarization insensitive light-matter interaction stemming from the Er doped fibre. This feature is not common in most of the media used for QM. In order to prepare the polarization qubits we used an heralded photon source based on a periodically-poled SPDC crystal.

The ease of manipulation and measurement of polarization qubits at telecommunication wavelength makes them an attractive platform for photonic quantum information tasks. The work presented in this paper, together with the work exposed in paper 2, despite of current limited perfomance of operation, demonstrate the flexibility and the potential for the use of such a technology in future quantum information processing tasks.

Contributions - This experiment was conducted in collaboration with Jeongwan Jin, Erhan Saglamyurek and Daniel Oblak. The single photon detectors were designed, built and tested by Francesco Marsili, Matthew D. Shaw, Varun B. Verma and Sae Woo Nam. The experiment was supervised by Wolfgang Tittel. I specifically contributed to the design and development of the setup of the SPDC photon pair source as well as its interface with the AFC based QM. I also contributed in data taking and the analysis of the measurement results. Regarding the manuscript, I contributed writing the technical details of the experiment and, in conjunction with the other co-authors, to all the editing steps until publication.

Telecom-wavelength atomic quantum memory in optical fiber for heralded polarization qubits

Physical review Letters, 115, 140501

2 October 2015

J. Jin[1†], E. Saglyamurek[1], M. Grimau Puigibert[1], V. B. Verma[2], F. Marsili[3] , S. W. Nam[2], D. Oblak[1] and W. Tittel[1]

[1]*Institute for Quantum Science and Technology, and Department of Physics and Astronomy, University of Calgary, 2500 University Drive NW, Calgary, Alberta T2N 1N4, Canada*

[2]*National Institute of Standards and Technology, Boulder, Colorado 80305, USA*

[3]*Jet Propulsion Laboratory, California Institute of Technology, 4800 Oak Grove Drive, Pasadena, California 91109, USA*

† *Present address: Institute for Quantum Computing, Department of Physics and Astronomy, University of Waterloo, 200 University Ave West, Waterloo, Ontario, Canada*

Abstract

Photon-based quantum information processing promises new technologies including optical quantum computing, quantum cryptography, and distributed quantum networks. Polarization-encoded photons at telecommunication wavelengths provide a compelling platform for practical realization of these technologies. However, despite important success towards building elementary components compatible with this platform, including sources of entangled photons, efficient single photon detectors, and on-chip quantum circuits, a missing element has been atomic quantum memory that directly allows for reversible mapping of quantum states encoded in the polarization degree of a telecom-wavelength photon. Here we demonstrate the quantum storage and retrieval of polarization states of heralded single-photons at telecom-wavelength by implementing the atomic frequency comb protocol in an ensemble of erbium atoms doped into an optical fiber. Despite remaining limitations in our proof-of-principle demonstration such as small storage efficiency and storage time, our broadband light-matter interface reveals the potential for use in future quantum information processing.

5.4.1 Introduction

Photonic quantum communication technologies rely on encoding quantum information (e.g. qubits) into single photons, and processing and distributing it to distant locations. In principle, a qubit can be encoded into any photonic degree of freedom, but the polarization degree has often been a preferred choice due to the ease of performing single qubit manipulations and projection measurements using wave-plates and polarizing beam-splitters, and the availability of polarization-entangled photon-pair sources [1]. On this background many seminal demonstrations of quantum information processing have employed polarization qubits, such as teleportation [2], entanglement swapping [3],

and secure quantum key distribution over more than hundred kilometers [4], pointing towards the possibility to build secure quantum networks [5].

In addition to polarization encoding, the realization of future quantum networks will be greatly facilitated by the use of existing fiber optic infrastructure, which allows low propagation loss for photons at wavelengths around 1550 nm, commonly referred to as telecom-wavelengths [6]. Nevertheless, propagation loss still limits the distance of such quantum links to a few hundreds kilometers. This distance barrier may be overcome by the development of quantum repeaters [7]. These, in turn, rely on the ability to store photonic qubits in quantum memories to overcome the probabilistic nature of photon transmission through lossy quantum channels and emission from currently used single-photon sources [8, 9]. However, to date, no quantum memory for polarization qubits encoded into telecom wavelength photons has been demonstrated. In fact, until recently [18], direct quantum storage of telecom-wavelength photons was an unsolved problem. The most promising candidate, erbium, has the required transition wavelength but exhibits atomic-level dynamics that have shown to be challenging for non-classical light storage [10, 11]. This has prompted indirect approaches such as quantum state teleportation [12] or coherent conversion techniques [13] from telecom-wavelength photons to photons at other wavelengths at which existing quantum memories can operate.

Furthermore, storage of polarization qubits at any wavelength is inhibited by the fact that the interaction of polarized light with most atomic media has orientational dependence, and birefringence in solid state materials often complicates matters further. In a few experiments – using light outside the telecom range – this has been circumvented by storing each polarization component in two spatially separated parts of a memory that each only interact with a single polarization component [14, 15, 16, 17]. However, this begs the question if there exists a solid-state material in which absorbers in an ensemble are aligned uniformly so that, in essence, all polarizations of light are equally coupled.

Recent advances in the development of quantum memories based on erbium doped glass fiber point exactly in this direction [18]. Because glass constitutes an amorphous host, the transition dipole moment of embedded rare-earth ions has no preferred direction, resulting in uniform coupling of an ensemble to all light polarizations. Moreover, the possibility to splice fiber-based memories with standard telecommunication fibers promises simple and low-loss integration with other components in a network.

In this letter, we report the faithful storage of polarization states of heralded telecom-wavelength single-photons in collective excitation of an atomic ensemble by implementing the atomic frequency comb (AFC) protocol in a cryogenically cooled erbium-doped optical fiber. We verify the memory's ability to store any polarization state with close to equal probability, and demonstrate its quantum nature by showing that recalled single photon quantum states have a near unity fidelity with the originally prepared states.

5.4.2 Measurement and results

Our experimental setup, sketched in Fig 5.12, is composed of three main parts: A fiber-based atomic quantum memory, a source of heralded polarization qubits, and a qubit analyzer. In the first step (middle panel of Fig. 5.12) we prepare the AFC memory using an optical pumping beam from a continuous wave laser. The beam is frequency and amplitude modulated before entering a 20 meter-long erbium-doped fiber cooled to 0.8 K with a cryostat based on a pulse-tube cooler and an adiabatic demagnetization refrigerator. The spectral profile of the pump light is chosen to be a square modulation with a period Δ. As indicated in Fig. 5.13a, this results in frequency-selective excitation of the erbium ions on their large inhomogeneously broadened transition line at 1532 nm. The polarization of the pump light can be actively scrambled to address erbium ions interacting with different polarization modes in the fiber. We maintain the optical pumping for 500 ms, which leads to atoms with transition frequencies matching the

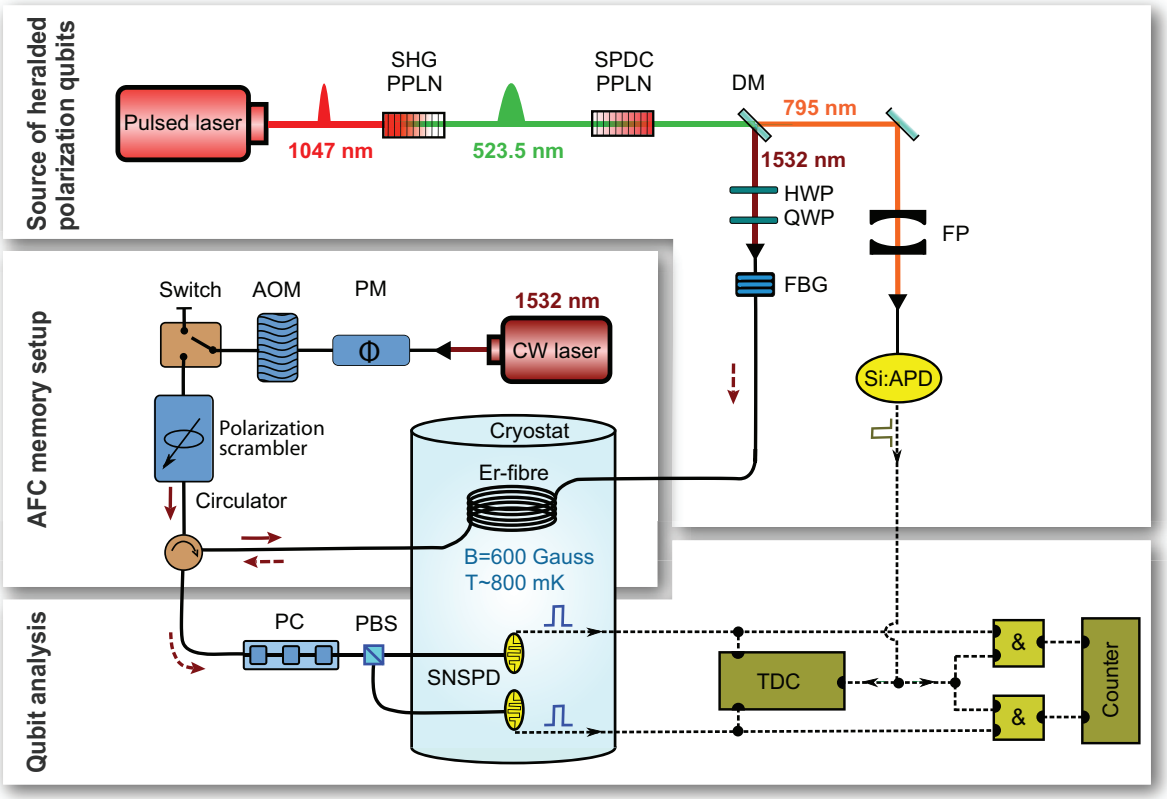

Figure 5.12: Experimental setup: In the heralded polarization qubit source, 6 ps long, 80 MHz repetition-rate pulses at 1047 nm wavelength are frequency doubled and subsequently downconverted in periodically poled lithium niobate crystals (PPLN). This generates photon pairs at 795 nm and 1532 nm (telecom) wavelengths, which are spectrally filtered with a Fabry-Perot (FP) cavity and a Fiber-Bragg grating (FBG), respectively. Detection of the 795 nm photon by a Si-APD (60% detection efficiency and 600 ps timing-jitter) heralds the presence of the telecom photon, and a half-wave-plate (HWP) and quarter-wave-plate (QWP) prepare it in any desired polarization qubit state. The quantum memory consists of a 20-meter-long erbium doped fiber exposed to a 600 G magnetic field and cooled to 0.8 K using a cryostat. The polarization-insensitive AFC is prepared by optical pumping with continuous wave (CW) laser light at 1532 nm, which is frequency and amplitude modulated by phase modulator (PM) and an acousto-optic modulator (AOM), respectively, and polarization-randomized by a polarization scrambler with 5 KHz cycling frequency. For the qubit analysis, the recalled photons pass through a fiber-optic polarization controller (PC) and polarizing beam splitter (PBS) after which they impinge on one of two superconducting nano-wire single photon detectors (SNSPD) held at 0.8 K (60% system efficiency and 350 ps time-jitter). A set of AND gates counts coincidences between the qubit detection signals and the heralding signal, and a time–to-digital (TDC) converter additionally provides time mapping of the single detections of the 1532 nm photons compared to the moment of detection of the heralding photons at 795 nm wavelength.

pumping light to accumulate in a long lived electronic Zeeman level that arises under the application of a magnetic field of 600 Gauss. This process allows us to generate an 8 GHz broad comb-shaped absorption profile – that is an AFC – having a tooth spacing of $\Delta = 200$ MHz and finesse (ratio of peak spacing to width) of 2 (a 1 GHz broad section is shown in the inset of Fig. 5.13b). To avoid photons stemming from spontaneous decay of atoms in the excited state during qubit recall, a wait time of 300 ms is set after the optical pumping. During 700 ms, following the wait time, we can map a photon onto our AFC, giving rise to collective excitation of the erbium ions in what is commonly referred to as a Dicke state:

$$|\Psi\rangle = \frac{1}{\sqrt{N}} \sum_{j=1}^{N} c_j e^{i2\pi m_j \Delta t} e^{-ikz_j} |g_1, \cdots e_j, \cdots g_N\rangle \ . \tag{5.16}$$

Here, $|g_j\rangle$ ($|e_j\rangle$) is the ground (excited) state of atom j, $m_j\Delta$ is the detuning of the transition frequency of the atom from the photon carrier frequency, z_j is the atom's position measured along the propagation direction of the light, and the factor c_j depends on the resonance frequency and position of the atom. Due to the different atomic transition frequencies, each excitation term in the Dicke state accumulates a different phase over time. However, the periodic structure of the transition frequencies of atomic absorbers in the AFC leads the phases to realign at a time given by the inverse of the peak spacing $t_{storage} = 1/\Delta$ [[19]]. Consequently, for Δ=200 MHz, an input photon is retrieved after $t_{storage} = 5$ ns in the originally encoded state, as shown in Fig. 5.13b.

The second step is to prepare heralded polarization qubits, that are compatible with our light-matter interface, using the photon pair source (top panel of Fig. 5.12). To this end, short pulses produced from a mode-locked laser operating at 1047 nm wavelength are frequency doubled via second harmonic generation (SHG). The resulting pulses at 523 nm are sent to a periodically-poled lithium niobate crystal where they take part in a spontaneous parametric down conversion (SPDC) process. The phase matching condition

for SPDC results in a pair of photons at 1532 nm and 795 nm, named *signal* and *idler* photons, respectively. In order to match the acceptance bandwidth of our storage device, the bandwidths of the 1532 nm and 795 nm photons are filtered down to nearly 10 GHz. The 795 nm photons are then directly detected by a Si-APD single-photon detector to provide a heralding signal. The 1532 nm photons pass through a free-space Half-Wave Plate (HWP) and Quarter-Wave Plate, which allow us to encode the polarization states

$$|\psi\rangle = \cos\theta|H\rangle + e^{i\varphi}\sin\theta|V\rangle \ , \tag{5.17}$$

where $|H\rangle$ and $|V\rangle$ denote a horizontally and vertically polarized 1532 nm photon, and $\cos\theta$ and $\sin\theta$ are the probability amplitudes for $|H\rangle$ and $|V\rangle$, respectively. At this point the prepared polarization qubits are sent to the prepared AFC memory for storage and recall.

The final step is to analyze the recalled qubits using the analyzer shown in the bottom panel of Fig. 5.12. Its optical part consists of a polarization controller followed by a polarizing beam-splitter (PBS) with super-conducting nanowire single-photon detectors (SNSPD) at each output. These allow making projection measurements onto any set of orthogonal polarization qubit states. The electronic part consists of logic gates that enable counting coincidences with the heralding signal.

In our measurements we first characterize the polarization sensitivity of our fiber-based atomic memory with and without the polarization scrambling of the optical pumping light. We gradually change the polarization state of the 1532 nm photons from horizontal to vertical by rotating the free-space HWP in steps of 15 degrees. For each polarization setting we store the 1532-nm photons in our AFC memory first without, and then with the polarization scrambler engaged. In this test, we disregard the heralding signal from the 795 nm photon detection and bypass the PBS such that we detect the retrieved 1532 nm photons using a single SNSPD, and normalize to the 5% polarization

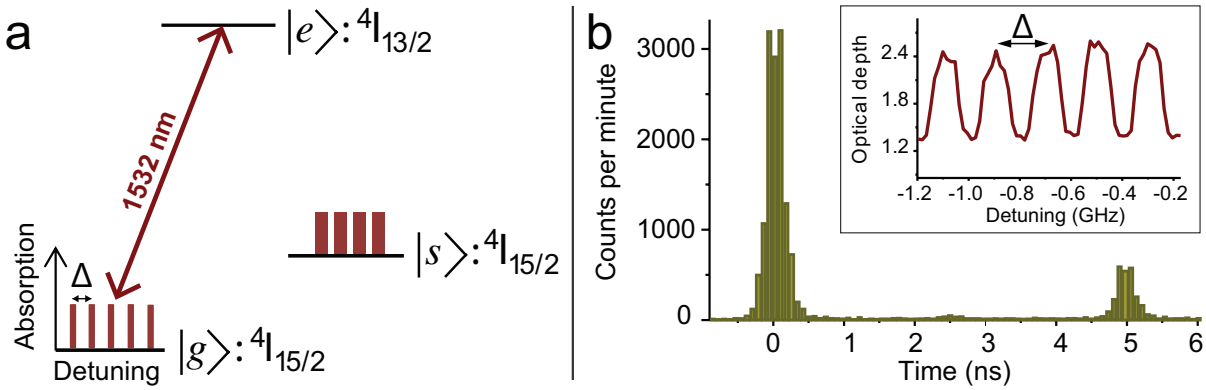

Figure 5.13: (a) Simplified erbium level scheme: The AFC is prepared via frequency-selective population transfer from the ${}^4I_{15/2}$ electronic ground state ($|g\rangle$) through the ${}^4I_{13/2}$ excited state ($|e\rangle$) into an auxiliary (spin) state ($|s\rangle$). (b) Detection signal from a single SNSPD recorded by the TDC, showing directly transmitted and stored photons spaced by 5 ns. The inset shows a 1 GHz wide section of a typical AFC of 8 GHz total bandwidth. The background absorption arises from imperfect optical pumping.

dependence of its detection efficiency [20].

Without the polarization scrambler we observe that the number of counts, and hence the efficiency of the memory, varies by about 25% with the polarization setting. This is due to the mismatch of the polarization state of the optical pumping light and the 1532 nm single photons, which counter-propagate through the fiber. This phenomenon is also known as "polarization hole-burning" in the operation of erbium-doped fiber amplifiers [21]. However, *with* polarization scrambling the generated AFC in any spatial section of the fiber consists of erbium ions that can be excited by arbitrary polarization state of the heralded single photons. In this case, the recall efficiency is near the maximum for all the utilized input polarization states. Remaining fluctuations of the overall AFC efficiency (up to 7%) are due to unstable operation of the optical pumping laser over the course of the measurements.

Next, in order to verify the quantum nature of the storage we measure the second-

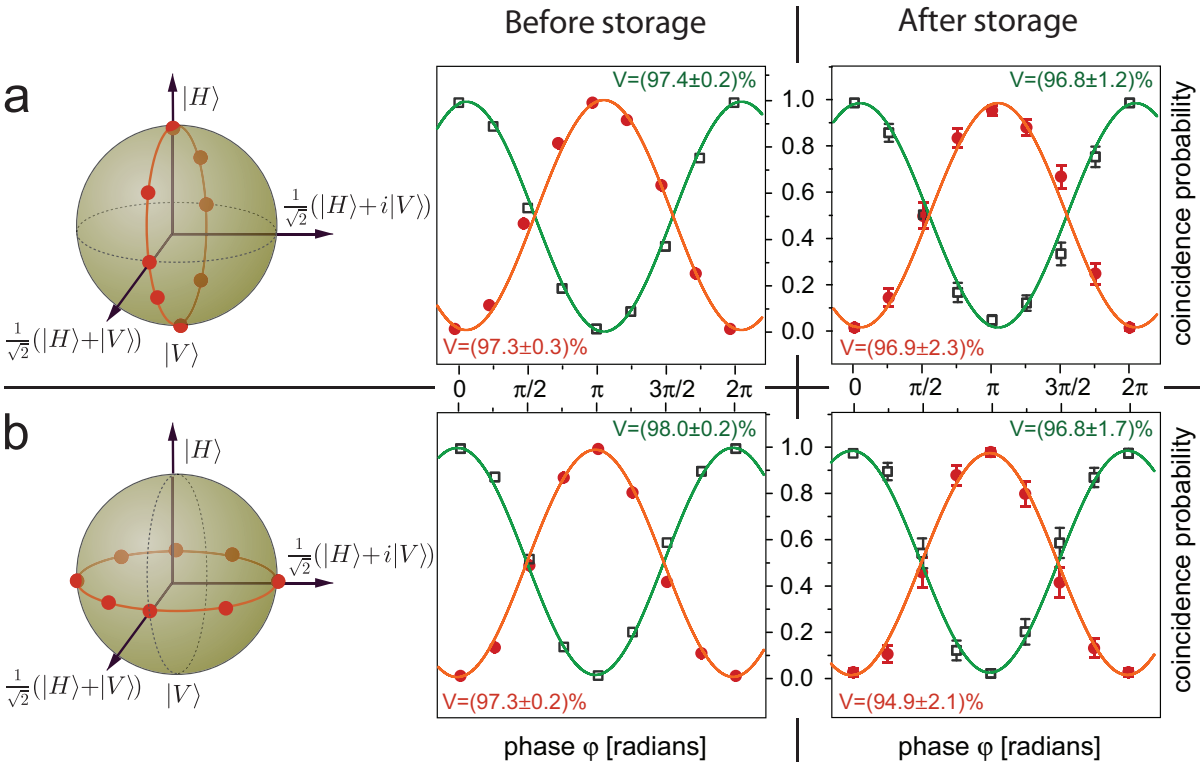

Figure 5.14: Measured coincidence probabilities for qubit states of the form (a) $|\psi\rangle = \cos\theta|H\rangle + \sin\theta|V\rangle$ projected onto $|H\rangle$ (squares) and $|V\rangle$ (circles) and of the form (b) $|\psi\rangle = \frac{1}{\sqrt{2}}(|H\rangle + e^{i\varphi}|V\rangle$ projected onto $|+\rangle = \frac{1}{\sqrt{2}}(|H\rangle + |V\rangle$ (squares) and $|-\rangle = \frac{1}{\sqrt{2}}(|H\rangle - |V\rangle$ (circles). The left-hand-side and the right-hand-side are before and after storage in the AFC, respectively. Probabilities are calculated by dividing the coincidence counts at each PBS output during 5 minutes by the total coincidence counts (i.e. the sum of the counts in the two PBS outputs), which is approximately 1 Hz. Error-bars are based on Poissonian detection statistics and all visibility values are based on sine fits to the data.

order cross-correlation $g_{si}^{(2)}$

$$g_{si}^{(2)} = \frac{P_{si}}{P_i P_s} \ , \tag{5.18}$$

where P_{si} is the probability of coincidence detection between the heralding signal and the two qubit analyzer outputs combined. P_s and P_i are the detection probabilities for the 795 nm and the 1532 nm photons, respectively. Measuring a value $g_{si}^{(2)} > 2$ indicates the presence of quantum correlations between the photons in each pair, where we assume that the auto-correlation values for the signal and idler photons are in between 1 and 2, corresponding to a coherent and a thermal state, respectively. We find $g_{si}^{(2)}$ to be 14.1 ± 0.3 before storage and, crucially, 18.4 ± 1.2 after storage, which demonstrates that quantum correlations between the members of the photon pairs are preserved during the storage. The reason for $g_{si}^{(2)}$ to increase after storage is due to spectral filtering of the input photons (10 GHz bandwidth) caused by the slightly smaller bandwidth of the AFC memory (8 GHz), which results in a lower effective mean-photon number.

With this in hand, we now store of heralded polarization qubits. To begin, we either vary the phase θ to create the states $|\psi\rangle = \cos\theta|H\rangle + \sin\theta|V\rangle$ and set the qubit analyzer to project onto the states $|H\rangle$ and $|V\rangle$, or we vary φ to create the states $|\psi\rangle = (|H\rangle + e^{i\varphi}|V\rangle)/\sqrt{2}$ and set the qubit analyzer to project onto $(|H\rangle \pm |V\rangle)/\sqrt{2}$. In both cases, the projection rates are expected to vary sinusoidally with either θ or φ. To assess if our memory affects the stored qubits we perform the measurements both when the 1532 nm photons are recalled from the memory, and when they are just passing through the fiber, i.e. when the AFC is not activated. For each projection setting we monitor the outputs of the qubit analyzer over 5 minutes and count the detections of the 1532 nm photons that are in coincidence with the detections of the 795 nm photons (heralding signal) using an AND-gate. The data points and the resulting visibility curves in Fig. 5.14a-b show the variation of the coincidence probability for the two sets of input states as a function of the input polarization before and after storage. From the fitted visibilities we find

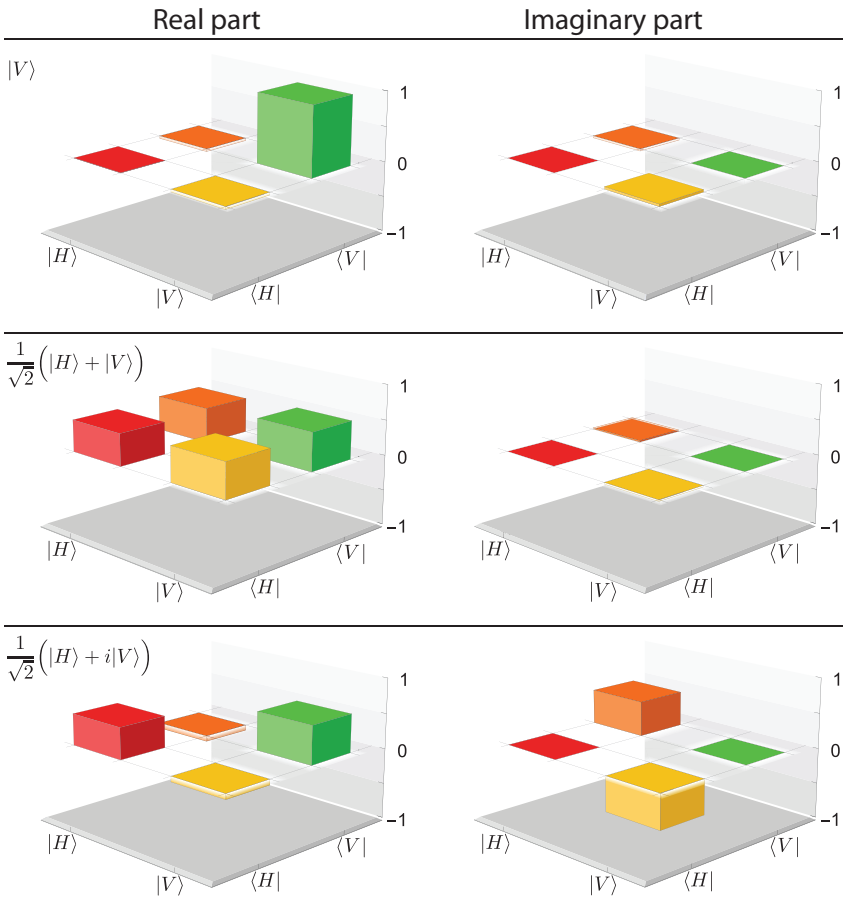

Figure 5.15: Density matrices reconstructed from projection measurements of a set of input qubit states after storage of the heralded telecom photon. Fidelities with photons in ideal input states are indicated in Table 5.2.

Target qubit	Fidelity (%)	Target qubit	Fidelity (%)
$\|H\rangle$	99.7 ± 1.7	$\|V\rangle$	99.6 ± 3.0
$\frac{1}{\sqrt{2}}(\|H\rangle + \|V\rangle)$	99.6 ± 2.6	$\frac{1}{\sqrt{2}}(\|H\rangle - \|V\rangle)$	99.5 ± 2.6
$\frac{1}{\sqrt{2}}(\|H\rangle + i\|V\rangle)$	99.0 ± 5.0	$\frac{1}{\sqrt{2}}(\|H\rangle - i\|V\rangle)$	99.7 ± 1.8

Table 5.2: Fidelities of reconstructed density matrices with target states.

the average fidelities $F_{H/V} = (2 + \mathcal{V}_H + \mathcal{V}_V)/4$ for projections onto $|H\rangle$ and $|V\rangle$ to be $(98.67 \pm 0.09)\%$ and $(98.4 \pm 0.6)\%$ before and after storage, respectively. Similarly for projections onto $(|H\rangle + e^{i\varphi}|V\rangle)/\sqrt{2}$ the fidelities are $(98.83 \pm 0.07)\%$ and $(97.93 \pm 0.7)\%$. These result show, within experimental uncertainty, that the qubit states have not been altered during storage.

To confirm this conclusion, we additionally perform quantum state tomography of several qubit states after recall from our AFC memory. In separate measurements we encode the states $|H\rangle$, $|V\rangle$, $(|H\rangle \pm |V\rangle)/\sqrt{2}$ and $(|H\rangle \pm i|V\rangle)/\sqrt{2}$, which form three mutually unbiased qubit bases, and map them to our memory. We retrieve the photons and, for each qubit, set the analyzers to project them onto the states $|H\rangle$ and $|V\rangle$, $(|H\rangle \pm |V\rangle)/\sqrt{2}$, and $(|H\rangle \pm i|V\rangle)/\sqrt{2}$. Using the outcomes of the coincidence measurements described previously, we reconstruct the quantum state of each retrieved qubit in terms of the density matrix [22] (See Fig. 5.15). All reconstructed density matrices have fidelities with the intended qubit states (listed in Table 5.2) of 0.99 or above, which confirms that the memory preserves polarization qubit states. We associate the small difference of these fidelities from unity with imperfect state preparation and thus not as being due to the storage.

5.4.3 Discussion and conclusions

Despite these important results, the performance of our storage device needs to be improved for practical use in quantum photonic applications. First, the recall efficiency

is limited to ∼1% (for 5 ns storage), due to imperfect preparation of the AFC (see Fig. 5.13b). However, as discussed in detail in [18], the optical pumping dynamics may be optimized so as to appreciably improve the recall efficiency. Second, the storage time in our current implementation is limited to 50 ns. This is mainly due to optical coherence time being affected by coupling of erbium ions to two-level systems, which are intrinsic in glass-like disordered hosts, as well as magnetic interactions between the erbium ions. Although the coherence time in lightly doped erbium fibers, such as ours, is expected to exceed 5 μs at temperatures approaching 100 mK, it remains a challenge to achieve the storage times required for quantum repeaters.

Yet, even with short storage times our light-matter interface possesses a number of features – such as a large time-bandwidth product, multimode storage capacity, and ability to process qubits – that makes it a good candidate for realizing on-demand single-photon sources [23] or programmable atomic processors [24]. In addition, erbium-based memories may be employed as quantum interfaces between telecommunication photons and superconducting circuits [25].

Finally, we note that our implementation provides a pre-programmed delay given by the inverse of the AFC peak spacing. Yet, spectrally-multiplexed storage with fixed storage time supplemented by feed-forward controlled recall is sufficient to implement quantum communication schemes [26].

In conclusion, we have realized quantum storage of polarization states encoded into heralded telecom-wavelength photons by implementing the AFC protocol in an erbium-doped optical fiber. Despite current limitations in terms of storage time and efficiency, the large bandwidth and multimode capacity of our light-matter interface are ideally suited for various applications in a future quantum Internet, e.g. for linear optics quantum computing and photonic quantum state processing. Furthermore, the robust and simple fiber-based platform of our light-matter interface offers full compatibility with quantum

photonics relying on telecom-fiber technology.

Acknowledgments

We thank Raju Valivarthi, Qiang Zhou, Matthew D. Shaw and Vladimir Kiselyov for useful discussions and technical support, and gratefully acknowledge support through Alberta Innovates Technology Futures (AITF) and the National Science and Engineering Research Council of Canada (NSERC). W.T. is a senior fellow of the Canadian Institute for Advanced Research (CIFAR). VBV and SWN acknowledge partial funding for detector development from the Defense Advanced Research Projects Agency (DARPA) Information in a Photon (InPho) program. Part of the research was carried out at the Jet Propulsion Laboratory, California Institute of Technology, under a contract with the National Aeronautics and Space Administration.

J.J. and E.S. contributed equally to this work.

Bibliography

[1] P. G. Kwiat, K. Mattle, H. Weinfurter, A. Zeilinger, A. V. Sergienko, and Y. Shih. *Phys. Rev. Lett.*, **75**, 4337–4341 (1995).

[2] D. Bouwmeester, J.-W. Pan, K. Mattle, M. Eibl, H. Weinfurter, and A. Zeilinger. *Nature*, **390**, 575–579 (1997).

[3] J.-W. Pan, D. Bouwmeester, H. Weinfurter, and A. Zeilinger. *Phys. Rev. Lett.*, **80**, 3891–3894 (1998).

[4] C.-Z. Peng, J. Zhang, D. Yang, W.-B. Gao, H.-X. Ma, H. Yin, H.-P. Zeng, T. Yang, X.-B. Wang, and J.-W. Pan. *Phys. Rev. Lett.*, **98**, 010505 (2007).

[5] N. Gisin, G. Ribordy, W. Tittel, and H. Zbinden. *Rev. Mod. Phys.*, **74**, 145–195 (2002).

[6] H. J. Kimble. *Nature*, **453**, 1023–1030 (2008).

[7] N. Sangouard, C. Simon, H. de Riedmatten, and N. Gisin. *Rev. Mod. Phys.*, **83**, 33–80 (2011).

[8] A. I. Lvovsky, B. C. Sanders, and W. Tittel. *Nature Photon.*, **3**, 706–714 (2009).

[9] F. Bussières, N. Sangouard, M. Afzelius, H. de Riedmatten, C. Simon, and W. Tittel. *J. Mod. Opt.*, **60**, 1519–1537 (2013).

[10] B. Lauritzen, J. Minář, H. de Riedmatten, M. Afzelius, N. Sangouard, C. Simon, and N. Gisin. *Phys. Rev. Lett.*, **104**, 080502 (2010).

[11] J. Dajczgewand, J. L. Le Gouët, A. Louchet-Chauvet, and T. Chanelière. *Opt. Lett.*, **39**, 2711–2714 (2014).

[12] F. Bussières *et al. Nature Photon.*, **8**, 775–778 (2014).

[13] N. Maring, K. Kutluer, J. Cohen, M, Cristiani, M. Mazzera, P. M Ledingham, and H. de Riedmatten. *New J. Phys.*, **16**, 113021 (2014).

[14] D. G England, P. S. Michelberger, T. F. M. Champion, K. F. Reim, K. C. Lee, M. R. Sprague, X.-M. Jin, N. K. Langford, W. S. Kolthammer, J. Nunn, and I. A. Walmsley. *J. Phys. B*, **45**, 24008 (2012).

[15] C. Clausen, F. Bussières, M. Afzelius, and N. Gisin. *Phys. Rev. Lett.*, **108**, 190503 (2012).

[16] M. Gündoğan, P. M. Ledingham, A. Almasi, M. Cristiani, and H. de Riedmatten. *Phys. Rev. Lett.*, **108**, 190504 (2012).

[17] Z.-Q. Zhou, W.-B. Lin, M. Yang, C.-F. Li, and G.-C. Guo. *Phys. Rev. Lett.*, **108**, 190505 (2012).

[18] E. Saglamyurek, J. Jin, V. B. Verma, M. D. Shaw, F. Marsili, S. W. Nam, D. Oblak, and W. Tittel. *Nature Photon.*, **9**, 83–87 (2015).

[19] M. Afzelius, C. Simon, H. de Riedmatten, and N. Gisin. *Phys. Rev. A*, **79**, 052329 (2009).

[20] F. Marsili, V. B. Verma, J. A. Stern, S. Harrington, A. E. Lita, T. Gerrits, I. Vayshenker, B. Baek, M. D. Shaw, R. P. Mirin, and S. W. Nam. *Nature Photon.*, **7**, 210–214 (2013).

[21] P. C. Becker, N. A. Olsson, and J. R. Simpson. *Erbium-Doped Fiber Amplifiers - Fundamentals and Technology.* Academic Press, 1999.

[22] J. B. Altepeter, E. R. Jeffrey, and P. G. Kwiat. *Adv. At., Mol., Opt. Phys.*, **52**, 105–159 (2005).

[23] J. Nunn, N. K. Langford, W. S. Kolthammer, T. F. M. Champion, M. R. Sprague, P. S. Michelberger, X.-M. Jin, D. G. England, and I. A. Walmsley. *Phys. Rev. Lett.*, **110**, 133601 (2013).

[24] E. Saglamyurek, N. Sinclair, J. A. Slater, K. Heshami, D. Oblak, and W. Tittel. *New J. Phys.*, **16**, 065019 (2014).

[25] C. O'Brien, N. Lauk, S. Blum, G. Morigi, and M. Fleischhauer. *Phy., Rev. Lett.*, **113**, 063603 (2014).

[26] N. Sinclair, E. Saglamyurek, H. Mallahzadeh, J. A. Slater, M. George, R. Ricken, M. P. Hedges, D. Oblak, C. Simon, W. Sohler, and W. Tittel. *Phys. Rev. Lett.*, **113**, 053603 (2014).

Chapter 6

Entanglement swapping operations for quantum repeaters

Two of the main ingredients in a QR are the capabilities to distribute and herald the presence of entanglement at the elementary link level and to interconnect and swap entanglement across neighboring elementary links (see figure 3.1). In order to accomplish these tasks, entangling joint projective measurements involving two qubits are required. This operation is achieved by performing a Bell-state Measurment (BSM), which project two qubits onto one of the four Bell-states (equation 2.9). Other than for QR applications, BSMs also play a key role in linear-optics quantum computation [61] and different quantum communication protocols, e.g. some quantum key distribution protocols [62], super dense coding [63] and quantum teleportation [64].

BSMs have been implemented with 100 % efficiency, allowing deterministic projection onto the four Bell-states, in different systems such as trapped ions, NV centers, and superconducting qubits [25]. Even though a deterministic BSM projection is not possible using photonic qubits and linear optics, the latter is still a convenient approach for QRs because of its simplicity. In particular, it does not require an additional, possibly inefficient and complicated mapping of a photonic qubit onto a matter qubit. In this section we will focus on describing how to perform a photonic BSM based on linear optics and what are the requirements and challenges. Two experiments relevant for the future development of QRs, involving as a key ingredient a photonic BSM, will be presented and discussed.

6.1 Photonic Bell-State measurements

Is straigthforward to see how a BSM can be performed deterministically with 100% efficiency if a CNOT gate [10] between two qubits can be implemented, since

$$\widehat{U}_{CNOT}|\Psi^{\pm}\rangle_{AB} = \frac{1}{\sqrt{2}}|1\rangle_A \otimes (|0\rangle \pm |1\rangle)_B \tag{6.1}$$

$$\widehat{U}_{CNOT}|\Phi^{\pm}\rangle_{AB} = \frac{1}{\sqrt{2}}|0\rangle_A \otimes (|0\rangle \pm |1\rangle)_B \,, \tag{6.2}$$

Where $\widehat{U}_{CNOT}$ represents the CNOT gate transformation. Unfortunately, photonic CNOT gates are difficult to implement since photons do not interact strongly with each other [65]. Alternatively, a photonic BSM based on linear optics and a two-photon interferece effect was proposed in 1994 [66]. This approach relies on the two-photon interference occurred when two photons impinge on different input ports of a 50:50 Beam-splitter (BS) due tue their bosonic nature (see next section). It has been theoretically shown that this approach can not be implemented with an efficiency greater than 50% [64] efficiency if no extra resources are used. However, photonic BSMs can approach arbitrary close to unity efficiency if extra resources are used, for example by using ancillary entangled photons pairs [67]. In this section we will describe the two-photon interference effect and how this can be used to implement a photonic Bell-State analyzer.

Two-photon interference and insdistinguishability

When two identical photons impinge onto two different inputs of a 50:50 BS they bunch and exit the BS from the same output due to their bosonic nature (bosonic particles tend to occupy the same quantum state). This effect can also be interpreted as a destructive interference between indistinguishable cases: either the two photons are

transmitted or reflected on the BS. The first experiment showing this interference effect was performed by Hong, Ou and Mandel in 1987 [68]. Honoring its first demonstration this effect is commonly referred as HOM interference.

The transformations introduced by a 50:50 BS can be expressed as

$$\widehat{a}^{\dagger} \rightarrow \frac{1}{\sqrt{2}}\left(\widehat{c}^{\dagger} + i\widehat{d}^{\dagger}\right) \tag{6.3}$$

$$\widehat{b}^{\dagger} \rightarrow \frac{1}{\sqrt{2}}\left(\widehat{d}^{\dagger} + i\widehat{c}^{\dagger}\right) \tag{6.4}$$

where $\widehat{a}^{\dagger}$ and $\widehat{b}^{\dagger}$ represent the creation of a photon in the input modes (a,b), and $\widehat{c}^{\dagger}$ and $\widehat{d}^{\dagger}$ the creation of a photon in the output modes of the BS (c,d) (see figure 6.1). Previous relations basically represent that an outgoing photon from the BS can be found with equal probability (50%) in either of the output modes c and d, no matter through which input port they came. The factor i account for the extra π phase shift acquired when a photon is reflected (consequence of unitarity). Applying the previous relations for two photons impinging onto different imput ports of a BS simultaneously, we obtain

$$|\Psi_{HOM}\rangle = \widehat{a}^{\dagger}\widehat{b}^{\dagger}|0_a 0_b\rangle = \frac{i}{2}\left(\widehat{c}^{\dagger 2} + \widehat{d}^{\dagger 2} + \widehat{c}^{\dagger}\widehat{d}^{\dagger} - \widehat{d}^{\dagger}\widehat{c}^{\dagger}\right)|00\rangle_{cd}. \tag{6.5}$$

In the case that photons in modes c and d are indistinguishable in all degrees of freedom (spatial mode, temporal mode, polarization and frequency), due to their bosonic, this leads to

$$|\Psi_{HOM}\rangle = \frac{i}{2}\left(\widehat{c}^{\dagger 2} + \widehat{d}^{\dagger 2}\right)|00\rangle_{cd}, \tag{6.6}$$

representing the two photons exiting the BS with equal probability in either of the BS outputs.

The typical HOM interference experiment (see figure 6.1) consists in recording the coincidence events between two photon detectors placed at each ouptut of the BS while

varying one of the degrees of freedom of the photons, thereby changing their degree of indistinguishably. The less distinguishable the photons are, the lower the coincident events will be recorded, i.e. HOM dip. This effect allows to easily measure the degree of indistinguishability (V) between two independently emitted photons by just recording the contrast between coicidence events in (C_{in}) and out (C_{out}) of the HOM dip ($V = \frac{C_{out}-C_{in}}{C_{out}}$).

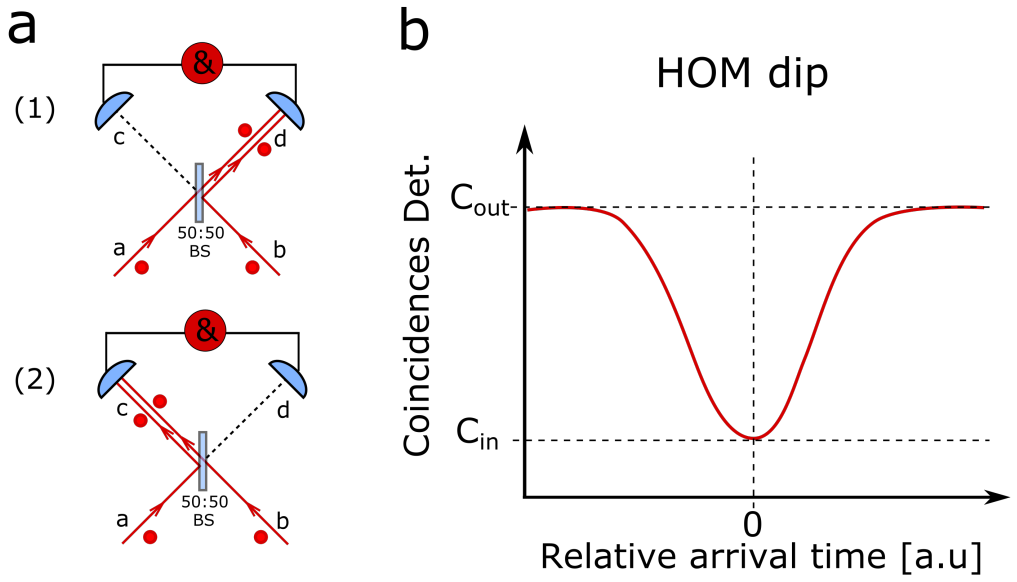

Figure 6.1: **Two-photon interference: HOM effect**. **a** Two possible detection patterns (1, 2) after two indistinguishable photons have interfered impinging onto a 50:50 Beam-splitter (BS). Photon detectors are symbolized by blue semi-circles. **b** Characteristic HOM dip interference pattern obtained when coincidence events between photon detectors are recorded at each output of the BS while varying their relative time overlap. For pure single photons impinging on the BS its indistinguishability (V) can be estimated by $V = \frac{C_{in}}{C_{out}-C_{in}}$, where C_{in} correspond to the coincidence events recorded inside the HOM dip (minimum) and C_{out} to the coincidence events outside the HOM dip (maximum). The width of the HOM dip is related to the temporal duration of both photons and can be used to determine its coherence lenghts.

The HOM effect is found to be useful and necessary in various applications. For example, it allows, the implementation of quantum gates, or two measure the degree

of indistinguishablity between independent emitted photons from different emitters e.g. quantum dots [69], color centers in diamond [70], etc. A characteristic feature of the HOM interference is that it is sensitive to path length differences on the order of the coherence length of the photons (second order interference), while if using a Mach-Zehnder interferometer one has a sub-wavelength sensitivity (first order interference), this makes interferometers based on HOM interference flexible and stable. For instance, in Paper 5 we use the HOM interference to stabilize the arrival time of two independent photons impinging on BS in order to make a BSM possible.

Time-bin qubits Bell-analyzer

In this section we focus in describing how to implement a Bell-State analyzer for time bin qubits. Such a photonic Bell-state analyzer [66] is based on the HOM interference effect and a coincidence analysis between different photonic modes at the BS output. Different coincindence pattern between photonic modes result onto a different Bell-State projection. As shown in [64] just two out of the four Bell-states can be unambiguously distinguished, $|\Psi^-\rangle$ and $|\Psi^+\rangle$ using such approach.

Originally the photonic Bell-State analyzer was implemented with polarization qubits, where different polarization modes are analyzed in coincidence [66]. This approach can be easily extended for different degrees of freedom, in order to implement a BSM for time-bin qubits two indistinguishable photons need to impinge simultaneously onto a 50:50 BS, and by analyzing the temporal detection pattern of photons in coincidence, different Bell-states can be distinguished. It can be shown in [64, 71] that a projection onto the state $|\Psi^-\rangle$ occurs if one of detector, at one BS output, registers a photon in the early time bin and the second detector, placed in the other BS output, registers a photon in the late time bin. On the other hand, a projection onto the state $|\Psi^+\rangle$ happens if

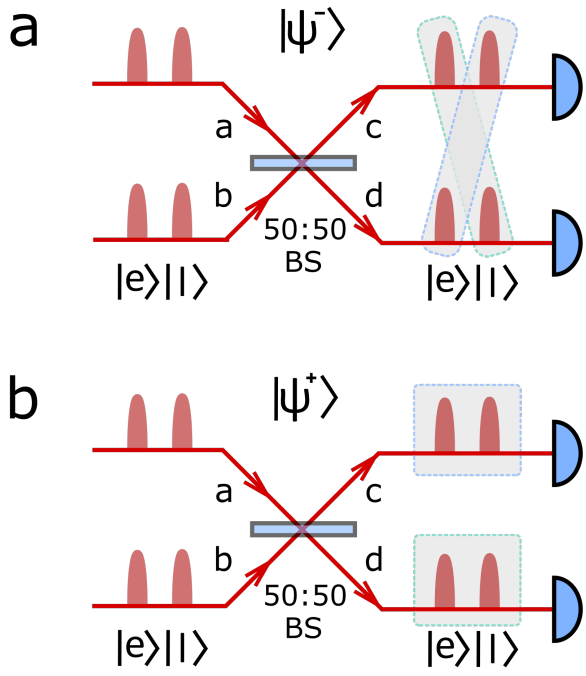

Figure 6.2: **Time-bin photonic Bell-State analyzer**. Arbitrary time-bin photonic qubits impinging onto a 50:50 Beam-splitter (BS), photon detectors are symbolized by blue semi-circles. **a** Coincidence patterns required to project the incoming photonic qubits onto $|\Psi^-\rangle$ are shadowed in grey,: early detection in upper detector and late detection in lower detector (or viceversa). **b** Coincidence patterns required to project the incoming photonic qubits onto $|\Psi^+\rangle$ are shadowed in grey: early detection in upper (lower) detector and late detection in upper (lower) detector.

the two photons are detected in the same BS output, one in an early time-bin and the second in the late bin. In order to project onto the remaining two Bell-states, $|\Phi^+\rangle$ and $|\Phi^-\rangle$, it would be necessary to detect events where two photons are present in the same time-bin and BS output, thus not being able to unambiguously discriminate onto which state were the photons projected. This is why a BSM based on linear optics is limited up to a 50 % a efficiency (unambiguously detect two out of four Bell-states) if implemented with linear optics and no extra resources are used.

Commonly, in quantum communication applications exploiting time-bin qubits just

projections onto $|\Psi^-\rangle$ states are performed (25 % BSM efficiency). This is usually due to the fact that, a projection onto the $|\Psi^+\rangle$ requires single photon detectors with recovery times (dead-times) shorter than the time bin-separation (usually 1-50ns), which ideally is defined as small as possible in order to increase the final communication throughput. Current state of the art single photon detectors based on superconducting nanowires [72, 73] feature efficiencies of around 90 %, even at telcomunication wavelengths, with short recovery times $\sim$ 50 ns, allowing to efficiently project onto two Bell-states simultaneously (50 % BSM efficiency) if time-bins are defined with $\geq$ 50 ns temporal separation [74].

6.2 Paper 4: Entanglement swapping with quantum-memory-compatible photons

Summary - By performing a BSM between two members of different entangled photon states, the entanglement is transferred to the remaining photons, this operation is called entanglement swapping and was first demonstrated in 1998 [75]. In the QR context entanglement swapping is employed to herald the presence of entanglement that needs to be stored in the corresponding QMs. This means that the photons used to be projected on a BSM need to be at a telecommunication wavelength, to experience low loss when travelling through an optical fibre, and the photons receiving the entangled state need to match the specifications required by the QMs i.e. wavelength, spectral bandwidth and polarization. Here we demonstrate for the first time entanglement swapping using photons at the telecommunication range together with photons interfaceable with our Tm^{3+}:$LiNbO_3$ based AFC QM [50].

Contributions - This experiment was conducted in collaboration with Jeongwan Jin, Joshua Slater, Lambert Giner and Daniel Oblak. The single photon detectors were designed, built and tested by Francesco Marsili, Matthew D. Shaw, Varun B. Verma and Sae Woo Nam. The experiment was conceived and supervised by Wolfgang Tittel. I specifically contributed in the the design and development of the setup of the time-bin entangled photon pair sources based on SPDC, as well as to the implementation and analysis of the measurement results. I contributed writing the manuscript and in conjuction with the other co-authors to all the editing steps until publication.

Entanglement swapping with quantum-memory-compatible photons

Physical Review A 92, 012329

27 July 2015

J. Jin[1*], M. Grimau Puigibert[1], L. Giner[1†], J. A. Slater[‡], M. R. E. Lamont[1], V. B. Verma[2], M. D. Shaw[3], F. Marsili[3] , S. W. Nam[2], D. Oblak[1] and W. Tittel[1]

[1]*Institute for Quantum Science and Technology, and Department of Physics and Astronomy, University of Calgary, 2500 University Drive NW, Calgary, Alberta T2N 1N4, Canada*

[2]*National Institute of Standards and Technology, Boulder, Colorado 80305, USA*

[3]*Jet Propulsion Laboratory, California Institute of Technology, 4800 Oak Grove Drive, Pasadena, California 91109, USA*

∗ *Present address: Institute for Quantum Computing, Department of Physics and Astronomy, University of Waterloo, 200 University Ave West, Waterloo, Ontario, Canada*

†*Present Address: Department of Physics, University of Ottawa, 150 Louis Pasteur, Ottawa, Ontario, Canada K1N 6N5*

‡*Present address: Vienna Center for Quantum Science and Technology, Faculty of Physics, University of Vienna, Boltzmanngasse 5, A-1090, Vienna, Austria*

Abstract

We report entanglement swapping with time-bin entangled photon pairs, each constituted of a 795 nm photon and a 1533 nm photon, that are created via spontaneous parametric down conversion in a non-linear crystal. After projecting the two 1533 nm photons onto a Bell state, entanglement between the two 795 nm photons is verified by means of quantum state tomography. As an important feature, the wavelength and bandwidth of the 795 nm photons is compatible with Tm:$LiNbO_3$-based quantum memories, making our experiment an important step towards the realization of a quantum repeater.

6.2.1 Introduction

Entanglement swapping entangles two photons that have no common past [1]. This fascinating phenomenon not only stimulated curiosity to understand quantum correlations [2, 3, 4, 5, 6, 7], but also plays an important role in various applications of quantum information science, including quantum computing [8, 9] and quantum repeaters [10]. A quantum repeater-based communication channel, for instance, exploits entanglement swapping to entangle interim nodes in a heralded fashion, and connect elementary entangled links (connecting interim nodes) to distribute entanglement in principle over arbitrarily long distances [11, 12]. In turn, the resulting entanglement can be used to generate a secret key between distant users [13].

Necessary ingredients for quantum repeaters, in addition to entangled photon pairs and entanglement swapping, are optical quantum memories [14]. Such memories allow the reversible mapping of (entangled) states between light and atoms, and thereby remove the necessity for all elementary links to establish entanglement simultaneously. While entanglement swapping has been reported before [15, 16, 17, 18, 19, 20], the spectra of the resulting entangled photons were either orders of magnitude too large, or their wave-

length were not suitable to allow subsequent interfacing with optical quantum memory. Here we remove this impediment: using cavities, we spectrally engineer swapped photons in time-bin qubit states in such a way that their wavelengths (around 795 nm) and bandwidths become compatible with our solid-state quantum memories [21]. Furthermore, we accordingly increase the coherence times of the photons used to swap the entanglement (both around 1533 nm wavelength), which will, in the future, allow such quantum interference measurements even with photons that have traveled through tens of kilometres of deployed standard telecommunication fibre [22]. To verify successful entanglement swapping, we measure (conditional) two-photon visibility curves. For more complete information, we additionally employ quantum state tomography to derive the concurrence and the fidelity of the swapped state with the nearest maximally entangled state, and we compare the latter with the predictions of a recently developed model [23]. As with the use of quantum state tomography, this has not been done previously for time-bin qubits after entanglement swapping.

6.2.2 Measurement and results

A schematics of our experimental setup is depicted in Fig. 6.3. A 1047 nm wavelength laser emits 6 ps long pulses at 80 MHz repetition rate. After second harmonic generation (SHG) in a periodically poled lithium niobate crystal (PPLN), the now 18 ps long pulses, centered at 523.5 nm wavelength, travel through an unbalanced Mach-Zehnder interferometer (MZI) whose path length difference corresponds to 1.4 ns travel time difference, thereby splitting every pulse into two. Pairs of pulses emitted from the two outputs of the interferometer then pump two 10 mm-long PPLN crystals, in which spontaneous parametric down-conversion (SPDC) leads to time-bin entangled qubits [24] encoded into pairs of photons with wavelengths centred around 795 nm and 1533 nm. Assuming, for the sake of explanation, for the moment that only individual photon pairs are created,

this process yields states of the form $|\Phi^+\rangle_{AB} = \frac{1}{\sqrt{2}}(|e\rangle_A|e\rangle_B + |\ell\rangle_A|\ell\rangle_B)$ emitted from one crystal, and $|\Phi^-\rangle_{CD} = \frac{1}{\sqrt{2}}(|e\rangle_C|e\rangle_D - |\ell\rangle_C|\ell\rangle_D)$ emitted from the other crystal, where $|e\rangle$ and $|\ell\rangle$ represent *early* and *late* time-bin qubit states.

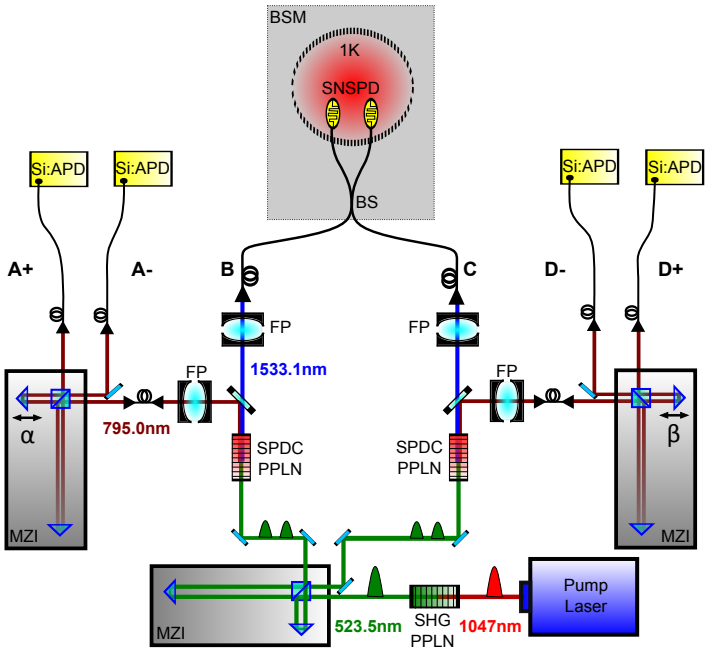

Figure 6.3: Schematics of of our setup. See text for details.

Using a grating monochromator connected to a single photon detector, we measure the spectral width of the 795 nm photon at full width half maximum (FWHM) to be 1.5 nm. By energy conservation, and taking into account the bandwidth of the pump photons, we calculate the spectral width of the 1533 nm photons to be 5.6 nm (FWHM). These values by far exceed the maximum bandwidth of 10 GHz (corresponding to 21 pm at 795 nm wavelength), over which quantum memories have so far been reported to operate [21]. Hence, to allow future interfacing with memories, we filter the 795 nm photons using Farbry-Perot cavities (FP; one per source) to 6 GHz, and also reduce the bandwidth of the 1533 nm photons to 12 GHz (again using Fabry-Perot cavities), which corresponds to 94 pm. (The filter cavities feature only one spectral order within the spectral width of the

created photons.) This additionally ensures that the photons' coherence time, around 37 ps, exceeds that of the pump pulses, as required for entanglement swapping. The cavities are based on Corning ultra-low expansion glass spacers and fused silica mirrors to reduce thermal noise, and their transmissions are 35% and 90% for 795 nm and 1533 nm photons, respectively. Using the approach described in [25], we find the probability of having a photon pair per source and pump laser pulse after filtering, i.e. per qubit, to be about $19.1 \pm 1.8\%$.

To swap entanglement to the two 795 nm qubits (propagating along spatial modes A and D), the two 1533 nm qubits (in modes B and C) are subjected to a so-called Bell-state measurement (BSM) after travelling through short standard telecommunication fibres. This measurement is performed by sending the two photons into the different input ports of a 50/50 beam splitter. Provided they exit through two different output ports and in different temporal modes (one photon early, the other one late), their joint state is projected onto the $|\Psi^-\rangle_{BC} = \frac{1}{\sqrt{2}}\left(|e\rangle_B|\ell\rangle_C - |\ell\rangle_B|e\rangle_C\right)$ Bell state, leaving the two 795 nm photons in the entangled $|\Psi^+\rangle_{AD} = \frac{1}{\sqrt{2}}\left(|e\rangle_A|\ell\rangle_D + |\ell\rangle_A|e\rangle_D\right)$ Bell state. We note that, in principle, it is also possible to make projection measurements onto the $|\Psi^+\rangle$ Bell state, thereby increasing the measurement's efficiency from maximally 25% to 50% [26]. To detect the 1533 nm photons, we use free-running, tungsten silicide (WSi)-based superconducting nanowire single-photon detectors (SNSPD) cooled to around 0.9 Kelvin [27]. However, due to fibre transmission loss inside our cryostat, we find a system efficiency of around 50%. Furthermore, we measure a detection-time jitter of 250 ps (FWHM), which is sufficiently small to allow resolving the temporal qubit modes (spaced by 1.4 ns), and the dark-count rate of 10 Hz ensures little noise-pollution of detection signals.

For the Bell-state measurement to work, the two 1532 nm photons must be indistinguishable at the beam splitter, i.e, their spatial, temporal, spectral, and polarization modes must be identical. This is verified using so-called Hong-Ou-Mandel (HOM) in-

terference [28]: if two indistinguishable photons (not qubits) impinge on a symmetric beam splitter from different input ports, then they bunch and leave together by the same output port due to destructive interference between the probability amplitudes associated with both input photons being transmitted or both reflected. Conversely, if the two photons are distinguishable, no such interference occurs, and they leave the beamsplitter with 50% probability through different outputs, resulting in coincident detections. The HOM visibility, defined as $V_{HOM} = (N_{max} - N_{min})/N_{max}$ [29], where N_{max} and N_{min} denote coincidence count rates measured with completely distinguishable and (maximally) indistinguishable photons, respectively, is a common way to characterize the degree of indistinguishability. We find $V_{HOM} = 27.5 \pm 2.5\%$. This value is consistent with the fact that our 1533 nm inputs are not single photons, but are mixtures of photon Fock states with thermal distribution, for which the HOM visibility is upper bounded by 1/3 [29].

Repeating the measurement conditioned on the detection of two 795 nm photons (described below) and with small pump power, which projects the 1533 nm inputs onto approximate single photons, the HOM visibility increases up to $87.5 \pm 5.5\%$. We attribute the gap to the theoretical value of 100% to insufficient spectral filtering of the photons, and, to a much smaller extent, to remaining contributions from the simultaneous emission of more than two photons. Indeed, using $V_{HOM}^{Max} = 1/\sqrt{1 + (\frac{\Delta T}{\tau})^2}$ [30, 31], where ΔT denotes the duration of the pump pulses, and τ the coherence time of the 1533 nm photons after filtering, we find that the maximum visibility achievable with our setup is 89%, which corresponds to our result within experimental error.

To assess the quality of the entangled state after the entanglement swapping, the two 795 nm photons are sent through Mach-Zehnder interferometers that introduce the same travel-time difference of 1.4 ns as the interferometer that acts on the pump beam and thus allow projecting photon states onto various time-bin qubit states [24]. To ensure phase stability during the measurements, i.e. constant projectors, the interferometers

are passively temperature stabilized. Additionally, their phases are actively locked using a frequency-stabilized laser at 1550 nm wavelength that is also sent through the interferometers, and a home-made feedback loop. Finally, the 795 nm photons are detected using four standard silicon avalanche photodiode-based single photon detectors with efficiencies around 50%, detection jitter of 500 ps, and dark counts around a few hundred Hz. All detection signals are recorded using a time-to-digital converter that is started by a successful BSM.

We also measure the total heralding efficiency [32], which, for the 795 nm (1533 nm) photon, we define as the ratio between the rate of photon pair coincidence detections and the rate of the detection of 1533 nm (795 nm) photons. Hence, for the low mean photon number in our experiments, the heralding efficiency is equal to the probability of detecting a photon that has been created by downconversion in the source. This takes into account all transmission loss (such as loss in filter cavities, prisms and fibre coupling loss), non-unity detection efficiency, and a fundamental restriction caused by the bandwidth mismatch between the pump and downconverted photons. A simple calculation of the bandwidth restriction (see appendix) shows that the latter alone limits the heralding efficiency for the 795 nm (1533 nm) photons to 17.4% (34.8%). Considering furthermore the known values of 50% (70%) for detection efficiency, 40% (80%) for transmission through the cavity, and 85% (85%) for transmission through the prism, we anticipate a heralding efficiency of 2.96% (16.6%) for the 795 nm (1533 nm) photons. Experimentally we obtain heralding efficiencies of 1.96% for 795 nm and 5.8% for 1533 nm photons. The difference between the measured and expected values is predominantly due to imperfect fibre coupling, which we assess to be 66% and 35% for the 795 nm and 1533 nm photons, respectively. Hence, we find that one of the main limitations to achieving higher heralding efficiencies is the bandwidth mismatch between the pump photon and the downconverted photons. This can be improved by using a spectrally narrower pump, as further described

in the Appendix.

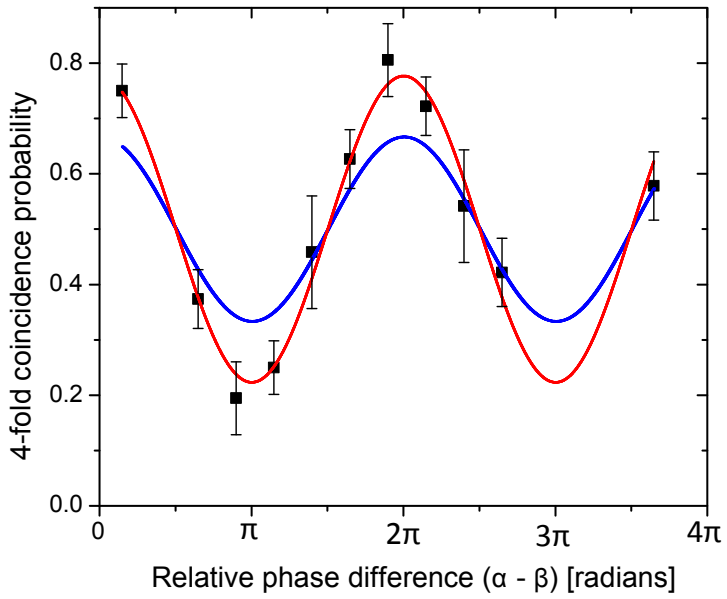

Figure 6.4: color online) Coincidence detection probabilities (conditioned on a successful Bell-state measurement) of the 795 nm photons as a function of the phase difference in the measurement interferometers. The uncertainty bars indicate one standard deviation and are calculated from measured rates assuming Poissonian detection statistics. The visibility of the sinusoidal fit is 56.2 ± 5.7%. The blue curve features a visibility of 1/3, indicating the classical bound for a separable Werner state.

To investigate the presence of entanglement between the two 795 nm photons after the BSM with the 1533 nm photons, first, we measure the probability for coincidence detection of two 795 nm photons in detectors A and D, conditioned on projecting the two 1533 nm photons onto the $|\Psi^-\rangle$ Bell state, as a function of the phase difference $\alpha - \beta$ of the two analyzing interferometers. This corresponds to projecting each 795 nm photon onto equal superpositions of $|e\rangle$ and $|\ell\rangle$. (For these as well as the following measurements, the mean photon pair number was set to 19.1%.) The results, depicted in Fig. 6.4, show a sinusoidal curve with a fitted visibility of (56.2 ± 5.7)%. The phase difference axis is recalibrated based on the fit so that $\alpha - \beta = 0$ corresponds to a maximum of the coincidence probability. The sinus period is fixed to 2π, however,

refitting the data with the period as a free parameter yields an almost identical curve with a period of $(0.98 \pm 0.03)2\pi$. This confirms the excellent stability and calibration of the relative interferometer phases during our measurements, which required a total of 36 hours (the average four-fold coincidence rate was about 10/hour). Furthermore, the visibility clearly exceeds the maximum visibility of 33% that can be obtained using a separable Werner state [33]. This confirms the presence of entanglement, provided the often made assumption of having a Werner state is satisfied.

To remove this assumption, we reconstruct the density matrix of the 795 nm photons' joint quantum state by means of maximum likelihood quantum state tomography (QST) [34], which will allows assessing additional measures that quantify entanglement and derive more information about experimental imperfections. Towards this end we perform a total of 36 joint projection measurements corresponding to all combinations of projections onto eigenstates of σ_X, σ_Y and σ_Z. Each combination requires a coincidence measurement (conditioned on a successful Bell-state measurement) with specific (local) interferometer phase settings (for projections onto eigenstates of σ_X and σ_Y), or measurements of photon arrival times (for projections onto eigenstates of σ_Z). We emphasize the importance of interferometer phase stability, which we verified above, to ensure proper (and stable) measurements. The reconstructed density matrix is depicted in Fig. 6.5. It allows calculating the concurrence (C), an entanglement measure that is zero for a separable state and larger than zero for an entangled state [35]. We find $C = 0.36 \pm 0.07$, which exceeds the threshold by five standard deviations (for this and the further experimental values the uncertainty is calculated by means of Monte Carlo simulation and assuming the coincidence counts follow Poissonian statistics), thereby confirming the conclusion of having an entangled state derived from the visibility in Fig. 6.4. We also compute our reconstructed state's fidelity with the expected state $|\Psi^+\rangle$ to be $F = (68 \pm 3)\%$. Optimization over all maximally entangled states also shows that $|\Psi^+\rangle$ yields the largest

fidelity with our reconstructed state (within the step size of the optimization algorithm).

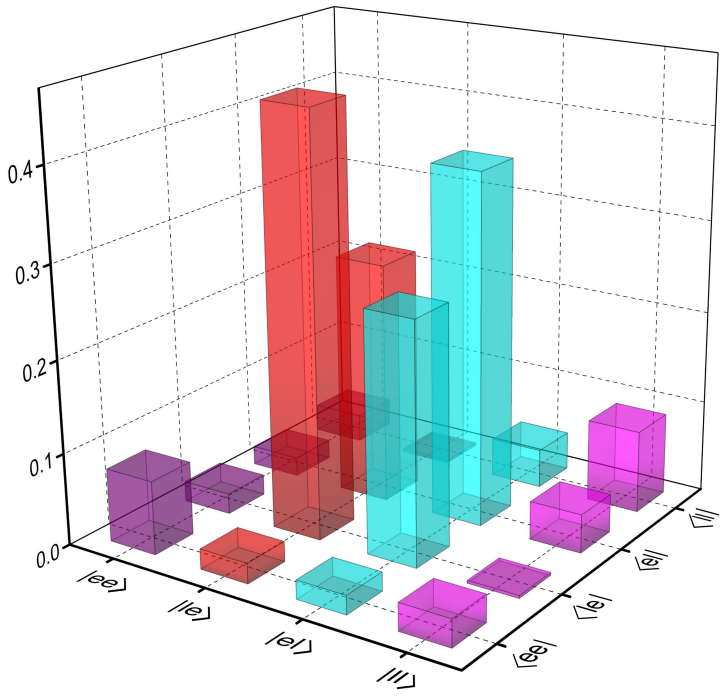

Figure 6.5: color online) Density matrix characterizing the joint state of the two 795 nm photons after entanglement swapping. The fidelity with respect to the $|\Psi^+\rangle$ Bell state – which we find to be the nearest maximally entangled state – is $(68 \pm 3)\%$.

Furthermore, we can now assess how well the reconstructed density matrix is described by a Werner state by calculating the fidelity of the swapped state with the nearest Werner state $\sigma = v|\psi\rangle\langle\psi| + \frac{1}{4}(1-v)\mathbb{1}$. Here, $|\psi\rangle$ is any maximally entangled two-qubit state, $\mathbb{1}$ is the identity matrix and v is a variable that parametrizes the state. Evaluating $F = (tr\sqrt{\sqrt{\sigma}\rho\sqrt{\sigma}})^2$ over all $|\psi\rangle$ and v, we find that the maximal value $F = 97.5^{+0.5}_{-4.4}\%$ is achieved for $|\psi\rangle = |\Psi^+\rangle$ and $v = 0.592$. Hence, using the fidelity measure indicates that the reconstructed state is close to a Werner state. The remaining difference is due to the admixture of non-white noise in the reconstructed state, which we primarily attribute to the residual distinguishability in the Bell-state measurement (this imperfection only affects measurements of σ_x and σ_y – not σ_z [36]). Hence, it is reasonable to use the fitted

visibility in Fig. 6.4, which is based on measurements in the σ_x and σ_y bases, to infer the presence of entanglement in the state after entanglement swapping. However, the observation that our state is not an exact Werner state also leads to a note of caution, in that a visibility measurement comprising projections onto σ_z – which in our experiment is less affected by experimental imperfections – may provide an inflated measure of the entanglement in the swapped state.

To independently assess how experimental imperfections limit the amount of entanglement in the final bi-photon state, we employ the method described in [23] with measured experimental parameters for heralding efficiency (1.96% at 795 nm and 5.8% at 1533 nm), HOM visibility (89%), mean photon pair number (19%) and fidelities (95%) for the individual sources. This leads to a density matrix having a concurrence of 0.43, i.e. a state that is slightly closer to a maximally entangled state than the measured one. We find the fidelity of the density matrix predicted by this model and the one we measured to be $98.1^{+0.3}_{-4.0}$%, which suggests that we understand the noise sources affecting the swapped state. Because this model accounts for non-white noise arising from the limited HOM visibility in the BSM, the predicted density matrix features a slightly larger fidelity with our measured state as that resulting from the comparison with the closest Werner state.

Based on our analysis, we identify multi photon pair emissions, due to the probabilistic nature of SPDC sources, as our main source of errors that limits the value of the concurrence. To improve our result, we therefore have to decrease the probability of generating a photon pair per pulse below our current value of 19%. For instance, reducing the mean photon pair emission probability to 10% would, according to our model [23], result in an increase of the concurrence to 0.53 (keeping all other parameters unchanged). Note that alternative way to reduce the impact of multi-pair emissions are to exploit a quantum Zeno blockade to suppresses multi photons [37] or a quantum non-demolition measurement that reveals the number of simultaneously emitted photon pairs

[38], thereby allowing in theory to completely ignore detections stemming from multi pair emissions. According to the model this would yield a concurrence of 0.82.

6.2.3 Discussion and conclusions

Before concluding, let us briefly discuss the possibility to extend the current implementation into an elementary quantum repeater link, in which case the two 1533 nm photons have to travel tens of km before being submitted to the Bell-state measurement, and the two 795 nm photons have to be stored in optical quantum memories. We note that these criteria are easily met as, first, their long coherence time makes the 1533 nm photons robust against travel-time fluctuations during long-distance transmission, second, loss in optical fibres at this wavelength is minimal, and third, as quantum memories for 795 nm photons with 6 GHz bandwidth are available [21]. However, even assuming memory efficiencies exceeding 50%, which remains to be demonstrated for memories of such large bandwidth, the coincidence count rates are currently too small to demonstrate an elementary quantum repeater link - let alone building a useful one. Solutions, on the one hand, are relaxed focussing of the 523 nm laser pulses into the SPDC crystals, which has been shown to significantly improve the coupling efficiency [39]. Secondly, the lossy cavities for the 795 nm photons can be removed as the memories themselves will work as filters. The latter will increase the coincidence rates by one order of magnitude. Furthermore, given the large bandwidth of the SPDC photons (of which we currently use only a few GHz), and the large bandwidth and spectral multi-mode storage capacity of, e.g., atomic frequency comb-based Tm:$LiNbO_3$ quantum memories, it is possibility to work with many frequency channels in parallel using a quantum repeater architecture that we described in [12].

To summarize, we have experimentally demonstrated the creation of entanglement

between two 795 nm photons, whose properties are suitable for further storage in broadband quantum memories such as our Tm:$LiNbO_3$ waveguides, by means of a Bell-state measurement with two 1533 nm photons, each of which was initially entangled with one of the two 795 nm photons. Our demonstration constitutes an important step towards the generation of a quantum repeater: the heralded entanglement of two quantum memory-compatible photons.

Acknowledgments

The authors thank Vladimir Kiselyov for support with electrical engineering. We gratefully acknowledge support through Alberta Innovates Technology Futures (AITF), the National Science and Engineering Research Council of Canada (NSERC), the US Defense Advanced Research Projects Agency (DARPA) Quiness and InPho Programs, and the Killam Trusts. Part of the research was carried out at the Jet Propulsion Laboratory, California Institute of Technology, under a contract with the National Aeronautics and Space Administration. W.T. is a senior fellow of the Canadian Institute for Advanced Research (CIFAR).

6.2.4 Supplementary information

Heralding efficiency vis-a-vis photon bandwidth

The bandwidth mismatch between the pump light and the filters used in our experiment for the downconverted photons fundamentally limits the maximum attainable heralding efficiency for each of the down-converted photons (commonly referred as signal and idler). In this section we develop a simple model – inspired by the pictorial

representation in [40] – that captures the main consequences of this effect.

As described in the main text, we define the heralding efficiency for the signal (η_{H_s}) as the ratio between the coincidence detection rate (C_{si}) and the single detection rate for the idler (S_i):

$$\eta_{H_s} = \frac{C_{si}}{S_i}. \tag{6.7}$$

Similarly, the idler heralding efficiency is found as:

$$\eta_{H_i} = \frac{C_{si}}{S_s}. \tag{6.8}$$

The pump laser has a spectral bandwidth $\Delta\nu_p$ given by the pump pulse duration. Since the down-conversion process must conserve energy, the frequencies of any pair of down-converted photons are correlated to within the pump bandwidth. As a result, the Joint Spectral Amplitude (JSA) of the down-converted photons (see Fig. 6.6) can be illustrated by a diagonal band (green region) with a cross sectional width corresponding to the spectral width of the pump ($\Delta\nu_p$). Note that we assume that, over the relevant bandwidth, the phase-matching condition is less restrictive than that resulting from energy conservation, and thus we do not indicate it on the figure. However, phase-matching determines the total extent of the diagonal band (outside the view of the figure) and thus sets the overall bandwidth of down-converted photons.

Next we explore the effect of restricting the bandwidth of either the signal or the idler photon by means of spectral filters with bandwidths $\Delta\nu_s$ and $\Delta\nu_i$, respectively. In Fig. 6.6, and for the case in which we filter the idler, this corresponds to carving out a horizontal band in the JSA. The idler photon single detection rate is proportional to the overlap of this horizontal band with the diagonal band representing energy conservation (red area in Fig. 6.6a), i.e. $A_i = \sqrt{2}\Delta\nu_p\Delta\nu_i$. Similarly, for the case of filtering the signal, the single count rate is proportional to the area of the blue region in Fig. 6.6b, which is $A_s = \sqrt{2}\Delta\nu_p\Delta\nu_s$. These expressions are approximate because they assume that the

count rates of the filtered photons are directly proportional to the specified areas. This, however, is only correct if the spectral profile of the filters and the JSA given by the pump bandwidth are box-shaped (flat-top). Moreover, the area is only calculated as above if the filter bandwidths are smaller than the pump-bandwidth i.e. $\Delta\nu_{s(i)} < \Delta\nu_p$.

Finally, we extend this picture to the case in which we filter both signal and idler and measure the coincidence count rate. As illustrated by Fig. 6.6c the coincidence count rate is proportional to the area (in pink), i.e. the intersection of the horizontal and vertical bands given by the filters – $A_{si} = \Delta\nu_s\Delta\nu_i$. Clearly, this area is smaller than both A_s and A_i, thus limiting the heralding efficiency. More precisely the heralding efficiencies can be expressed as:

$$\begin{aligned} \eta_{H_s} &= \frac{C_{si}}{S_i} = \frac{A_{si}}{A_i} = \frac{\Delta\nu_s}{\sqrt{2}\Delta\nu_p} \\ \eta_{H_i} &= \frac{C_{si}}{S_s} = \frac{A_{si}}{A_s} = \frac{\Delta\nu_i}{\sqrt{2}\Delta\nu_p}. \end{aligned} \tag{6.9}$$

In our experiments $\Delta\nu_s = 6$ GHz (795 nm photon), $\Delta\nu_s = 12$ GHz (1533 nm photon) and $\Delta\nu_p = 24.4$ GHz (523 nm photon). Using these values in Eq. 6.9, we obtain $\eta_{H_s} = 17.4\%$ and $\eta_{H_i} = 34.8\%$. Though these values are calculated using a simple model, they provide a qualitative explanation of the maximum attainable heralding efficiency for each of the signal and idler photons in our system and allows us to assess the loss due to other factors such as optical elements, optical fibre coupling, and detector efficiency.

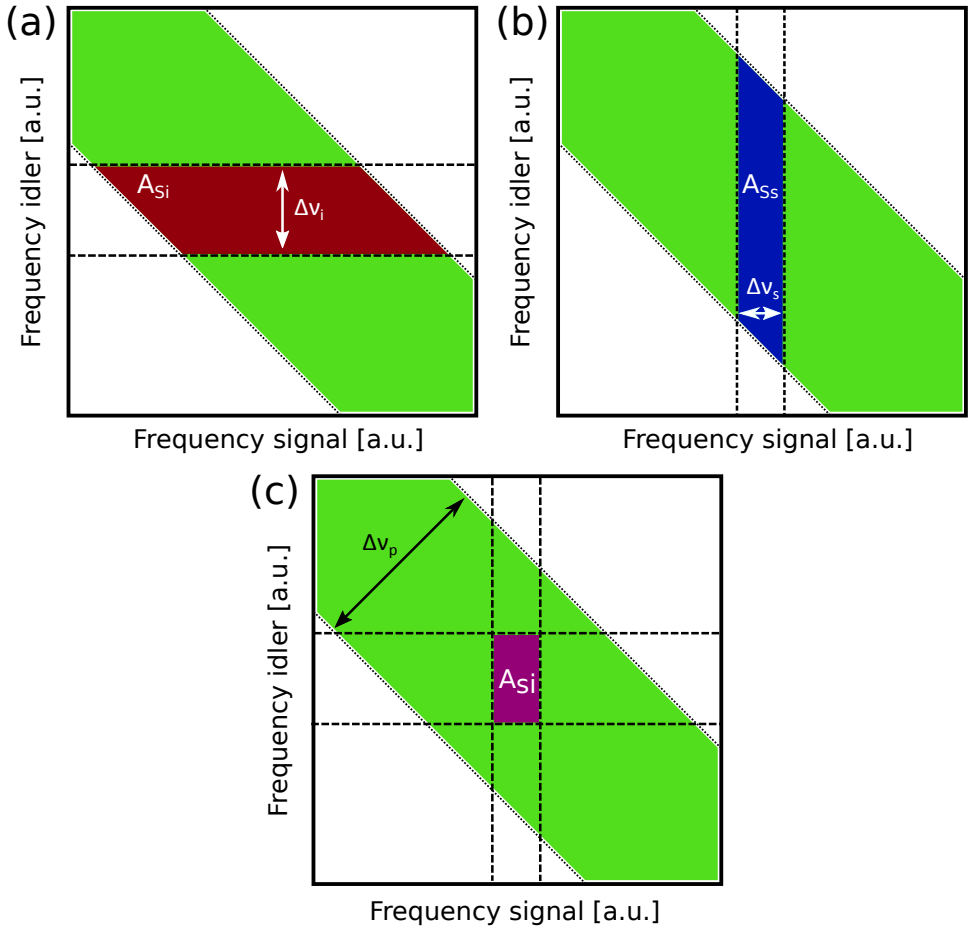

Figure 6.6: color online) Joint Spectral Amplitude of photon pairs generated via an SPDC process with bandwidths of pump-pulse and spectral filters indicated.

Bibliography

[1] M. Zukowski, A. Zeilinger, M. A. Horne, and A. K. Ekert, Phys. Rev. Lett. 71, 4287 (1993).

[2] E. Megidish, A. Halevy, T. Shacham, T. Dvir, L. Dovrat, and H. S. Eisenberg, Phys. Rev. Lett. 110, 210403 (2013).

[3] X. -S. Ma, S. Zotter, J. Kofler, R. Ursin, T. Jennewein, . Brukner, and A. Zeilinger, Nature Physics 8, 480 (2012).

[4] A. J. Short, S. Popescu, and N. Gisin, Phys. Rev. A 73, 012101 (2006).

[5] C. Branciard, D. Rosset, N. Gisin, and S. Pironio, Phys. Rev. A 85, 032119 (2012).

[6] W. Klobus, W. Laskowski, M. Markiewicz, and A. Grudka, Phys. Rev. A 86, 020302 (2012).

[7] S. Bose, V. Vedral, and P. L. Knight, Phys. Rev. A 57, 822 (1998).

[8] T. D. Ladd et al. Quantum computers. Nature 464, 45-53 (2010).

[9] E. Knill, R. Laflamme, and G. Milburn, Nature 409, 46-52 (2001).

[10] H. -J. Briegel, W. Dür, J. I. Cirac, and P. Zoller, Phys. Rev. Lett. 81, 5932 (1998).

[11] N. Sangouard, C. Simon, H. de Riedmatten, and N. Gisin, Rev. Mod. Phys. 83, 33 (2011).

[12] N. Sinclair, E. Saglamyurek, H. Mallahzadeh, J. A. Slater, M. George, R. Ricken, M. P. Hedges, D. Oblak, C. Simon, W. Sohler, and W. Tittel, Phys. Rev. Lett. 113, 053603 (2014).

[13] A. K. Ekert, Phys. Rev. Lett. 67, 661 (1991).

[14] A. I. Lvovsky, B. C. Sanders, and W. Tittel, Nature Photon. 3, 706-714 (2009).

[15] J. W. Pan, D. Bouwmeester, H. Weinfurter, and A. Zeilinger, Phys. Rev. Lett. 80, 3891 (1998).

[16] T. Jennewein, G. Weihs, J. -W. Pan, and A. Zeilinger, Phys. Rev. Lett. 88, 017903 (2001).

[17] H. de Riedmatten, I. Marcikic, J.A.W. van Houwelingen, W. Tittel, H. Zbinden, and N. Gisin, Phys. Rev. A 71, 050302 (2005).

[18] M. Halder, A. Beveratos, N. Gisin, V. Scarani, C. Simon, and H. Zbinden, Nature Physics 3, 692-695 (2007).

[19] Z.-S. Yuan, Y. -A. Chen, B. Zhao, S. Chen, J. Schmiedmayer, and J. -W. Pan, Nature 454, 1098-1101 (2008).

[20] R. Kaltenbaek, R. Prevedel, M. Aspelmeyer, and A. Zeilinger, Phys. Rev. A 79, 040302 (2009).

[21] E. Saglamyurek, N. Sinclair, J. Jin, J. A. Slater, D. Oblak, F. Bussières, M. George, R. Ricken, W. Sohler, and W. Tittel, Nature 469, 512 (2011).

[22] A. Rubenok, J. A. Slater, P. Chan, I. Lucio-Martinez, and W. Tittel, Phys. Rev. Lett. 111, 130501 (2013).

[23] S. Guha, H. Krovi, C. A. Fuchs, Z. Dutton, J. A. Slater, C. Simon, and W. Tittel, arXiv : 1404.7183 (2014).

[24] W. Tittel, and G. Weihs, Quantum Information and Computation 1, Rinton Press (2001).

[25] I. Marcikic, H. de Riedmatten, W. Tittel, V. Scarani, H. Zbinden, and N. Gisin, Phys. Rev. A 66 062308 (2002).

[26] R. Valivarthi, I. Lucio-Martinez, A. Rubenok, P. Chan, F. Marsili, V. B. Verma, M. D. Shaw, J. A. Stern, J. A. Slater, D. Oblak, S. W. Nam, and W. Tittel, Optics Express 22(20): 24497-24506, (2014).

[27] F. Marsili, V. B. Verma, J. A. Stern, S. Harrington, A. E. Lita, T. Gerrits, I. Vayshenker, B. Baek, M. D. Shaw, R. P. Mirin, and S. W. Nam, Nature Photon. 7, 210-214 (2013).

[28] C. K. Hong, Z. Y. Ou, and L. Mandel, Phys. Rev. Lett. 59, 2044 (1987).

[29] H. de Riedmatten, I. Marcikic, W. Tittel, H. Zbinden, and N. Gisin, Phys. Rev. A 67, 022301 (2003).

[30] M. Zukowski, A. Zeilinger, and H. Weinfurter, Annals of the New York Academy of Sciences 755, 91 (1995).

[31] J. G. Rarity, Annals of the New York Academy of Sciences 755, 624 (1995).

[32] E. Pomarico. B. Sanguinetti, T. Guerreiro, R. Thew, and H. Zbinden, Opt. Express 20, 23846–23855 (2012).

[33] A. Peres, Phys. Rev. Lett. 77, 1413 (1996).

[34] J. B. Altepeter, E. R. Jeffrey, and P. G. Kwiat, Adv. At. Mol. Opt. Phys. 52, 105 (2005).

[35] W. K. Wootters, Phys. Rev. Lett. 80, 2245 (1998).

[36] P. Chan, J. A. Slater, I. Lucio-Martinez, A. Rubenok, and W. Tittel, Optics Express 22 (11), 12716 (2014).

[37] Y. -P. Huang and P. Kumar, Phys. Rev. Lett. 108, 030502 (2012).

[38] L. Liang, G. W. Lin, Y. M. Hao, Y. P. Niu, and S. Q. Gong, Phys. Rev. A 90, 055801 (2014).

[39] T. Guerreiro, A. Martin, B. Sanguinetti, N. Bruno, H. Zbinden and R. T. Thew, Optics Express 21, 27641 (2013).

[40] K. Garay-Palmett, Y. Jeronimo-Moreno and A. B. U'Ren, Laser Physics 23, 015201 (2013).

6.3 Paper 5: Quantum teleportation across a metropolitan fibre network

Summary - If a photon interacts with a member of an entangled photon pair via a BSM, its state is teleported onto the second member of the pair. Quantum teleportation was first experimentally demonstrated in 1997 [76], but in all previous demonstrations, the photons partaking in the BSM would not travel over a long distance before being projected in a BSM. For quantum networks or QR applications is indispensable to perform BSM with photons undergoing over a long fibre transmission in a real-world environment before subjected to a BSM. This remains a challenge since real-world fibre links are not under controlled environment, thereby introduce random transformation to photons that need to be compensated before the BSM takes place in order to guarantee its indistinguishability.

Here we demonstrate quantum teleportation using Calgary's fibre network, where photons involved in the BSM travel over long distances through optical fibres in a real-world environment. We implement novel feedback mechanisms that stabilize the transformations introduced by the fibre links, allowing in that way a succesful and reliable BSM in real-world conditions, leveraging future QR implementations.

Contributions - This experiment was conducted in collaboration with Raju Valivarthi, Gabriel H. Aguilar, and Qiang Zhou. The single photon detectors were designed, built and tested by Francesco Marsili, Matthew D. Shaw, Varun B. Verma and Sae Woo Nam. The experiment was co-supervised by Daniel Oblak and Wolfgang Tittel. I specifically contributed to the conception of the experiment, to the design, development and setup of the experiment as well as to data taking and analysis of the measurement results

and manuscript writing. In conjunction with the other co-authors I contributed to all the editing steps until publication.

Quantum teleportation across a metropolitan fibre network

Nature Photonics, 10, 676680

19 September 2016

R. Valivarthi[1†], M. Grimau Puigibert[1†], Q. Zhou[1†], G. H. Aguilar[1†], V. B. Verma[2], F. Marsili[3], M. D. Shaw[3], S. W. Nam[2], D. Oblak[1] and W. Tittel[1]

[1]*Institute for Quantum Science and Technology, and Department of Physics and Astronomy, University of Calgary, 2500 University Drive NW, Calgary, Alberta T2N 1N4, Canada*

[2]*National Institute of Standards and Technology, Boulder, Colorado 80305, USA*

[3]*Jet Propulsion Laboratory, California Institute of Technology, 4800 Oak Grove Drive, Pasadena, California 91109, USA*

†: *these authors contributed equally to this work*

Abstract

If a photon interacts with a member of an entangled photon pair via a Bell-state measurement (BSM), its state is teleported over principally arbitrary distances onto the pair's second member [1]. Since 1997, this puzzling prediction of quantum mechanics has been demonstrated many times [2]; however, with two exceptions [3, 4], only the photon that received the teleported state, if any, travelled far while the photons partaking in the BSM were always measured closely to where they were created. Here, using the Calgary fibre network, we report quantum teleportation from a telecom-photon at 1532 nm wavelength, interacting with another telecom-photon after both have travelled several kilometres and over a combined bee-line distance of 8.2 km, onto a photon at 795 nm wavelength. This improves the distance over which teleportation takes place to 6.2 km. Our demonstration establishes an important requirement for quantum repeater-based communications [5] and constitutes a milestone towards a global quantum internet [6].

6.3.1 Introduction

While the possibility to teleport quantum states, including the teleportation of entangled states, has been verified many times using different physical systems (see Ref. [2] for a recent review), the maximum distance over which teleportation is possible — which we define to be the spatial separation between the BSM and the photon, at the time of this measurement, that receives the teleported state — has so far received virtually no experimental attention. (See the Supplementary Information for a motivation of this arguably most natural definition and for a description of various experiments in its light). To date, only two experiments have been conducted in a setting that resulted in a teleportation distance that exceeds the laboratory scale [4, 3], even if in a few demon-

strations the bee-line distance travelled by the photon that receives the teleported state has been much longer [8, 7].

The reason to stress the importance of distances is linked to the ability of exploiting teleportation in various quantum information applications. One important example is the task of extending quantum communication distances using quantum repeaters [5], most of which rely on the creation of light-matter entanglement, e.g. by creating an entangled two-photon state out of which one photon is absorbed by a quantum memory for light [9], and entanglement swapping [10]. The latter shares the Bell state measurement (BSM) with standard teleportation; however, the photon carrying the state to be teleported is itself a member of an entangled pair. Entanglement swapping is therefore sometimes referred-to as teleportation of entanglement. To be useful in such a repeater, two entangled photon pairs must be created far apart, and the BSM, which heralds the existence of the two partaking photons and hence of the remaining members of the two pairs, should, for optimal performance, take place approximately halfway in-between these two locations.

Yet, due to the difficulty to guarantee indistinguishability of the two interacting photons after their transmission through long and noisy quantum channels [11], entanglement swapping or standard teleportation in the important midpoint configuration has only been reported very recently outside the laboratory [4]. This work exploited the heralding nature of the BSM for the first loophole-free violation of a Bell inequality — a landmark result that exemplifies the importance of this configuration. However, the two photons featured a wavelength of about 637 nm, which, due to high loss during transmission through optical fibre, makes it impossible to extend the transmission distance to tens, let alone hundreds, of kilometers. In all other demonstrations, either the travel distances of the two photons were small, or they were artificially increased using fibre on spool [3, 12, 13, 38, 39], effectively increasing travel time and transmission loss — and

hence decreasing communication rates — rather than real separation. Here we report the first demonstration of quantum teleportation over several kilometers in the mid-point configuration and with photons at telecommunication wavelength.

6.3.2 Measurement and results

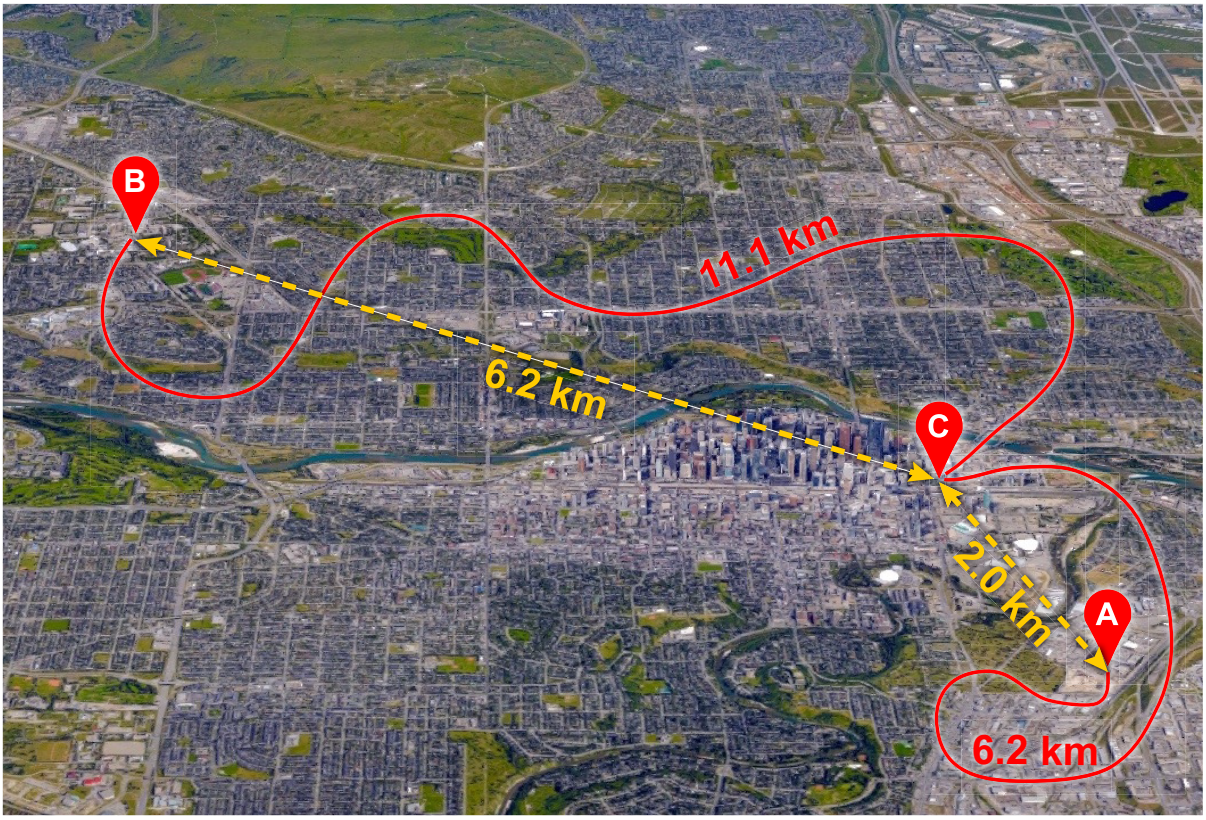

Figure 6.7: **Aerial view of Calgary.** Alice 'A' is located in Manchester, Bob 'B' at the University of Calgary, and Charlie 'C' in a building next to City Hall in Calgary downtown. The teleportation distance — in our case the distance between Charlie and Bob — is 6.2 km. All fibres belong to the Calgary telecommunication network but, during the experiment, they only carry signals created by Alice, Bob or Charlie and were otherwise "dark".

An aerial map of Calgary, identifying the locations of Alice, Bob and Charlie, is shown in Fig. 6.7, and Fig. 6.8 depicts the schematics of our experimental setup. Alice, located in Manchester (a Calgary neighbourhood), prepares phase-randomized attenuated laser

pulses at 1532 nm wavelength with different mean photon numbers $\mu_{\mathrm{A}} \ll 1$ in various time-bin qubit states $|\psi\rangle_A = \alpha|e\rangle + \beta e^{i\phi}|\ell\rangle$, where $|e\rangle$ and $|\ell\rangle$ denote early and late temporal modes, respectively, ϕ is a phase-factor, and α and β are real numbers that satisfy $\alpha^2 + \beta^2 = 1$. Using 6.2 km of deployed fibre, she sends her qubits to Charlie, who is located 2.0 km away in a building next to Calgary City Hall. Bob, located at the University of Calgary (UofC) 6.2 km from Charlie, creates pairs of photons — one at 1532 nm and one at 795 nm — in the maximally time-bin entangled state $|\phi^+\rangle = 2^{-1/2}(|e,e\rangle + |\ell,\ell\rangle)$. He sends the telecommunication-wavelength photons through 11.1 km of deployed fibre to Charlie, where they are probabilistically projected jointly with the photons from Alice onto the maximally entangled state $|\psi^-\rangle = 2^{-1/2}(|e,\ell\rangle - |\ell,e\rangle)$. As we show in the Supplementary Information, this leads to the 795 nm wavelength photon at Bob acquiring the state $|\psi\rangle_B = \sigma_y|\psi\rangle_A$, where σ_y is the Pauli operator describing a bit-flip combined with a phase-flip. In other words, Charlie's measurement results in the teleportation of Alice's photon's state, modulo a unitary transformation, over 6.2 km distance onto Bob's 795 nm wavelength photon.

To confirm successful quantum teleportation, Bob then performs a variety of projective measurements on this photon, whose outcomes, conditioned on a successful BSM at Charlie, are analyzed using different approaches (see the Methods section for more information on how data is taken). We point out that the 795 nm wavelength photons are measured prior to the BSM, thus realizing a scenario where teleportation is achieved *a posteriori* [16, 17].

The main difficulty in long-distance quantum teleportation is to ensure the required indistinguishability (in spectral, temporal, spatial, and polarization degrees of freedom) between the two photons subjected to the BSM at Charlie (which, in our case, are only 70 ps long) despite them being created by independent sources and having travelled over several kilometres of deployed fibre. As we show in Fig. 6.9, varying environmental

conditions during the measurements significantly impact the polarization and arrival times of the photons. Thus, quantum teleportation is only possible with active and automated stabilization of the polarization and of the path-length difference. For the former we employ a polarization tracker and for the latter we use a novel approach based on Hong-Ou-Mandel quantum interference (see the Methods and Supplementary Information for details).

To verify successful teleportation, first, Alice creates photons in an equal superposition of $|e\rangle$ and $|\ell\rangle$ with a fixed phase, and Bob makes projection measurements onto states described by such superpositions with various phases. Conditioned on a successful BSM at Charlie's, we find sinusoidally varying triple-coincidence count rates with a visibility of $(38 \pm 4)\%$ and an average of 17.0 counts per minute. This result alone already represents a strong indication of quantum teleportation: assuming that the teleported state is a statistical mixture of a pure state and white noise, the visibility consistent with the best classical strategy and assuming Alice creates single photons is 1/3 [48]. However, here we use this result merely to establish absolute phase references for Alice's and Bob's interferometers (see the Supplementary Information).

Being able to control the absolute phase values, we can now create photons in, and project them onto, well defined states, e.g. $|e\rangle$, $|\ell\rangle$, $|\pm\rangle \equiv 2^{-1/2}(|e\rangle \pm |\ell\rangle)$, and $|\pm i\rangle \equiv 2^{-1/2}(|e\rangle \pm i|\ell\rangle)$. This allows us to reconstruct the density matrices ρ_{out} of various quantum states after teleportation, and, in turn, calculate the fidelities $F = {}_{\text{B}}\langle\psi|\rho_{\text{out}}|\psi\rangle_{\text{B}}$ with the expected states $|\psi\rangle_{\text{B}}$. The results, depicted in Figs. 6.10 and 6.11, show that the fidelity for all four prepared states exceeds the maximum classical value of 2/3 [48]. In particular, the average fidelity $\langle F\rangle = [F_e + F_l + 2(F_+ + F_{+i})]/6 = (78 \pm 1)\%$ violates this threshold by 12 standard deviations.

One may conclude that this result shows the quantum nature of the disembodied state transfer between Charlie and Bob. However, strictly speaking, the 2/3 bound only

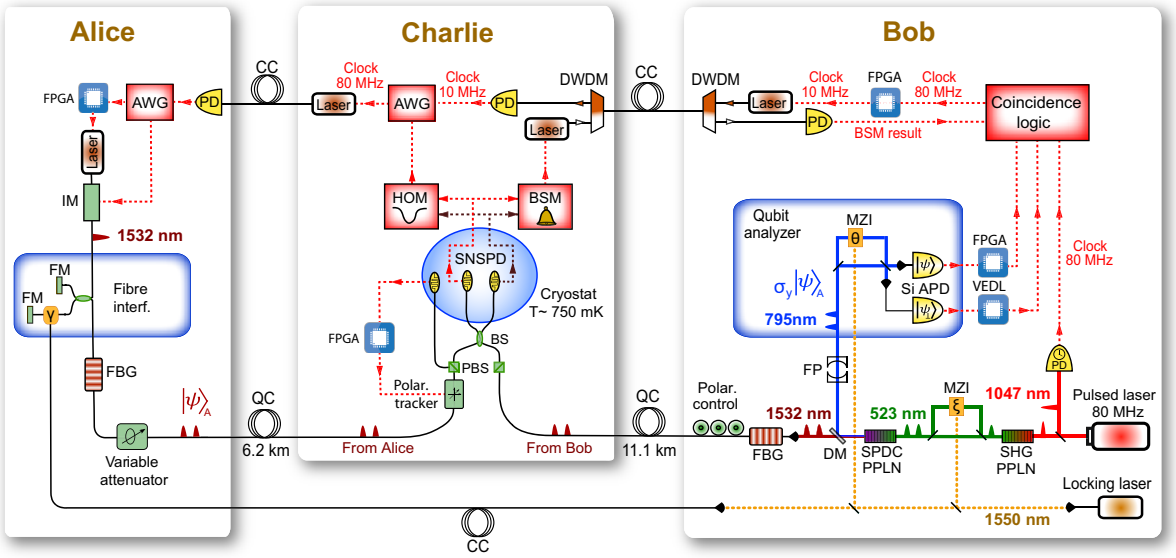

Figure 6.8: **Schematics of the experimental setup. a,** Alice's setup: An intensity modulator (IM) tailors 20 ps-long pulses of light at an 80 MHz rate out of 10 ns-long, phase randomized laser pulses at 1532 nm wavelength. Subsequently, a widely unbalanced fibre interferometer with Faraday mirrors (FM), active phase control (see the Methods sections) and path-length difference equivalent to 1.4 ns travel time difference creates pulses in two temporal modes or bins. Following their spectral narrowing by means of a 6 GHz wide fibre Bragg grating (FBG) and attenuation to the single-photon level the time-bin qubits are sent to Charlie via a deployed fibre — referred to as a quantum channel (QC) — featuring 6 dB loss. **b**, Bob's setup: Laser pulses at 1047 nm wavelength and 6 ps duration from a mode-locked laser are frequency doubled (SHG) in a periodically poled lithium-niobate (PPLN) crystal and passed through an actively phase–controlled Mach-Zehnder interferometer (MZI) that introduces the same 1.4 ns delay as between Alice's time-bin qubits. Spontaneous parametric down-conversion (SPDC) in another PPLN crystal and pump rejection using an interference filter (not shown) results in the creation of time-bin entangled photon-pairs [21] at 795 and 1532 nm wavelength with mean probability μ_{SPDC} up to 0.06. The 795 nm and 1532 nm (telecommunication-wavelength) photons are separated using a dichroic mirror (DM), and subsequently filtered to 6 GHz by a Fabry-Perot (FP) cavity and an FBG, respectively. The telecom photons are sent through deployed fibre featuring 5.7 dB loss to Charlie, and the state of the 795 nm wavelength photons is analyzed using another interferometer — again introducing a phase-controlled travel-time difference of 1.4 ns — and two single photon detectors based on Silicon avalanche photodiodes (Si-APD) with 65% detection efficiency. **c,** Charlie's setup: A beamsplitter (BS) and two WSi superconducting nanowire single photon detectors [22] (SNSPD), cooled to 750 mK in a closed-cycle cryostat and with 70% system detection efficiency, allow the projection of bi-photon states — one from Alice and one from Bob — onto the $|\psi^-\rangle$ Bell state. To ensure indistinguishability of the two photons at the BSM, we actively stabilize the photon arrival times and polarization, the latter involving a polarization tracker and polarizing beamsplitters (PBS), as explained in the Methods. Various synchronization tasks are performed through deployed fibres, referred to as classical channels CC, and aided by dense-wavelength division multiplexers (DWDM), photo-diodes (PD), arbitrary waveform generators (AWG), and field-programmable gate-arrays (FPGA), with details in the Methods.

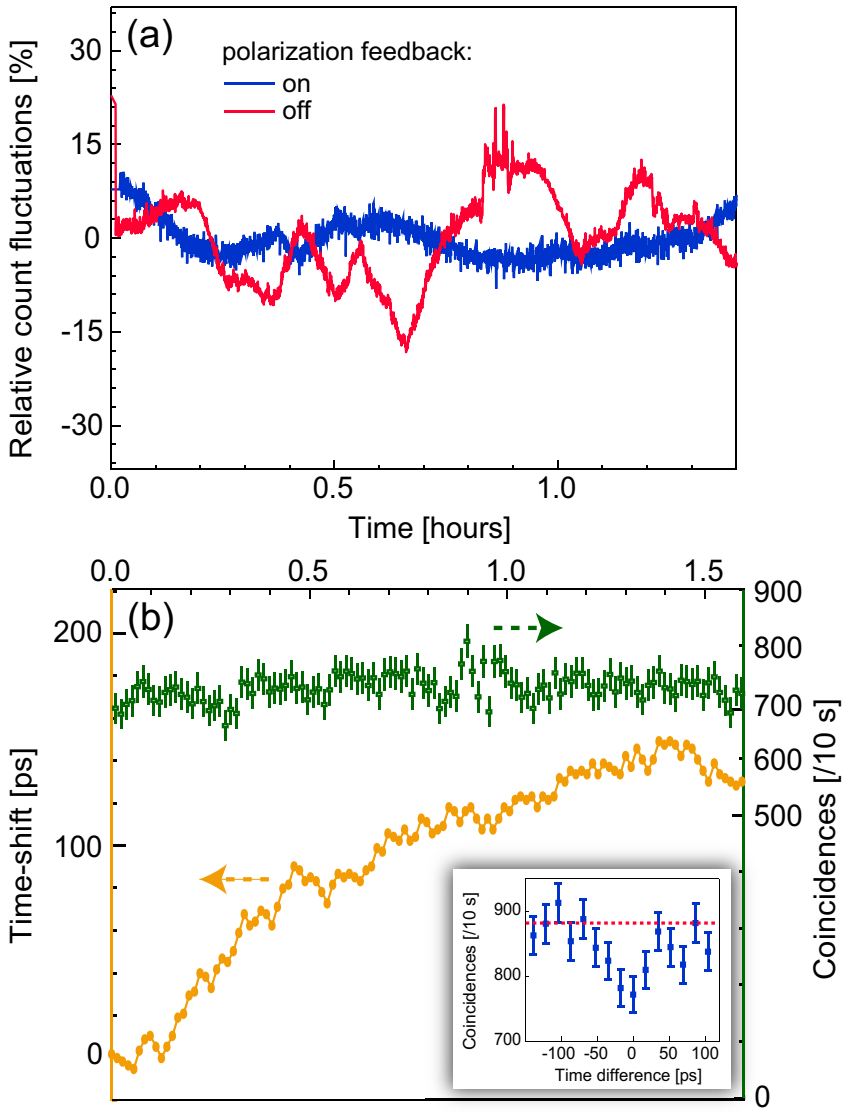

Figure 6.9: **Indistinguishability of photons at Charlie. a**, Fluctuations of the count rate of a single SNSPD at the output of Charlie's BS with and without polarization feedback **b**, Inset: rate of coincidences between counts from SNSPDs as a function or arrival time difference, displaying a Hong-Ou-Mandel (HOM) dip [43] when photon-arrival times at the BS are equal. Orange filled circles: The change in the generation time of Alice's qubits that is applied to ensure they arrive at Charlie's BSM at the same time as Bob. Green empty squares: Coincidence counts per 10 s with timing feedback engaged, showing locking to the minimum of the HOM dip (see Methods and Supplementary Information for details). All error bars (one standard deviation) are calculated assuming Poissonian detection statistics.

applies to Alice's state being encoded into a single photon, while our demonstration, as others before, relied on attenuated laser pulses. To extract the appropriate experimental value, we therefore take advantage of the so-called decoy-state method, which was developed for quantum key distribution (QKD) to assess an upper bound on the error rate introduced by an eavesdropper on single photons emitted by Alice [46, 20]. Here, we rather use it to characterize how a quantum channel — in our case the concatenation of the direct transmission from Alice to Charlie and the teleportation from Charlie to Bob — impacts on the teleportation fidelity of quantum states encoded into individual photons [36]. Towards this end, we vary the mean number of photons per qubit emitted at Alice between three optimized values, $\mu_{\mathrm{A}} \in \{0, 0.014, 0.028\}$, and measure error rates and transmission probabilities for each value independently (see the Supplementary Information for details of how to extract the single-photon fidelity from these measurements). The results, also depicted in Fig. 6.11, show again that the fidelities for all tested states exceed the maximum value of 2/3 achievable in classical teleportation. We note the good agreement between the measured values and those predicted by our model (described in the Supplementary Information), which takes into account various, independently characterized system imperfections (no fit). This allows us to identify that deviations of the measured fidelities from unity — i.e. from ideal teleportation — are mostly due to remaining distinguishability of the two photons subjected to the BSM at Charlie, followed by multi-pair emissions by the pair-source. Finally, by averaging the single-photon fidelities over all input states, weighted as above, we find $\langle F^{(1)} \rangle \geq (80 \pm 2)\%$ — as before significantly violating the threshold between classical and quantum teleportation.

6.3.3 Discussion and conclusions

Our measurements establish the possibility for quantum teleportation over many kilo-

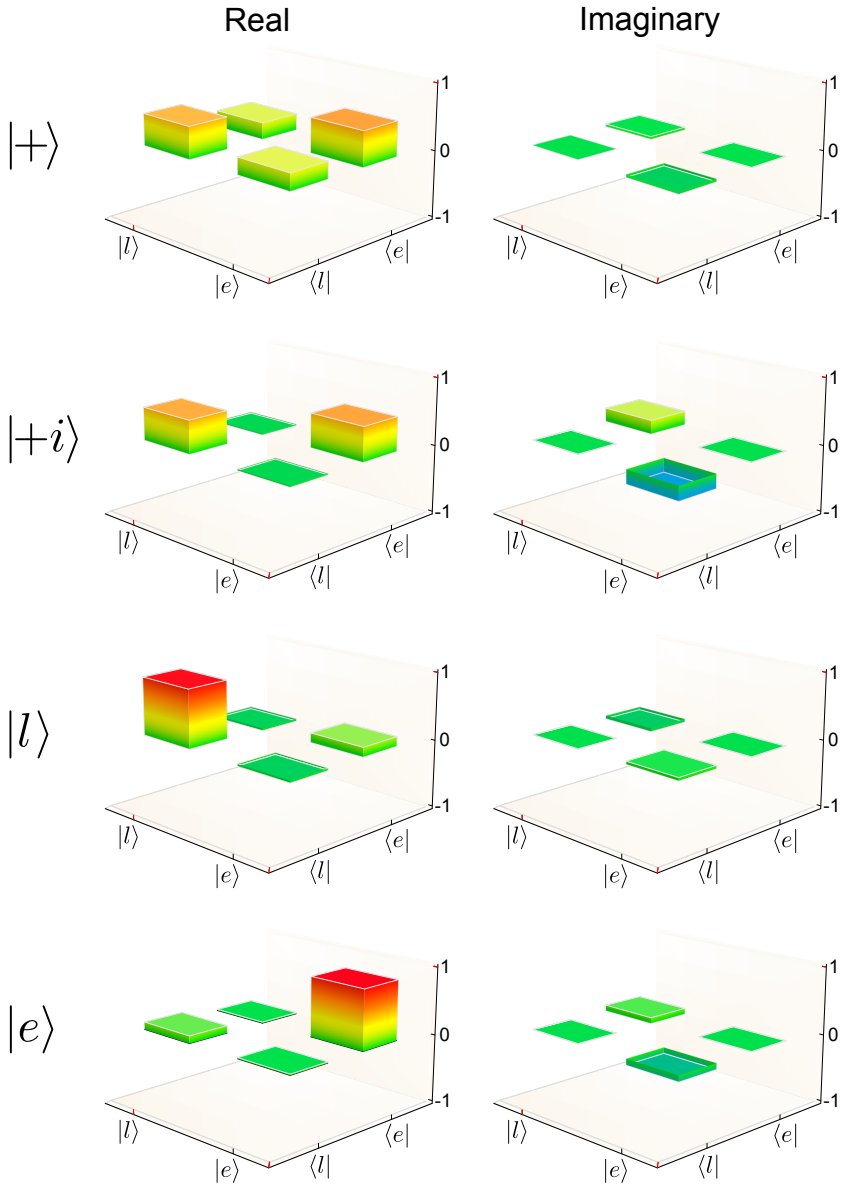

Figure 6.10: **Density matrices of four states after teleportation.** Shown are the real and imaginary parts of the reconstructed density matrices for four different input states created at Alice. The mean photon number per qubit is $\mu_{\mathrm{A}} = 0.014$, and the mean photon pair number is $\mu_{\mathrm{SPDC}} = 0.045$. The state labels denote the states expected after teleportation.

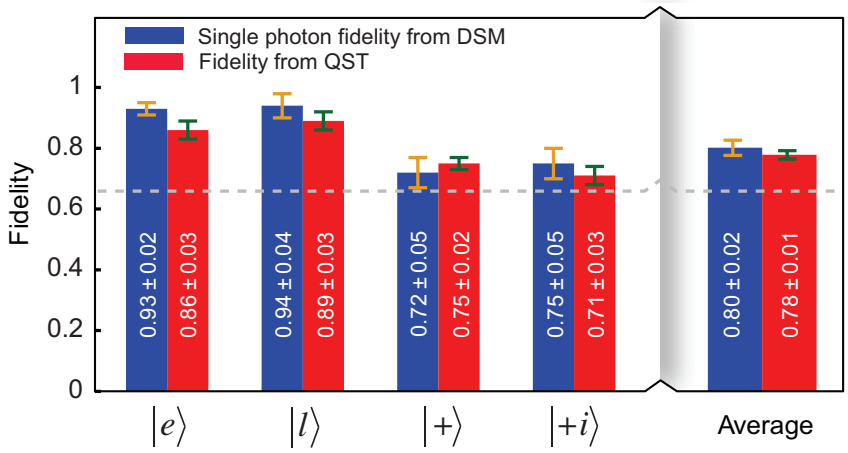

Figure 6.11: Individual and average fidelities of four teleported states with expected (ideal) states, measured using quantum state tomography (QST) and the decoy-state method (DSM). For the DSM we set $\mu_{\mathrm{SPDC}} = 0.06$. Error bars (one standard deviation) are calculated assuming Poissonian detection statistics and using Monte-Carlo simulation. Count rates for both methods are provided in the Supplementary Information. The somewhat larger degradation of $|+\rangle$ and $|+i\rangle$ states is due to the limited quality of the BSM (see Supplementary Information) and imperfect interferometers. Neither cause an effect for $|e\rangle$ and $|l\rangle$ states.

metres in the important mid-point configuration — as is required for extending the distance of quantum communications using quantum repeaters. We emphasize that both photons travelling to Charlie are at telecommunication wavelength, making it possible to extend the Alice-Bob distance from its current value of 8 kilometres by at least one order of magnitude. This corresponds to the distance of an elementary link, which includes teleportation of entanglement, at which communication links based on spectrally multiplexed quantum repeaters start to outperform direct qubit transmission [36, 25].

We also note that the 795 nm photon, both in terms of central wavelength as well as spectral width, is compatible with quantum memory for light — a key element of a quantum repeater — in cryogenically-cooled thulium-doped crystals [26]. This, in conjunction with projection onto two Bell states [27], would allow us to implement active feed-forward on the teleported photon. An interesting question is if our implementation

- in particular the laser used to stabilize the phase in Alices and Bobs interferometers - opens side channels for eavesdropping. While this topic is beyond the scope of our investigation, we emphasize that lasers with sufficient stability to allow for local (independent) stabilization are available [28].

Finally, we point out that quantum teleportation involves the interesting aspect of Alice transferring her quantum state in a disembodied fashion to Bob without him ever receiving any physical particle. In other words, Bob is only sending photons (all of them members of an entangled pair) and thus better able to protect his system from any outside interference, e.g. from an adversary [29].

We note that, a related experimental demonstration has been reported in a concurrent manuscript [30].

Acknowledgments

The authors thank Tyler Andruschak and Harpreet Dhillon from the City of Calgary for providing access to the fibre network and for help during the experiment, Vladimir Kiselyov for technical support, and Pascal Lefebvre for help with aligning the entangled photon pair source. This work was funded through Alberta Innovates Technology Futures (AITF), the National Science and Engineering Research Council of Canada (NSERC), and the Defense Advanced Research Projects Agency (DARPA) Quiness program (contract no. W31P4Q-13-l-0004). WT furthermore acknowledges funding as a Senior Fellow of the Canadian Institute for Advanced Research (CIFAR), and VBV and SWN acknowledge partial funding for detector development from the Defense Advanced Research Projects Agency (DARPA) Information in a Photon (InPho) program. Part of the detector research was carried out at the Jet Propulsion Laboratory, California Institute of Technology, under a contract with the National Aeronautics and Space Administration.

Author contributions

The SNSPDs were fabricated and tested by VBV, FM, MDS, and SWN. The experiment was conceived and guided by WT. The setup was developed, measurements were performed and the data analyzed by RV, MGP, QZ, GHA, and DO. The manuscript was written by WT, RV, MGP, QZ, GHA, and DO.

Additional information

Supplementary information is available in the online version of the paper. * Correspondence and requests for materials should be addressed to W. Tittel (email: wtittel@ucalgary.ca).

Competing finantial interests

The authors declare no competing financial interests.

6.3.4 Methods

Synchronization

For the following discussion, please refer to experimental setup outlined in Fig. 6.8. Charlie is connected via pairs of optical fibres both to Alice and to Bob. In each pair, one fibre — referred to as the quantum channel (QC) — carries single photons, while the other — referred to as the classical channel (CC) — distributes various strong optical signals whose purpose will be described in the following. In addition, Alice and Bob are directly connected via an optical fibre that transmits narrow-line-width laser light at 1550 nm in order to lock the phases of all interferometers , i.e. γ, ξ and θ shown in Fig. 6.8. This is crucial for maintaining a common phase reference for the qubit states generated at Alice and Bob, and analyzed at Bob. In each interferometer, the power

of the locking laser in one output arm (measured on a classical detector) is used to derive a feedback signal to a piezo-element that regulates the path-length difference of the interferometer to maintain a fixed phase. For instance, for free-space-optics-based interferometers at Bob, the path-length difference is changed by moving a mirror with the piezo stack, while for the fibre-optics interferometer at Alice, the path-length is adjusted by stretching a fibre wrapped around a piezo-tube. Additionally, all interferometers are kept in temperature-controlled boxes.

The master clock for all devices is derived from detection of the mode-locked laser pulses (80 MHz) and converted back into an optical signal for distribution through the CC via Charlie to Alice.

Stabilization to ensure photon indistinguishability

For a successful BSM, the photons arriving at Charlie from Alice and Bob need to be indistinguishable despite being generated by independent and different sources, and having travelled through several kilometres of deployed fibre. The spatial indistinguishability is naturally ensured by the propagation in single-mode optical fibres. To ensure that the photons have the same spectral profile, they are sent through separate, temperature-stabilized fibre Bragg gratings (FBG) that narrow their spectra to 6 GHz. The spectral overlap of the FBGs at Alice and Bob needs to be set only once. However, due to temperature-dependent properties of fibre such as birefringence and length, the polarization and arrival time of the photons change with external environmental conditions, making it difficult to implement the BSM in a real-world environment. Towards this end, we apply feedback mechanisms to compensate for drifts in polarization and arrival time.

Timing

The short duration of our photons (70 ps) prevents us from using the SNSPDs (featuring a time jitter of ∼150 ps) to directly determine their arrival times with the required precision to adjust the difference to zero. Instead, we compensate for arrival-time drifts with the novel approach of observing the degree of quantum-interference (Hong-Ou-Mandel or HOM effect [43]) of the photons. The signals from the two SNSPDs (which are used to perform the BSM) are also sent to a HOM analyzing unit (see Fig. 6.8) that monitors the number of coincidences between detections corresponding to either both photons arriving in an early time bin mode, or both in a late bin. As shown in the inset of Fig. 6.9b, the HOM interference causes photon bunching and thus the coincidences to be reduced when the photons arrive at the beam splitter at the same time. Hence, to counteract the drift in travel time of the photons, we vary the qubit generation time at Alice with a precision of about ∼4 ps to keep the coincidence count rate at the minimum value of around 750 per 10 sec., as shown in Fig. 6.9b. In practice Alice's time-shift is triggered at Charlie by shifting the phase of the master clock signal that he forwards to Alice. Fig. 6.9b, shows that, during a typical 1.5 hour measurement, we apply a time shift of ∼200 ps to compensate drifts in timing. Since the shift is larger than the duration of the photons, the teleportation protocol would fail without the active stabilization.

Polarization

Because photons from Alice and Bob pass through polarizing beam-splitters (PBS) at Charlie, their polarization indistinguishability is naturally satisfied. However, correct photon polarizations must be set and maintained to maximize the transmission through the PBSs, or else the channel loss will vary over time. In our system, the QC between Bob and Charlie experiences only a slow drift, which allows for manual compensation

using a polarization controller — located at Bob — once a day. However, an automated polarization feedback system is required for the channel between Alice and Charlie, which drifts significantly on the time-scale of the experiment. To that end, we monitor the count rate of an additional SNSPD, located in the reflection port of the PBS at Charlie, with a field-programmable gate-array (FPGA) so as to generate a feedback signal that minimizes the rate by adjusting the polarization by means of a polarization tracker (also located at Charlie). As seen in Fig. 6.9, the intensity fluctuations in 1.5 hours (a typical time scale to acquire results for one qubit setting) are limited to 5% with feedback, and to about 15% without feedback.

Data collection

Using Alice's qubits and the 1532 nm-members of the entangled pairs, Charlie performs $|\psi^-\rangle$ Bell-state projections. Such a projection occurs when one SNSPD detects a photon arriving in the early time-bin and the other SNSPD records a photon in the late time-bin. Successful Bell-state projection measurements are communicated via the CC and using classical laser pulses to Bob, who converts them back to electrical signals. Each signal is then used to form a triple coincidence with the detection signal of the 795 nm wavelength photon exiting Bob's qubit analyzer. Towards this end, the latter is delayed using a variable electronic delay-line (VEDL) implemented on an FPGA by the time it takes the 1532 nm entangled photon to travel from Bob to Charlie plus the travel time of the BSM signal back to Bob.

6.3.5 Supplementary information

Teleportation protocol

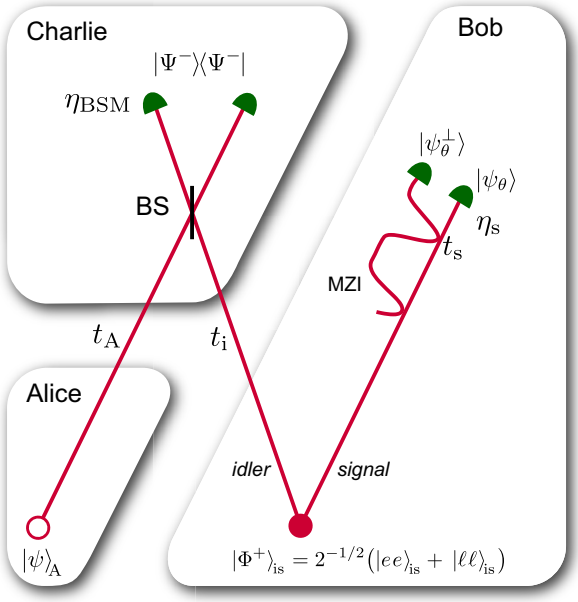

Figure 6.12: Schematics of the teleportation experiment. Alice encodes time-bin qubits $|\psi\rangle_{\mathrm{A}}$ using attenuated laser pulses with mean photon number μ_{A} and sends them to Charlie. Bob prepares photon pairs in the maximally entangled time-bin qubit state $|\Phi^+\rangle_{\mathrm{is}}$ with mean photon number μ_{SPDC} and sends the 'idler' member of each photon pair to Charlie. Charlie interferes the photons he receives from Alice and Bob on a beam-splitter and probabilistically projects them onto the Bell-state $|\Psi^-\rangle_{\mathrm{Ai}}$. This results in Bob's 'signal' photons acquiring the state $|\psi\rangle_{\mathrm{s}} = \sigma_y|\psi\rangle_{\mathrm{A}}$. The 'signal' photons are then sent to a time-bin qubit analyzer which allows projections onto two orthogonal states (here $|\psi_\theta\rangle$ and $|\psi_\theta^\perp\rangle = |\psi_{(\theta+\pi)}\rangle$ where θ is the phase-difference between the two MZI arms). The transmission probabilities of the three channels are labelled as t_{c}, t_{i} and t_{s}, and η_{BSM}, η_{s} are the efficiencies of the employed detectors.

In this section we will briefly outline the steps in our teleportation protocol. In Supplementary Figure 6.12, we show a typical schematic of the teleportation experiment. The quantum teleportation protocol[1] can be described as follows:

1. Bob prepares a maximally time-bin entangled two-photon state $|\Phi^+\rangle_{\mathrm{is}} = 2^{-1/2}(|e,e\rangle_{\mathrm{is}} + |\ell,\ell\rangle_{\mathrm{is}})$, where s and i denote the 'signal' and 'idler' photons from the spontaneous parametric down conversion process (SPDC), and $|e\rangle$ and $|\ell\rangle$ denote early and late temporal modes (or bins), respectively.

2. Alice prepares an arbitrary time-bin qubit encoded into two temporal modes of an attenuated laser pulse. It can be written as $|\psi\rangle_{\mathrm{A}} = \alpha|e\rangle_{\mathrm{A}} + \beta e^{i\phi}|\ell\rangle_{\mathrm{A}}$, where ϕ is the relative phase between the two temporal modes, α and β are real, and $\alpha^2 + \beta^2 = 1$.

3. Charlie receives the 'idler' photon of the entangled pair from Bob, and the photon from Alice. He then probabilistically projects the state of these photons onto one of the four Bell-states (in our experiment $|\Psi^-\rangle_{\mathrm{Ai}}$, defined below). This is known as a Bell state measurement (BSM).

4. Conditioned on the outcome of the BSM, the 'signal' photon that is with Bob acquires the qubit state that Alice prepared her photon in, modulo a known unitary transformation U. Bob can choose to apply the unitary, $U^\dagger$ on the 'signal' photon to recover Alice's original state, or just account for the transformation when analyzing the data of the measurement that this photon was part of.

The mathematical description of the above protocol starts with the three-photon state from Bob and Alice:

$$|\Psi\rangle_{\mathrm{Ais}} = |\psi\rangle_{\mathrm{A}} \otimes |\Phi^+\rangle_{\mathrm{is}}. \tag{6.10}$$

Rewriting this state in terms of the four maximally entangled Bell-states of Alice's and the 'idler' photon, defined as $|\Phi^\pm\rangle_{\mathrm{Ai}} = 2^{-1/2}(|e,e\rangle_{\mathrm{Ai}} \pm |\ell,\ell\rangle_{\mathrm{Ai}})$ and $|\Psi^\pm\rangle_{\mathrm{Ai}} = 2^{-1/2}(|e,\ell\rangle_{\mathrm{Ai}} \pm |\ell,e\rangle_{\mathrm{Ai}})$, we obtain

$$\begin{aligned} |\Psi\rangle_{\mathrm{Ais}} = \frac{1}{2}\Big[& |\Phi^+\rangle_{\mathrm{Ai}} \left(\alpha|e\rangle_{\mathrm{s}} + e^{i\phi}\beta|\ell\rangle_{\mathrm{s}}\right) \\ & + |\Phi^-\rangle_{\mathrm{Ai}} \left(\alpha|e\rangle_{\mathrm{s}} - e^{i\phi}\beta|\ell\rangle_{\mathrm{s}}\right) \\ & + |\Psi^+\rangle_{\mathrm{Ai}} \left(e^{i\phi}\beta|e\rangle_{\mathrm{s}} + \alpha|\ell\rangle_{\mathrm{s}}\right) \\ & + |\Psi^-\rangle_{\mathrm{Ai}} \left(e^{i\phi}\beta|e\rangle_{\mathrm{s}} - \alpha|\ell\rangle_{\mathrm{s}}\right) \Big]. \end{aligned} \tag{6.11}$$

Since each term is equally weighted, the probability of projecting onto any of the Bell-states is 1/4. In our setup we only project onto $|\Psi^-\rangle_{\mathrm{Ai}}$, in which case we keep only the last term and, hence, the qubit state of the 'signal' photon reduces to

$$|\psi\rangle_{\mathrm{s}} = e^{i\phi}\beta|e\rangle_{\mathrm{s}} - \alpha|\ell\rangle_{\mathrm{s}}. \tag{6.12}$$

It can be seen that the unitary operator to be applied to $|\psi\rangle_{\mathrm{s}}$ in order to recover Alice's qubit is the Pauli operator σ_y — corresponding to a bit flip combined with a phase flip. That is

$$|\psi\rangle_{\mathrm{A}} = \sigma_y|\psi\rangle_{\mathrm{s}}. \tag{6.13}$$

Teleportation distance

In this section, first, we discuss the differences between what we call the teleportation distance and the total distance over which the quantum state travels, which we will refer to as the state-transfer distance, and relate these two distances to long distance quantum communications using quantum repeaters (QR). In particular, we describe a few important examples of teleportation experiments and identify their teleportation distance and state-transfer distances as well as the technology platform (fibre or free-space). With an eye on the practical application of the realizations, we refer to distances measured in bee-line throughout this section

The teleportation distance, as defined in the main text, is the spatial separation, at the time of the BSM, between the BSM and the photon that receives the teleported state. To motivate this definition, we first note that after the measurement of one member of an entangled pair, quantum information is transmitted quasi-instantaneously onto the second member, as was shown by the Geneva group [31] and USTC in Hefei [32]. Applied to quantum teleportation this means that at the exact time at which the BSM is

performed the quantum state of Alice's photon is, almost instantaneously and without exchange of any physical entity, transferred to the other member of the entangled pair (modulo a unitary operation). For example, in the experiment categorized in Supplementary Figure 6.13c), the teleportation distance would be of only a few meters. The total distance of the state-transfer, in contrast, corresponds to the spatial separation between the initial position of the photon encoding the quantum state at the time it is emitted and the final position of the photon that receives the final state at the time it is measured. In the same example, this distance is between 100 and 150 km [33, 34].

In conjunction with the above-described fundamental aspect of teleportation vs. state-transfer distance, the distinction is also important in light of long distance quantum communication based on quantum repeaters. In this application, a large teleportation distance (as per our definition) is a necessary (yet not sufficient) condition to ensure optimal performance. To elaborate, quantum repeater architectures are based on entanglement swapping (teleportation of entanglement) between an arbitrary long chain of so-called elementary links [35] from Alice to Bob. A successful BSM heralds the entanglement distribution (or swapping) between the end points of an elementary link where photons are stored until the information of the BSM is received. When entanglement has been heralded in two adjacent elementary links, either at different times or in different spectral channels, the photons at the interconnect of the two links are recalled from the quantum memory and entanglement swapping is performed over the combined distance of the two elementary links. The sequence is repeated until Alice and Bob share an entangled state.

It can be shown that the midpoint configuration, in which the BSM station is located at the middle of an elementary link as illustrated in Supplementary Figure 6.13a), is required for optimal performance of a quantum repeater-based communication link – at least if the protocol in Ref. [36] is considered. This configuration minimizes the storage time in

the quantum memories at the end-points of the elementary links. We conjecture that the symmetric setup (mid-point configuration) also optimizes other repeater architectures. Hence, a large teleportation distance is necessary.

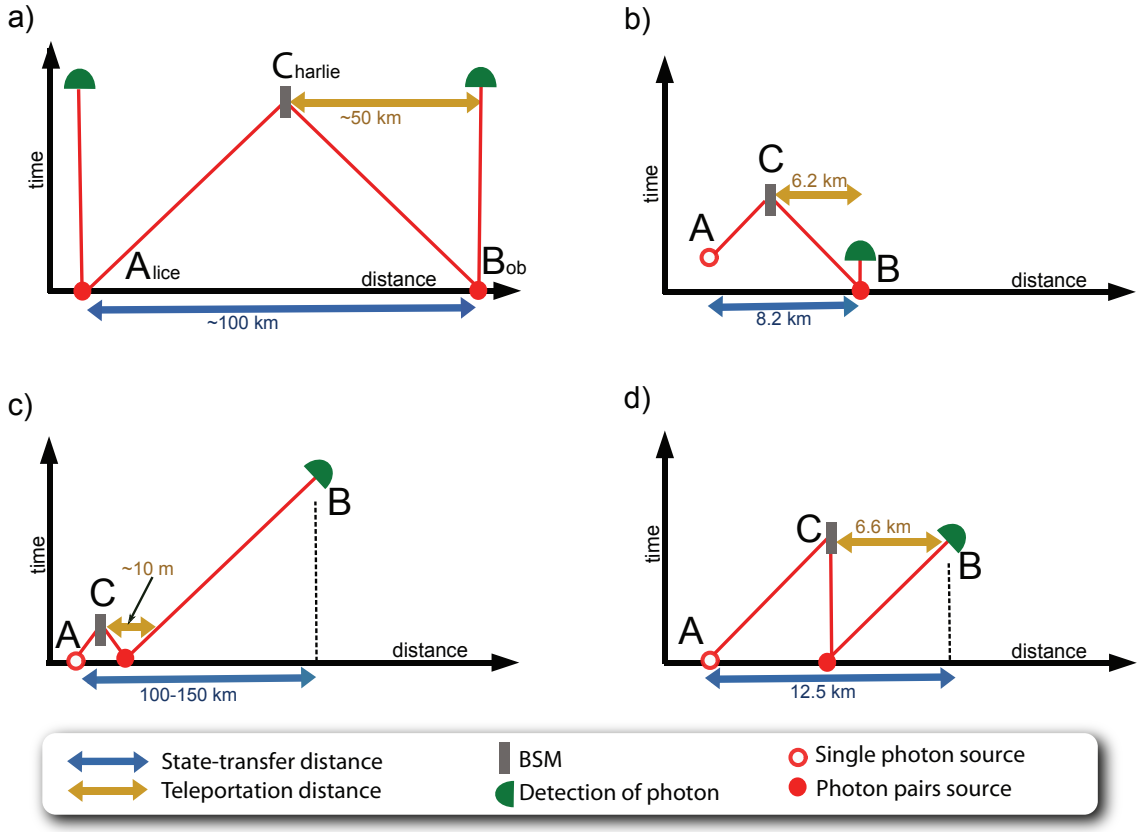

Figure 6.13: **Space-time diagrams teleportation experiments. a)** Elementary link of an optimal quantum repeater [36, 35]. **b)** Our experiment. **c)** Quantum teleportation experiments with large state-transfer distances [33, 34]. **d)** Experiment performed by Hefei group in concurrence with ours [37]. Distances or times in all panels are not to scale (they only indicate general features). For simplicity we assume the speed of light to be in air.

In Supplementary Figure 6.13, we show the space-time diagrams of different experimental implementations of quantum teleportation in which at least one of the photons travels a long distance in bee-line. Supplementary Figure 6.13a) displays the diagram for the optimized elementary link of a quantum repeater based on spectral multiplexing [36]. Pairs of entangled photons are created by the sources at A and B. One of the photons from each pair is stored in a quantum memory, represented by a vertical red line. The other

two photons are sent to C, where a BSM is performed. In the optimized configuration of the quantum repeater, C is at the mid-point of the link between A and B and the teleportation distance is thus half of the total distance. The diagrams in Supplementary Figure 6.13b-d) show the experimental realizations of quantum teleportation over distances that exceed the laboratory scale. The diagram corresponding to our experiment is shown in Supplementary Figure 6.13b): Photons and pairs of entangled photons are created at A and B, respectively. One of the photons of each pair is detected at B while the BSM is performed on the remaining photon of the pair and a photon coming from A. Hence, in our realization the teleportation distance is the distance between C and B (6.2 km in bee-line) and the total distance corresponds to A-B (8.2 km in bee-line). Though still somewhat asymmetric, our experimental setup thus resembles the optimal configuration for a QR. Supplementary Figure 6.13c) shows the diagram corresponding to long state-transfer-distance quantum teleportation experiments over free space and fiber links implemented in the recent years [33, 34]. Single photons and pairs of entangled photons are generated near each other. The BSM is performed in close proximity (we assume a lab-scale of about 10 m at most) while the other photon of each pair is transmitted over a long distance before being detected. Although the total distance over which the quantum state is transferred exceeds 100 km, the teleportation distance is very small and, as a consequence, these experiments are not useful for optimal quantum repeater architectures. In Supplementary Figure 6.13d) we show the diagram for an experiment realized at the same time as ours[37]: Individual photons and pairs of entangled photons are generated at A and C, respectively. The BSM, which is situated at C, is performed on the photons from A after having travelled over 5.9 km in bee-line and one of the photons of the pair, which stayed at C in a optical fibre delay line. The other photon of each pair travels 6.6 km in bee-line before being detected. In this case, the teleportation distance is the distance between C and B (6.6 km in bee-line). While far away from a symmetric

configuration, this experiment nevertheless features a a long teleportation distance. The state-transfer distance is on the order of 12.5 km in bee-line.

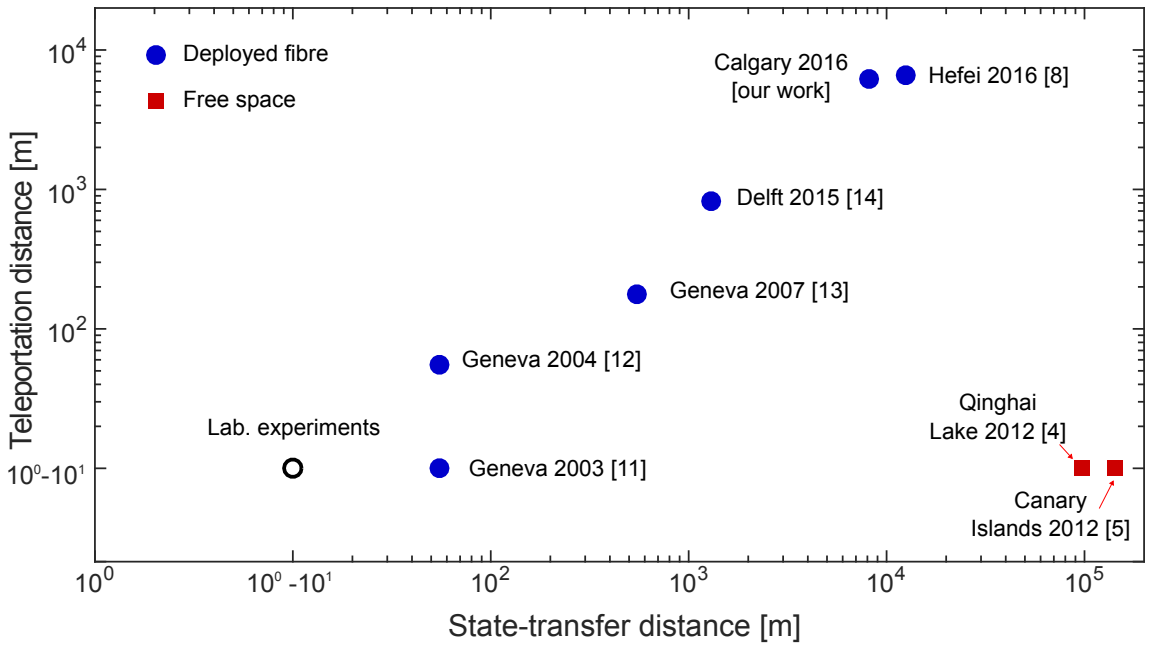

Figure 6.14: **Teleportation distance vs. total quantum state-transfer distance** for different experimental implementations of quantum teleportation (all distances measured in bee-line). Black circles represent all experiments performed within a lab. Blue filled circles correspond to experiments where photons propagated through optical fibers outside a lab (deployed fibre). Red filled squares represent experiments where one photon propagates through a free-space link outside the lab.

To summarize the state-of-the-art in teleportation experiments we plot in Supplementary Figure 6.14 the teleportation and state-transfer distances for different experimental implementations of quantum teleportation (all distances measured in bee-line). We can see that the longest state-transfer distances have been achieved in the demonstrations in which the photon that receives the teleported state traveled over a long distance free space [34, 33], however, the associated teleportation distances were limited to a few meters (i.e. the size of an optical table). As illustrated in Supplementary Figure 6.13c), this is because the BSM was performed in proximity of both the single-photon as well as photon-pair source. A few experiments have been performed using spooled fibre [38, 39].

While being important steps towards the use of deployed fiber, teleportation distances and state-transfer distances were thus limited to a few meters in bee-line.

To conclude, please note that teleportation and state-transfer distances have steadily increased since 1998 from their original values of a few metres up to around 10 and 150 km, respectively. This gives confidence that quantum teleportation will soon meet the requirements to be useful for long distance quantum communication links based on quantum repeaters.

Estimating indistinguishability of photons at Charlie

We use Hong-Ou-Mandel (HOM) quantum interference[43] to estimate the indistinguishability of photons involved in the BSM. The HOM effect is measured by observing the number of coincidence counts between two detectors placed at each output of a beamsplitter (BS) when photons are sent into both inputs of the BS. If indistinguishable single photons are input to the BS, they will always bunch at the outputs of the BS and thus coincidences will never occur. However, if the two single photons are distinguishable, the HOM interference disappears and the photons pick outputs independently, i.e. coincidences occur half of the time. The HOM effect is quantified by the visibility, defined as

$$\mathrm{V_{HOM}} = \frac{C_{\max} - C_{\min}}{C_{\max}}, \tag{6.14}$$

where $C_{\max}$ and $C_{\min}$ are the maximum and minimum coincidence counts per unit of time for the least and most indistinguishable setting achievable in an experiment, respectively. Hence, for perfectly indistinguishable single photons, $\mathrm{V_{HOM}} = 1$. If instead of perfect single photons we input pulses with certain photon number statistics, the bunching is no longer perfect, but is bounded by a value that can be predicted based on the photon number distribution. For example, assuming Poissonian (thermal) distributions at both

BS inputs, the visibility is bounded by $V_{HOM} = 1/2$ (1/3). Regardless the photon-number distributions we have at the inputs, we can thus gauge the degree of indistinguishability of the photons by measuring how close the visibility is to the expected bound. In our case, we have a coherent state (with Poissonian-distributed photons) from Alice and a thermal state from Bob at the inputs of Charlie's BS. To model the behaviour of V_{HOM}, we follow a similar approach as in Ref. [44]. We find that the maximum HOM visibility in our situation depends on the mean photon number μ_A of Alice's attenuated laser pulses, and the mean pair number μ_{SPDC} of Bob's entangled pairs.

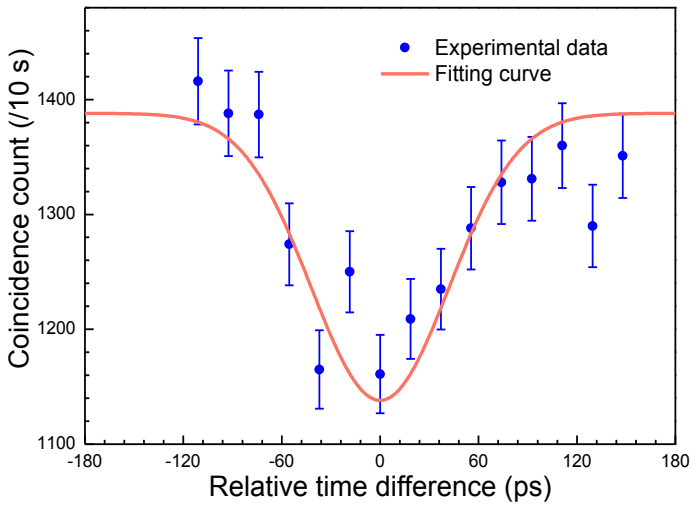

Figure 6.15: A typical HOM dip in the two-fold coincidences observed in our experiment with $\mu_A = 0.0027$ and $\mu_{SPDC} = 0.03$. From the fit, we estimate the duration of the photons to be 70 ps, which is determined by the filtering bandwidth of 6 GHz.

As shown in Supplementary Figure 6.15, we gradually change the indistinguishability of the photons by changing their relative arrival time at the BS, thereby observing a HOM dip with visibility $V_{HOM} = 0.20$. Varying μ_A while keeping μ_{SPDC} constant, we then obtain the values for V_{HOM} shown in Supplementary Figure 6.16. The solid line is a fit of our model to the experimental data. From this fit, we estimate the indistinguishability of photons at Charlie to be $(68 \pm 2)\%$. We note that most of the reduction in the indistinguishability from the ideal value of 1 is due to imperfect spectral overlap as well as timing jitter caused by imperfect synchronization of the sources at Alice and Bob.

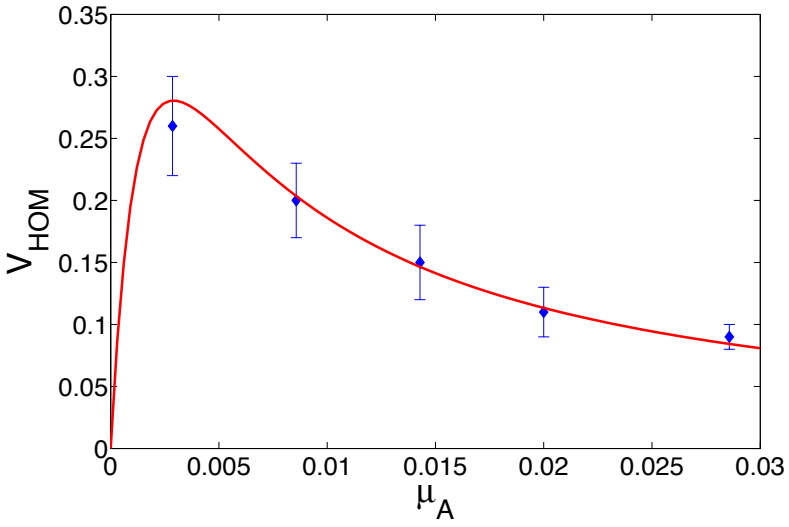

Figure 6.16: Visibility of the HOM dip (V_{HOM}) versus mean photon number of Alice's laser pulses (μ_A). For all the measurements, $\mu_{SPDC} = 0.03$.

Phase calibration of interferometers

In this section, we describe how we establish absolute phase values for the interferometers at Alice and Bob. Following the protocol described in Supplementary Section 6.1, Alice prepares the state $|\psi\rangle_A = 2^{-1/2}(|e\rangle_A + e^{i\phi}|\ell\rangle_A)$, and, according to Eq. (6.12), the state of the 'signal' photon after a successful BSM becomes $|\psi\rangle_s = 2^{-1/2}(|e\rangle_s - e^{-i\phi}|\ell\rangle_s)$ (making use of the fact that $\alpha = \beta = 2^{-1/2}$). The two output ports of Bob's unbalanced Mach Zehnder interferometer (MZI) correspond to projections onto the states $|\psi_\theta\rangle = 2^{-1/2}(|e\rangle + e^{i\theta}|\ell\rangle)$ and $|\psi_\theta^\perp\rangle = 2^{-1/2}(|e\rangle - e^{i\theta}|\ell\rangle)$, respectively. Hence, the probability to find the photon in the first output port is

$$|\langle\psi_\theta|\psi\rangle_s|^2 = \frac{1}{2}\big(1 + \cos\Delta\phi\big) \ , \tag{6.15}$$

and for the second is:

$$|\langle\psi_\theta^\perp|\psi\rangle_s|^2 = \frac{1}{2}\big(1 - \cos\Delta\phi\big) \ , \tag{6.16}$$

where $\Delta\phi = \phi - \theta$. Thus, we expect the count rates at each output of Bob's MZI to show a sinusoidal dependence on ϕ (the phase of Alice's interferometer) and θ (the phase of

Bob's analyzing interferometer).

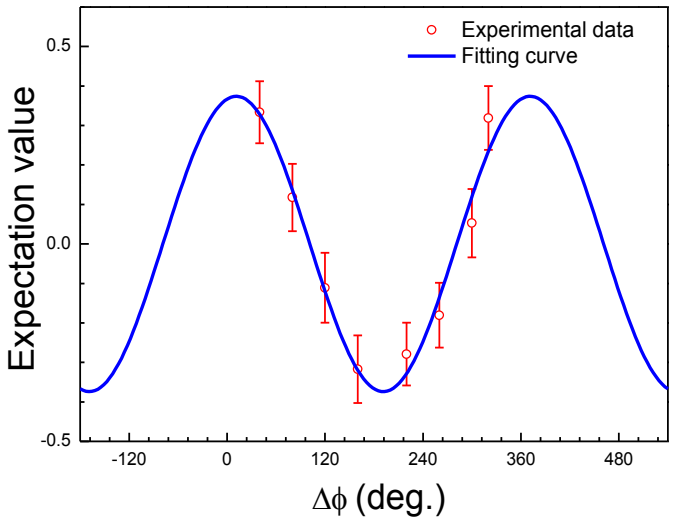

Figure 6.17: Expectation value $\langle E \rangle$ as a function of the phase difference $\Delta\phi$. Circles indicate experimental data and the solid line is a sinusoidal fit. From the fit, we find a fidelity of 0.69 ± 0.02.

Because of experimental imperfections, we do not expect complete constructive and destructive interference in the MZI outputs for $\Delta\phi = \pi$, as predicted by Eqs. (6.15) and (6.16). However, conditioned on a successful BSM, we still expect to observe a sinusoidal dependence of the count rates in both output ports when varying the phase θ of the MZI. To quantify the result, we use the expectation value

$$\langle E \rangle = \frac{C(|\psi_\theta\rangle) - C(|\psi_\theta^\perp\rangle)}{C(|\psi_\theta\rangle) + C(|\psi_\theta^\perp\rangle)}, \tag{6.17}$$

where $C(|\psi_\theta\rangle)$ ($C(|\psi_\theta^\perp\rangle)$) is the number of coincidences per unit of time in one or the other output with Bob's interferometer set to a phase θ. In the Supplementary Figure 6.17 we show the expectation value $\langle E \rangle$ as a function of the phase difference $\Delta\phi$. When it reaches the maximum, we define the qubit prepared at Alice to be $|+\rangle$, and the two output ports of the MZI to correspond to projections onto $|+\rangle$ and $|-\rangle$, respectively. Recall that the entangled state prepared at Bob is $|\Phi^+\rangle_{\rm is} = 2^{-1/2}(|e,e\rangle_{\rm is} + |\ell,\ell\rangle_{\rm is})$.

An additional result of this measurement is the fidelity of teleportation, which can be extracted directly from the curve as $F = [1 + max(\langle E \rangle)]/2$. From a sinusoidal fit, we obtain $F = 0.69 \pm 0.02$.

Predicting fidelities

In this section, we develop a simple model that aids our understanding of the main limiting factors in our experiment. Our model, which is inspired by that in Ref. [38], allows us to predict the measured fidelity of the teleported state conditioned on a successful BSM projection (3-fold photon coincidence detection). The model takes into account the different photon number statistics of our sources (Poissonian for Alice and thermal for Bob), the degree of indistinguishability of the photons partaking in the BSM and the total transmissions as well as the detector efficiencies.

As described in the previous section, we can set the phase θ of Bob's MZI qubit-analyzer such that for a perfect teleported state, we would observe detection events in only one of his detectors, say in the port labelled $|\psi_\theta\rangle$ (see Supplementary Figure 6.12). Any detections in the other output port $|\psi_\theta^\perp\rangle$ would thus stem from a deviation of the actually teleported state $|\psi\rangle_{\rm s}$ from the ideal one. Such deviation may be caused by imperfections of either the initial state $|\psi\rangle_{\rm A}$, or of the implementation of the teleportation protocol. The fidelity of the teleported state can be estimated by measuring the probabilities of 3-fold coincidence involving Bob's detector in the desired output (P_D) as well as that for the undesired output (P_U)

$$F = \frac{P_D}{P_D + P_U}. \tag{6.18}$$

Our model allows predicting the projection probabilities P_D and P_U.

The starting point of the model is to use the knowledge of the probabilities of projecting onto $|\Psi^-\rangle_{\rm Ai}$ given certain combinations of photon numbers at the BS inputs. For example with a single photon at each BS input the probability to project onto $|\Psi^-\rangle_{\rm Ai}$ is 1/4 [see Eq. (6.11)]. Hence, we define $P(n_{\rm A}, n_{\rm i}, n_{\rm s})$ as the probability to detect a 3-fold coincidence (i.e. projection onto the $|\Psi^-\rangle$ Bell-state and onto *either* $|\psi_\theta\rangle$ *or* $|\psi_\theta^\perp\rangle$) in the

case where n_{A} photons and n_{i} photons arrive at the beam-splitter (BS) from Alice and Bob, respectively, and n_s 'signal' photons are generated by the entangled photon pair source. It is important to note that probability $P(n_{\mathrm{A}}, n_{\mathrm{i}}, n_{\mathrm{s}})$ is not conditioned on having certain photon numbers at the inputs, rather it provides a means to treat the various contributions to the total 3-fold coincidence probability for separate cases, which have different probabilities to project onto $|\Psi^-\rangle_{\mathrm{Ai}}$. We take into account the probabilities of 3-fold coincidences for all cases in which $n_{\mathrm{A}} \leq 2$, $n_{\mathrm{i}} \leq 2$, $n_{\mathrm{A}} + n_{\mathrm{i}} \leq 2$ and $n_{\mathrm{s}} \leq 2$. We note that for small mean photon numbers, higher order contributions are negligible.

For instance, the probability $P(1_{\mathrm{A}}, 1_i, 1_s)$ for a 3-fold coincidence detection is calculated as follows. The probability to generate exactly one pair at Bob (please recall that the underlying distribution is thermal) is μ_{SPDC}, and that of generating one photon (with Poissonian distribution) at Alice is $\mu_{\mathrm{A}} e^{-\mu_{\mathrm{A}}}$. Hence, the probability to have one photon at the BS from both Alice and Bob is $\mu_{\mathrm{A}} t_{\mathrm{A}} e^{-\mu_{\mathrm{A}} t_{\mathrm{A}}} \mu_{\mathrm{SPDC}} t_{\mathrm{i}}$, where t_{A} is the transmission probability from Alice to Charlie and t_{i} is the transmission probability from Bob to Charlie. Since the probability for these photons to be projected onto $|\Psi^-\rangle_{\mathrm{Ai}}$ is 1/4, we get

$$P(1_{\mathrm{A}}, 1_{\mathrm{i}}, 1_{\mathrm{s}}) = \frac{1}{4} \mu_{\mathrm{SPDC}} \mu_{\mathrm{A}} t_{\mathrm{A}} e^{-\mu_{\mathrm{A}} t_{\mathrm{A}}} t_{\mathrm{i}} t_{\mathrm{s}} \eta_{\mathrm{BSM}}^2 \eta_{\mathrm{s}}, \tag{6.19}$$

where η_{BSM} is the efficiency of the detectors used for the BSM, η_{s} is the efficiency of the detectors used for the signal photons, and t_{s} is the transmission of the signal photons. Refer to Supplementary Figure 6.12.

Following a similar procedure we find

$$\begin{aligned}
P(0_{\mathrm{A}}, 2_{\mathrm{i}}, 2_{\mathrm{s}}) &= \frac{1}{4} \mu_{\mathrm{SPDC}}^2 e^{-\mu_{\mathrm{A}} t_{\mathrm{A}}} t_{\mathrm{i}}^2 \eta_{\mathrm{BSM}}^2 (1 - (1 - t_{\mathrm{s}} \eta_{\mathrm{s}})^2), \\
P(2_{\mathrm{A}}, 0_{\mathrm{i}}, 1_{\mathrm{s}}) &= \frac{1}{4} \mu_{\mathrm{SPDC}} (\mu_{\mathrm{A}} t_{\mathrm{A}})^2 \frac{e^{-\mu_{\mathrm{A}} t_{\mathrm{A}}}}{2} (1 - t_{\mathrm{i}}) \eta_{\mathrm{BSM}}^2 t_{\mathrm{s}} \eta_{\mathrm{s}}, \\
P(1_{\mathrm{A}}, 1_{\mathrm{i}}, 2_{\mathrm{s}}) &= \frac{1}{2} \mu_{\mathrm{SPDC}}^2 (\mu_{\mathrm{A}} t_{\mathrm{A}}) e^{-\mu_{\mathrm{A}} t_{\mathrm{A}}} (1 - t_{\mathrm{i}}) t_{\mathrm{i}} \eta_{\mathrm{BSM}}^2 (1 - (1 - t_{\mathrm{s}} \eta_{\mathrm{s}})^2).
\end{aligned} \tag{6.20}$$

If the photons at the BS are partially indistinguishable and assuming input states are

prepared as equal superpositions of $|e\rangle$ and $|l\rangle$, e.g. $|+\rangle$, the teleported state will correspond to the desired state with probability $\mathcal{V}$, and with probability $(1-\mathcal{V})$, it will correspond to a completely mixed state ($\mathcal{V}$ is the degree of indistinguishability). From Eq. (6.18), the teleportation fidelity of these input states is given by

$$F_{+/-} = \frac{1}{2} + \frac{\mathcal{V}[P(1_{\rm A}, 1_{\rm i}, 1_{\rm s}) + P(1_{\rm A}, 1_{\rm i}, 2_{\rm s})]}{2[P(1_{\rm A}, 1_{\rm i}, 1_{\rm s}) + P(1_{\rm A}, 1_{\rm i}, 2_{\rm s}) + P(0_{\rm A}, 2_{\rm i}, 2_{\rm s}) + P(2_{\rm A}, 0_{\rm i}, 1_{\rm s})]}. \tag{6.21}$$

Likewise, we can also estimate the fidelity for the teleportation of $|e\rangle$ or $|\ell\rangle$. Note that for these states, multiphoton contributions from Alice will not result in any $|\Psi^-\rangle_{\rm Ai}$ BSM detection. Also, the degree of indistinguishability, $\mathcal{V}$, has no effect since HOM interference is not required to faithfully complete the protocol in this basis. Thus, the fidelity is

$$F_{e/l} = \frac{P(1_{\rm A}, 1_{\rm i}, 1_{\rm s}) + P(1_{\rm A}, 1_{\rm i}, 2_{\rm s}) + 0.5P(0_{\rm A}, 2_{\rm i}, 2_{\rm s})}{P(1_{\rm A}, 1_{\rm i}, 1_{\rm s}) + P(1_{\rm A}, 1_{\rm i}, 2_{\rm s}) + P(0_{\rm A}, 2_{\rm i}, 2_{\rm s})}. \tag{6.22}$$

Supplementary Figure 6.18 shows fidelities predicted by our model as a function of $\mu_{\rm A}$, for $\mu_{\rm SPDC} = [0.03; 0.06; 0.09]$. The transmission probabilities, detector efficiencies and the degree of indistinguishability were chosen according to our experimental conditions: $t_{\rm i} = 0.015$, $t_{\rm s} = 0.01$, $t_{\rm A} = 0.24$, $\eta_{\rm BSM} = 0.7$, $\eta_{\rm s} = 0.65$, and $\mathcal{V} = 0.68$. The fidelities are plotted for values of $\mu_{\rm A}$ between 0 and 0.12. As $\mu_{\rm A}$ increases, we see a steady increase in the fidelity, reaching a maximum when the probabilities for the BS input receiving exactly one photon from Alice and exactly one from Bob are equal [45]. For larger values of $\mu_{\rm A}$, the contribution of multiphoton events increases, thus reducing the fidelity. Conversely, we find higher fidelities for smaller values of $\mu_{\rm SPDC}$. For $|e\rangle$ and $|\ell\rangle$, the fidelity increases as we increase $\mu_{\rm A}$.

Since we found in Supplementary Section 6.1 that the indistinguishability is not perfect in our experimental setup, in Supplementary Figure 6.19, we plot $F_{+/-}$ as a function of $\mu_{\rm A}$ for different values of $\mathcal{V}$. We set $\mu_{\rm SPDC} = 0.06$, and the rest of the parameters were chosen as in Supplementary Figure 6.18. As expected, we observe that better fidelities

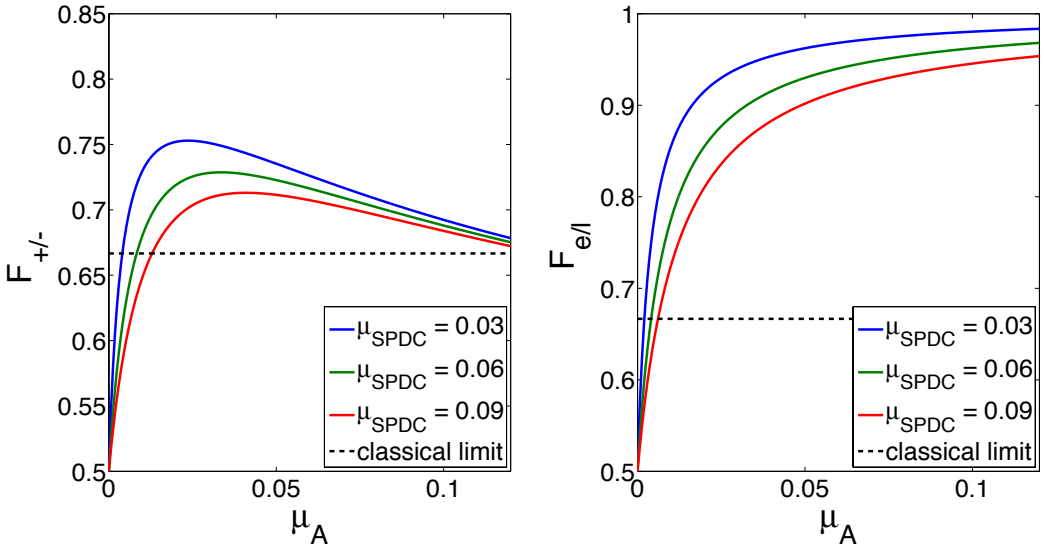

Figure 6.18: Fidelities for different μ_{SPDC} as a function of μ_{A}. The curves with $\mu_{\mathrm{SPDC}} = 0.06$ correspond to our experimental conditions. **Left:** Fidelity for equal-superposition states $F_{+/-}$. Notice that, by lowering μ_{SPDC}, the maximum fidelity increases due to reduced contribution of multiphoton events. **Right:** Fidelity for early or late states $F_{e/l}$. Notice that, by decreasing μ_{SPDC}, the fidelity increases due to the reduction of multiphoton events stemming from the SPDC source. For a given μ_{SPDC}, the fidelity keeps increasing with μ_{A} since multiphoton events from Alice do not result in any BSM.

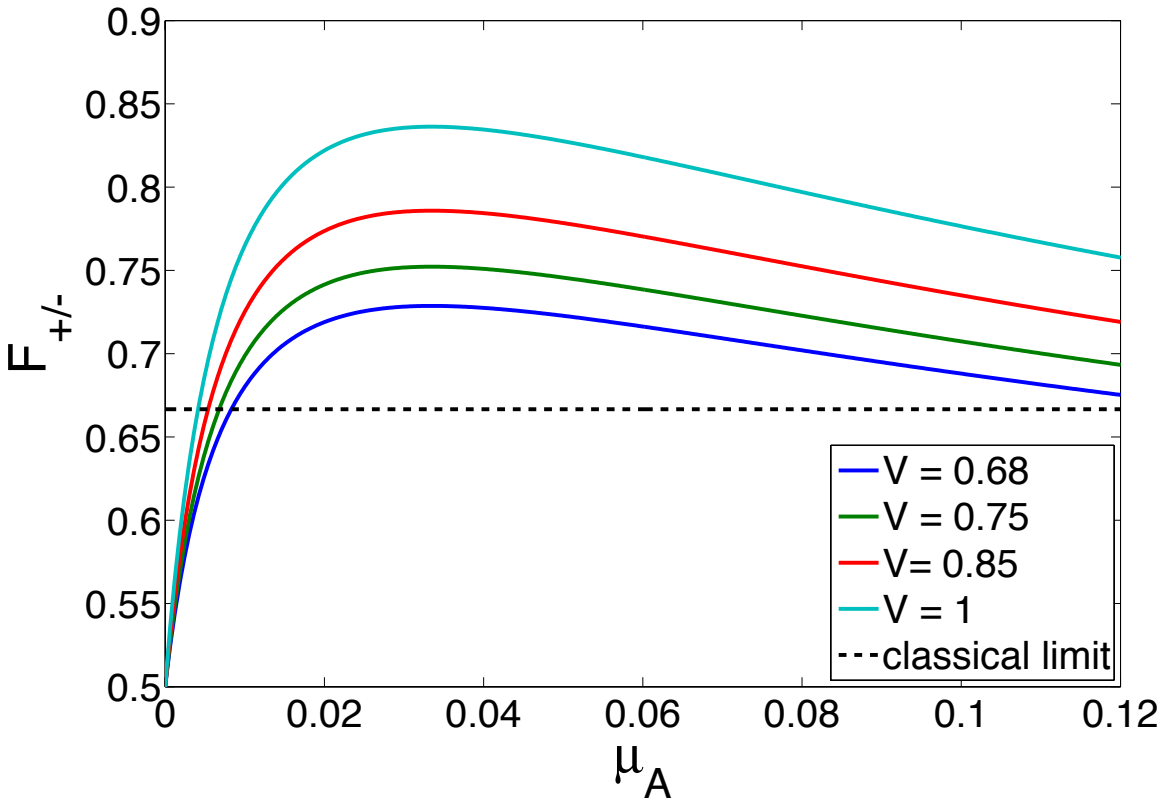

Figure 6.19: Fidelity $F_{+/-}$ for different degrees of indistinguishability $\mathcal{V}$ as a function of μ_{A}. Note that the maximum fidelity increases as the indistinguishability of photons, $\mathcal{V}$ increases.

are obtained as $\mathcal{V}$ increases. The maximum fidelity attainable is 0.835 for $\mathcal{V} = 1$. This provides an upper limit of the fidelity $F_{+/-}$ that we can obtain in our experiment.

Bounding the teleportation fidelity of single photon using decoy state method

The decoy state method was originally developed to overcome the photon number splitting attack in quantum key distribution — it allows estimating the amount of key obtained from states containing one, and only one, photon[46, 47]. We recently expanded the decoy state method to verify the quantum nature of a memory[36], and here we use it for the first time to demonstrate the quantum nature of teleportation in our experiment[47]. This requires the average fidelity over a certain set of input states to exceed 2/3, provided these states are encoded into individual photons.

First, we define the error rate

$$E_\phi = \frac{C_{|\phi_\perp\rangle\langle\phi_\perp|}}{C_{|\phi_\perp\rangle\langle\phi_\perp|} + C_{|\phi\rangle\langle\phi|}}, \tag{6.23}$$

where, $C_{|\phi_\perp\rangle\langle\phi_\perp|}$ denotes the number of measured events corresponding to the state $|\phi_\perp\rangle$, while the expected teleported state is $|\phi\rangle$. Since $|\phi_\perp\rangle$ corresponds to a state orthogonal to $|\phi\rangle$, a count of this type constitutes an error. Comparing with the expression for the fidelity of the quantum teleportation in Eq. (6.18), we find the simple relation $F_\phi = 1 - E_\phi$. The decoy state method allows us to estimate the impact of a quantum channel on qubits encoded onto single photons. In the method, Alice creates phase-randomized attenuated laser pulses and randomly modulates between different intensities for each pulse, known as signal and decoy states. The individual measurement statistics collected for different intensities goes into an estimate of the lower bound of the count rates, and an upper bound on the errors, that would have resulted from single-photon emissions from Alice. Based on Eq. (25) from Ref. [47], the error rate $E^{(1)}$ for the single photon component in

a coherent pulses is upper bounded by $E_{\mathrm{U}}^{(1)}$, which is

$$E^{(1)} \leq E_{\mathrm{U}}^{(1)} = \frac{E^{(\mu_{\mathrm{d}})} Q^{(\mu_{\mathrm{d}})} e^{\mu_{\mathrm{d}}} - E^{(0)} Y^{(0)}}{\mu_{\mathrm{d}} Y_{\mathrm{L}}^{(1)}}. \tag{6.24}$$

Here, μ_{d} is the mean photon number per qubit encoded into a decoy state; $Q^{(\mu_{\mathrm{d}})}$ is the corresponding gain (i.e. the probability for a 3-fold coincidence when creating pulses with mean photon number μ_{d} at Alice's), and $E^{(\mu_{\mathrm{d}})}$ is the corresponding error rate; $E^{(0)}$ is the error rate for a zero-photon (vacuum) input at Alice's; $Y^{(0)}$ and $Y_{\mathrm{L}}^{(1)}$ are the yield for a zero-photon input and the lower bound for the yield of a single photon input, respectively. The values $Q^{(\mu_{\mathrm{d}})}$, $E^{(\mu_{\mathrm{d}})}$, $Y^{(0)}$ and $E^{(0)}$ can be measured directly in the experiment.

Given a phase randomized coherent state with a mean photon number of μ, the gain can be expressed as

$$Q^{(\mu)} = \sum_{n=0}^{\infty} \frac{Y^{(n)} \mu^n e^{-\mu}}{n!}, \tag{6.25}$$

where the yield of an n-photon state, $Y^{(n)}$, is the conditional probability of a detection given that an n-photon state was sent from Alice. These yields, with an exception of the yield of the vacuum state $Y^{(0)}$, can generally not be measured directly. Fortunately, one can derive a lower bound $Y_{\mathrm{L}}^{(1)}$ for the single photon yield (applied in Eq. 6.24), which is discussed in Ref. [8]:

$$Y^{(1)} \geq Y_{\mathrm{L}}^{(1)} = \frac{\mu_{\mathrm{s}}}{\mu_{\mathrm{s}}\mu_{\mathrm{d}} - \mu_{\mathrm{d}}^2} (Q^{(\mu_{\mathrm{d}})} e^{\mu_{\mathrm{d}}} \tag{6.26}$$

$$- \frac{\mu_{\mathrm{d}}^2}{\mu_{\mathrm{s}}^2} Q^{(\mu_{\mathrm{s}})} e^{\mu_{\mathrm{s}}} - \frac{\mu_{\mathrm{s}}^2 - \mu_{\mathrm{d}}^2}{\mu_{\mathrm{s}}^2} Y^{(0)}), \tag{6.27}$$

where $\mu_{\mathrm{s}} > \mu_{\mathrm{d}}$ is the mean photon number of the signal state. $Q^{(\mu_{\mathrm{s}})}$ is the corresponding gain of the signal state; it is also measurable. Thus, we can calculate an upper bound of the error rate $E_U^{(1)}$ from Eqs. (6.24) and (6.26). In turn, this allows computing a lower bound on the fidelity in the quantum teleportation experiment:

$$F^{(1)} = 1 - E^{(1)} \geq 1 - E_{\mathrm{U}}^{(1)} \equiv F_{\mathrm{L}}^{(1)}. \tag{6.28}$$

In our experiment, the quantum channel, whose effect on single photons emitted at Alice's we want to characterize, is given by the concatenation of direct qubit transmission from Alice to Charlie, and teleportation from Charlie to Bob. To implement the decoy state method, Alice prepares qubits with three different mean photon numbers ($\mu_{\rm s}$, $\mu_{\rm d}$ and vaccuum) and sends them to Charlie. This allows us to obtain a bound on the fidelity of the teleportation experiment that we would obtained had we utilized true single photons to encode qubits.

We also use our theoretical model to predict the results of the decoy state protocol. We express Q^{μ} and $E^{\mu}_{1/0}$ using the variables in our model as

$$Q^{\mu} = P(1_{\rm A}, 1_{\rm i}, 1_{\rm s}) + P(0_{\rm A}, 2_{\rm i}, 2_{\rm s}) + P(2_{\rm A}, 0_{\rm i}, 1_{\rm s}) + P(1_{\rm A}, 1_{\rm i}, 2_{\rm s}) \tag{6.29}$$

$$E^{\mu}_{+/-\ (e/l)} = 1 - F_{+/-\ (e/l)}. \tag{6.30}$$

We calculate the lower bound of $F^{(1)}_{+/-}$, and $F^{(1)}_{e/l}$ using Eqs. (6.24), (6.26) and (6.29). Finally, we obtain $F^{(1)}_{\rm avg} = 2/3\ F^{(1)}_{+/-} + 1/3\ F^{(1)}_{e/l}$, with different $\mu_{\rm d}$ and $\mu_{\rm s}$, as shown in Supplementary Figure 6.20. Two different areas are shown, the white area corresponds to the fidelities that can be reached by classical strategies. The coloured area (not grey) corresponds to fidelities that can not be obtained classically. Note that $F^{(1)}_{\rm avg}$ depends mostly on $\mu_{\rm d}$. $F^{(1)}_{\rm avg}$ increases as $\mu_{\rm d}$ decreases, since the decoy method can bound the contribution of higher multiphoton events more tightly.

With the help of this model, we set $\mu_{\rm s}$ and $\mu_{\rm d}$ in our experiment to be 0.028 and 0.014, respectively. With these values, we can exceed the classical bound of 2/3 for the single photon fidelity significantly, as shown in Supplementary Figure 6.20. Moreover, these values of $\mu_{\rm s}$ and $\mu_{\rm d}$ result in rates for 3-fold coincidence counts of several per minute (see Supplementary section 6.1). Also, this choice leads to a HOM visibility (see Supplementary Figure 6.16) that is sufficiently large to allow for the timing feedback (see Methods

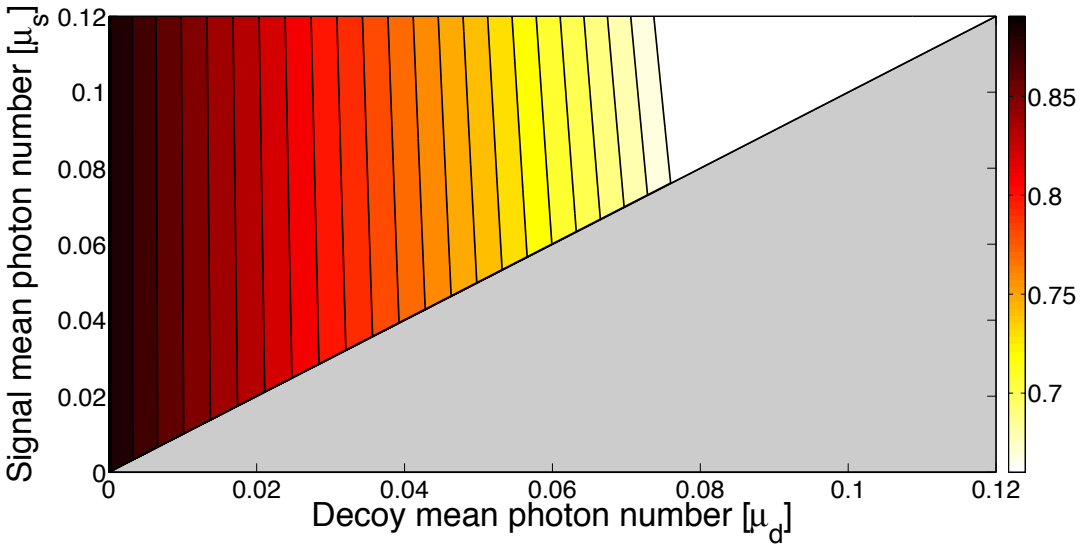

Figure 6.20: Predicted average single photon fidelity $F^{(1)}_{\text{avg}}$ as a function of μ_{d} and μ_{s}. Fidelities are indicated using the colour gradient shown on the right. The region in white corresponds to $F^{(1)}_{\text{avg}} < 2/3$, which can be achieved using classical strategies. The grey area corresponds to ($\mu_{\text{d}} > \mu_{\text{s}}$), which is not covered by decoy state method.

in the main text).

Experimental data and model comparison

In this section, we present the experimental data that is used to calculate fidelities using the decoy state method.

Decoy state method

Table 6.1 and 6.2 shows measured gains and fidelities for different mean photon numbers ($\mu_{\text{s}} = 0.028$ and $\mu_{\text{d}} = 0.014$).

Comparison of measured and predicted fidelities

Table 6.3 compares experimentally obtained and predicted fidelities (from our model) for the two mean photon numbers ($\mu_{\text{s}} = 0.028$ and $\mu_{\text{d}} = 0.014$) that were chosen in

Table 6.1: Gains [Hz] for different input states and signal and decoy mean photon numbers.

state	signal	decoy	vacuum
$\|+\rangle$	0.35 ± 0.01	0.18 ± 0.01	0.038 ± 0.003
$\|+i\rangle$	0.35 ± 0.02	0.18 ± 0.01	0.038 ± 0.003
$\|e\rangle$	0.14 ± 0.01	0.09 ± 0.01	0.016 ± 0.002
$\|\ell\rangle$	0.14 ± 0.01	0.08 ± 0.01	0.016 ± 0.002

Table 6.2: Fidelities for different mean photon number and states.

state	signal	decoy	vacuum
$\|+\rangle$	0.70 ± 0.02	0.72 ± 0.02	0.50 ± 0.05
$\|+i\rangle$	0.70 ± 0.02	0.73 ± 0.02	0.50 ± 0.05
$\|e\rangle$	0.91 ± 0.01	0.87 ± 0.02	0.63 ± 0.07
$\|\ell\rangle$	0.89 ± 0.02	0.88 ± 0.03	0.63 ± 0.07

the decoy state method per qubit emitted at Alice's. Table 6.4 compares experimentally observed fidelities, derived after quantum state tomography of different input states, with predicted fidelities from our model. The experimental values are in good agreement with the expected fidelities.

Table 6.3: Comparison of fidelities obtained experimentally using the decoy values with predicted values for $\mu_{\mathrm{SPDC}} = 0.06$.

	experiment		model	
	μ_s	μ_d	μ_s	μ_d
$\|+\rangle$	0.70 ± 0.02	0.72 ± 0.02	0.73	0.70
$\|+i\rangle$	0.70 ± 0.02	0.73 ± 0.02	0.73	0.70
$\|e\rangle$	0.91 ± 0.01	0.87 ± 0.02	0.89	0.82
$\|l\rangle$	0.89 ± 0.02	0.88 ± 0.03	0.89	0.82

Table 6.4: Comparison of fidelities obtained after quantum state tomography with predicted values for $\mu_{SPDC} = 0.045$ and $\mu_c = 0.014$.

	experiment	model
$\|+\rangle$	0.75 ± 0.03	0.72
$\|+i\rangle$	0.71 ± 0.03	0.72
$\|e\rangle$	0.86 ± 0.03	0.85
$\|l\rangle$	0.89 ± 0.03	0.85

Bibliography

[1] Bennett, C. H. *et al.* Teleporting an unknown quantum state via dual classical and Einstein-Podolsky-Rosen channels. *Phys. Rev. Lett.* **70**, 1895-1899 (1993).

[2] Pirandola, S. Eisert, J. Weedbrook, C. Furusawa, A. & Braunstein, S. L. Advances in quantum teleportation. *Nat. Phot.* **9**, 641-652 (2015)

[3] Landry, O. van Houwelingen, J. A. W. Beveratos, A. Zbinden, H. & Gisin, N. Quantum teleportation over the Swisscom telecommunication network. *JOSA B* **24**, 398-403 (2007).

[4] Hensen, B. *et al.*, Loophole-free Bell inequality violation using electron spins separated by 1.3 kilometres. *Nature* **526**, 682-686 (2015).

[5] Sangouard, N. Simon, C. De Riedmatten, H. & Gisin, N. Quantum repeaters based on atomic ensembles and linear optics. *Rev. of Mod. Phys.* **83**, 33-80 (2011).

[6] Kimble, H. J. The quantum Internet. *Nature* **453**, 1023-1030 (2008).

[7] Yin, J. *et al.* Quantum teleportation and entanglement distribution over 100-kilometre free-space channels. *Nature* **488**, 185-188 (2012).

[8] Ma, X-S. *et al.* Quantum teleportation over 143 kilometres using active feed-forward. *Nature* **489**, 269-273 (2012).

[9] Lvovsky, A. I. Sanders, B. C. & Tittel, W. Optical quantum memory. *Nat. Phot.* **3**, 706-714 (2009).

[10] Żukowski, M. Zeilinger, A. Horne, M. A. & Ekert, A. K. "Event-ready-detectors" Bell experiment via entanglement swapping. *Phys. Rev. Lett.* **71**, 4287-4290 (1993).

[11] Rubenok, A. Slater, J. A. Chan, P. Lucio-Martinez, I. & Tittel, W. Real-world two-photon interference and proof-of-principle quantum key distribution immune to detector attacks. *Phys. Rev. Lett.* **111**, 130501 (2013).

[12] Marcikic, I. De Riedmatten, H. Tittel, W. Zbinden, H. & Gisin, N. Long-distance teleportation of qubits at telecommunication wavelengths. *Nature* **421**, 509-513 (2003).

[13] de Riedmatten, H. *et al.* Long distance quantum teleportation in a quantum relay configuration. *Phys. Rev. Lett.* **92**, 047904 (2004).

[14] Bussières, F. *et al.* Quantum teleportation from a telecom-wavelength photon to a solid-state quantum memory. *Nat. Phot.* **8**, 775-778 (2014).

[15] Takesue, H. *et al.* Quantum teleportation over 100 km of fiber using highly efficient superconducting nanowire single-photon detectors. *Optica* **2**, 832-835 (2015).

[16] Ma, X. S. *et al.* Experimental delayed-choice entanglement swapping. *Nat. Phys.* **8**, 479-484 (2012).

[17] Megidish, E. *et al.* Entanglement swapping between photons that have never coexisted. *Phys. Rev. Lett.* **110**, 210403 (2013).

[18] Massar, S. & Popescu, S. Optimal extraction of information from finite quantum ensembles. *Phys. Rev. Lett.* **74**, 1259–1263 (1995).

[19] Lo, H-K. Ma, X. & Chen, K. Decoy state quantum key distribution. *Phys. Rev. Lett.* **94**, 230504 (2005).

[20] Wang, X. B. Beating the photon-number-splitting attack in practical quantum cryptography. *Phys. Rev. Lett.* **94**, 230503 (2005).

[21] Brendel, J. Gisin, N. Tittel, W. & Zbinden, H. Pulsed energy-time entangled twin-photon source for quantum communication. *Phys. Rev. Lett.* **82**, 2594-2597 (1999).

[22] Marsili, F. *et al.* Detecting single infrared photons with 93 % system efficiency. *Nat. Phot.* **7**, 210-214 (2013).

[23] Sinclair, N. *et al.* Spectral multiplexing for scalable quantum photonics using an atomic frequency comb quantum memory and feed-forward control. *Phys. Rev. Lett.* **113**, 053603 (2014).

[24] Hong, C. K. Ou, Z. Y. & Mandel, L. Measurement of subpicosecond time intervals between two photons by interference. *Phys. Rev. Lett.* **59**, 2044-2046 (1987).

[25] Krovi, H. *et al.* W. Practical quantum repeaters with parametric down-conversion sources. *Applied Physics B* **122**, 52 (2016).

[26] Thiel, C. W. Sinclair, N. Tittel, W. & Cone, R. L. Optical decoherence studies of $Tm^{3+} : Y_3Ga_5O_{12}$. *Phys. Rev. B* **90**, 214301 (2014).

[27] Valivarthi, R. *et al.* Efficient Bell state analyzer for time-bin qubits with fast-recovery WSi superconducting single photon detectors. *Opt. Expr.* **22**, 24497-24506 (2014).

[28] http://www.wavelengthreferences.com/pdf/Data

[29] Braunstein, S. L. & Pirandola, S. Side-channel-free quantum key distribution. *Physical review letters* **108**, 130502 (2012).

[30] Sun, Q.-C. *et al.* Quantum teleportation with independent sources over an optical fibre network. *arXiv* **1602.07081**, (2016).

[31] Salart, D. et al. Testing the speed of 'spooky action at a distance'. *Nature* **454**, 861 (2008).

[32] Yin, J. et al. Lower bound on the speed of nonlocal correlations without locality and measurement choice loopholes. *Phys. Rev. Lett.* **110**, 260407 (2013).

[33] Yin, J. et al. Quantum teleportation and entanglement distribution over 100-kilometre free-space channels. *Nature* **488**, 185188 (2012).

[34] Ma, X.S. et al. Quantum teleportation over 143 kilometres using active feed-forward. *Nature* **489**, 269273 (2012).

[35] Sangouard, N. et al. Quantum repeaters based on atomic ensembles and linear optics. *Rev. Mod. Phys.* **83**, 33 (2011).

[36] Sinclair, N. et al. Spectral Multiplexing for Scalable Quantum Photonics using an Atomic Frequency Comb Quantum Memory and Feed-Forward Control. *Phys. Rev. Lett.* **113**, 053603 (2014).

[37] Sun, Q.C. et al. Quantum teleportation with independent sources over an optical fibre network. *arXiv* **1602.07081** (2016).

[38] Bussières, F. et al. Quantum teleportation from a telecom-wavelength photon to a solid-state quantum memory. *Nat. Phot.* **8**, 775 (2014).

[39] Takesue, H. et al. Quantum teleportation over 100 km of fiber using highly efficient superconducting nanowire single-photon detectors. *Optica* **2**, 832-835 (2015).

[40] Marcikic, I., de Riedmatten, H. Tittel, W. Zbinden, H. and Gisin N. Long-distance teleportation of qubits at telecommunication wavelengths. *Nature* **421**, 509-513 (2003).

[41] de Riedmatten, H. *et al.* Long Distance Quantum Teleportation in a Quantum Relay Configuration. *Phys. Rev. Lett.* **92**, 047904 (2004).

[42] Landry, O. et al. Quantum teleportation over the Swisscom telecommunication network. *J. Opt. Soc. Am. B* **24**, 2 (2007).

[43] Hong, C. K. Ou, Z. Y. and Mandel, L. Measurement of subpicosecond time intervals between two photons by interference. *Phys. Rev. Lett.* **59**, 2044-2046 (1987).

[44] de Riedmatten, H. Marcikic, I. Tittel, W. Zbinden, H. and Gisin, N. Quantum interference with photon pairs created in spatially separated sources. *Phys. Rev. A.* **67**, 022301 (2003).

[45] Rarity, J. G. Tapster, P. R. and Loudon, R. Non-classical interference between independent sources. *arXiv* preprint quant-ph/9702032 (1997).

[46] Lo, H-K. Ma, X. Chen, K. Decoy State Quantum Key Distribution. *Phys. Rev. Lett.* **94**, 230504 (2005).

[47] Ma, X. Qi, B. Zhao, Y. and Lo, H-K. Practical decoy state for quantum key distribution. *Phys. Rev. A* **72**, 012326 (2005).

[48] Massar, S. and Popescu, S. Optimal Extraction of Information from Finite Quantum Ensembles. *Phys. Rev. Lett.* **74**, 1259-1263 (1995).

Chapter 7

Conclusions and outlook

In this thesis the three basic elements required to build a quantum repeater, i.e. entangled photon pair sources, quantum memories and entanglement swapping operations, are introduced and described. In the different experiments presented, we show how these building blocks can be interfaced and hence eventually combined in order to implement a frequency-multiplexed quantum repeater [36]. This work represents a significant step towards the development of practical quantum repeaters, yet, substantial theoretical and experimental work remains to be done.

First, with regards to the development of entangled photon pair sources, we have shown that many features of sources based on SPDC makes them suitable for quantum repeater applications. This includes their spectral tunability, versatility and frequency multimode nature [45]. Beyond what we demonstrated, highly efficient SPDC sources, in terms of pure state generation and photon pair output, can be obtained by placing the non-linear medium inside a cavity with carefully engineered properties [77]. Despite the many favorable attributes of SPDC based photon-pair sources, multi-photon-pair emissions, which reduce the state and operation fidelities, together with their non-deterministic nature constitute major imperfections [78]. However, multi-photon events could be detected and thus mitigated by incorporating efficient photon number resolving detectors [79] and quantum non-demolition measurements [80]. At present, a more realistic approach is to use photon pair sources based on single emitters, e.g. quantum dots, [16, 81, 82], for which multiphoton events are inherently absent. Current experiments also show the possibility to frequency multiplex such sources and integrate them into a photonic chip [83].

Second, in this thesis we demonstrated the ideal match between the atomic frequency comb (AFC) quantum memory protocol, implemented in rare-earth ion doped solids and the frequency multiplexed quantum repeater. Note that, our quantum memory realizations still fall short in terms of efficiency and storage time. However, it is known how to overcome these challenges. First, the efficiency may be increased by embedding the quantum memory in an impedance matched cavity [49]. And second, to increase storage time to around 500 μs [36] further development and testing of rare-earth ion doped materials is needed to identify candidates with good atomic properties.

Lastly, we have shown that entanglement swapping operations, i.e. Bell-state measurement (BSM), can be performed with photons that have been transmitted over real-world channels and that are entangled with photons that are suitable for storage in quantum memories. In order to increase the BSM efficiency (which, using linear optics and no additional resources is bounded to 50%), photonic states could be mapped onto matter qubits for which CNOT gates can be implemented faithfully, and thus 100% efficient BSMs can be achieved [25]. Alternatively, with the use of auxiliary photons, higher BSM efficiencies can also be attained [67]. Additionally, to fully incorporate the spectral multiplexing with the BSM we require efficient spectrally resolved photon detection combined with a corresponding frequency shifting capability over a much larger bandwidth than now. Towards this end, commercially-available wavelength-division multiplexers already allow to multiplex narrow ($\sim$ 3GHz) and closely spaced frequency channels ($\sim$ 3-4GHz) [84]. Furthermore, our frequency shifting capabilities can be extended by using the same approach presented in paper 1 but with higher-bandwidth electronics. Alternatively, frequency conversion using non-linear optical processes could be used over practically arbitrary large bandwidths [85].

In conclusion, we presented the key ingredients of a quantum repeater, their figures of merit and requirements, and a number of experiments that point towards a possible

implementation. A combination of engineering and fundamental problems need to be addressed in order to achieve, in the near future, a fully functional quantum repeater, which will open new applications and possibilities for quantum communication. Certainly, in the same way basic science discoveries lead to tangible applications, the road towards this well-defined goal will foster new fundamental discoveries.

Bibliography

[1] N. Gisin and R. Thew. Quantum communication. *Nat Photon*, 1(3):165–171, March 2007.

[2] H. J. Kimble. The quantum internet. *Nature*, 453(7198):1023–1030, June 2008.

[3] J. P. Dowling and G. J. Milburn. Quantum technology: the second quantum revolution. *Philos Transact A Math Phys Eng Sci*, 361(1809):1655, August 2003.

[4] N. Gisin, G. Ribordy, W. Tittel, and H. Zbinden. Quantum cryptography. *Rev. Mod. Phys.*, 74:145–195, March 2002.

[5] B. Schumacher. Quantum coding. *Phys. Rev. A*, 51:2738–2747, April 1995.

[6] H. Hbel, M. R. Vanner, T. Lederer, B. Blauensteiner, T. Lornser, A. Poppe, and A. Zeilinger. High-fidelity transmission of polarization encoded qubits from an entangled source over 100 km of fiber. *Opt. Express*, 15(12):7853–7862, June 2007.

[7] J. Brendel, N. Gisin, W. Tittel, and H. Zbinden. Pulsed energy-time entangled twin-photon source for quantum communication. *Phys. Rev. Lett.*, 82:2594–2597, March 1999.

[8] D. Dieks. Communication by epr devices. 92(6):271–272, November 1982.

[9] C. H. Bennett, G. Brassard, C. Crépeau, R. Jozsa, A. Peres, and W. K. Wootters. Teleporting an unknown quantum state via dual classical and einstein-podolsky-rosen channels. *Phys. Rev. Lett.*, 70:1895–1899, March 1993.

[10] M. A. Nielsen and I. L. Chuang. *Quantum Computation and Quantum Information: 10th Anniversary Edition*. Cambridge University Press, Cambridge, 2010.

[11] P. G. Kwiat, K. Mattle, H. Weinfurter, A. Zeilinger, A. V. Sergienko, and Y. Shih. New high-intensity source of polarization-entangled photon pairs. *Phys. Rev. Lett.*, 75:4337–4341, December 1995.

[12] Q. Zhou, S. Dong, W. Zhang, L. You, Y. He, W. Zhang, Y. Huang, and J. Peng. Frequency-entanglement preparation based on the coherent manipulation of frequency nondegenerate energy-time entangled state. *J. Opt. Soc. Am. B*, 31(8):1801–1806, August 2014.

[13] J. D. Franson. Bell inequality for position and time. *Phys. Rev. Lett.*, 62:2205–2208, May 1989.

[14] W. Tittel, J. Brendel, H. Zbinden, and N. Gisin. Quantum cryptography using entangled photons in energy-time bell states. *Phys. Rev. Lett.*, 84:4737–4740, May 2000.

[15] I. Marcikic, H. de Riedmatten, W. Tittel, V. Scarani, H. Zbinden, and N. Gisin. Time-bin entangled qubits for quantum communication created by femtosecond pulses. *Phys. Rev. A*, 66:062308, December 2002.

[16] H. Jayakumar, A. Predojevi, T. Kauten, T. Huber, G. S. Solomon, and G. Weihs. Time-bin entangled photons from a quantum dot. 5:4251, June 2014.

[17] A. Dousse, J. Suffczynski, A. Beveratos, O. Krebs, A. Lemaitre, I. Sagnes, J. Bloch, P. Voisin, and P. Senellart. Ultrabright source of entangled photon pairs. *Nature*, 466(7303):217–220, July 2010.

[18] H. Takesue and K. Inoue. Generation of $1.5-\mu$m band time-bin entanglement using spontaneous fiber four-wave mixing and planar light-wave circuit interferometers. *Phys. Rev. A*, 72:041804, October 2005.

[19] S. Braunstein and HK Lo. Experimental proposals for quantum computation - foreword. *FORTSCHRITTE DER PHYSIK-PROGRESS OF PHYSICS*, 48(9-11):767, 2000.

[20] R. L. Rivest, A. Shamir, and L. Adleman. A method for obtaining digital signatures and public-key cryptosystems. *Commun. ACM*, 21(2):120–126, February 1978.

[21] P. Shor. Polynomial-time algorithms for prime factorization and discrete logarithms on a quantum computer. *SIAM J. Comput.*, 26(5):1484–1509, October 1997.

[22] C. E. Shannon. Communication theory of secrecy systems. 28(4):656–715, 1949.

[23] C. H. Bennett and G. Brassard. *Quantum cryptography: Public key distribution and coin tossing*, volume 175. January 1984.

[24] A. K. Ekert. Quantum cryptography based on bell s theorem. *Phys. Rev. Lett.*, 67:661–663, August 1991.

[25] S. Pirandola, J. Eisert, C. Weedbrook, A. Furusawa, and S. L. Braunstein. Advances in quantum teleportation. *Nat Photon*, 9(10):641–652, October 2015.

[26] Ji-Gang Ren, Ping Xu, Hai-Lin Yong, Liang Zhang, Sheng-Kai Liao, Juan Yin, Wei-Yue Liu, Wen-Qi Cai, Meng Yang, Li Li, Kui-Xing Yang, Xuan Han, Yong-Qiang Yao, Ji Li, Hai-Yan Wu, Song Wan, Lei Liu, Ding-Quan Liu, Yao-Wu Kuang, Zhi-Ping He, Peng Shang, Cheng Guo, Ru-Hua Zheng, Kai Tian, Zhen-Cai Zhu, Nai-Le Liu, Chao-Yang Lu, Rong Shu, Yu-Ao Chen, Cheng-Zhi Peng, Jian-Yu Wang, and Jian-Wei Pan. Ground-to-satellite quantum teleportation. *Nature*, advance online publication, August 2017.

[27] H-L. Yin, T-Y. Chen, Z-W. Yu, H. Liu, L-X. You, Y-H. Zhou, S-J. Chen, Y. Mao, M-Q. Huang, W-J. Zhang, H. Chen, M. Jun Li, D. Nolan, F. Zhou, X. Jiang, Z. Wang,

Q. Zhang, X-B. Wang, and J-W. Pan. Measurement-device-independent quantum key distribution over a 404 km optical fiber. *Phys. Rev. Lett.*, 117:190501, November 2016.

[28] J. F. Dynes, W. W.-S. Tam, A. Plews, B. Frhlich, A. W. Sharpe, M. Lucamarini, Z. Yuan, C. Radig, A. Straw, T. Edwards, and A. J. Shields. Ultra-high bandwidth quantum secured data transmission. 6:35149, October 2016.

[29] H.-J. Briegel, W. Dür, J. I. Cirac, and P. Zoller. Quantum repeaters: The role of imperfect local operations in quantum communication. *Phys. Rev. Lett.*, 81:5932–5935, December 1998.

[30] S. Muralidharan, L. Li, J. Kim, N. Ltkenhaus, M. D. Lukin, and L. Jiang. Optimal architectures for long distance quantum communication. 6:20463, February 2016.

[31] J-W Pan, C. Simon, C. Brukner, and A. Zeilinger. Entanglement purification for quantum communication. *Nature*, 410(6832):1067–1070, April 2001.

[32] L.-M. Duan, M. D. Lukin, J. I. Cirac, and P. Zoller. Long-distance quantum communication with atomic ensembles and linear optics. *Nature*, 414(6862):413–418, November 2001.

[33] L. Childress and R. Hanson. Diamond nv centers for quantum computing and quantum networks. *MRS Bulletin*, 38(2):134–138, 2013.

[34] N. Sangouard, C. Simon, H. de Riedmatten, and N. Gisin. Quantum repeaters based on atomic ensembles and linear optics. *Rev. Mod. Phys.*, 83:33–80, March 2011.

[35] C. Simon, H. de Riedmatten, M. Afzelius, N. Sangouard, H. Zbinden, and N. Gisin. Quantum repeaters with photon pair sources and multimode memories. *Phys. Rev. Lett.*, 98:190503, May 2007.

[36] N. Sinclair, E. Saglamyurek, H. Mallahzadeh, J. A. Slater, M. George, R. Ricken, M. P. Hedges, D. Oblak, C. Simon, W. Sohler, and W. Tittel. Spectral multiplexing for scalable quantum photonics using an atomic frequency comb quantum memory and feed-forward control. *Phys. Rev. Lett.*, 113:053603, July 2014.

[37] J-W. Pan, Z-B. Chen, C-Y. Lu, H. Weinfurter, A. Zeilinger, and M. Żukowski. Multiphoton entanglement and interferometry. *Rev. Mod. Phys.*, 84:777–838, May 2012.

[38] R. W. Boyd. *Nonlinear Optics*. Elsevier LTD, Oxford, 2008.

[39] D.F. Walls and G. J. Milburn. *Quantum Optics*. Springer, 2008 2nd edition.

[40] N. Ltkenhaus and M. Jahma. Quantum key distribution with realistic states: photon-number statistics in the photon-number splitting attack. *New Journal of Physics*, 4(1):44, 2002.

[41] M. Fiorentino, S. M. Spillane, R. G. Beausoleil, T. D. Roberts, P. Battle, and M. W. Munro. Spontaneous parametric down-conversion in periodically poled ktp waveguides and bulk crystals. *Opt. Express*, 15(12):7479–7488, June 2007.

[42] Jeffrey H. Shapiro and Franco N. Wong. On-demand single-photon generation using a modular array of parametric downconverters with electro-optic polarization controls. *Opt. Lett.*, 32(18):2698–2700, September 2007.

[43] X-S. Ma, S. Zotter, J. Kofler, T. Jennewein, and A. Zeilinger. Experimental generation of single photons via active multiplexing. *Phys. Rev. A*, 83:043814, April 2011.

[44] C. Simon, M. Afzelius, J. Appel, A. Boyer de la Giroday, S. J. Dewhurst, N. Gisin, C. Y. Hu, F. Jelezko, S. Krll, J. H. Mller, J. Nunn, E. S. Polzik, J. G. Rarity,

H. De Riedmatten, W. Rosenfeld, A. J. Shields, N. Skld, R. M. Stevenson, R. Thew, I. A. Walmsley, M. C. Weber, H. Weinfurter, J. Wrachtrup, and R. J. Young. Quantum memories. *The European Physical Journal D*, 58(1):1–22, May 2010.

[45] H. de Riedmatten and M. Afzelius. Quantum light storage in solid state atomic ensembles. In *Engineering the Atom-Photon Interaction: Controlling Fundamental Processes with Photons, Atoms and Solids*, pages 241–273. Springer International Publishing, Cham, 2015.

[46] W. Tittel, M. Afzelius, T. Chanelire, R.L. Cone, S. Krll, S.A. Moiseev, and M. Sellars. Photon-echo quantum memory in solid state systems. *Laser & Photonics Reviews*, 4(2):244–267, 2010.

[47] M. Afzelius, C. Simon, H. de Riedmatten, and N. Gisin. Multimode quantum memory based on atomic frequency combs. *Phys. Rev. A*, 79:052329, May 2009.

[48] J. Nunn, K. Reim, K. C. Lee, V. O. Lorenz, B. J. Sussman, I. A. Walmsley, and D. Jaksch. Multimode memories in atomic ensembles. *Phys. Rev. Lett.*, 101:260502, December 2008.

[49] M. Afzelius and C. Simon. Impedance-matched cavity quantum memory. *Phys. Rev. A*, 82:022310, August 2010.

[50] E. Saglamyurek, N. Sinclair, J. Jin, J. A. Slater, D. Oblak, F. Bussieres, M. George, R. Ricken, W. Sohler, and W. Tittel. Broadband waveguide quantum memory for entangled photons. *Nature*, 469(7331):512–515, January 2011.

[51] N. Sinclair, D. Oblak, C. W. Thiel, R. L. Cone, and W. Tittel. Properties of a rare-earth-ion-doped waveguide at sub-kelvin temperatures for quantum signal processing. *Phys. Rev. Lett.*, 118:100504, March 2017.

[52] E. Saglamyurek, J. Jin, V. B. Verma, M. D. Shaw, F. Marsili, S. W. Nam, D. Oblak, and W. Tittel. Quantum storage of entangled telecom-wavelength photons in an erbium-doped optical fibre. *Nat Photon*, 9(2):83–87, February 2015.

[53] L. Veissier, M. Falamarzi, T. Lutz, E. Saglamyurek, C. W. Thiel, R. L. Cone, and W. Tittel. Optical decoherence and spectral diffusion in an erbium-doped silica glass fiber featuring long-lived spin sublevels. *Phys. Rev. B*, 94:195138, November 2016.

[54] E. Saglamyurek, T. Lutz, L. Veissier, M. P. Hedges, C. W. Thiel, R. L. Cone, and W. Tittel. Efficient and long-lived zeeman-sublevel atomic population storage in an erbium-doped glass fiber. *Phys. Rev. B*, 92:241111, December 2015.

[55] M. Gündoğan, P. M. Ledingham, K. Kutluer, M. Mazzera, and H. de Riedmatten. Solid state spin-wave quantum memory for time-bin qubits. *Phys. Rev. Lett.*, 114:230501, June 2015.

[56] N. Timoney, B. Lauritzen, I. Usmani, M. Afzelius, and N. Gisin. Atomic frequency comb memory with spin-wave storage in 153 eu 3 + :y 2 sio 5. *Journal of Physics B: Atomic, Molecular and Optical Physics*, 45(12):124001, 2012.

[57] Y.-W. Cho, G. T. Campbell, J. L. Everett, J. Bernu, D. B. Higginbottom, M. T. Cao, J. Geng, N. P. Robins, P. K. Lam, and B. C. Buchler. Highly efficient optical quantum memory with long coherence time in cold atoms. *Optica*, 3(1):100–107, January 2016.

[58] M. Sabooni, Q. Li, S. Kröll, and L. Rippe. Efficient quantum memory using a weakly absorbing sample. *Phys. Rev. Lett.*, 110:133604, March 2013.

[59] M. P. Hedges, J. J. Longdell, Y. Li, and M. J. Sellars. Efficient quantum memory for light. *Nature*, 465(7301):1052–1056, June 2010.

[60] S. Massar and S. Popescu. Optimal extraction of information from finite quantum ensembles. *Phys. Rev. Lett.*, 74:1259–1263, February 1995.

[61] P. Kok, W. J. Munro, K. Nemoto, T. C. Ralph, J. P. Dowling, and G. J. Milburn. Linear optical quantum computing with photonic qubits. *Rev. Mod. Phys.*, 79:135–174, January 2007.

[62] H-K. Lo, M. Curty, and B. Qi. Measurement-device-independent quantum key distribution. *Phys. Rev. Lett.*, 108:130503, March 2012.

[63] K. Mattle, H. Weinfurter, P. G. Kwiat, and A. Zeilinger. Dense coding in experimental quantum communication. *Phys. Rev. Lett.*, 76:4656–4659, June 1996.

[64] N. Lütkenhaus, J. Calsamiglia, and K.-A. Suominen. Bell measurements for teleportation. *Phys. Rev. A*, 59:3295–3300, May 1999.

[65] E. Knill, R. Laflamme, and G. J. Milburn. A scheme for efficient quantum computation with linear optics. *Nature*, 409(6816):46–52, January 2001.

[66] H. Weinfurter. Experimental bell-state analysis. *EPL (Europhysics Letters)*, 25(8):559, 1994.

[67] W. P. Grice. Arbitrarily complete bell-state measurement using only linear optical elements. *Phys. Rev. A*, 84:042331, Octber 2011.

[68] C. K. Hong, Z. Y. Ou, and L. Mandel. Measurement of subpicosecond time intervals between two photons by interference. *Phys. Rev. Lett.*, 59:2044–2046, November 1987.

[69] T. Grange, N. Somaschi, C. Antón, L. De Santis, G. Coppola, V. Giesz, A. Lemaître, I. Sagnes, A. Auffèves, and P. Senellart. Reducing phonon-induced decoherence in

solid-state single-photon sources with cavity quantum electrodynamics. *Phys. Rev. Lett.*, 118:253602, June 2017.

[70] A. Sipahigil, K. D. Jahnke, L. J. Rogers, T. Teraji, J. Isoya, A. S. Zibrov, F. Jelezko, and M. D. Lukin. Indistinguishable photons from separated silicon-vacancy centers in diamond. *Phys. Rev. Lett.*, 113:113602, September 2014.

[71] S. L. Braunstein and A. Mann. Measurement of the bell operator and quantum teleportation. *Phys. Rev. A*, 51:R1727–R1730, March 1995.

[72] J. A.Stern S. Harrington A. E. Lita T. Gerrits I. Vayshenker B. Baek M. D. Shaw R. P. Mirin F. Marsili, V. B. Verma and S. W. Nam. Detecting single infrared photons with 93 *Nat Photon*, 7(3):210–214, March 2013.

[73] M. D. Eisaman, J. Fan, A. Migdall, and S. V. Polyakov. Invited review article: Single-photon sources and detectors. *Review of Scientific Instruments*, 82(7):071101, July 2011.

[74] R. Valivarthi, I. Lucio-Martinez, A. Rubenok, P. Chan, F. Marsili, V. B. Verma, M. D. Shaw, J. A. Stern, J. A. Slater, D. Oblak, S. W. Nam, and W. Tittel. Efficient bell state analyzer for time-bin qubits with fast-recovery wsi superconducting single photon detectors. *Opt. Express*, 22(20):24497–24506, October 2014.

[75] J-W. Pan, D. Bouwmeester, H. Weinfurter, and A. Zeilinger. Experimental entanglement swapping: Entangling photons that never interacted. *Phys. Rev. Lett.*, 80:3891–3894, May 1998.

[76] D. Bouwmeester, J-W. Pan, K. Mattle, M. Eibl, H. Weinfurter, and A. Zeilinger. Experimental quantum teleportation. *Nature*, 390(6660):575–579, December 1997.

[77] B. Brecht, K-H. Luo, H. Herrmann, and C. Silberhorn. A versatile design for resonant guided-wave parametric down-conversion sources for quantum repeaters. *Applied Physics B*, 122(5):116, April 2016.

[78] H. Krovi, S. Guha, Z. Dutton, J. A. Slater, C. Simon, and W. Tittel. Practical quantum repeaters with parametric down-conversion sources. *Applied Physics B*, 122(3):52, March 2016.

[79] A. E. Lita, A. J. Miller, and S. W. Nam. Counting near-infrared single-photons with 95 *Opt. Express*, 16(5):3032–3040, March 2008.

[80] N. Sinclair, K. Heshami, C. Deshmukh, D. Oblak, C. Simon, and W. Tittel. Proposal and proof-of-principle demonstration of non-destructive detection of photonic qubits using a tm:linbo3 waveguide. 7:13454, November 2016.

[81] J-S. Tang, Z-Q. Zhou, Y-T. Wang, Y-L. Li, X. Liu, Y-L. Hua, Y. Zou, S. Wang, D-Y. He, G. Chen, Y-N. Sun, Y. Yu, M-F. Li, G-W. Zha, H.-Q. Ni, Z.-C. Niu, C-F. Li, and G-C. Guo. Storage of multiple single-photon pulses emitted from a quantum dot in a solid-state quantum memory. 6:8652, October 2015.

[82] I. Aharonovich, D. Englund, and M. Toth. Solid-state single-photon emitters. *Nat Photon*, 10(10):631–641, October 2016.

[83] A. W. Elshaari, I. E. Zadeh, A. Fognini, M. E. Reimer, D. Dalacu, P. J. Poole, V. Zwiller, and K. D. Jns. On-chip single photon filtering and multiplexing in hybrid quantum photonic circuits. *Nature Communications*, 8(1):379, August 2017.

[84] Kylia. www.kylia.com. Accessed: 2017-10-21.

[85] C. Joshi, A. Farsi, S. Clemmen, S. Ramelow, and A. L. Gaeta. Frequency multiplexing for quasi-deterministic heralded single-photon sources. *arXiv:1707.00048*.

Appendix A

Copyright and permissions

This appendix states the copyright permissions required to include papers 1-5 as well as the permissions from all the co-author to include the publications in this thesis.

Papers 1, 3 and 4 are published in journals of the American Physical Society (APS). As an author of an APS-published journal the I jhave the right to include an article or a portion of it in my thesis. An screenshot showing the reprint and permission policy is included below (See figure A.1).

Papers 2 and 5 are published in Nature group journals. It this case, it suffices to acknowledge and cite the article in question. An screenshot showing the reprint and permission policy is included below (See figure A.2).

A list with all the co-authors is included below. An email granting permission to include in this thesis all the publications in which they are co-autors is included for each co-author.

A.1 Journal copyright permissions

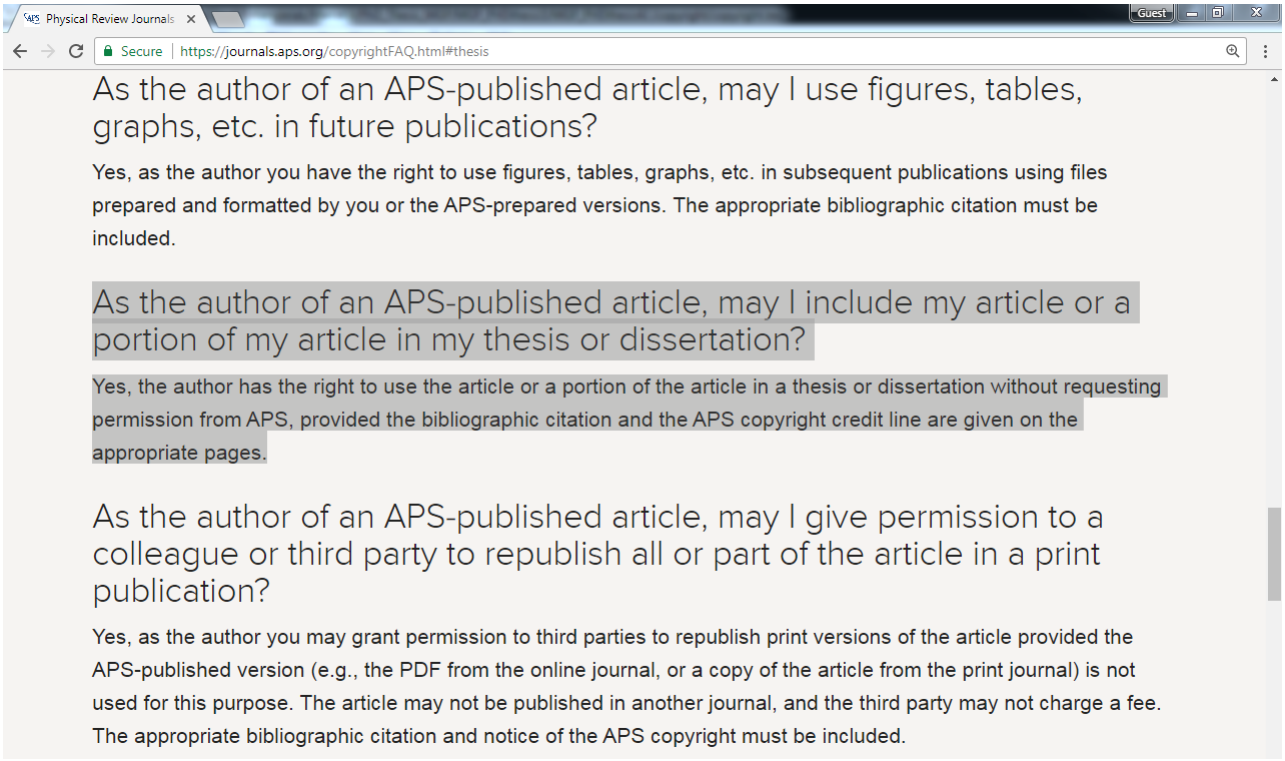

Figure A.1: Proof of copyright of papers 1, 3 and 4. Webpage accessed in December 2017

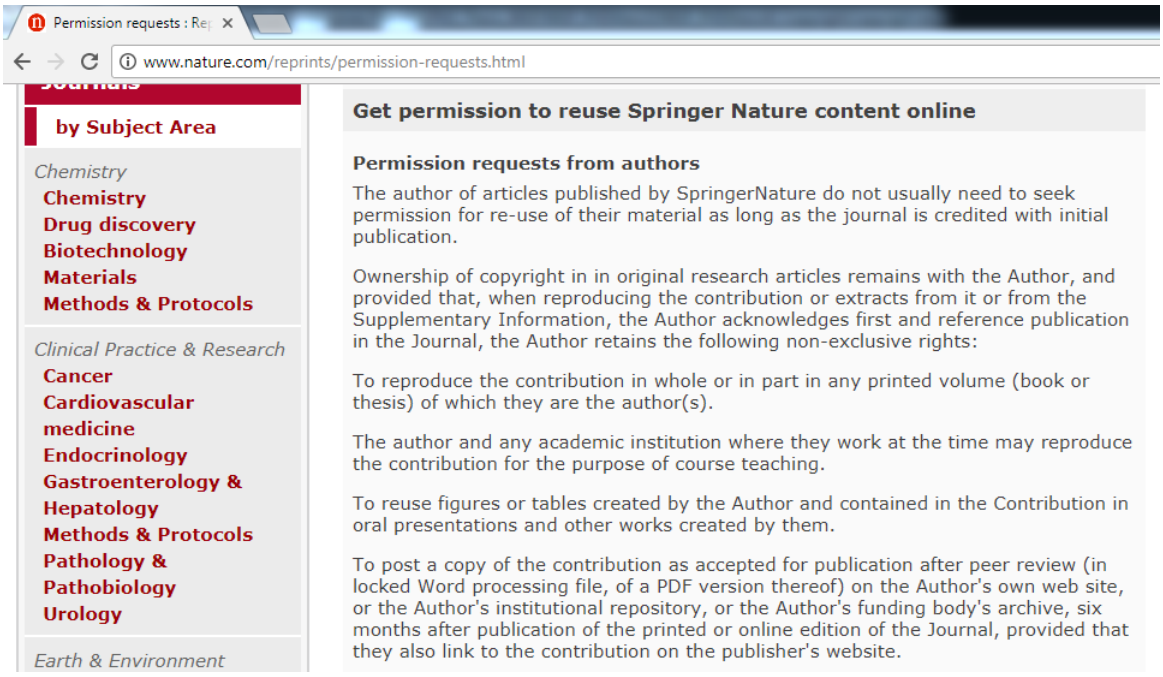

Figure A.2: Proof of copyright of papers 2 and 5. Webpage accessed in December 2017

A.2 Permissions from co-authors

- W. Tittel, figure A.3.
- D. Oblak, figure A.4.
- G. H. Aguilar, A.5.
- V. R. Valivarthi, A.6.
- Qiang Zhou, A.7.
- Lambert Giner, A.8.
- Joshua Slater, A.9.
- V. B. Verma, A.10.

- M. D. Shaw, A.11.
- S. W. Nam, A.12.
- F. Marsili, A.13.
- E. Saglamyurek, A.14.
- J. Jin, A.15.
- M. R. E Lamont, A.16.
- L. Oesterling, A.17.
- D. Nippa, A.18.

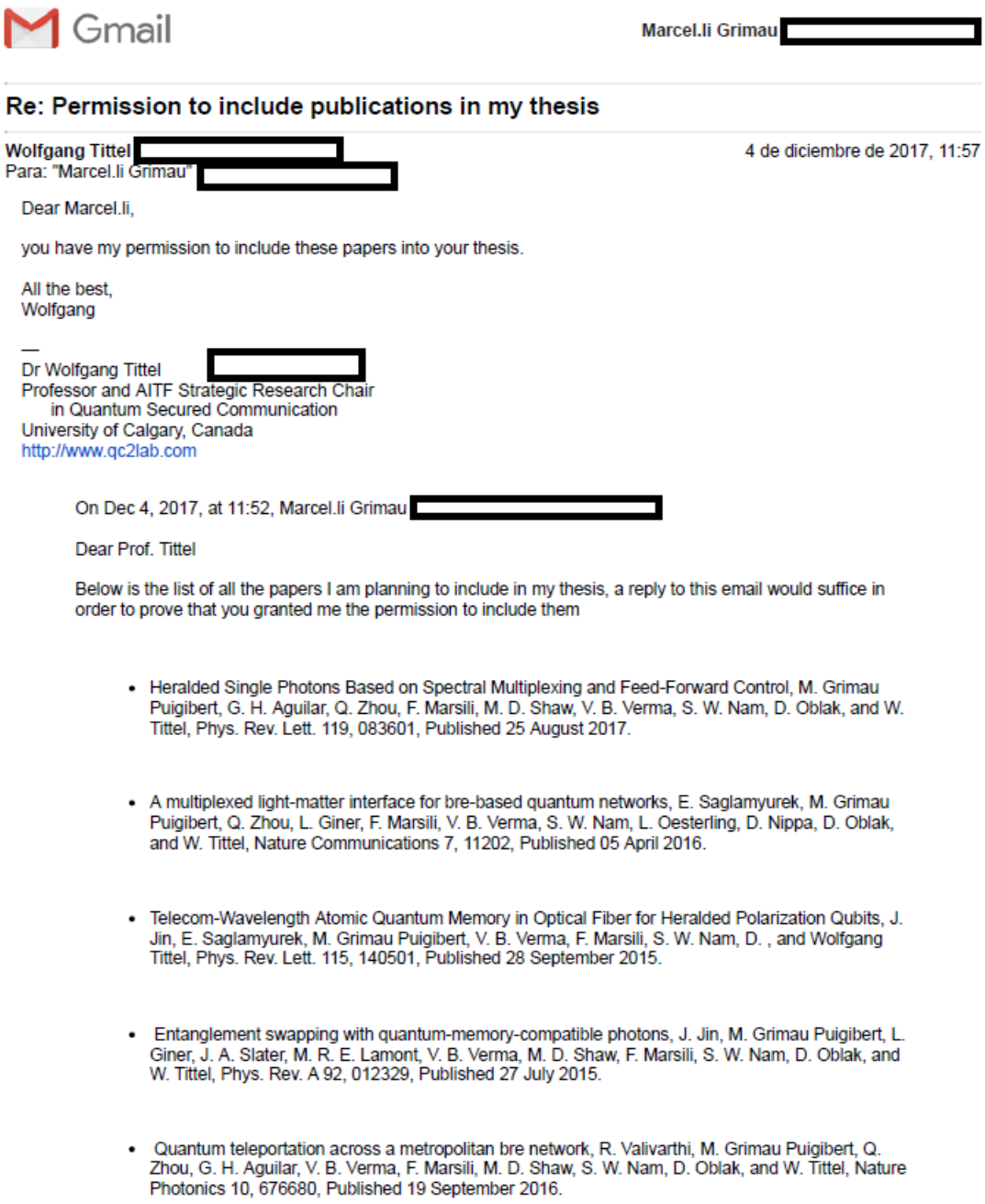

Gmail Marcel.li Grimau [redacted]

Re: Permission to include publications in my thesis

Wolfgang Tittel [redacted] 4 de diciembre de 2017, 11:57
Para: "Marcel.li Grimau" [redacted]

Dear Marcel.li,

you have my permission to include these papers into your thesis.

All the best,
Wolfgang

—
Dr Wolfgang Tittel [redacted]
Professor and AITF Strategic Research Chair
in Quantum Secured Communication
University of Calgary, Canada
http://www.qc2lab.com

On Dec 4, 2017, at 11:52, Marcel.li Grimau [redacted]

Dear Prof. Tittel

Below is the list of all the papers I am planning to include in my thesis, a reply to this email would suffice in order to prove that you granted me the permission to include them

- Heralded Single Photons Based on Spectral Multiplexing and Feed-Forward Control, M. Grimau Puigibert, G. H. Aguilar, Q. Zhou, F. Marsili, M. D. Shaw, V. B. Verma, S. W. Nam, D. Oblak, and W. Tittel, Phys. Rev. Lett. 119, 083601, Published 25 August 2017.

- A multiplexed light-matter interface for bre-based quantum networks, E. Saglamyurek, M. Grimau Puigibert, Q. Zhou, L. Giner, F. Marsili, V. B. Verma, S. W. Nam, L. Oesterling, D. Nippa, D. Oblak, and W. Tittel, Nature Communications 7, 11202, Published 05 April 2016.

- Telecom-Wavelength Atomic Quantum Memory in Optical Fiber for Heralded Polarization Qubits, J. Jin, E. Saglamyurek, M. Grimau Puigibert, V. B. Verma, F. Marsili, S. W. Nam, D. , and Wolfgang Tittel, Phys. Rev. Lett. 115, 140501, Published 28 September 2015.

- Entanglement swapping with quantum-memory-compatible photons, J. Jin, M. Grimau Puigibert, L. Giner, J. A. Slater, M. R. E. Lamont, V. B. Verma, M. D. Shaw, F. Marsili, S. W. Nam, D. Oblak, and W. Tittel, Phys. Rev. A 92, 012329, Published 27 July 2015.

- Quantum teleportation across a metropolitan bre network, R. Valivarthi, M. Grimau Puigibert, Q. Zhou, G. H. Aguilar, V. B. Verma, F. Marsili, M. D. Shaw, S. W. Nam, D. Oblak, and W. Tittel, Nature Photonics 10, 676680, Published 19 September 2016.

Figure A.3: Email from W. Tittel granting me permission to include co-authored papers.

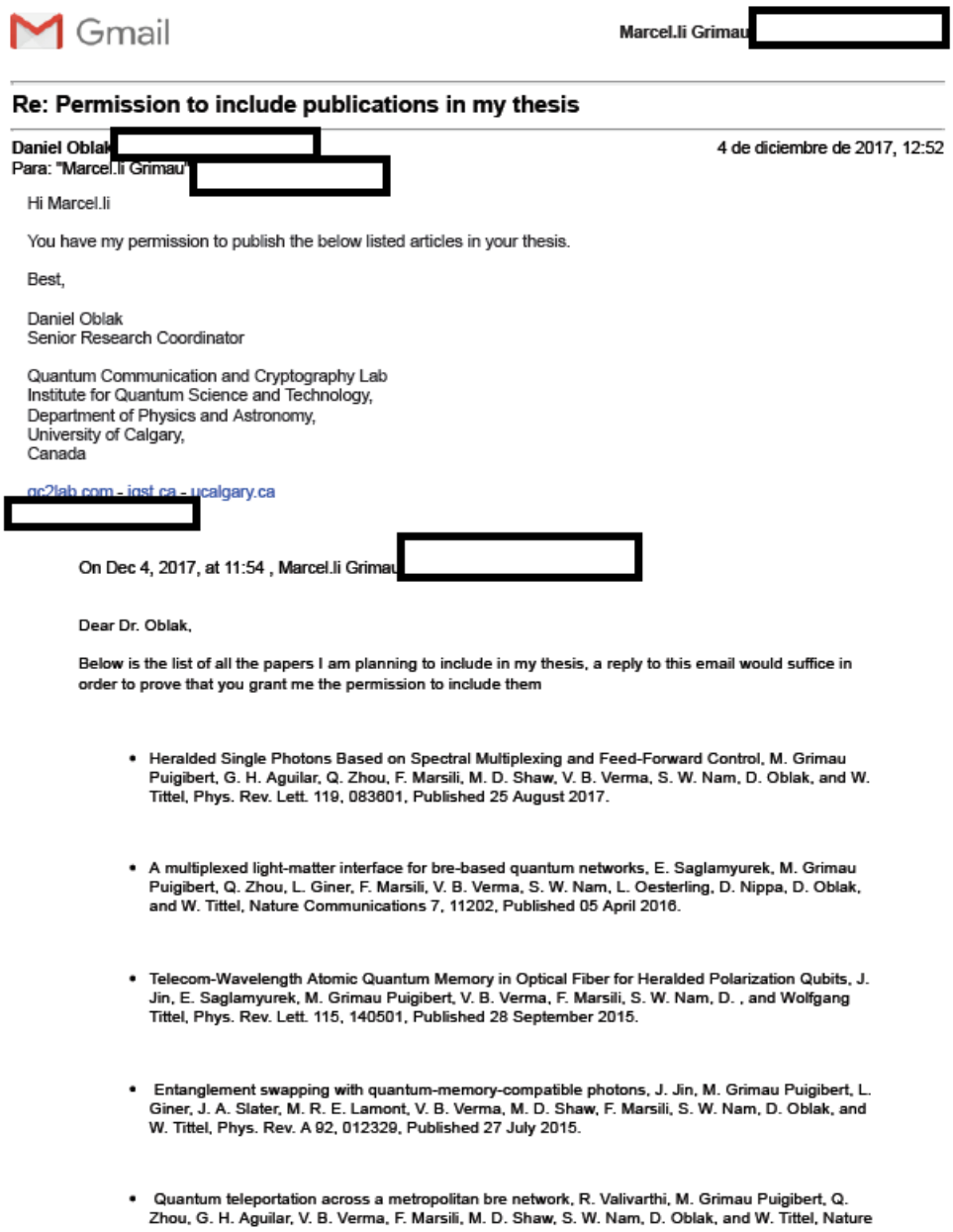

Gmail Marcel.li Grimau [redacted]

Re: Permission to include publications in my thesis

Daniel Oblak [redacted] 4 de diciembre de 2017, 12:52
Para: "Marcel.li Grimau" [redacted]

Hi Marcel.li

You have my permission to publish the below listed articles in your thesis.

Best,

Daniel Oblak
Senior Research Coordinator

Quantum Communication and Cryptography Lab
Institute for Quantum Science and Technology,
Department of Physics and Astronomy,
University of Calgary,
Canada

qc2lab.com - iqst.ca - ucalgary.ca

[redacted]

On Dec 4, 2017, at 11:54 , Marcel.li Grimau [redacted]

Dear Dr. Oblak,

Below is the list of all the papers I am planning to include in my thesis, a reply to this email would suffice in order to prove that you grant me the permission to include them

- **Heralded Single Photons Based on Spectral Multiplexing and Feed-Forward Control, M. Grimau Puigibert, G. H. Aguilar, Q. Zhou, F. Marsili, M. D. Shaw, V. B. Verma, S. W. Nam, D. Oblak, and W. Tittel, Phys. Rev. Lett. 119, 083601, Published 25 August 2017.**
- **A multiplexed light-matter interface for bre-based quantum networks, E. Saglamyurek, M. Grimau Puigibert, Q. Zhou, L. Giner, F. Marsili, V. B. Verma, S. W. Nam, L. Oesterling, D. Nippa, D. Oblak, and W. Tittel, Nature Communications 7, 11202, Published 05 April 2016.**
- **Telecom-Wavelength Atomic Quantum Memory in Optical Fiber for Heralded Polarization Qubits, J. Jin, E. Saglamyurek, M. Grimau Puigibert, V. B. Verma, F. Marsili, S. W. Nam, D. , and Wolfgang Tittel, Phys. Rev. Lett. 115, 140501, Published 28 September 2015.**
- **Entanglement swapping with quantum-memory-compatible photons, J. Jin, M. Grimau Puigibert, L. Giner, J. A. Slater, M. R. E. Lamont, V. B. Verma, M. D. Shaw, F. Marsili, S. W. Nam, D. Oblak, and W. Tittel, Phys. Rev. A 92, 012329, Published 27 July 2015.**
- **Quantum teleportation across a metropolitan bre network, R. Valivarthi, M. Grimau Puigibert, Q. Zhou, G. H. Aguilar, V. B. Verma, F. Marsili, M. D. Shaw, S. W. Nam, D. Oblak, and W. Tittel, Nature**

Figure A.4: Email from D. Oblak granting me permission to include co-authored papers.

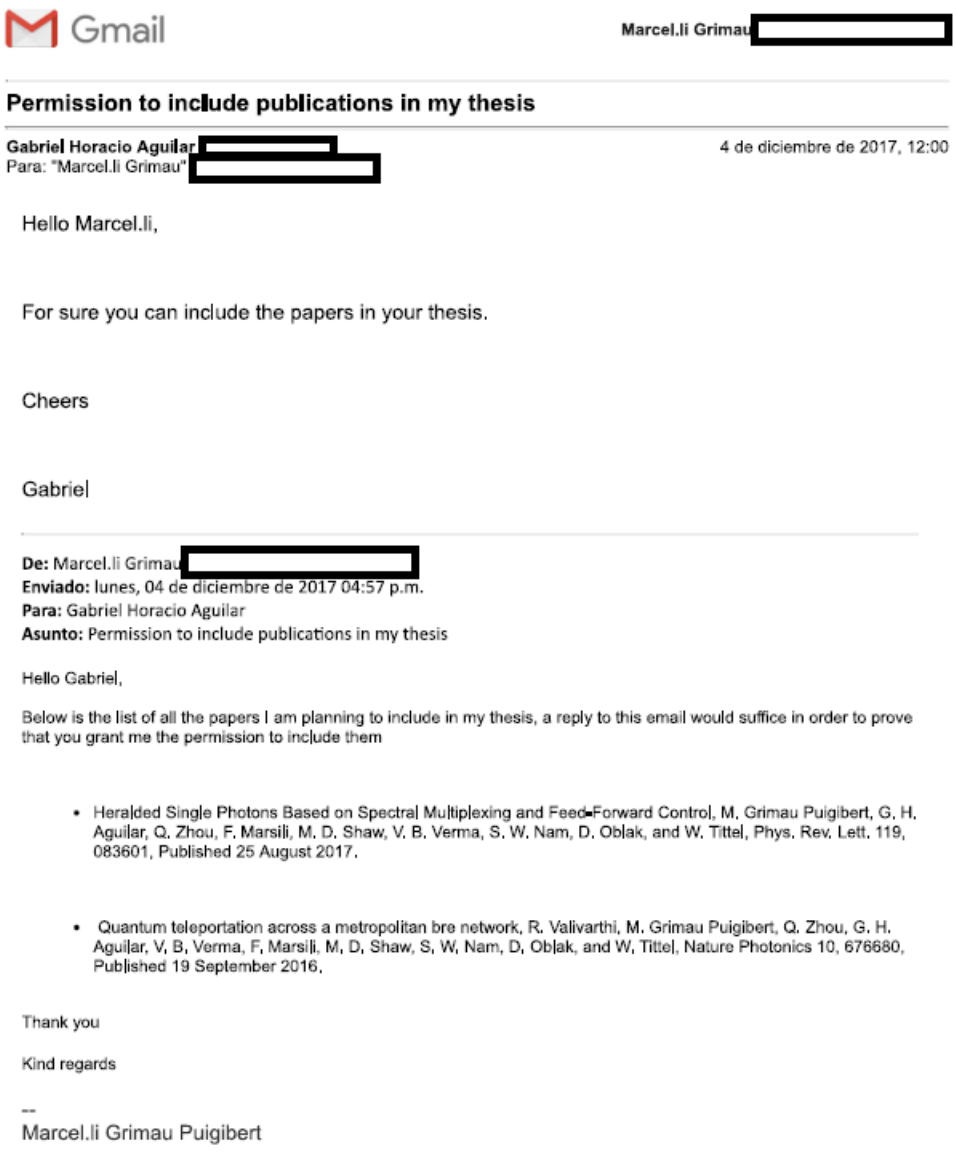

Gmail Marcel.li Grimau [redacted]

Permission to include publications in my thesis

Gabriel Horacio Aguilar [redacted] 4 de diciembre de 2017, 12:00
Para: "Marcel.li Grimau" [redacted]

Hello Marcel.li,

For sure you can include the papers in your thesis.

Cheers

Gabriel

De: Marcel.li Grimau [redacted]
Enviado: lunes, 04 de diciembre de 2017 04:57 p.m.
Para: Gabriel Horacio Aguilar
Asunto: Permission to include publications in my thesis

Hello Gabriel,

Below is the list of all the papers I am planning to include in my thesis, a reply to this email would suffice in order to prove that you grant me the permission to include them

- Heralded Single Photons Based on Spectral Multiplexing and Feed-Forward Control, M. Grimau Puigibert, G. H. Aguilar, Q. Zhou, F. Marsili, M. D. Shaw, V. B. Verma, S. W. Nam, D. Oblak, and W. Tittel, Phys. Rev. Lett. 119, 083601, Published 25 August 2017.

- Quantum teleportation across a metropolitan bre network, R. Valivarthi, M. Grimau Puigibert, Q. Zhou, G. H. Aguilar, V, B, Verma, F, Marsili, M, D, Shaw, S, W, Nam, D, Oblak, and W, Tittel, Nature Photonics 10, 676680, Published 19 September 2016,

Thank you

Kind regards

--
Marcel.li Grimau Puigibert

Figure A.5: Email from G. H. Aguilar granting me permission to include co-authored papers.

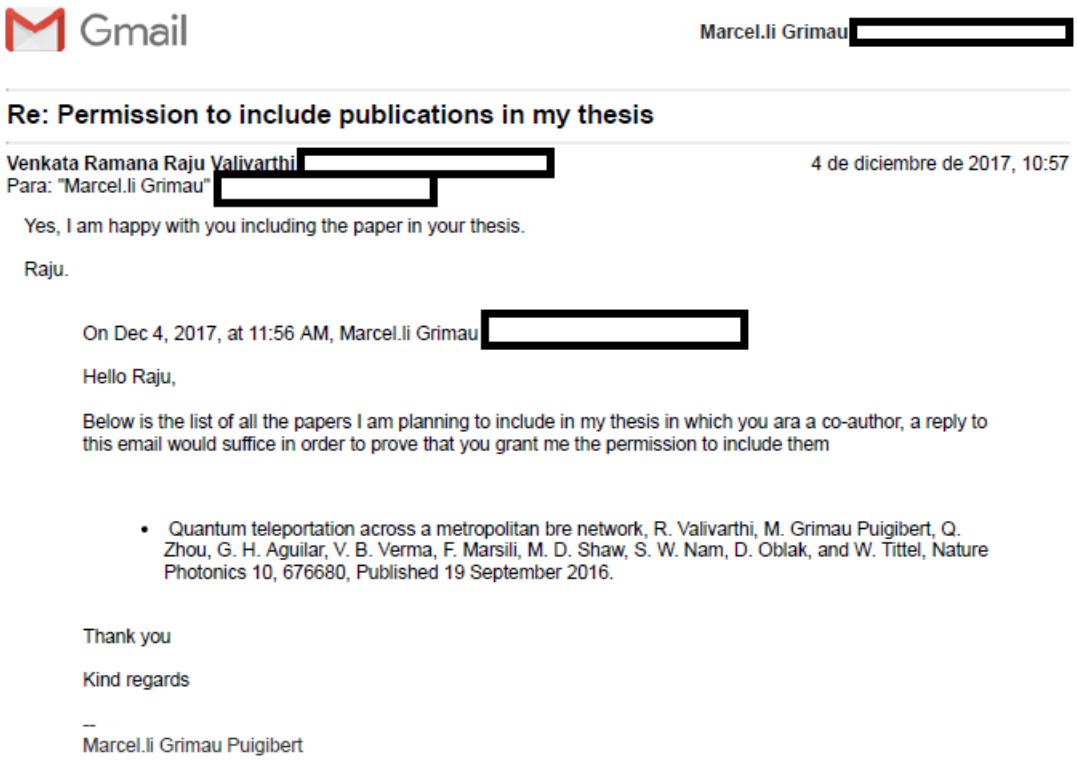

Gmail Marcel.li Grimau [redacted]

Re: Permission to include publications in my thesis

Venkata Ramana Raju Valivarthi [redacted] 4 de diciembre de 2017, 10:57
Para: "Marcel.li Grimau" [redacted]

Yes, I am happy with you including the paper in your thesis.

Raju.

On Dec 4, 2017, at 11:56 AM, Marcel.li Grimau [redacted]

Hello Raju,

Below is the list of all the papers I am planning to include in my thesis in which you ara a co-author, a reply to this email would suffice in order to prove that you grant me the permission to include them

- Quantum teleportation across a metropolitan bre network, R. Valivarthi, M. Grimau Puigibert, Q. Zhou, G. H. Aguilar, V. B. Verma, F. Marsili, M. D. Shaw, S. W. Nam, D. Oblak, and W. Tittel, Nature Photonics 10, 676680, Published 19 September 2016.

Thank you

Kind regards

--
Marcel.li Grimau Puigibert

Figure A.6: Email from V. R. Valivarthi granting me permission to include co-authored papers.

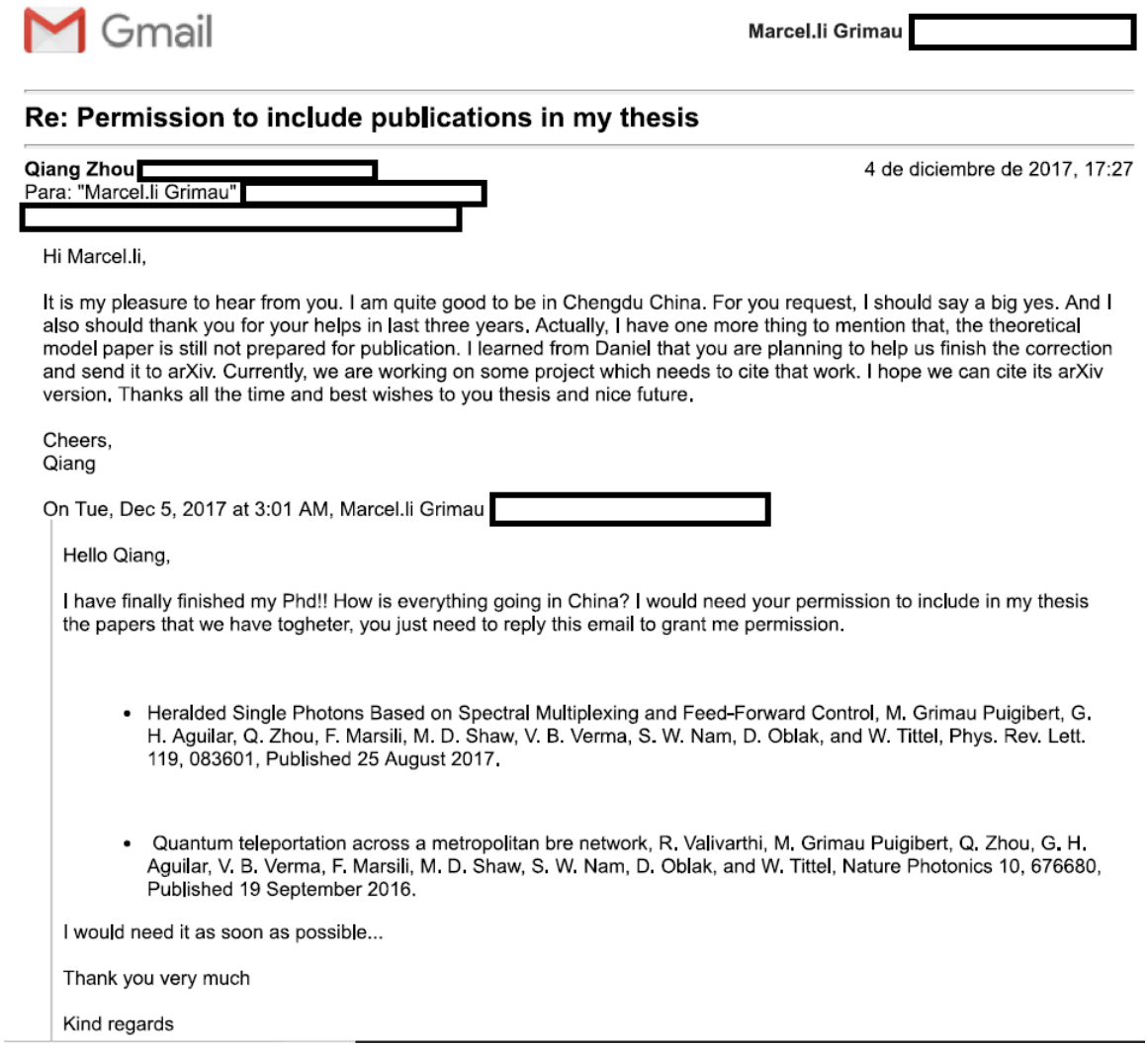

Gmail Marcel.li Grimau [redacted]

Re: Permission to include publications in my thesis

Qiang Zhou [redacted] 4 de diciembre de 2017, 17:27
Para: "Marcel.li Grimau" [redacted]

Hi Marcel.li,

It is my pleasure to hear from you. I am quite good to be in Chengdu China. For you request, I should say a big yes. And I also should thank you for your helps in last three years. Actually, I have one more thing to mention that, the theoretical model paper is still not prepared for publication. I learned from Daniel that you are planning to help us finish the correction and send it to arXiv. Currently, we are working on some project which needs to cite that work. I hope we can cite its arXiv version. Thanks all the time and best wishes to you thesis and nice future.

Cheers,
Qiang

On Tue, Dec 5, 2017 at 3:01 AM, Marcel.li Grimau [redacted]

> Hello Qiang,
>
> I have finally finished my Phd!! How is everything going in China? I would need your permission to include in my thesis the papers that we have togheter, you just need to reply this email to grant me permission.
>
> - Heralded Single Photons Based on Spectral Multiplexing and Feed-Forward Control, M. Grimau Puigibert, G. H. Aguilar, Q. Zhou, F. Marsili, M. D. Shaw, V. B. Verma, S. W. Nam, D. Oblak, and W. Tittel, Phys. Rev. Lett. 119, 083601, Published 25 August 2017.
>
> - Quantum teleportation across a metropolitan bre network, R. Valivarthi, M. Grimau Puigibert, Q. Zhou, G. H. Aguilar, V. B. Verma, F. Marsili, M. D. Shaw, S. W. Nam, D. Oblak, and W. Tittel, Nature Photonics 10, 676680, Published 19 September 2016.
>
> I would need it as soon as possible...
>
> Thank you very much
>
> Kind regards

Figure A.7: Email from Q. Zhou granting me permission to include co-authored papers.

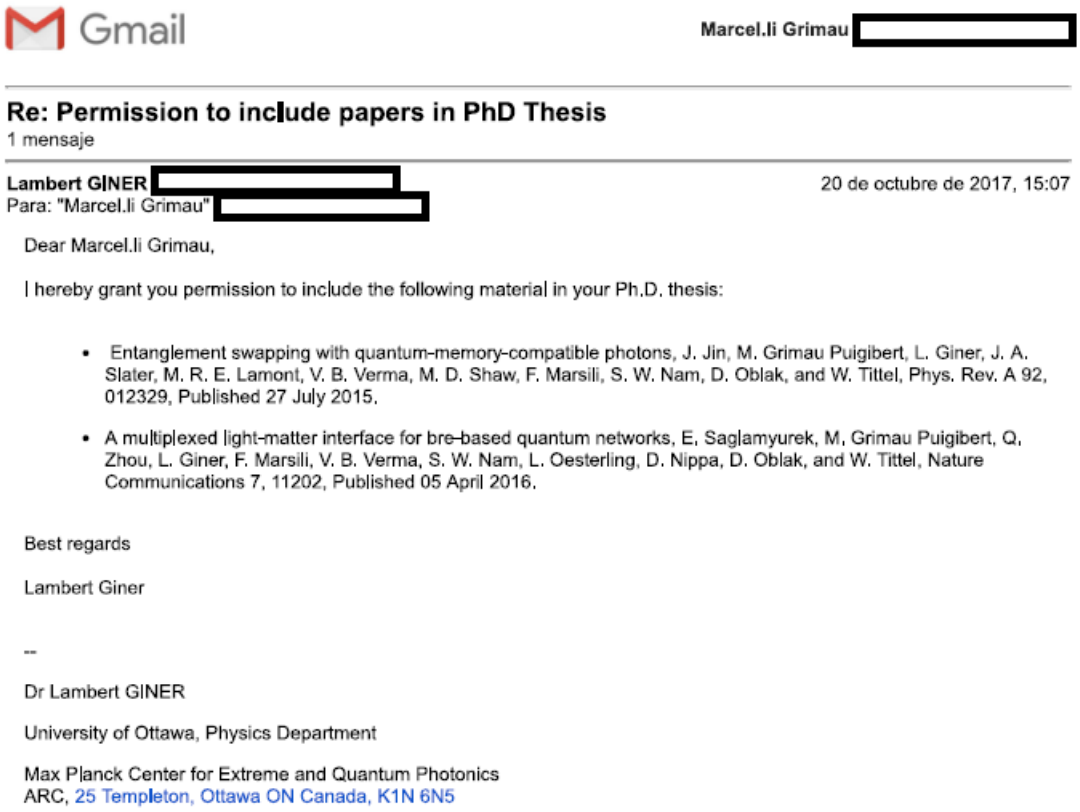

Gmail Marcel.li Grimau [redacted]

Re: Permission to include papers in PhD Thesis

1 mensaje

Lambert GINER [redacted] 20 de octubre de 2017, 15:07

Para: "Marcel.li Grimau" [redacted]

Dear Marcel.li Grimau,

I hereby grant you permission to include the following material in your Ph.D. thesis:

- Entanglement swapping with quantum-memory-compatible photons, J. Jin, M. Grimau Puigibert, L. Giner, J. A. Slater, M. R. E. Lamont, V. B. Verma, M. D. Shaw, F. Marsili, S. W. Nam, D. Oblak, and W. Tittel, Phys. Rev. A 92, 012329, Published 27 July 2015.
- A multiplexed light-matter interface for bre-based quantum networks, E, Saglamyurek, M, Grimau Puigibert, Q, Zhou, L. Giner, F. Marsili, V. B. Verma, S. W. Nam, L. Oesterling, D. Nippa, D. Oblak, and W. Tittel, Nature Communications 7, 11202, Published 05 April 2016.

Best regards

Lambert Giner

--

Dr Lambert GINER

University of Ottawa, Physics Department

Max Planck Center for Extreme and Quantum Photonics
ARC, 25 Templeton, Ottawa ON Canada, K1N 6N5

Figure A.8: Email from L. Giner granting me permission to include co-authored papers.

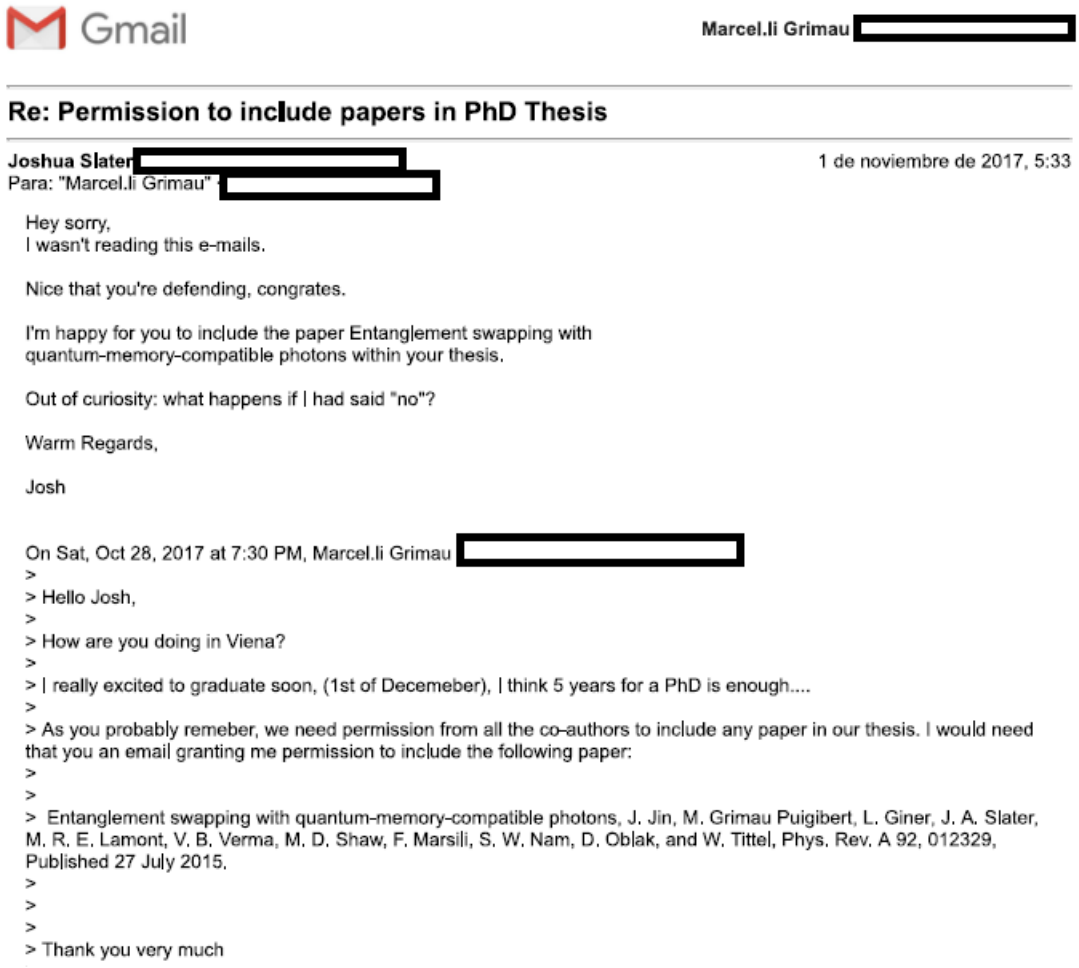

Gmail Marcel.li Grimau [redacted]

Re: Permission to include papers in PhD Thesis

Joshua Slater [redacted] 1 de noviembre de 2017, 5:33
Para: "Marcel.li Grimau" [redacted]

Hey sorry,
I wasn't reading this e-mails.

Nice that you're defending, congrates.

I'm happy for you to include the paper Entanglement swapping with quantum-memory-compatible photons within your thesis.

Out of curiosity: what happens if I had said "no"?

Warm Regards,

Josh

On Sat, Oct 28, 2017 at 7:30 PM, Marcel.li Grimau [redacted]
>
> Hello Josh,
>
> How are you doing in Viena?
>
> I really excited to graduate soon, (1st of Decemeber), I think 5 years for a PhD is enough....
>
> As you probably remeber, we need permission from all the co-authors to include any paper in our thesis. I would need that you an email granting me permission to include the following paper:
>
>
> Entanglement swapping with quantum-memory-compatible photons, J. Jin, M. Grimau Puigibert, L. Giner, J. A. Slater, M. R. E. Lamont, V. B. Verma, M. D. Shaw, F. Marsili, S. W. Nam, D. Oblak, and W. Tittel, Phys. Rev. A 92, 012329, Published 27 July 2015.
>
>
>
> Thank you very much

Figure A.9: Email from J. A. Slater granting me permission to include co-authored papers.

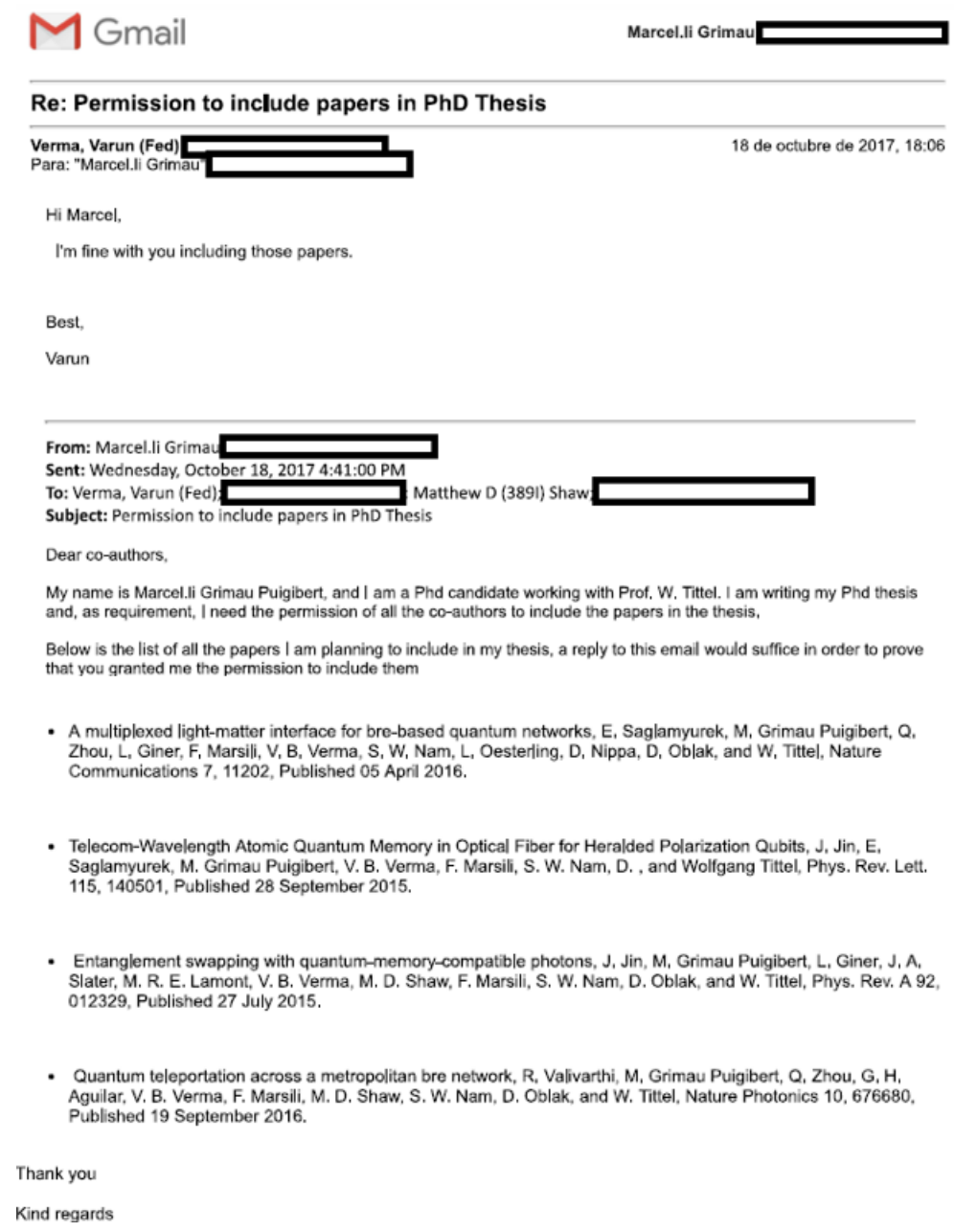

Gmail Marcel.li Grimau [redacted]

Re: Permission to include papers in PhD Thesis

Verma, Varun (Fed) [redacted] 18 de octubre de 2017, 18:06
Para: "Marcel.li Grimau" [redacted]

Hi Marcel,

I'm fine with you including those papers.

Best,

Varun

From: Marcel.li Grimau [redacted]
Sent: Wednesday, October 18, 2017 4:41:00 PM
To: Verma, Varun (Fed); [redacted] Matthew D (389I) Shaw; [redacted]
Subject: Permission to include papers in PhD Thesis

Dear co-authors,

My name is Marcel.li Grimau Puigibert, and I am a Phd candidate working with Prof. W. Tittel. I am writing my Phd thesis and, as requirement, I need the permission of all the co-authors to include the papers in the thesis.

Below is the list of all the papers I am planning to include in my thesis, a reply to this email would suffice in order to prove that you granted me the permission to include them

- A multiplexed light-matter interface for bre-based quantum networks, E, Saglamyurek, M, Grimau Puigibert, Q, Zhou, L, Giner, F, Marsili, V, B, Verma, S, W, Nam, L, Oesterling, D, Nippa, D, Oblak, and W, Tittel, Nature Communications 7, 11202, Published 05 April 2016.

- Telecom-Wavelength Atomic Quantum Memory in Optical Fiber for Heralded Polarization Qubits, J, Jin, E, Saglamyurek, M. Grimau Puigibert, V. B. Verma, F. Marsili, S. W. Nam, D. , and Wolfgang Tittel, Phys. Rev. Lett. 115, 140501, Published 28 September 2015.

- Entanglement swapping with quantum-memory-compatible photons, J, Jin, M, Grimau Puigibert, L, Giner, J, A, Slater, M. R. E. Lamont, V. B. Verma, M. D. Shaw, F. Marsili, S. W. Nam, D. Oblak, and W. Tittel, Phys. Rev. A 92, 012329, Published 27 July 2015.

- Quantum teleportation across a metropolitan bre network, R, Valivarthi, M, Grimau Puigibert, Q, Zhou, G, H, Aguilar, V. B. Verma, F. Marsili, M. D. Shaw, S. W. Nam, D. Oblak, and W. Tittel, Nature Photonics 10, 676680, Published 19 September 2016.

Thank you

Kind regards

Figure A.10: Email from V. B. Verma granting me permission to include co-authored papers.

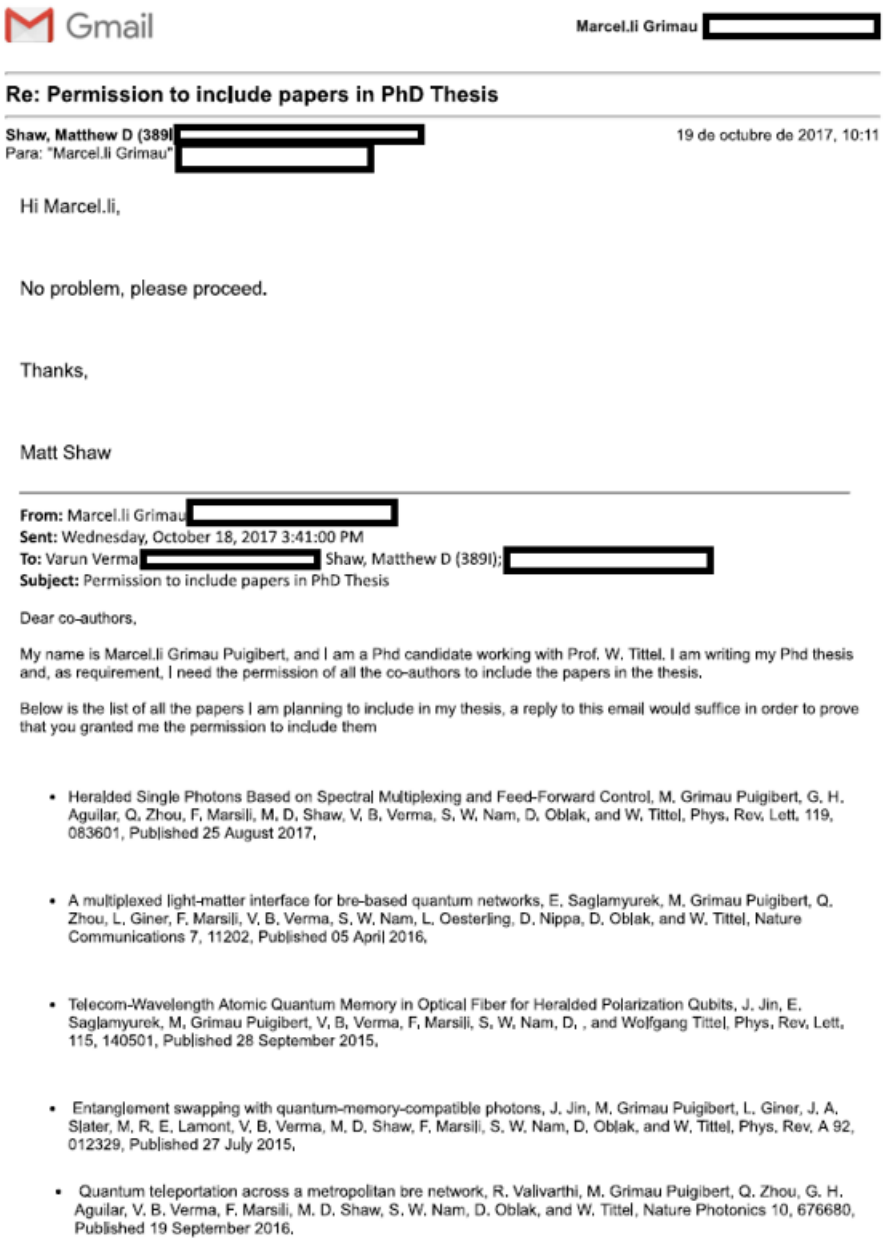

Gmail Marcel.li Grimau [redacted]

Re: Permission to include papers in PhD Thesis

Shaw, Matthew D (389I [redacted] 19 de octubre de 2017, 10:11
Para: "Marcel.li Grimau" [redacted]

Hi Marcel.li,

No problem, please proceed.

Thanks,

Matt Shaw

From: Marcel.li Grimau [redacted]
Sent: Wednesday, October 18, 2017 3:41:00 PM
To: Varun Verma [redacted] Shaw, Matthew D (389I); [redacted]
Subject: Permission to include papers in PhD Thesis

Dear co-authors,

My name is Marcel.li Grimau Puigibert, and I am a Phd candidate working with Prof. W. Tittel. I am writing my Phd thesis and, as requirement, I need the permission of all the co-authors to include the papers in the thesis.

Below is the list of all the papers I am planning to include in my thesis, a reply to this email would suffice in order to prove that you granted me the permission to include them

- Heralded Single Photons Based on Spectral Multiplexing and Feed-Forward Control, M. Grimau Puigibert, G. H. Aguilar, Q. Zhou, F. Marsili, M. D. Shaw, V. B. Verma, S. W. Nam, D. Oblak, and W. Tittel, Phys. Rev. Lett. 119, 083601, Published 25 August 2017,

- A multiplexed light-matter interface for bre-based quantum networks, E. Saglamyurek, M. Grimau Puigibert, Q. Zhou, L. Giner, F. Marsili, V. B. Verma, S. W. Nam, L. Oesterling, D. Nippa, D. Oblak, and W. Tittel, Nature Communications 7, 11202, Published 05 April 2016,

- Telecom-Wavelength Atomic Quantum Memory in Optical Fiber for Heralded Polarization Qubits, J. Jin, E. Saglamyurek, M. Grimau Puigibert, V. B. Verma, F. Marsili, S. W. Nam, D. , and Wolfgang Tittel, Phys. Rev. Lett. 115, 140501, Published 28 September 2015,

- Entanglement swapping with quantum-memory-compatible photons, J. Jin, M. Grimau Puigibert, L. Giner, J. A. Slater, M. R. E. Lamont, V. B. Verma, M. D. Shaw, F. Marsili, S. W. Nam, D. Oblak, and W. Tittel, Phys. Rev. A 92, 012329, Published 27 July 2015,

- Quantum teleportation across a metropolitan bre network, R. Valivarthi, M. Grimau Puigibert, Q. Zhou, G. H. Aguilar, V. B. Verma, F. Marsili, M. D. Shaw, S. W. Nam, D. Oblak, and W. Tittel, Nature Photonics 10, 676680, Published 19 September 2016.

Figure A.11: Email from M. D. Shaw granting me permission to include co-authored papers.

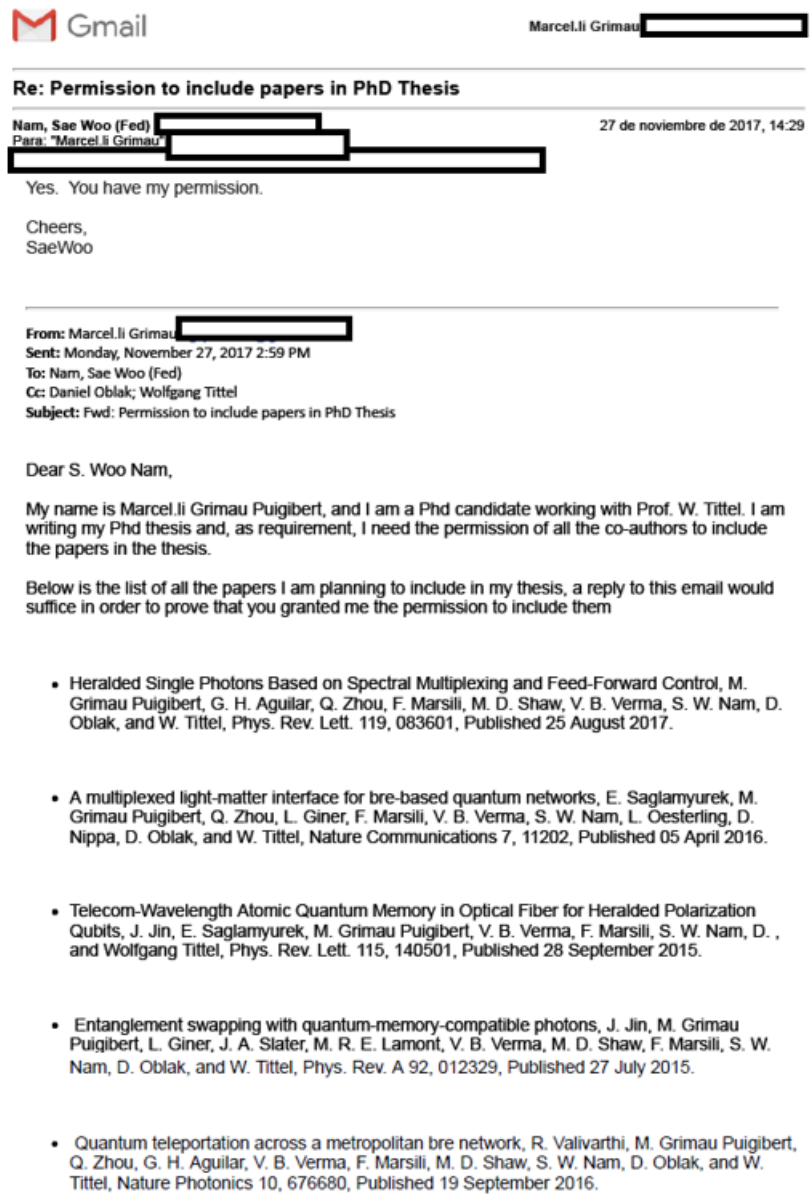

Gmail Marcel.li Grimau [redacted]

Re: Permission to include papers in PhD Thesis

Nam, Sae Woo (Fed) [redacted] 27 de noviembre de 2017, 14:29
Para: "Marcel.li Grimau" [redacted]

Yes. You have my permission.

Cheers,
SaeWoo

From: Marcel.li Grimau [redacted]
Sent: Monday, November 27, 2017 2:59 PM
To: Nam, Sae Woo (Fed)
Cc: Daniel Oblak; Wolfgang Tittel
Subject: Fwd: Permission to include papers in PhD Thesis

Dear S. Woo Nam,

My name is Marcel.li Grimau Puigibert, and I am a Phd candidate working with Prof. W. Tittel. I am writing my Phd thesis and, as requirement, I need the permission of all the co-authors to include the papers in the thesis.

Below is the list of all the papers I am planning to include in my thesis, a reply to this email would suffice in order to prove that you granted me the permission to include them

- Heralded Single Photons Based on Spectral Multiplexing and Feed-Forward Control, M. Grimau Puigibert, G. H. Aguilar, Q. Zhou, F. Marsili, M. D. Shaw, V. B. Verma, S. W. Nam, D. Oblak, and W. Tittel, Phys. Rev. Lett. 119, 083601, Published 25 August 2017.

- A multiplexed light-matter interface for bre-based quantum networks, E. Saglamyurek, M. Grimau Puigibert, Q. Zhou, L. Giner, F. Marsili, V. B. Verma, S. W. Nam, L. Oesterling, D. Nippa, D. Oblak, and W. Tittel, Nature Communications 7, 11202, Published 05 April 2016.

- Telecom-Wavelength Atomic Quantum Memory in Optical Fiber for Heralded Polarization Qubits, J. Jin, E. Saglamyurek, M. Grimau Puigibert, V. B. Verma, F. Marsili, S. W. Nam, D. , and Wolfgang Tittel, Phys. Rev. Lett. 115, 140501, Published 28 September 2015.

- Entanglement swapping with quantum-memory-compatible photons, J. Jin, M. Grimau Puigibert, L. Giner, J. A. Slater, M. R. E. Lamont, V. B. Verma, M. D. Shaw, F. Marsili, S. W. Nam, D. Oblak, and W. Tittel, Phys. Rev. A 92, 012329, Published 27 July 2015.

- Quantum teleportation across a metropolitan bre network, R. Valivarthi, M. Grimau Puigibert, Q. Zhou, G. H. Aguilar, V. B. Verma, F. Marsili, M. D. Shaw, S. W. Nam, D. Oblak, and W. Tittel, Nature Photonics 10, 676680, Published 19 September 2016.

Figure A.12: Email from S. W. Nam granting me permission to include co-authored papers.

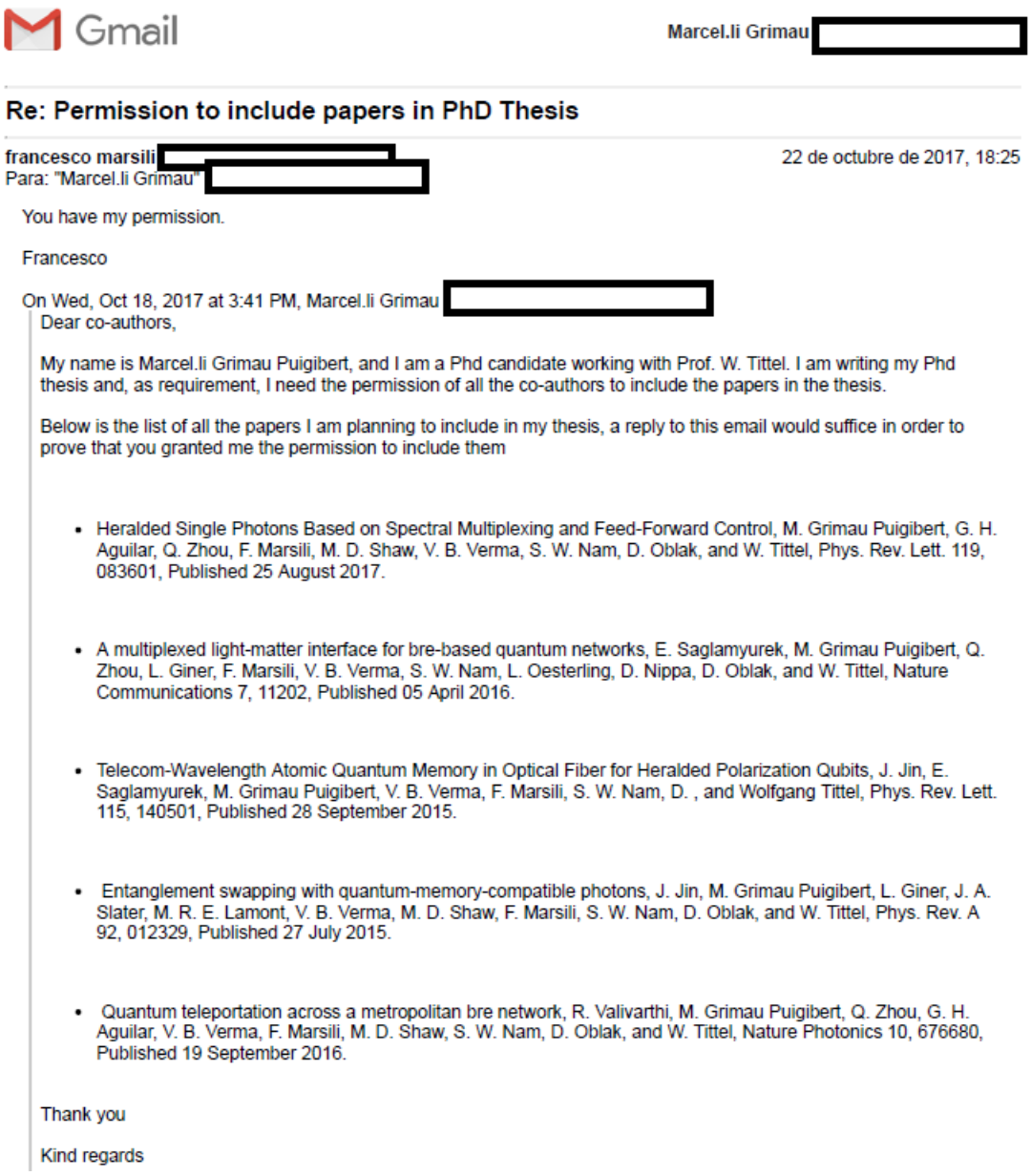

Gmail Marcel.li Grimau [redacted]

Re: Permission to include papers in PhD Thesis

francesco marsili [redacted] 22 de octubre de 2017, 18:25
Para: "Marcel.li Grimau" [redacted]

You have my permission.

Francesco

On Wed, Oct 18, 2017 at 3:41 PM, Marcel.li Grimau [redacted]

> Dear co-authors,
>
> My name is Marcel.li Grimau Puigibert, and I am a Phd candidate working with Prof. W. Tittel. I am writing my Phd thesis and, as requirement, I need the permission of all the co-authors to include the papers in the thesis.
>
> Below is the list of all the papers I am planning to include in my thesis, a reply to this email would suffice in order to prove that you granted me the permission to include them
>
> - Heralded Single Photons Based on Spectral Multiplexing and Feed-Forward Control, M. Grimau Puigibert, G. H. Aguilar, Q. Zhou, F. Marsili, M. D. Shaw, V. B. Verma, S. W. Nam, D. Oblak, and W. Tittel, Phys. Rev. Lett. 119, 083601, Published 25 August 2017.
> - A multiplexed light-matter interface for bre-based quantum networks, E. Saglamyurek, M. Grimau Puigibert, Q. Zhou, L. Giner, F. Marsili, V. B. Verma, S. W. Nam, L. Oesterling, D. Nippa, D. Oblak, and W. Tittel, Nature Communications 7, 11202, Published 05 April 2016.
> - Telecom-Wavelength Atomic Quantum Memory in Optical Fiber for Heralded Polarization Qubits, J. Jin, E. Saglamyurek, M. Grimau Puigibert, V. B. Verma, F. Marsili, S. W. Nam, D. , and Wolfgang Tittel, Phys. Rev. Lett. 115, 140501, Published 28 September 2015.
> - Entanglement swapping with quantum-memory-compatible photons, J. Jin, M. Grimau Puigibert, L. Giner, J. A. Slater, M. R. E. Lamont, V. B. Verma, M. D. Shaw, F. Marsili, S. W. Nam, D. Oblak, and W. Tittel, Phys. Rev. A 92, 012329, Published 27 July 2015.
> - Quantum teleportation across a metropolitan bre network, R. Valivarthi, M. Grimau Puigibert, Q. Zhou, G. H. Aguilar, V. B. Verma, F. Marsili, M. D. Shaw, S. W. Nam, D. Oblak, and W. Tittel, Nature Photonics 10, 676680, Published 19 September 2016.
>
> Thank you
>
> Kind regards

Figure A.13: Email from F. Marsili granting me permission to include co-authored papers.

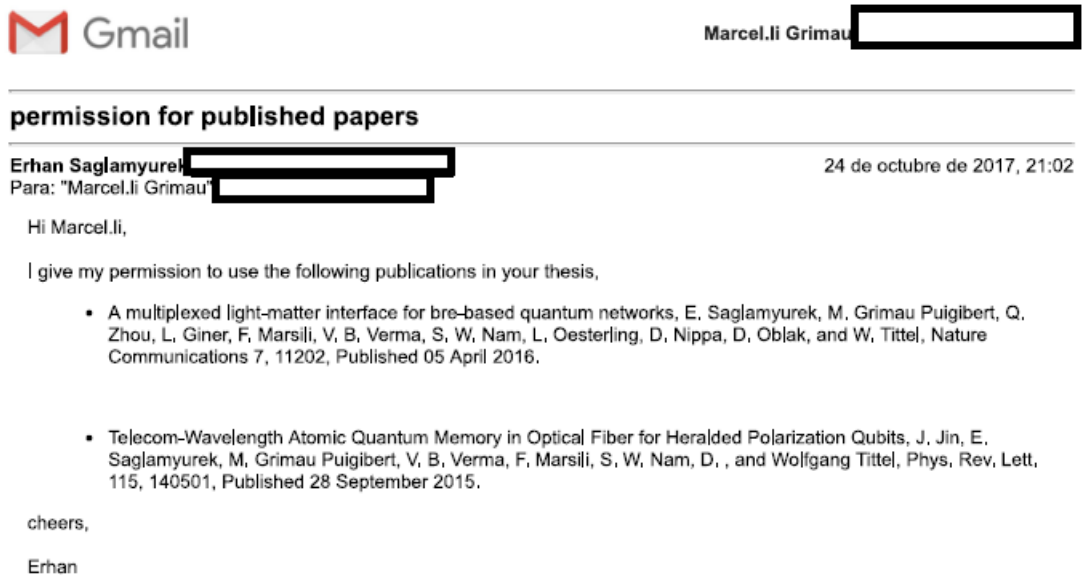

Gmail Marcel.li Grimau [redacted]

permission for published papers

Erhan Saglamyurek [redacted] 24 de octubre de 2017, 21:02
Para: "Marcel.li Grimau" [redacted]

Hi Marcel.li,

I give my permission to use the following publications in your thesis,

- A multiplexed light-matter interface for bre-based quantum networks, E. Saglamyurek, M. Grimau Puigibert, Q. Zhou, L. Giner, F. Marsili, V. B. Verma, S. W. Nam, L. Oesterling, D. Nippa, D. Oblak, and W. Tittel, Nature Communications 7, 11202, Published 05 April 2016.

- Telecom-Wavelength Atomic Quantum Memory in Optical Fiber for Heralded Polarization Qubits, J. Jin, E. Saglamyurek, M. Grimau Puigibert, V. B. Verma, F. Marsili, S. W. Nam, D. , and Wolfgang Tittel, Phys. Rev. Lett. 115, 140501, Published 28 September 2015.

cheers,

Erhan

Figure A.14: Email from E. Saglamyurek granting me permission to include co-authored papers.

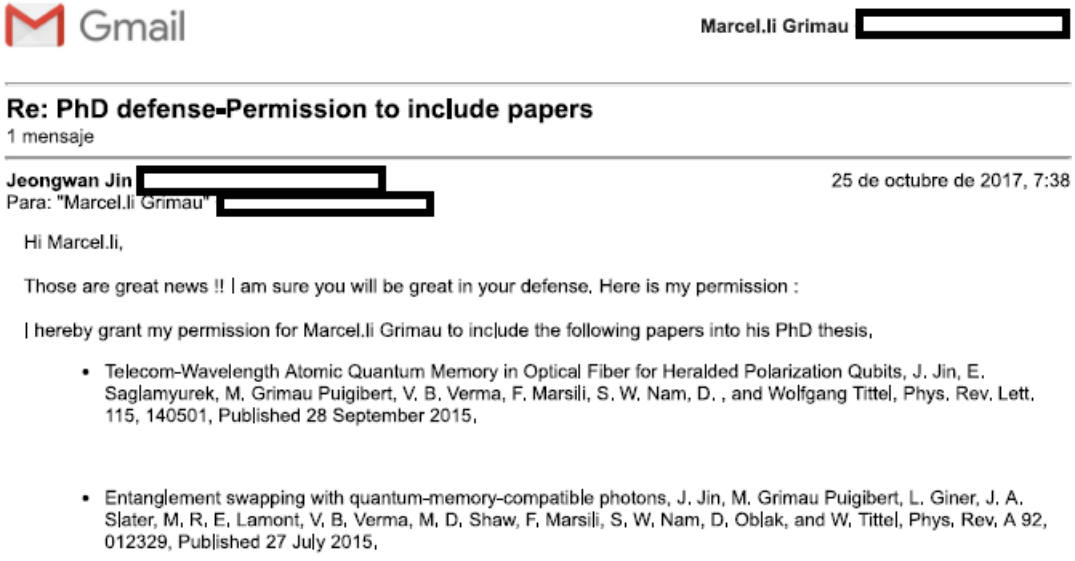

Gmail Marcel.li Grimau [redacted]

Re: PhD defense-Permission to include papers
1 mensaje

Jeongwan Jin [redacted] 25 de octubre de 2017, 7:38
Para: "Marcel.li Grimau" [redacted]

Hi Marcel.li,

Those are great news !! I am sure you will be great in your defense. Here is my permission :

I hereby grant my permission for Marcel.li Grimau to include the following papers into his PhD thesis,

- Telecom-Wavelength Atomic Quantum Memory in Optical Fiber for Heralded Polarization Qubits, J. Jin, E. Saglamyurek, M. Grimau Puigibert, V. B. Verma, F. Marsili, S. W. Nam, D. , and Wolfgang Tittel, Phys. Rev. Lett. 115, 140501, Published 28 September 2015,

- Entanglement swapping with quantum-memory-compatible photons, J. Jin, M. Grimau Puigibert, L. Giner, J. A. Slater, M. R. E. Lamont, V. B. Verma, M. D. Shaw, F. Marsili, S. W. Nam, D. Oblak, and W. Tittel, Phys. Rev. A 92, 012329, Published 27 July 2015,

Figure A.15: Email from J. Jin granting me permission to include co-authored papers.

Gmail Marcel.li Grimau [redacted]

Phys Rev A paper for thesis

Michael Lamont [redacted] 30 de octubre de 2017, 8:47
Para: [redacted]

Hi Marcel.li,

You are very welcome to use the following paper in your thesis:

Entanglement swapping with quantum-memory-compatible photons, J. Jin, M. Grimau Puigibert, L. Giner, J. A. Slater, M. R. E. Lamont, V. B. Verma, M. D. Shaw, F. Marsili, S. W. Nam, D. Oblak, and W. Tittel, Phys. Rev. A 92, 012329, Published 27 July 2015.

Best of luck!

Mike

Michael R.E. Lamont

Postdoctoral Associate
Adie Lab
Nancy E. and Peter C. Meinig School of Biomedical Engineering
Cornell University
B56 Weill Hall
Ithaca, NY 14853

Web : http://adie.research.engineering.cornell.edu

Figure A.16: Email from M. R. E. Lamont granting me permission to include co-authored papers.

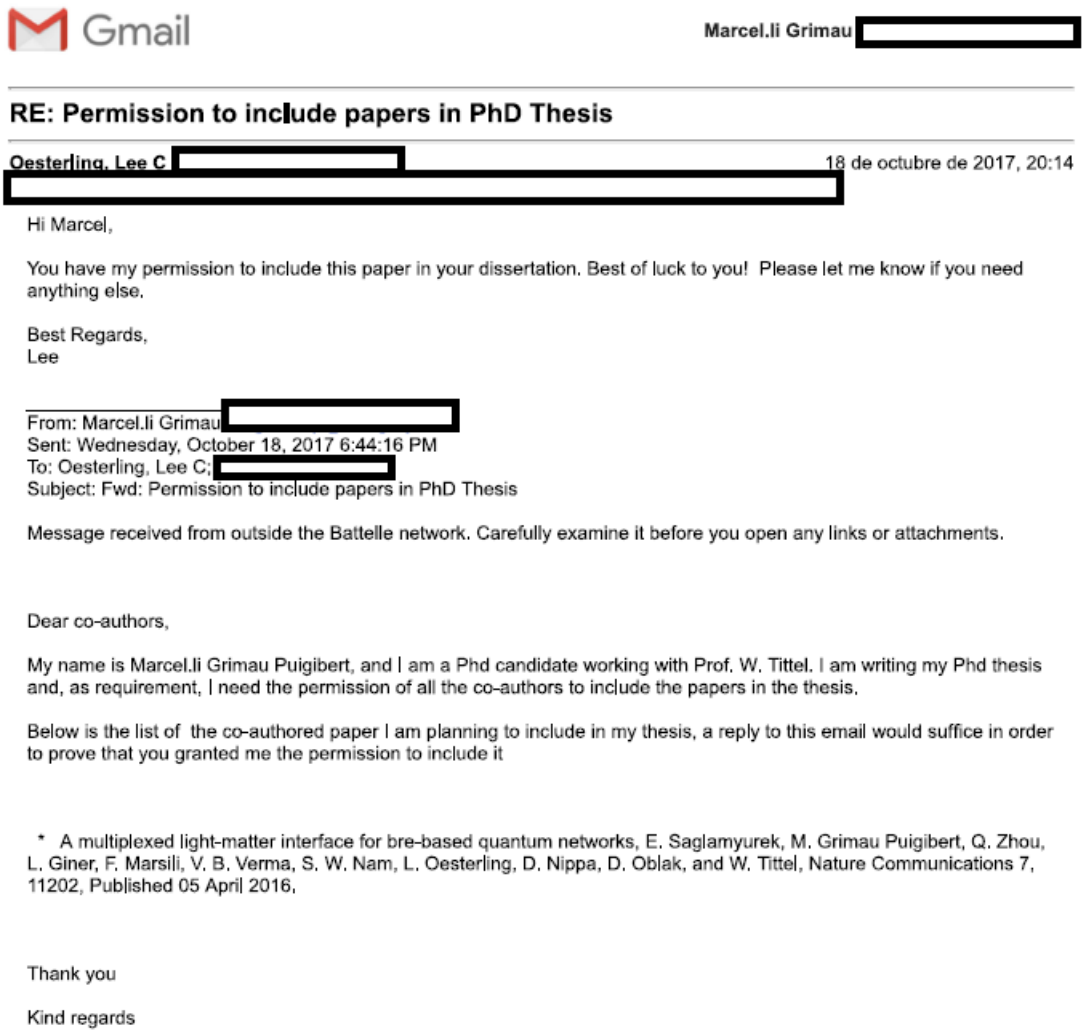

Gmail Marcel.li Grimau [redacted]

RE: Permission to include papers in PhD Thesis

Oesterling, Lee C [redacted] 18 de octubre de 2017, 20:14

Hi Marcel,

You have my permission to include this paper in your dissertation. Best of luck to you! Please let me know if you need anything else.

Best Regards,
Lee

From: Marcel.li Grimau [redacted]
Sent: Wednesday, October 18, 2017 6:44:16 PM
To: Oesterling, Lee C; [redacted]
Subject: Fwd: Permission to include papers in PhD Thesis

Message received from outside the Battelle network. Carefully examine it before you open any links or attachments.

Dear co-authors,

My name is Marcel.li Grimau Puigibert, and I am a Phd candidate working with Prof. W. Tittel. I am writing my Phd thesis and, as requirement, I need the permission of all the co-authors to include the papers in the thesis.

Below is the list of the co-authored paper I am planning to include in my thesis, a reply to this email would suffice in order to prove that you granted me the permission to include it

* A multiplexed light-matter interface for bre-based quantum networks, E. Saglamyurek, M. Grimau Puigibert, Q. Zhou, L. Giner, F. Marsili, V. B. Verma, S. W. Nam, L. Oesterling, D. Nippa, D. Oblak, and W. Tittel, Nature Communications 7, 11202, Published 05 April 2016,

Thank you

Kind regards

Figure A.17: Email from L. Oesterling granting me permission to include co-authored papers.

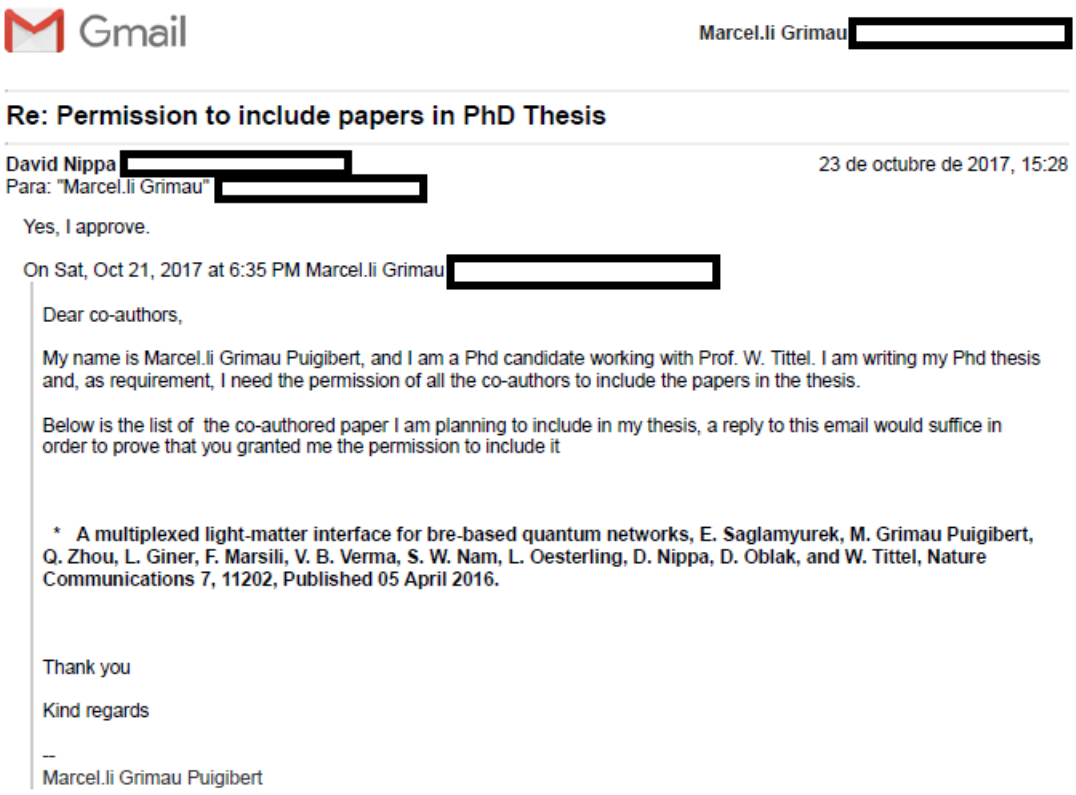

Gmail Marcel.li Grimau [redacted]

Re: Permission to include papers in PhD Thesis

David Nippa [redacted] 23 de octubre de 2017, 15:28
Para: "Marcel.li Grimau" [redacted]

Yes, I approve.

On Sat, Oct 21, 2017 at 6:35 PM Marcel.li Grimau [redacted]

> Dear co-authors,
>
> My name is Marcel.li Grimau Puigibert, and I am a Phd candidate working with Prof. W. Tittel. I am writing my Phd thesis and, as requirement, I need the permission of all the co-authors to include the papers in the thesis.
>
> Below is the list of the co-authored paper I am planning to include in my thesis, a reply to this email would suffice in order to prove that you granted me the permission to include it
>
> * **A multiplexed light-matter interface for bre-based quantum networks, E. Saglamyurek, M. Grimau Puigibert, Q. Zhou, L. Giner, F. Marsili, V. B. Verma, S. W. Nam, L. Oesterling, D. Nippa, D. Oblak, and W. Tittel, Nature Communications 7, 11202, Published 05 April 2016.**
>
> Thank you
>
> Kind regards
>
> --
> Marcel.li Grimau Puigibert

Figure A.18: Email from D. Nippa granting me permission to include co-authored papers.